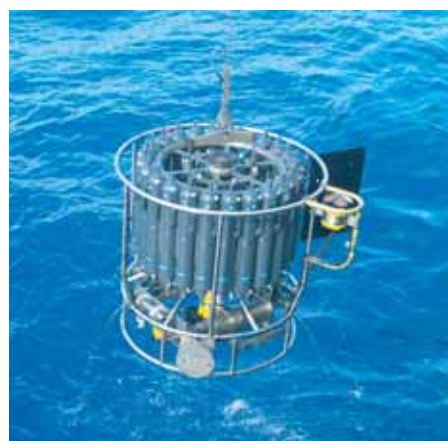




Developing and testing a hydrostatic
atmospheric dynamical core
on triangular grids

Hui Wan



Hinweis

Die Berichte zur Erdsystemforschung werden vom Max-Planck-Institut für Meteorologie in Hamburg in unregelmäßiger Abfolge herausgegeben.

Sie enthalten wissenschaftliche und technische Beiträge, inklusive Dissertationen.

Die Beiträge geben nicht notwendigerweise die Auffassung des Instituts wieder.

Die "Berichte zur Erdsystemforschung" führen die vorherigen Reihen "Reports" und "Examensarbeiten" weiter.



Notice

The Reports on Earth System Science are published by the Max Planck Institute for Meteorology in Hamburg. They appear in irregular intervals.

They contain scientific and technical contributions, including Ph. D. theses.

The Reports do not necessarily reflect the opinion of the Institute.

The "Reports on Earth System Science" continue the former "Reports" and "Examensarbeiten" of the Max Planck Institute.

Anschrift / Address

Max-Planck-Institut für Meteorologie
Bundesstrasse 53
20146 Hamburg
Deutschland

Tel.: +49-(0)40-4 11 73-0
Fax: +49-(0)40-4 11 73-298
Web: www.mpimet.mpg.de

Layout:

Bettina Diallo, PR & Grafik

Titelfotos:

vorne:

Christian Klepp - Jochem Marotzke - Christian Klepp

hinten:

Clotilde Dubois - Christian Klepp - Katsumasa Tanaka

Developing and testing a hydrostatic
atmospheric dynamical core
on triangular grids

Dissertation zur Erlangung des Doktorgrades der Naturwissenschaften
im Department Geowissenschaften der Universität Hamburg
vorgelegt von

Hui Wan

aus Hubei, China

Hamburg 2009

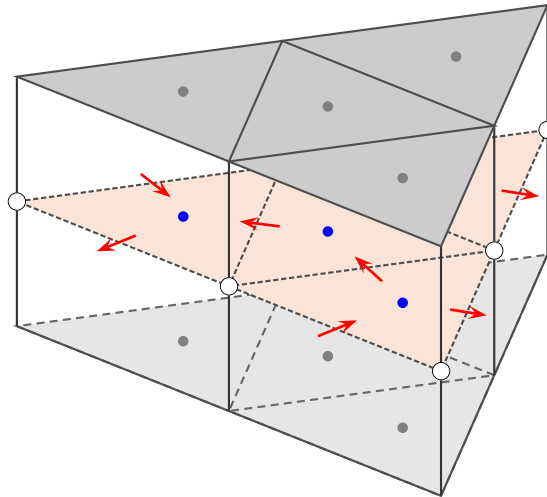
Hui Wan
Max-Planck-Institut für Meteorologie
Bundesstrasse 53
20146 Hamburg
Germany

Als Dissertation angenommen
vom Department Geowissenschaften der Universität Hamburg

auf Grund der Gutachten von
Prof. Dr. Guy Brasseur
und
Dr. Marco A. Giorgetta

Hamburg, den 30. Januar 2009
Prof. Dr. Jürgen Oßenbrügge
Leiter des Departments für Geowissenschaften

Developing and testing a hydrostatic atmospheric dynamical core on triangular grids



Hui Wan

Hamburg 2009

Abstract

Atmospheric general circulation models (AGCMs) view the atmosphere as a fluid, and simulate the time evolution of its three-dimensional (3D) motions. At the base of an AGCM is the so-called dynamical core which numerically solves the governing equations of the atmosphere. In recent years, non-conventional grids and finite-difference methods have gained popularity due to their suitability for massively parallel computing and for achieving important conservation properties. The joint project ICON initiated by the Max Planck Institute for Meteorology and the German Weather Service aims at developing new dynamical cores for climate research and numerical weather forecast using the spherical triangular grid. The study presented in this thesis is carried out within this project. Based on a two-dimensional (2D) testbed developed before this work, a 3D hydrostatic atmospheric dynamical core is established.

In order to facilitate the comparison with already-existing models, the new dynamical core is constructed by combining the horizontal discretization of the ICON 2D model with a set of numerical schemes widely used for vertical discretization and time integration. Since the vertical discretization scheme was originally designed for latitude-longitude mesh, adaptations are made to apply it to the triangular grid. As for the horizontal discretization, a theoretical analysis is performed to assess the accuracy of the differencing operators. It is found that the divergence operator defined on a single triangle according to the Gauss's theorem introduces grid-scale noise. This noise is reduced by the leading error of the discrete Laplace operator. The impact of the compensating error terms is discussed. Possible ways to get rid of this artifact and achieve higher accuracy are also investigated.

The performance of the new dynamical core is evaluated in a series of idealized experiments. Results show that the new model can successfully simulate important barotropic and baroclinic processes. Good numerical stability is observed both in deterministic tests and in an idealized climate simulation. When the horizontal resolution is increased, a clear trend of convergence is observed in the numerical solutions. In the most challenging baroclinic vortex test, the simulations from the new model with a 64 km grid size compare well with the reference solution. In the barotropic test cases, high-quality results are obtained already at lower resolutions. The new dynamical core thus forms a good basis for a full AGCM.

Contents

1	Introduction	1
1.1	Potential problems in models employing the spectral transform method	1
1.2	The ICON project in a new trend in atmospheric model development	2
1.3	Intermediate steps towards the long-term goal	4
1.4	Research topic and outline of this thesis	6
2	The triangular grid and horizontal differencing operators	9
2.1	The horizontal grid	9
2.1.1	Triangles on the sphere	9
2.1.2	C-type staggering	11
2.1.3	Grid optimization	12
2.1.4	Notations for topology and geometry	14
2.2	Discrete operators used in the ICON shallow water model	15
2.3	Truncation error of the discrete operators	16
2.3.1	The uniform grid on a plane	17
2.3.2	Pointwise values and averages	17
2.3.3	The basic differencing operators	20
2.3.4	Laplace operator for scalar function and vector field	24
2.3.5	Horizontal diffusion	26
2.3.6	Reducing the grid-scale noise in divergence	28
2.4	Impact of the irregularity of the spherical triangular grid	30
2.4.1	Inequality of the grid spacing	30
2.4.2	Deformation of the triangular cells	33
3	Discrete formulation of the icosahedral hydrostatic dynamical core	35
3.1	The hybrid vertical coordinate and the 3D grid system	35
3.2	Overview of the discrete formulation	38
3.3	Horizontal interpolation of scalar and vector fields	40
3.4	The continuity equation	41
3.5	Vorticity flux and kinetic energy gradient	41
3.6	Advection of momentum and temperature	43
3.6.1	Vertical advection	43
3.6.2	Horizontal advection of temperature	43

3.7	Hydrostatic equation and pressure gradient force	45
3.8	Adiabatic heating	47
3.9	Time integration	48
3.9.1	Leap-frog scheme with Asselin filter	48
3.9.2	The basic idea of the semi-implicit approach	49
3.9.3	Application of the semi-implicit scheme in the hydrostatic dynamical core	50
3.9.4	Solving the divergence equation	52
4	Evaluation of the hydrostatic dynamical core	53
4.1	Introduction	53
4.2	Rossby-Haurwitz wave	57
4.2.1	Rossby-Haurwitz wave and barotropic instability	57
4.2.2	Rossby-Haurwitz wave as a test case	58
4.2.3	The steady propagation of wavenumber four	61
4.2.4	A dynamically unstable case	63
4.3	Mountain-induced Rossby wave train	67
4.4	Jablonowski-Williamson steady state test	73
4.4.1	Initial conditions and diagnostics	73
4.4.2	Results from the spectral dynamical core	75
4.4.3	Experiments with the ICOHDC	75
4.5	Jablonowski-Williamson baroclinic wave test	81
4.5.1	Reference solution from the dynamical core of ECHAM5	81
4.5.2	Experiments with the ICOHDC	84
4.5.3	Sensitivity of the numerical solution to horizontal resolution	87
4.5.4	Impact of the modification in the divergence operator	92
4.6	Held-Suarez test	96
4.6.1	Test specification	97
4.6.2	Reference solution from the spectral model	98
4.6.3	Experiments with the ICOHDC	98
4.6.4	The simulated climate state	101
4.6.5	Sensitivity to horizontal resolution	104
5	Summary and outlook	107
5.1	Summary	107
5.2	Outlook	111
A	The primitive equations: assumptions and conservation properties	113
B	Derivation of the truncation error of the horizontal differencing operators	118
B.1	Taylor expansion of the edge average	118
B.2	Truncation error of the normal gradient operator	119
B.3	Truncation error of the curl operator	120
B.4	Truncation error of the divergence operator	123

B.5	The cell-averaged divergence of a particular vector field	126
B.6	Truncation error of the scalar Laplacian	128
B.7	Truncation error of the vector Laplacian	130
C	Notes on linear horizontal diffusion in numerical models	133
C.1	Damping effect in the continuous case	133
C.2	Damping time and stability in the discrete case	135
C.2.1	The temporally discretized cases	135
C.2.2	The fully discretized 1D problem	135
C.2.3	Numerical stability	136
D	Horizontal wind reconstruction using the radial basis functions	137
E	Supplementary figures	139
	Bibliography	145
	Acknowledgements	153

Chapter 1

Introduction

This chapter presents the background and provides an overview of the work presented in this thesis. Section 1.1 justifies the need for establishing new model systems for numerical weather prediction and climate research. Section 1.2 highlights the key features of the development in the ICON project, and Section 1.3 introduces the intermediate steps that are needed to reach the challenging long-term goal. The task carried out in this thesis is briefly introduced in Section 1.4 together with the outline of the contents of the thesis.

1.1 Potential problems in models employing the spectral transform method

Atmospheric general circulation models (AGCMs) are an important tool for numerical weather prediction (NWP) and atmospheric research, as they represent the three-dimensional (3D) structure of the atmosphere and its time evolution. The part of an AGCM that numerically solves the governing equations of the adiabatic dynamics of the atmosphere is usually called the dynamical core. The most commonly used numerical methods in dynamical cores include finite-difference/finite-volume methods and the series-expansion approach. In the so-called spectral models, the horizontal structure of the atmospheric state variables is represented as a truncated series of spherical harmonics. Since the development of the transform method by Orszag (1970) and Eliassen *et al.* (1970), spectral models – or more precisely, spectral transform models – have been playing a particularly important role in atmospheric sciences.

The spectral transform method has some distinct advantages. First of all, solutions of high accuracy can be achieved when the simulated flow is relatively smooth; Second, due to the fact that the spherical harmonics are eigenfunctions of the Laplace operator, semi-implicit time stepping schemes can be conveniently applied, allowing for longer time steps at relatively low computational costs. Furthermore, the adiabatic dynamics of the atmosphere can essentially be described as a set of multi-dimensional wave propagation problems. The use of spherical harmonics as the basis functions for series expansion suits this type of problems very well. Com-

pared to finite-difference models, spectral models usually produce much smaller phase errors, especially at medium and low resolutions. Due to these merits, spectral models prevailed worldwide at operational weather forecast centers in the 1980's and 1990's, and are still widely used today.

As the computer power develops further at a dramatic rate, and as the applications of the numerical simulations keep extending rapidly, spectral transform method starts to show some serious limitations. One example is the transform between spectral and grid point spaces, which has to be performed at each time integration step. This operation requires information from the whole computational domain. High scalability is hence not easy to achieve in massively parallel computing using distributed memory.

Another well-known fact about the spectral method is that it is not at all a good choice for handling tracer transport processes, since it does not guarantee mass conservation or monotonicity. In most of the spectral AGCMs that are operationally used in NWP and atmospheric research, the large-scale advection of water vapour (in some cases cloud ice and cloud water as well) are treated with a different method, for instance the semi-Lagrangian, finite-difference, or finite-volume methods. An exception is the AGCM3 of the Canadian Centre for Climate Modelling and Analysis (Scinocca *et al.*, 2008), which uses the spectral transform method to transport a hybrid moisture variable that is a function of the specific humidity (Boer, 1995; Merryfield *et al.*, 2003). This treatment alleviates the tendency to develop negative values associated with spectral advection, whilst exact conservation of tracer mass has to be enforced by a *posteriori* correction.

As the traditional climate modelling gradually extends its scope and includes biogeochemical processes, a large number of chemical species or aerosols that exist in the atmosphere and play important roles in the climate system are introduced into numerical models. This has posed new challenges on numerical advection schemes. In particular, it has been recognized that if the mass conservation law of the atmosphere (which is a part of the governing equations) and that of the tracers are numerically approximated in independent ways, large errors can appear – not only in the concentration of each individual tracer, but also in the correlation between different species, which in turn causes biases in atmospheric chemistry. This issue has drawn a lot of attention in recent years (e.g., Lin and Rood, 1996; Jöckel *et al.*, 2001; Gross *et al.*, 2002; Ringler and Randall, 2002a). Examples of this kind of problem have been experienced in the climate model ECHAM5 of the Max Planck Institute for Meteorology, as well. Although meticulous design and careful implementation of a relatively robust transport scheme can alleviate the problem to some extent, the ultimate solution resides in a consistent discretization for both the continuity equation and the tracer mass equation.

1.2 The ICON project in a new trend in atmospheric model development

In the mid-1990's, the AGCM development community started revisiting the finite-difference method and moving towards the next generation of dynamical cores. In the history of numerical weather prediction, finite-difference was the choice of Lewis F. Richardson in his pioneering but

unsuccessful attempt (Richardson, 1922; Lynch, 2006); It was also the method that led to the early success in the 1950's and 60's (e.g., Charney *et al.*, 1950). The loss of its popularity in the following decades was closely related to the nice properties of the spectral transform method mentioned in the previous section. A disadvantage that is often believed as inherent to the finite-difference models is the strong Courant-Friedrichs-Lewy constraint on time step. In the polar regions the converging meridians in the latitude-longitude grid lead to extremely small zonal grid sizes compared to the equatorial areas. A longitudinal filter is hence needed to strongly damp short waves which otherwise would impose a very short time step on the integration. It is foreseeable that this issue would become even more prominent in the future since the ever-growing computer power will allow for simulations of high resolutions that were only a dream in the early years of AGCM development.

To address this problem, "reduced" latitude-longitude grids were proposed, in which the number of computational points along a constant latitude line decreases toward the poles. Different reduction algorithms were introduced (e.g., Gates and Riegel, 1962; Kurihara, 1965; Hortal and Simmons, 1991; Courtier and Naughton, 1994) and their impact on the discretization error investigated. It seems that the reduced grid is less suitable for finite difference models than for spectral transform models, because the longer longitudinal increment near the poles tends to introduce large discretization errors in gradient terms involving spherical coordinate vector components (Williamson and Browning, 1973; Williamson and Rosinski, 2000).

Seeing these problems, many of the modelling groups that were starting new grid-point model developments decided to use totally different horizontal grids to obtain quasi-uniform coverage of the sphere. Examples of the nonconventional grids include the cubed sphere (Giraldo and Rosmond, 2004; Nair *et al.*, 2004), the icosahedral hexagonal or triangular grids (Heikes and Randall, 1995a,b; Thuburn, 1997; Giraldo, 2000; Majewski *et al.*, 2002; Tomita *et al.*, 2001; Bonaventura and Ringler, 2005), the Fibonacci grid (Swinbank and Purser, 2006) and the Yin-Yang grid (Li *et al.*, 2008). Non-spectral methods on nonconventional grids – this becomes the key feature of the next generation of GCMs.

The idea of using the icosahedral grid for atmospheric modelling is in fact not really new. The earliest work seen in the literature dates back to the year 1968, when Williamson and Sadourny *et al.* independently discussed the feasibility of solving the nondivergent barotropic vorticity equation using finite-difference methods and triangular meshes derived from the icosahedron. Later the case of the two-dimensional (2D) divergent flow was investigated (Williamson, 1969; Sadourny and Morel, 1969; Williamson, 1970), and alternative grid configurations were considered as well (Sadourny and Morel, 1969). Cullen (1974) used a similar grid to solve the 2D nonlinear problem, but applied the finite-element method. Unfortunately these initial efforts didn't bring forth an approach that was – in terms of accuracy and efficiency – comparable to the then-emerging spectral transform method. To a large extent, this was due to the significant numerical error induced by irregularities in the icosahedral grids at the low resolutions employed at that time. Research in this direction then came to a halt.

About ten years later, Baumgardner and Frederickson (1985) designed a recursive algorithm to derive from the icosahedron a nearly uniform triangulation of the sphere. They demonstrated that using spherical barycentric coordinates, a fully second-order accurate finite-volume formu-

lation could be obtained. This work, although originally used in modelling mantle convection, actually triggered the new trend mentioned above in AGCM development.

By the year 2001, a number of shallow water models had been established on different versions of the icosahedral grids (Masuda and Ohnishi, 1986; Heikes and Randall, 1995a,b; Thuburn, 1997; Stuhne and Peltier, 1996, 1999; Giraldo, 2000; Tomita *et al.*, 2001). Some of these works went further. In December 1999, the 3D global model GME (Majewski *et al.*, 2002) and its data assimilation system started providing operational weather forecast at the German Weather Service; At the Colorado State University, the shallow water model of Heikes and Randall (1995a,b) evolved to a 3D AGCM (Ringler *et al.*, 2000); At the Frontier Research Center for Global Change in Japan, the high-resolution nonhydrostatic global model NICAM has been established (Tomita and Satoh, 2004; Satoh *et al.*, 2008).

In 2001, the Max Planck Institute for Meteorology (MPI-M) and the German Weather Service (DWD) decided to put expertise together and develop a new unified model system for global Earth System simulations. A joint project was initiated to design icosahedral nonhydrostatic (ICON) dynamical cores of high resolution with the functionality of local zooming. For the climate research at MPI-M, it is planned that this new model system will contain a consistent numerical approximation to the adiabatic dynamics of the atmosphere and the tracer transport processes, so that the *a posteriori* corrections used in the spectral model ECHAM5 can be avoided and a better basis can be provided for the modelling of chemistry related processes. Moreover, the possibility of local zooming can provide sufficient accuracy in regions of, e.g., complex topography, and at the same time keep the overall computational expense affordable in the long-term climate simulations. For the operational weather services at DWD, the high-resolution global- and regional-scale weather forecasts can then be unified in a single system that solves the fully compressible nonhydrostatic equations.

1.3 Intermediate steps towards the long-term goal

A global high-resolution nonhydrostatic AGCM on nonconventional horizontal grids with local grid refinement is a challenging goal that can only be achieved in steps. The first research activity in the ICON project was the development of a shallow water prototype that solves the hyperbolic equations

$$\frac{\partial \mathbf{v}}{\partial t} = -(f + \xi) \mathbf{k} \times \mathbf{v} - \nabla K - \nabla h, \quad (1.1)$$

$$\frac{\partial h}{\partial t} = -\nabla \cdot (\mathbf{v}h) . \quad (1.2)$$

Here \mathbf{v} is the velocity vector; h is the height of the fluid surface; \mathbf{k} is the local unit vector pointing to the upward direction; f and ξ denote the Coriolis parameter and relative vorticity ($\xi := \nabla \times \mathbf{v} \cdot \mathbf{k}$), respectively; K is the kinetic energy per unit mass ($K := \frac{1}{2} \mathbf{v} \cdot \mathbf{v}$). The shallow water equations represent the hydrodynamics of an incompressible fluid on the rotating sphere. Although there are only two spatial dimensions, many of the physical phenomena that are described by the full 3D governing equations can already be found in this system, including slow

and balanced rotational motions and fast gravity waves. The shallow water system is thus a useful testbed for new numerical designs.

During the development of the ICON shallow water prototype, it has been decided that the velocity equation in the discrete model takes the form of Eqn. (1.1) (i.e., the so-called invariant vector form); The prognostic variables – velocity and fluid depth (mass) – are predicted at different locations of the horizontal domain. Each mass point is assigned to a triangle as its control volume (see also Section 2.1). The horizontal discretization scheme and time integration methods are also defined. In a series of standard numerical tests, the prototype with global uniform resolution has produced encouraging results (Bonaventura and Ringler, 2005), indicating that the selected numerical techniques can provide a good basis for the more complex 3D problems.

It is worth pointing out that compared to the other new AGCM dynamical cores that are under development or active in operation, the grid configuration and discretization schemes used in ICON are unique. GME and NICAM are both discretized on unstaggered grids with all the prognostic variables located at vertices of the spherical triangles (Majewski *et al.*, 2002; Tomita and Satoh, 2004; Satoh *et al.*, 2008). In the model of Ringler *et al.* (2000), the grid points are defined in the same way, although the vorticity-divergence formulation of the governing equations are used instead of the momentum formulation. The resulting discrete grid system was named the Z-grid. Ringler and Randall (2002a,b) have proposed the alternative ZM-grid that places mass at the vertices of the triangles and velocity at the triangle centers. In all these models, the control volume of mass points are hexagons, while, in contrast, the ICON shallow water model utilizes a staggered grid that has triangular control volumes.

One of the main reasons for choosing staggered grids for ICON was the well-known conclusion that on a rectangular mesh, this arrangement of discrete variables displays superior wave propagation behaviour compared to the unstaggered grid in simulating the process of geostrophic adjustment (Winninghoff, 1968; Arakawa and Lamb, 1977; Randall, 1994). However, when the cell shape changes from a regular rectangle to a triangle, the traditional tool for wave propagation analysis can no longer be applied in a straightforward way. There is not yet a conclusive answer to the question how this theoretical analysis should be carried out and the results interpreted (Bonaventura *et al.*, 2006, unpublished). In the standard numerical tests of the shallow water model (Williamson *et al.*, 1992), no evident discrepancies have been observed between the converged high-resolution solutions produced by the ICON prototype and those from the other 2D models. Performance of the ICON prototype is neither evidently superior nor clearly inferior to other models employing an unstaggered grid. It is worth noting that in the shallow water test suite, the two test cases representing the generation and propagation of the Rossby wave are commonly regarded as the most dynamically interesting ones and have become *de facto* standard tests. Given the fact that the Rossby wave is essentially a solution to the *nondivergent barotropic* vorticity equation, the lack of distinct differences among model results might also have resulted from the incompleteness of the test suite as well as the simplifications involved in deriving the 2D problem. To find out whether this is true, it is probably necessary to apply the same numerical methods to a similar but more complex problem.

Till today, most of the 3D dynamical cores applied to global weather forecast (20 – 60 km horizontal resolution) and climate simulations (100 – 300 km) have not yet considered the vertical

acceleration of air parcels. Nonhydrostatic models are mainly used in regional models of limited area and very high resolution (3 – 30 km). In a generic pressure-based vertical coordinate η , the governing equations of the atmosphere under the hydrostatic assumption can be derived following Kasahara (1974). This equation set, also known as the primitive equations, reads

$$\frac{\partial \mathbf{v}}{\partial t} = - (f + \xi) \mathbf{k} \times \mathbf{v} - \nabla K - \dot{\eta} \frac{\partial \mathbf{v}}{\partial \eta} - \frac{R_d T}{p} \nabla p - \nabla \phi \quad (1.3)$$

$$\frac{\partial T}{\partial t} = - \mathbf{v} \cdot \nabla T - \dot{\eta} \frac{\partial T}{\partial \eta} + \frac{R_d T}{C_p} \frac{dp}{dt} \quad (1.4)$$

$$\frac{\partial}{\partial t} \left(\frac{\partial p}{\partial \eta} \right) = - \nabla \cdot \left(\mathbf{v} \frac{\partial p}{\partial \eta} \right) - \frac{\partial}{\partial \eta} \left(\dot{\eta} \frac{\partial p}{\partial \eta} \right) \quad (1.5)$$

$$0 = \frac{\partial \phi}{\partial \eta} + \frac{R_d T}{p} \frac{\partial p}{\partial \eta}. \quad (1.6)$$

Here p and T denote pressure and temperature, respectively. ϕ is geopotential, R_d is the gas constant of dry air, and C_p is the specific heat capacity of dry air under constant pressure. (Note that here and throughout this thesis we have ignored the water substances in the atmosphere. In most AGCMs with representations of the moist processes, the governing equations are generalized for moist air by replacing temperature by the virtual temperature in Eqns. (1.3) and (1.6), and the last term in the thermodynamic equation (1.4).)

Comparing Eqns. (1.3) – (1.6) with the shallow water system, we see clearly that a large part of the right-hand-side terms in the hydrostatic equations are essentially the same as in the 2D system. Yet the newly introduced terms bring along different dynamics and additional challenges. The last two terms in the velocity equation have been known for long time as subject to large numerical error in the vicinity of steep orography when a terrain-following vertical coordinate is used. The adiabatic heating term in the temperature equation which converts energy between different forms, also needs to be handled with care.

Beyond the shallow water test cases, quantitative evaluation of AGCM dynamical cores becomes very difficult, mainly because a generic solution to the nonlinear 3D governing equations does not exist. In the AGCM development community, in-depth model evaluations are often carried out through intercomparison between different models. The two institutions that have initiated the ICON project each have a well-established hydrostatic model (ECHAM5 and GME, respectively). Both models have employed the Simmons and Burridge (1981) scheme for vertical discretization. It is thus a reasonable choice to extend the ICON shallow water model to a hydrostatic dynamical core using this vertical differencing, and compare the new dynamical core with the two existing models. In this way we will be able to evaluate the impact of the newly designed schemes on the triangular grid in a clean manner.

1.4 Research topic and outline of this thesis

In this thesis a hydrostatic atmospheric dynamical core is established on an icosahedral grid with triangular control volume by combining the horizontal differencing operators of the ICON shallow water model and the vertical and temporal discretization schemes proposed by Simmons

and Burridge (1981). The new dynamical core is referred to as the ICOHDC, and its performance is evaluated in a series of idealized tests. The spectral transform dynamical core of the ECHAM5 model is used as the reference model.

The contents of the thesis are arranged as follows:

Chapter 2 introduces the spherical triangular grid and the horizontal differencing operators used in the ICON shallow water model, which are important building blocks for the hydrostatic dynamical core. Truncation error analysis is performed in the context of a regular grid in planar geometry, shedding some light on the properties of the triangular mesh and the accuracy of the discrete operators. For completeness, the analysis is performed for all the horizontal differencing operators used in the ICON 2D testbed. Several different viewpoints that may have implications for the conclusions are taken into account. The detailed derivations are presented in Appendix B. In Chapter 2, in order to avoid distraction from the continuous thread of the thesis, we focus only on the divergence and Laplace operators. The horizontal diffusion scheme is also discussed, and some supplementary materials are provided in Appendix C. The impact of the irregularity of the spherical grid is investigated in the last section of Chapter 2.

Chapter 3 describes in detail the vertical coordinate used in the dynamical core, the complete formulation of the spatially discretized hydrostatic equations, as well as the time integration schemes. The conservation properties of the schemes are discussed.

In Chapter 4 the ICOHDC is tested in numerical experiments. The selected test cases include the generation and propagation of barotropic waves, the formation of cyclone-like structures through the evolution of baroclinic instability, and one idealized dry climate simulation that reveals the long-term response of the ICOHDC to analytically prescribed forcing. The convergence properties of the numerical solutions are assessed with respect to horizontal resolution. The quality of the results obtained with the new model is compared with that of the simulations from the ECHAM5 dynamical core.

Chapter 5 summarizes the conclusions and highlights of this thesis. It also opens the discussion about the future steps.

Chapter 2

The triangular grid and horizontal differencing operators

This chapter introduces the spherical grid and the horizontal discretization schemes used in the new hydrostatic dynamical core. The spherical triangular grid system is inherited from the ICON shallow water model without any modification. For completeness, a short description of the grid generation and optimization procedures are included in the first section. The approximation schemes for the spatial derivatives – referred to as the discrete operators in this thesis – are then introduced. Truncation error analysis is performed for the operators in the context of planar geometry. Possible modifications of the operators are also discussed.

2.1 The horizontal grid

In order to represent the three-dimensional structure of the atmospheric motions, a discrete grid system consisting of a finite number of grid points needs to be constructed. This section introduces the horizontal mesh employed by the ICON shallow water model and the hydrostatic dynamical core. The description of the vertical grid is deferred until the next chapter.

2.1.1 Triangles on the sphere

The ideal way to obtain a horizontal mesh of uniform resolution would be to project onto the sphere a convex regular polyhedron (Platonic solid) which had as many faces as we wished. However, the only Platonic solids consisting of triangles are the tetrahedron, octahedron, and icosahedron, among which the icosahedron has the biggest number of faces.

The grid generation algorithm used here starts from inscribing an icosahedron inside the unit sphere, with two of its twelve vertices coinciding with the North and South Poles. The other five vertices in each hemisphere are spaced at equal longitude intervals of 72° . The latitudinal

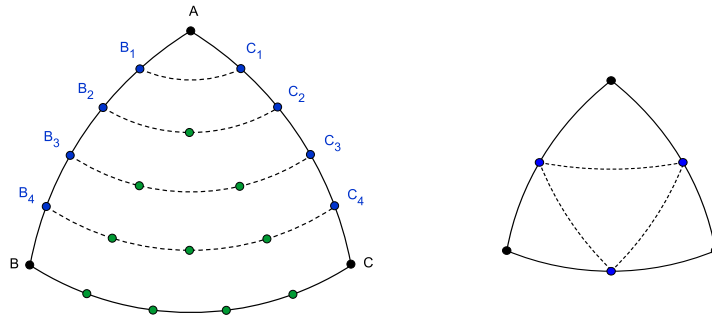


Fig. 2.1: The basic method of generating a triangle grid from an icosahedron. Left: Root division of the spherical icosahedron (after Sadourny *et al.*, 1968); Right: Division of a spherical triangle into four pieces via bisection of the edges. See Section 2.1.1 for the details.

location is

$$\varphi = \frac{\pi}{2} - 2 \arcsin \left(\sqrt{\frac{2}{5 + \sqrt{5}}} \right) \approx 26.565^\circ . \quad (2.1)$$

The twelve vertices define a mesh consisting of twenty identical spherical triangles bounded by thirty geodesic arcs. The great circle arcs connecting each pair of vertices have a length of about 7054 km if the mean radius of the Earth is assumed to be 6371 km. This mesh is designated as grid level -1 in this thesis. To obtain from level -1 a triangular mesh at the desired resolution, a "root division" of the icosahedron edges is performed which is then followed by successive bisection of the triangle edges.

For the root division the algorithm of Sadourny *et al.* (1968) is used: Let ABC be a spherical triangle at grid level -1 (see the left panel of Fig. 2.1). Divide edges AB and AC into n_r equal arcs, with n_r being a small number (typically 2, 3, 5 or 7). The division points are labeled B_1, B_2, \dots, B_{n_r} and C_1, C_2, \dots, C_{n_r} , with B_{n_r} and C_{n_r} coinciding with B and C , respectively. For each integer $i \in [1, n_r]$, connect B_i and C_i with a great circle arc and divide it into i equal arcs. Then connect the new division points on neighbouring arcs, again with great circle arcs, to form smaller triangles. The mesh obtained by this procedure is named grid level 0. From this level on, only the twelve icosahedron vertices are surrounded by five triangular faces; All the other newly introduced points are shared by six faces. Moreover, the triangles are no longer equilateral or identical, although the irregularity occurs equally in each of the 20 faces of the icosahedron.

Further refinement of the global grid is done by successively connecting the midpoints of the three edges of each triangle with great circle arcs, yielding four smaller triangles (Fig. 2.1, right panel). After obtaining grid level n_b via the initial root division in n_r sections and n_b bisections, the original icosahedron edges are divided into $n_r 2^{n_b}$ equal arcs. Throughout this thesis, the resulting grid is referred to as the "R n_r B n_b grid" or "R n_r B n_b resolution". The total number of triangle cells, edges and vertices read

$$n_c = 20 n_r^2 4^{n_b} , \quad (2.2)$$

$$n_e = 30 n_r^2 4^{n_b} , \quad (2.3)$$

$$n_v = 10 n_r^2 4^{n_b} + 2 , \quad (2.4)$$

Tab. 2.1: Total number of triangle faces, edges and vertices at various grid levels. The numbers correspond to the root division $n_r = 2$. The rightmost column shows the length of the triangle edges along the original icosahedron edge, assuming the Earth’s radius is 6371.229 km.

grid level	number of triangle cells (n_c)	number of triangle edges (n_e)	number of triangle vertices (n_v)	characteristic edge length
-1	20	30	12	7053.90 km
0	80	120	42	3526.95 km
1	320	480	162	1763.47 km
2	1280	1920	642	881.74 km
3	5120	7680	2562	440.87 km
4	20480	30720	10242	220.43 km
5	81920	122880	40962	110.22 km
6	327680	491520	163842	55.11 km
7	1310720	1966080	655362	27.55 km

respectively. Tab. 2.1 shows the values of n_c , n_e and n_v for various grid levels in the special case of $n_r = 2$. This triangulation of the sphere is in fact a Delaunay triangulation, meaning none of the triangle vertices lies inside the circumcircle of any other triangle.

2.1.2 C-type staggering

In the numerical simulation of geophysical flows, the Arakawa C-grid (Arakawa and Lamb, 1977) is widely used. The discrete mass values are located at the center of grid cells, while the normal velocity component at a boundary between two cells is computed at the midpoint of the boundary. The popularity of this specific choice is mainly due to the fact that when the finite difference method is employed to discretize the velocity-mass form of the shallow water equation, the C-type staggering simulates the geostrophic adjustment well in the sense that the dispersion of the linear waves is well represented (Winninghoff, 1968; Arakawa and Lamb, 1977; Randall, 1994).

In order to apply the C-staggering to the triangular cells, the definition of cell center needs to be clarified. Here the circumcenter is used as the mass point, resulting in an important feature that the arc connecting two neighbouring mass points is orthogonal to and bisects the boundary between the corresponding triangles. These bisection points are used as velocity points, and the staggered triangular grid is referred to as the primal grid (Fig. 2.2, left). This naturally allows calculating the divergence of each grid cell using the Gauss’s theorem.

The horizontal grid constructed in this way provides a quasi-uniform coverage of the sphere, thus solving automatically the pole problem caused by the convergence of the meridians in a geographical latitude-longitude grid. The hierarchical structure of the grid provides a very natural setting for multi-grid and multi-resolution approaches. The use of triangular cells as control volumes allows for straightforward development of mass-conserving local refinement approaches (Bonaventura and Ringler, 2005).

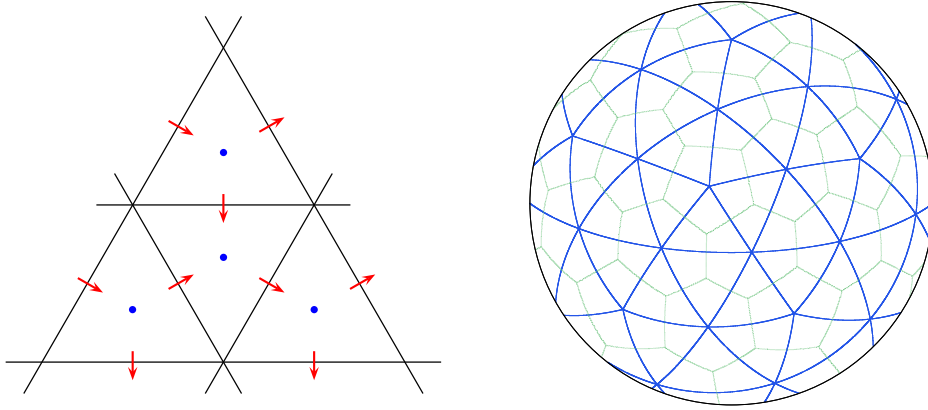


Fig. 2.2: Left: Schematic plot of the triangular C-grid. The blue dots are the mass points and the red arrows indicate the velocity component normal to each edge. Right: the Delaunay-Voronoi mesh. In this thesis the grid indicated by the blue lines is referred to as the primal grid. The green mesh obtained via connecting centers of the neighbouring triangles by great circle arc is referred to as the dual mesh.

Connecting the mass points yields the dual mesh consisting of 12 pentagons and $(n_v - 12)$ hexagons where n_v denotes the number of vertices of the primal grid (Fig. 2.2, right panel). The dual cells are Voronoi cells, meaning that each of them is the set of all points on the sphere closer to the cell center than to any other of the triangle vertices. Since the normal component of the velocity at a primal edges is also the tangential component with respect to the corresponding dual edge, it is a natural choice to locate the discrete relative vorticity at the vertices of the triangles and calculate its value using the Stokes' theorem.

2.1.3 Grid optimization

The grid generation procedure described above ensures that each edge of the dual grid bisects orthogonally the corresponding primal edge. However, there is no guarantee that the cross point bisects the dual edge as well. Heikes and Randall (1995b) have shown that when the horizontal resolution increases, the maximum off-centering[†] does not converge to zero but levels off (see Fig. 2 therein and Tab. 2.2 in this section). In the shallow water model of Heikes and Randall (1995a), this leads to the problem that the discrete Laplace operator defined at the center of the hexagonal/pentagonal cells is inconsistent because the numerical error does not vanish as the cell size approaches zero.

To solve this problem, Heikes and Randall (1995b) designed a grid optimization algorithm. Each time the horizontal resolution is increased by one grid level, the newly introduced triangle vertices are allowed to position themselves so as to minimize the cost function defined as the sum of the fourth power of the off-centering at all Voronoi edges.

Although in the ICON shallow water model and the new hydrostatic dynamical core there is no need for calculating the Laplacian at the Voronoi cell centers, the relative vorticity has to be

[†]The off-centering is defined as the distance between the cross point and the midpoint of the dual edge divided by the dual edge length.

Tab. 2.2: Some characteristic quantities of two different versions of the spherical triangular C-grid. "ORI" denotes the original grid obtained by simple subdivision of the icosahedron. "HR" stands for the grid obtained using the Heikes and Randall (1995b) optimization algorithm.

grid level	Ratio of the shortest to the longest primal edge		Ratio of the shortest to the longest dual edge		Maximum off-centering of the velocity point with respect to the dual edge	
	ORI	HR	ORI	HR	ORI	HR
-1	1.000	1.000	1.000	1.000	0.0000	0.0000
0	0.881	0.881	0.803	0.803	0.0997	0.0997
1	0.858	0.878	0.599	0.596	0.0974	0.0597
2	0.848	0.804	0.544	0.511	0.0969	0.0334
3	0.840	0.803	0.530	0.482	0.0968	0.0178
4	0.839	0.799	0.527	0.472	0.0967	0.0097
5	0.838	0.796	0.526	0.467	0.0967	0.0061
6	0.838	0.796	0.526	0.462	0.0967	0.0040
7	0.838	0.795	0.526	0.459	0.0967	0.0035

Tab. 2.3: List of symbols used for describing the horizontal grid.

symbol	term or quantity
i	triangular cell, and its center
l	edge of triangular cell, and its length
\varkappa	vertex of triangle, also center of dual cell (hexagon or pentagon)
\hat{l}	edge of dual cell, and its length. Dual edge \hat{l} is orthogonal to and bisect the primal edge l .
A_i	area of triangle i
A_{\varkappa}	area of dual cell \varkappa
A_l	area of the rhomboid defined by the two ends of edge l and the triangle centers $i(l, 1), i(l, 2)$
$A_{i, l}$	area of the triangle defined by the vertices of edge l and triangle center i
$\mathbf{n}_{i, l}$	outward normal unit vector at edge l of cell i
\mathbf{N}_l	normal unit vector of edge l
\mathbf{T}_l	tangential unit vector of edge l
$\mathbf{n}_{\varkappa, \hat{l}}$	outward normal unit vector at edge \hat{l} of the dual cell \varkappa
$\mathbf{t}_{\varkappa, \hat{l}}$	tangential unit vector at edge \hat{l} of the dual cell \varkappa
$\mathcal{E}(i)$	all the edges of triangle i
$\mathcal{E}(\varkappa)$	all the edges of dual cell \varkappa
$i(l, 1), i(l, 2)$	the two neighbouring triangles sharing edge l
$\varkappa(l, 1), \varkappa(l, 2)$	the two ends (vertices) of edge l

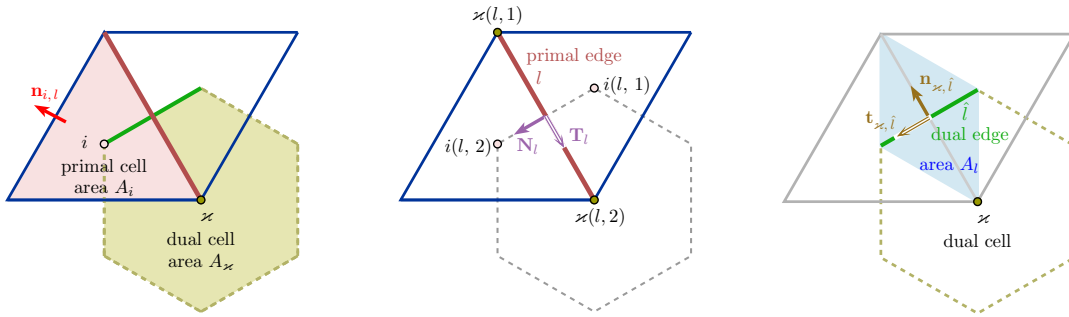


Fig. 2.3: The primal and dual cells and edges, and the associated unit vectors and areas. See Section 2.1.4 for the meaning of the symbols.

computed at the same locations in a similar way (i.e., through line integral along the boundary of the Voronoi cells). To avoid the nonconvergence in vorticity, the Heikes and Randall (1995b) optimization is used for all the refinements after the root division. Note that in order to reduce the computational cost, Heikes and Randall (1995b) chose to apply the optimization only to a sub-domain of the sphere. Modification of the rest of the globe was done by forcing the grid to have a periodicity of five in the longitudinal direction. In the ICON models, however, the periodicity constraint is removed and the optimization problem is solved on the entire global domain.

2.1.4 Notations for topology and geometry

In this thesis similar notations to those in Bonaventura and Ringler (2005) are used to describe the grid topology and geometry. A list of the main symbols is provided for reference in Tab. 2.3.

Let i denote the generic cell of the triangular mesh and $\mathcal{E}(i)$ the set of all edges of cell i . The area of triangle i is denoted by A_i . The generic triangle vertex, which is also the center of a hexagonal or pentagonal cell in the dual grid, is denoted by \varkappa . The area of dual cell \varkappa is A_{\varkappa} (cf. Fig. 2.3).

Let l denote the generic edge of a triangular cell and its length as well. A unit vector \mathbf{N}_l normal to the edge is assigned. \mathbf{T}_l denotes the unit vector tangential to the edge, chosen in such a way that $\mathbf{N}_l \times \mathbf{T}_l = \mathbf{k}_l$ holds, where \mathbf{k}_l denotes the unit vector in the upward direction of the local coordinate at the midpoint of edge l (Fig. 2.3, middle panel). Given a generic vector field \mathbf{v} , its value at the velocity point on edge l can be represented as

$$\mathbf{v}_l = v_{n_l} \mathbf{N}_l + v_{\tau_l} \mathbf{T}_l, \quad (2.5)$$

where v_{n_l} and v_{τ_l} denote the normal and the tangential components, respectively.

The adjacent triangular cells of edge l are denoted by the indices $i(l,1)$ and $i(l,2)$, respectively. The indices are chosen such that the direction from $i(l,1)$ to $i(l,2)$ is the positive direction of the normal vector \mathbf{N}_l . Vertex indices $\varkappa(l,1)$ and $\varkappa(l,2)$ are defined analogously, so that the direction from $\varkappa(l,1)$ to $\varkappa(l,2)$ is the positive direction of the vector \mathbf{T}_l (see the middle panel of Fig. 2.3).

Furthermore, the unit vector pointing in the outward normal direction at edge l of cell i is denoted by $\mathbf{n}_{i,l}$. The area of the triangle defined by the vertices of edge l and cell center i is labeled as $A_{i,l}$. The area of the rhomboid defined by the two vertices of edge l and the centers of the adjacent triangles is labeled as A_l .

The edge of the dual cell that bisects the primal edge l is denoted by \hat{l} , and the same symbol is used for its length. The outward unit vectors $\mathbf{n}_{\varkappa,\hat{l}}$ of the dual cells are also introduced. The corresponding tangential vectors $\mathbf{t}_{\varkappa,\hat{l}}$ are defined so that $\mathbf{n}_{\varkappa,\hat{l}} \times \mathbf{t}_{\varkappa,\hat{l}} = \mathbf{k}_l$ (Fig. 2.3, right panel). It can be seen that, by simple geometric arguments, one has $\mathbf{N}_l \cdot \mathbf{t}_{\varkappa,\hat{l}} = -\mathbf{T}_l \cdot \mathbf{n}_{\varkappa,\hat{l}}$.

2.2 Discrete operators used in the ICON shallow water model

Bonaventura and Ringler (2005) established a discretization scheme for solving the shallow water equations on the triangular grid described in the previous section. Their work forms the basis for the hydrostatic model discussed in this thesis. The discrete operators used in the ICON shallow water model are the following[†]:

The divergence and curl operators are defined as acting on a set of values v_n assigned at the edges of the triangles, which are interpreted as the components of a vector field \mathbf{v} normal to the cell edges. Applying the Gauss's theorem to the primal cells and the Stokes' theorem to the dual cells naturally results in the cell-averaged divergence and curl of a vector field \mathbf{v} :

$$\operatorname{div}(\mathbf{v})_i := \frac{1}{A_i} \sum_{l \in \mathcal{E}(i)} v_{n_l} (\mathbf{N}_l \cdot \mathbf{n}_{i,l}) l \quad (2.6)$$

$$\operatorname{curl}(\mathbf{v})_{\varkappa} := \frac{1}{A_{\varkappa}} \sum_{\hat{l} \in \mathcal{E}(\varkappa)} v_{n_l} (\mathbf{N}_l \cdot \mathbf{t}_{\varkappa,\hat{l}}) \hat{l}. \quad (2.7)$$

Note that in (2.6) and (2.7) the Voronoi-Delaunay property of the grid, i.e. the normal direction to the edges of the primal grid cell is the tangential direction to the corresponding edge of the dual grid cell, has been used in an essential way. By the same property, the discrete normal derivative at the primal edges can be approximated as

$$\operatorname{grad}_n(\varrho)_l := \frac{\varrho_{i(l,2)} - \varrho_{i(l,1)}}{\hat{l}}, \quad (2.8)$$

where ϱ_i is a generic scalar-valued discrete function defined at the centers of the triangular cells.

The discrete divergence and gradient operators have properties similar to those of their continuous counterparts. One example is the formula for integration by parts on the sphere:

$$\int_A \varrho (\nabla \cdot \mathbf{v}) dA = - \int_A (\nabla \varrho) \cdot \mathbf{v} dA, \quad (2.9)$$

with its discrete equivalent

$$\sum_i \varrho_i \operatorname{div}(\mathbf{v})_i A_i = - \sum_l \operatorname{grad}_n(\varrho)_l v_{n_l} l \hat{l}. \quad (2.10)$$

[†]Here and throughout this thesis, the discrete differencing operators are denoted either by dedicated strings (e.g., "div" on the left-hand side of Eqn. (2.6)), or by the subscript d (as in, e.g., Eqn. (2.12)). The notations ∇ , $\frac{\partial}{\partial n}$, $\frac{\partial}{\partial \tau}$, etc., when appearing without the subscript d , refer to the differential operators.

Note that in (2.10) the quantity $l\hat{l}$ is twice the area A_l of the rhomboid associate to edge l . The doubling of the area is due to the fact that only the normal components of the gradient and the vector \mathbf{v} appear in (2.10). Preserving (2.9) in the discrete model is crucial to preserving some of the important conservation properties of the original continuous system.

So as to employ the semi-implicit time stepping scheme and apply horizontal diffusion, the discrete Laplace operator also needs to be constructed. The scalar Laplacian is by definition the divergence of the gradient, i.e.,

$$\nabla^2 \varrho := \nabla \cdot \nabla \varrho, \quad (2.11)$$

where ϱ is a generic scalar function. The discrete counterpart (indicated by the subscript d in the following equations) is defined as a combination of the operators (2.6) and (2.8):

$$(\nabla_d^2 \varrho)_i := \text{div} \left[\text{grad}_n(\varrho) \right]_i. \quad (2.12)$$

As for vectors, the Laplacian in the continuous case is by definition

$$\nabla^2 \mathbf{v} := \nabla (\nabla \cdot \mathbf{v}) - \nabla \times (\nabla \times \mathbf{v}). \quad (2.13)$$

In a (generic) local natural coordinate system with $\mathbf{n} \times \boldsymbol{\tau} = \mathbf{k}$, the normal component is given by

$$\nabla^2 \mathbf{v} \cdot \mathbf{n} = \frac{\partial (\nabla \cdot \mathbf{v})}{\partial n} - \frac{\partial [\mathbf{k} \cdot (\nabla \times \mathbf{v})]}{\partial \tau}. \quad (2.14)$$

The discrete counterpart in the ICON models is defined as

$$(\nabla_d^2 \mathbf{v})_l \cdot \mathbf{N}_l := \text{grad}_n \left[\text{div}(\mathbf{v}) \right]_l - \text{grad}_\tau \left[\text{curl}(\mathbf{v}) \right]_l. \quad (2.15)$$

Here the operator $\text{grad}_\tau(\cdot)$ is the gradient along the tangential direction of a primal edge, computed at the edge center by

$$\text{grad}_\tau(\varrho)_l := \frac{\varrho_{\mathcal{X}(l,2)} - \varrho_{\mathcal{X}(l,1)}}{l}. \quad (2.16)$$

Note that the vector Laplacian is the only place where the tangential gradient is needed. This is related to the fact that the ICON models use a pure C-type staggering. At each edge only the normal component of the velocity field is predicted; The calculation of vorticity and divergence also only involves the normal velocity.

2.3 Truncation error of the discrete operators

The discrete operators introduced in the previous section are numerical approximations to spatial derivatives, and can be sorted into three types: The normal and tangential gradient operators are simple finite difference substitutes for the first-order derivatives; The divergence and curl operators are straightforward applications of important theorems of vector calculus. These two types can be regraded as the most basic operators of horizontal differencing used in the ICON models. The third type, the discrete Laplace operators, are constructed by combining the basic operators according to the definition of the differential counterparts. The basic operators are simple in form and meanwhile preserve important relationships between their continuous

counterpart (e.g., Eqn. (2.10)). This is beneficial to the conservation properties of the numerical model. On the other hand, apart from the normal and tangential gradient, the definition of the discrete operators do not directly reveal the accuracy, because the actual accuracy they provide is not only determined by the formulation itself, but also closely related to the characteristics of the grid on which they are used and the nature of the functions that they operate on.

In this section the order of accuracy of the aforementioned operators are investigated via the truncation error analysis. Let \mathcal{L}_d be a discrete version of a continuous operator \mathcal{L} . The truncation error is defined as

$$\mathbb{E}_{\mathcal{L}} := \mathcal{L}_d(\psi) - \mathcal{L}(\psi) . \quad (2.17)$$

Here ψ can be either a scalar function or a vector field, differentiable to a sufficiently high order. The analysis in the following will be based on the Taylor expansion of ψ . The operator \mathcal{L}_d is m -th order accurate if the leading term of the Taylor expansion of $\mathbb{E}_{\mathcal{L}}$ is proportional to l^m where l denotes the horizontal grid size.

2.3.1 The uniform grid on a plane

The icosahedral grid used in this thesis is characterized by the shape of the primal and dual cells (i.e., triangles and hexagons/pentagons, respectively), the curvature of the sphere, and the unavoidable irregularity caused by the subdivision of the icosahedron. In order to investigate the impact of the shape of the grid cells in an isolated manner, the analysis in this section is performed on a planar grid consisting of cells of the same size.

Assume the primal cells are equilateral triangles of edge length l . Associate a local Cartesian coordinate to each cell, with the origin located at the triangle center (Fig. 2.4). Each edge is assigned an index. The red arrows in Fig. 2.4 indicate the normal vector at the edge center, pointing to the outside of the primal cell. It is important to note that the triangles are symmetric about the y -axis, but not with respect to the x -axis. Here we take the viewpoint that the downward-pointing triangle shown by the right panel in Fig. 2.4 is obtained by mirroring the upward-pointing triangle in the left panel at the x -axis. To reflect this property, a label δ is assigned to each triangle, the value of which is

$$\delta := \begin{cases} 0, & \text{for the upward-pointing triangles;} \\ 1, & \text{for the downward-pointing triangles.} \end{cases} \quad (2.18)$$

For a generic vector field \mathbf{v} , its components in the x and y directions are denoted by u and v , respectively.

2.3.2 Pointwise values and averages

In numerical models the values of the physical quantities of interest are calculated only at a finite number of locations in the computational domain. Naturally the question arises whether these discrete values should be viewed as the approximation to the pointwise evaluation of the corresponding analytical function, or interpreted as some kind of average over a control volume, e.g., a triangular cell. Distinction between these two concepts is necessary, because the discrete operators give different results when applied to different types of values. In addition, the

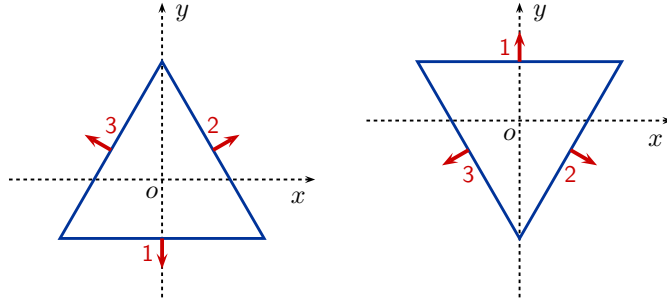


Fig. 2.4: The upward- and downward-pointing triangles, corresponding to the orientation parameter $\delta=0$ and $\delta=1$, respectively. The downward-pointing triangle is obtained by mirroring the upward-pointing one at the x-axis.

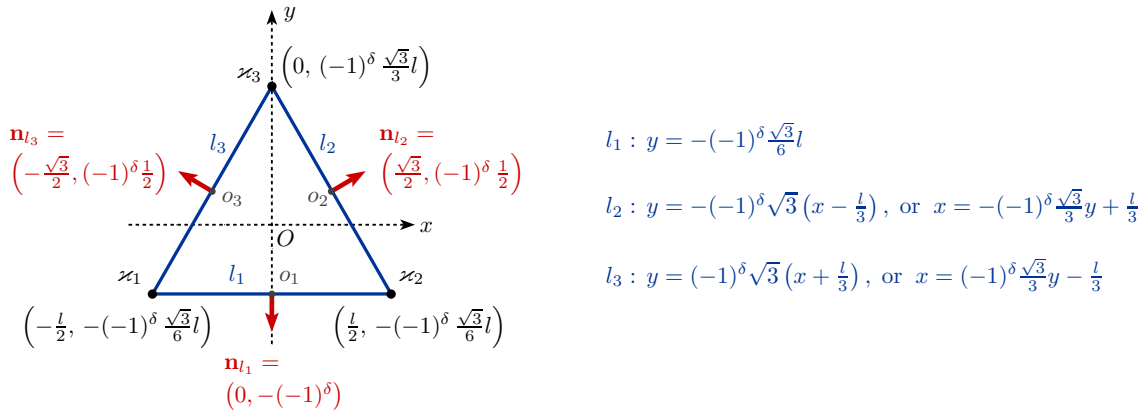


Fig. 2.5: The triangular cell on a plane.

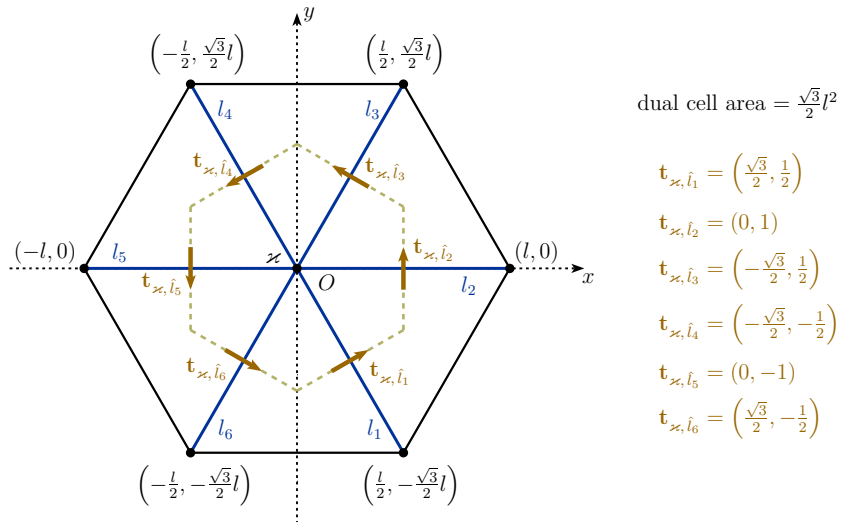


Fig. 2.6: The dual cell (i.e., the hexagon with dashed boundary) on a plane.

viewpoint we choose for the output of an operator determines what is considered as "correct" and "exact" when the accuracy of the operator is evaluated.

In the ICON models there are three different kinds of discrete variables: cell-based, edge-based and vertex-based, which, in principle, can either be regarded as average over a primal cell i , along an edge l or over a dual cell \varkappa , respectively, or be interpreted as pointwise values. For each operator there are two ways to interpret the input (i.e., the operand) and two for the output, leading to in total four possible definitions of the truncation error. Taking the divergence operator as an example, we can ask how the values of the following four expressions change with the grid size:

$$\operatorname{div}(\mathbf{v})_i - (\nabla \cdot \mathbf{v})_i \quad (2.19)$$

$$\operatorname{div}(\mathbf{v})_i - \overline{\overline{(\nabla \cdot \mathbf{v})}}^i \quad (2.20)$$

$$\operatorname{div}(\overline{\mathbf{v}}^e)_i - (\nabla \cdot \mathbf{v})_i \quad (2.21)$$

$$\operatorname{div}(\overline{\mathbf{v}}^e)_i - \overline{\overline{(\nabla \cdot \mathbf{v})}}^i \quad (2.22)$$

Here $(\nabla \cdot \mathbf{v})_i$ refers to the accurate pointwise evaluation of the divergence function at the center of triangle i ; $\overline{(\cdot)}^e$ and $\overline{\overline{(\cdot)}}^i$ denote the average along a primal edge and over a triangular cell, respectively. Definition (2.19) comes from a pure pointwise view point and allows for straightforward derivation of the order of accuracy; The other three involves certain kind of averages, and can be dealt with by expressing the averages in terms of pointwise values with a sufficiently high accuracy. For example, the average of a generic function ϱ over an edge l can be expanded using the Taylor series with respect to the edge center:

$$\overline{\varrho}^e := \frac{1}{l} \int_{-\frac{l}{2}}^{\frac{l}{2}} \varrho(s) ds = \varrho(0) + \frac{l^2}{24} \left(\frac{\partial^2 \varrho}{\partial s^2} \right)_{s=0} + \frac{l^4}{1920} \left(\frac{\partial^4 \varrho}{\partial s^4} \right)_{s=0} + \mathcal{O}(l^6) \quad (2.23)$$

(see also Section B.1). Similarly the average over a triangular cell (Fig. 2.5) can be expressed as

$$\begin{aligned} \overline{\varrho}^i &:= (-1)^\delta \left(\frac{\sqrt{3}}{4} l^2 \right)^{-1} \int_{(-1)^\delta \frac{\sqrt{3}}{6} l}^{(-1)^\delta \frac{\sqrt{3}}{3} l} \int_{(-1)^\delta \frac{\sqrt{3}}{3} y - \frac{l}{3}}^{(-1)^\delta \frac{\sqrt{3}}{3} y + \frac{l}{3}} \varrho(x, y) dx dy \\ &= \varrho_o + \frac{l^2}{48} (\nabla^2 \varrho)_o - (-1)^\delta \frac{\sqrt{3} l^3}{720} G(\varrho)_o + \frac{l^4}{5760} (\nabla^4 \varrho)_o + \mathcal{O}(l^5), \end{aligned} \quad (2.24)$$

in which

$$G(\varrho) := \frac{\partial^3 \varrho}{\partial x^2 \partial y} - \frac{1}{3} \frac{\partial^3 \varrho}{\partial y^3}, \quad (2.25)$$

and the subscript o denotes the center of the triangle. The average over a dual cell (i.e., the hexagon with dashed boundary in Fig. 2.6) is given by

$$\begin{aligned} \overline{\varrho}^\varkappa &:= \left(\frac{\sqrt{3}}{2} l^2 \right)^{-1} \left[\int_{-\frac{l}{2}}^0 \int_{-\frac{\sqrt{3}}{3}(x+l)}^{\frac{\sqrt{3}}{3}(x+l)} + \int_0^{\frac{l}{2}} \int_{\frac{\sqrt{3}}{3}(x-l)}^{-\frac{\sqrt{3}}{3}(x-l)} \right] \varrho(x, y) dy dx \\ &= \varrho_o + \frac{5l^2}{144} (\nabla^2 \varrho)_o + \frac{7l^4}{17280} (\nabla^4 \varrho)_o + \mathcal{O}(l^6), \end{aligned} \quad (2.26)$$

in which the subscript o denotes the dual cell center.

In Appendix B all four types of truncation error are derived for each of the horizontal differencing operators. Note that during the development of the ICON shallow water model, the choice of interpretation was that the edge-based variables and operators were regarded as approximations to the corresponding pointwise quantities, while the cell- and vertex-based ones were regarded as averages. This is a natural result of using the Gauss's theorem and the Stokes' theorem in defining the operators. Hereafter we referred to this interpretation as the "ICOSWM interpretation" or the "ICOSWM viewpoint". In the discussions in the remaining part of this section, we always start from this specific interpretation, and then check whether changes in the viewpoint can lead to qualitatively different conclusions about the accuracy of each operator. Since this chapter is dedicated to the horizontal differencing, it is justified to carry out the discussion in the context of the shallow water model.

2.3.3 The basic differencing operators

We start from the adiabatic part of the shallow water model, meaning only the right-hand-side terms in the shallow water equations (1.1) and (1.2) are considered. The horizontal diffusion and the time stepping are ignored for the moment. Regarding the differencing operators, only the basic ones (i.e., the normal gradient, the divergence and the curl) are considered. The truncation error of these operators is summarized in Tab. 2.4. The results corresponding to the ICOSWM interpretation are given in gray background. The normal gradient and the curl operator are always second-order accurate regardless of the choice of viewpoint (see also Sections B.2 – B.3). This is closely related to the fact that on the regular planar grid considered here, all the dual cells are regular hexagons, and the primal and dual edges are perpendicular to and bisect each other.

The case of the divergence operator is more complicated. As detailed in Section B.4, if the operand is regarded as having a pointwise nature, the result given by the operator can be expressed as

$$\begin{aligned} \operatorname{div}(\mathbf{v})_i &= \left(\frac{\sqrt{3}l^2}{4} \right)^{-1} l \sum_{j=1}^3 \mathbf{v}_{l_j} \cdot \mathbf{n}_j \\ &= (\nabla \cdot \mathbf{v})_o + (-1)^\delta l H(\mathbf{v})_o + \frac{l^2}{96} \left[\nabla^2 (\nabla \cdot \mathbf{v}) \right]_o + (-1)^\delta l^3 F(\mathbf{v})_o + \mathcal{O}(l^4) \end{aligned} \quad (2.27)$$

in which the subscript o denotes function evaluation at the triangle center (cf. Fig. 2.5), and the functions H and F read

$$H(\mathbf{v}) := \frac{\sqrt{3}}{24} \left(2 \frac{\partial^2 u}{\partial x \partial y} + \frac{\partial^2 v}{\partial x^2} - \frac{\partial^2 v}{\partial y^2} \right), \quad (2.28)$$

$$F(\mathbf{v}) := \frac{\sqrt{3}}{2^9 3^3} \left(12 \frac{\partial^4 u}{\partial x^3 \partial y} + 2 \frac{\partial^4 u}{\partial x \partial y^3} + 3 \frac{\partial^4 v}{\partial x^4} + 6 \frac{\partial^4 v}{\partial x^2 \partial y^2} - 5 \frac{\partial^4 v}{\partial y^4} \right). \quad (2.29)$$

Expression (2.27) is clearly a first-order approximation to the pointwise divergence at the triangle center. In addition, since the cell center value and the cell average can be considered as second-order approximations to each other (cf. Eqn. (2.24)), Eqn. (2.27) is first-order also

Tab. 2.4: Truncation error of the discrete divergence, curl, and normal gradient operators from different viewpoints. Definitions of the operators are given by Eqns. (2.6), (2.7) and (2.8), respectively. The four columns showing the order of accuracy correspond (from left to right) to the four definitions of the truncation error (see Eqns. (2.19) – (2.22) as an example). The shaded numbers correspond to the ICOSWM interpretation (see the last paragraph in Section 2.3.2).

operator	order of accuracy compared to		operator	order of accuracy compared to	
	pointwise value	average		pointwise value	average
$\text{grad}_n(\varrho)_l$	2	2	$\text{grad}_n(\overline{\varrho}^i)_l$	2	2
$\text{curl}(\mathbf{v})_\varkappa$	2	2	$\text{curl}(\overline{\mathbf{v}}^e)_\varkappa$	2	2
$\text{div}(\mathbf{v})_i$	1	1	$\text{div}(\overline{\mathbf{v}}^e)_i$	2	∞

accurate when compared with the cell average. Another important feature is that in (2.27) the leading error changes sign from an upward-pointing triangle to a downward-pointing one, or in other words, from one triangle to any of its neighbours that share an edge with it.

In order to verify this analysis and demonstrate the effect of the alternating sign of the first-order error, numerical calculations are performed. The spherical harmonics $Y_3^2(\lambda, \varphi)$ and $Y_2^1(\lambda, \varphi)$ are mapped onto a plane using the cylindrical equidistant projection

$$x = \lambda, \quad y = \varphi \quad (2.30)$$

to define a vector field:

$$\begin{cases} u(x, y) := \frac{1}{4} \sqrt{\frac{105}{2\pi}} \cos 2x \cos^2 y \sin y, \\ v(x, y) := -\frac{1}{2} \sqrt{\frac{15}{2\pi}} \cos x \cos y \sin y. \end{cases} \quad (2.31)$$

The vector field is depicted in Fig. 2.7. The analytical expression of its divergence reads

$$\nabla \cdot \mathbf{v} = \frac{\partial u}{\partial x} + \frac{\partial v}{\partial y} = \frac{-1}{2\sqrt{2\pi}} \left(\sqrt{105} \sin 2x \cos^2 y \sin y, + \sqrt{15} \cos x \cos 2y \right). \quad (2.32)$$

Numerical calculations are carried out on a series of planar grids at different resolutions. At each resolution, the grid consists of identical equilateral triangles (Fig. 2.8). To facilitate comparison, a rectangular mesh is also established, of which the grid sizes in the x and y directions are the same as the edge length and height of the triangles, respectively. On this mesh, a rectangular C-grid is used in computing the divergence in an equivalent way as defined by Eqn. (2.6). Taking the pointwise viewpoint for velocity, we can easily derive from the analytical expression (2.31) the normal wind at each edge. The true solution of the divergence averaged over the triangular cells is derived in Appendix B.5.

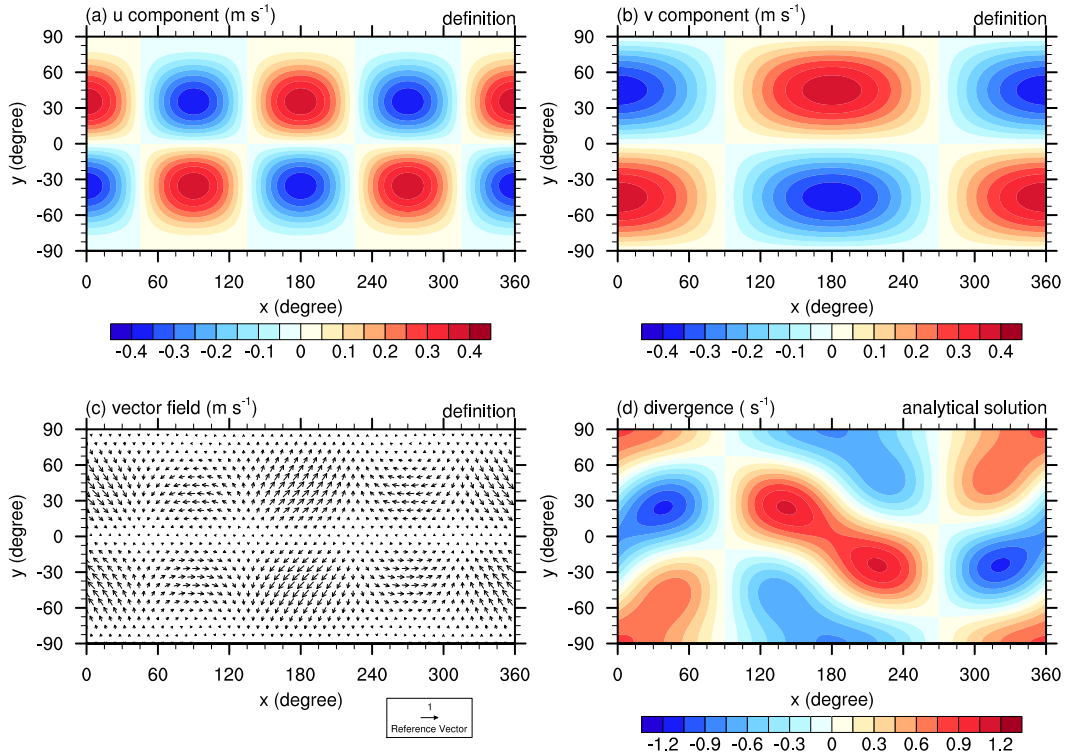


Fig. 2.7: The analytically defined vector field used in testing the discrete divergence operator in the context of planar geometry. The u and v components are the spherical harmonics Y_3^2 and Y_2^1 , respectively, mapped to the 2D Cartesian coordinate via cylindrical equidistance projection (cf. Eqn. (2.31)). Panel (c) shows the full vector field, and panel (d) the divergence (cf. Eqn. 2.32).

The absolute error of the cell-averaged divergence at 10.4° resolution (in the x direction) is shown in the left column of Fig. 2.9. On the triangular grid the error is characterized by a checkerboard pattern, with positive values surrounded by negative values and vice versa. This grid-scale feature is consistent with the truncation error analysis (2.27). In contrast, the distribution of the numerical error on the rectangular grid is reasonably smooth, and the maximum absolute error is one order of magnitude smaller than on the triangles. Convergence of the divergence operator as measured by the normalized l_∞ , l_1 and l_2 errors are shown in the right column of Fig. 2.9. It is clear that in this idealized context, the divergence operator (2.6) is first-order on the triangular grid, which further confirms the truncation error analysis.

One point worth mentioning here is that in the discretized shallow water model, the divergence operator is not applied directly to the horizontal wind but to the mass flux at triangle edges, so as to discretize the continuity equation (1.2) in the so-called flux form and conserve the total mass of the system. Since the fluid depth h is only predicted

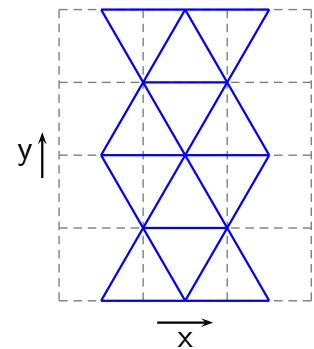


Fig. 2.8: Schematic plot of the regular triangular and rectangular grids on plane used in numerical test of the accuracy of the discrete divergence operator.

at cell centers, what is actually calculated in the model is $\operatorname{div}(\mathbf{v}\tilde{h})_i$, where \tilde{h} is some kind of interpolated fluid height defined at edge centers. We first consider an extreme case when $\tilde{h}=h_l$ where h_l denotes the exact pointwise evaluation of the function h at the midpoint of edge l . Making a simple variable substitution $\mathbf{V} = \mathbf{v}h$ and applying Eqn. (2.27), we obtain

$$\operatorname{div}(\mathbf{v}h)_i = \left[\nabla \cdot (\mathbf{v}h) \right]_o + (-1)^\delta l H(\mathbf{v}h)_o + \mathcal{O}(l^2) . \quad (2.33)$$

In the ICON shallow water model, the value of \tilde{h} at edge l is obtained by taking the arithmetic average of the height values associated to the two neighbouring triangles. From the ICOSWM viewpoint, this means

$$\tilde{h}_l := \frac{1}{2} \left(\overline{\tilde{h}}^{i(l,1)} + \overline{\tilde{h}}^{i(l,2)} \right) = h_l + \mathcal{O}(l^2) . \quad (2.34)$$

It can be verified that the resulting discrete mass flux divergence is

$$\operatorname{div}(\mathbf{v}\tilde{h})_i = \left[\nabla \cdot (\mathbf{v}h) \right]_o + (-1)^\delta l \left[h H(\mathbf{v}) + Q(\mathbf{v}, h) \right]_o + \mathcal{O}(l^2) , \quad (2.35)$$

in which the function Q reads

$$Q(\mathbf{v}, h) := \frac{\sqrt{3}}{12} \left[\frac{\partial}{\partial x} \left(u \frac{\partial h}{\partial y} + v \frac{\partial h}{\partial x} \right) + \frac{\partial}{\partial y} \left(u \frac{\partial h}{\partial x} - v \frac{\partial h}{\partial y} \right) \right] . \quad (2.36)$$

Similar to Eqn. (2.33), the leading error in the mass flux divergence in the model is of first-order and has its sign changing with the orientation of the triangles.

Another point worth discussing here is that if the velocity associated to each primal edge is understood as the edge average, then the divergence operator (2.6) provides the exact average divergence over the triangular cells (which is a trivial consequence of Gauss's theorem), and a second-order approximation to the pointwise divergence at the triangle center (cf. Tab. 2.4, last row, the last two columns). One might thus wonder whether the first-order accuracy derived above is just a result of improper interpretation. Note again that in the model the divergence operator is applied to the mass flux instead of velocity. Even if we regard the velocity as edge average, the mass flux through edge l is approximated by

$$\overline{\mathbf{v}}_l^e \tilde{h}_l = \overline{(\mathbf{v}h)}_l^e + \mathcal{O}(l^2) . \quad (2.37)$$

It can be verified that

$$\operatorname{div}(\overline{\mathbf{v}}^e \tilde{h})_i = \overline{\nabla \cdot (\mathbf{v}h)}^i + (-1)^\delta l \left[Q(\mathbf{v}, h) \right]_o + \mathcal{O}(l^2) . \quad (2.38)$$

The qualitative feature of the leading error remains unchanged comparing to Eqns. (2.33) and (2.35). Hence we conclude that in the ICON model numerical errors as shown in Fig. 2.9a,b do exist in the mass flux divergence. This is not a result of choosing a specific viewpoint in interpreting the nature of the discrete variables, but an inherent property associated to the definition of the divergence operator and the shape of the primal grid cells.

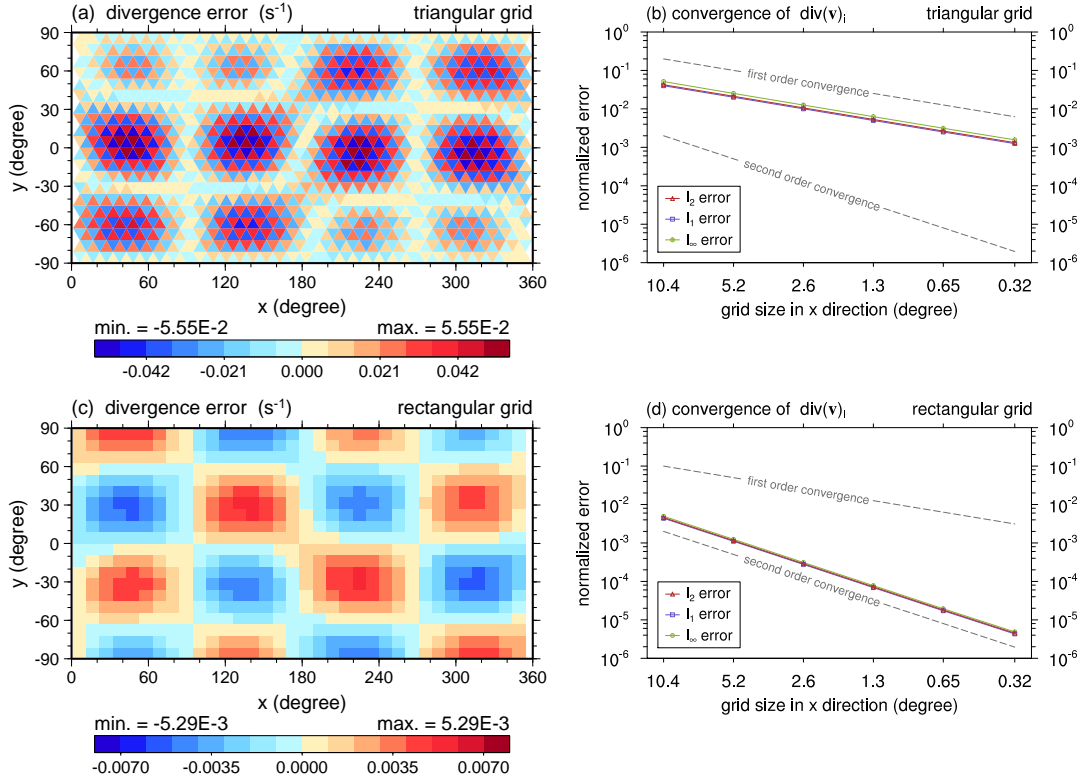


Fig. 2.9: (a) and (c): Numerical errors of the cell-averaged divergence calculated on the triangular and rectangular grids shown in Fig. 2.8 at 10.4° resolution in the x direction. (Note that the color scales are different). (b) and (d): The normalized errors at different resolutions. The discrete divergence is calculated by first evaluating the pointwise value of Eqn. (2.31) at edge centers and then applying formula (2.6).

2.3.4 Laplace operator for scalar function and vector field

The Laplace operator does not appear in the adiabatic part of the governing equations in the ICON models, but is needed by some widely used numerical techniques. For example, the key element of the semi-implicit time stepping scheme for handling gravity waves is to solve a Helmholtz equation of the divergence (Hoskins and Simmons, 1975; Simmons and Burridge, 1981); the horizontal diffusion, employed to remove small-scale noise and improve the stability of a numerical scheme, usually takes the form of hyper-Laplacian $\nabla_d^{2q}\psi$, in which ψ is a prognostic variable and q a positive integer.

As already mentioned in Section 2.2, the discrete scalar and vector Laplace operators ($\nabla_d^2\varrho$ and $\nabla_d^2\mathbf{v}$, respectively) in the ICON shallow water model are constructed by combining the basic operators. So as to achieve desirable scale selectivity in the horizontal diffusion, fourth-order hyper-Laplacian is obtained by applying the ∇_d^2 twice, namely

$$\nabla_d^4\varrho := \nabla_d^2(\nabla_d^2\varrho) \quad \text{and} \quad \nabla_d^4\mathbf{v} := \nabla_d^2(\nabla_d^2\mathbf{v}), \quad (2.39)$$

since in the continuous case we have

$$\nabla^4\varrho \equiv \nabla^2(\nabla^2\varrho) \quad \text{and} \quad \nabla^4\mathbf{v} \equiv \nabla^2(\nabla^2\mathbf{v}). \quad (2.40)$$

Tab. 2.5: Truncation error of the Laplace operators applied to scalar functions and vector fields. Definition of the ∇_d^2 operator is given by Eqn. (2.12) for scalar functions and (2.14) for vector fields, respectively. The fourth-order hyper-Laplacian is obtained by applying ∇_d^2 twice. The four columns showing the order of accuracy correspond (from left to right) to the four definitions of the truncation error (see Eqns. (2.19) – (2.22) as an example). The shaded numbers correspond to the ICOSWM interpretation (see the last paragraph in Section 2.3.2).

operator	order of accuracy compared to		operator	order of accuracy compared to	
	pointwise value	average		pointwise value	average
$\nabla_d^2 \varrho$	1	1	$\nabla_d^2 \overline{\varrho}^i$	1	1
$\nabla_d^4 \varrho$	-1	-1	$\nabla_d^4 \overline{\varrho}^i$	-1	-1
$\nabla_d^2 \mathbf{v}$	0	0	$\nabla_d^2 \overline{\mathbf{v}}^e$	2	2
$\nabla_d^4 \mathbf{v}$	-2	-2	$\nabla_d^4 \overline{\mathbf{v}}^e$	0	0

It should be noted that this straightforward way of constructing high order derivative has the potential danger of losing accuracy. Generally speaking, each time when finite differencing is applied, the accuracy of the resulting operator will decrease by one order, unless the leading error of the operands cancel. When the derivative reaches a very high order, the numerical approximation may not even converge to the desired quantity. Therefore it is worth checking the actual accuracy of the Laplace operators defined in the ICON shallow water model. Detailed derivations of the truncation error for different viewpoints are provided in Appendix B (see Sections B.6 and B.7). A summary of the results is given in Tab. 2.5.

Scalar Laplacian

Like the normal gradient and the curl, the discrete scalar Laplace operators have the same order of accuracy for all the four definitions of the truncation error. The ∇_d^2 operator is first-order accurate and the leading error takes the form

$$(-1)^\delta \gamma l G(\varrho)_o . \quad (2.41)$$

Here $G(\varrho)$ is the same as in Eqn. (2.25); γ is a constant; δ represents the orientation of the triangle for which the Laplacian is calculated, and the subscript o of $G(\varrho)$ denotes function evaluation at the triangle center (cf. Fig. B.3, Eqns. (B.35) and (B.36) in Section B.6). The error term (2.41) features a checkerboard pattern.

The probably surprising result in Tab. 2.5 is that the discrete scalar Laplacian ∇_d^4 is of order -1. In other words, this operator does not converge to the desired hyper-Laplacian. The reason for the nonconvergence can be seen from the definition of $\nabla_d^4 \varrho$. Combining Eqn. (2.12) and the first formula in (2.39) gives

$$(\nabla_d^4 \varrho)_i = \operatorname{div} \left\{ \operatorname{grad}_n \left[\operatorname{div} \left(\operatorname{grad}_n(\varrho) \right) \right] \right\}_i . \quad (2.42)$$

The two innermost operations correspond to $\nabla_d^2 \varrho$ and produces a numerical error of order 1 in the form of (2.41) at each of the triangles involved. The subsequent operation is computing the

normal gradient at the three edges of the target cell. Since the two triangles sharing the same edge have opposite orientations, the associated error terms (2.41) do not cancel but accumulate. One order of accuracy is hence lost during the gradient calculation. The outmost divergence calculation in formula (2.42) lead to decrease of accuracy by another order. The overall truncation error is therefore of order -1. Numerical calculations have confirmed this conclusion (see Fig. B.4 in Section B.6).

Vector Laplacian

The definition of the discrete vector Laplace operator (Eqn. (2.15)) involves all the three basic differencing operators discussed in the previous subsection as well as the tangential gradient operator defined at primal edges. The tangential gradient of curl (see Eqn. (2.15)) is the "well-behaved" part of this operator, since it gives a second-order approximation to the continuous counterpart regardless of the viewpoints taken (cf. Eqns. (B.49) and (B.50) in the appendix). The other part – normal gradient of divergence – can cause problem. As derived in the appendix and shown in the last row of Tab. 2.5, the discrete fourth-order vector Laplacian does not converge in any circumstances to the continuous counterpart. The reason is that from the definition (2.39) and Eqn. (2.15) we have

$$(\nabla_d^4 \bar{\mathbf{v}}^e)_l \cdot \mathbf{N}_l = \underline{\text{grad}_n} \left\{ \underline{\text{div}} \left[\text{grad}_n \left(\text{div}(\bar{\mathbf{v}}^e) \right) \right] \right\} + \dots \quad (2.43)$$

$$(\nabla_d^4 \mathbf{v})_l \cdot \mathbf{N}_l = \text{grad}_n \left\{ \underline{\text{div}} \left[\underline{\text{grad}_n} \left(\text{div}(\mathbf{v}) \right) \right] \right\} + \dots \quad (2.44)$$

The underlined operations, like in Eqn. (2.42), accumulate error and lead to a rapid decrease of the order of accuracy.

The analysis in this subsection reveals that the first-order truncation error in the divergence operator has not only introduced grid-scale noise in the mass flux divergence, but also changed the convergence property of the discrete Laplace operators.

2.3.5 Horizontal diffusion

In the ICON models the original plan for introducing diffusion was to employ the form of $-\nabla^4 \psi$ for velocity in the shallow water model, and for both velocity and temperature in the hydrostatic dynamical core. The previous two subsections have revealed that according to the truncation error analysis, the discrete fourth-order Laplace operators (i.e., the hyper-Laplacian) constructed from the divergence, curl and gradient operators do not converge to the continuous counterparts, mainly due to the property of the numerical error in the divergence operator. Nevertheless the ICON shallow water model equipped with the nonconverging vector Laplacian did produce reasonable results in the Williamson *et al.* (1992) test cases (see, e.g., Bonaventura and Ringler, 2005). In addition, during the development of the ICOHDC it has been observed that while the integrations without any diffusion can not remain numerically stable for long time, use of the hyper-Laplacian does improve the stability significantly. Naturally one would ask what exactly is the effect of the hyper-Laplace operators in the ICON models and how they help improve the numerical stability.

As derived in the appendix, if we take the ICOSWM interpretation (meaning regarding the edge-based normal velocity in the model as a pointwise quantity), the discrete fourth-order hyper-Laplacian can be expressed as

$$(\nabla_d^4 \mathbf{v})_l \cdot \mathbf{N}_l = (\nabla^4 \mathbf{v})_l \cdot \mathbf{N}_l + (-1)^\delta 48\sqrt{3}l^{-2} H(\mathbf{v})_l + \mathcal{O}(l^0) \quad (2.45)$$

In the ICON models, using Eqn. (2.45) for velocity diffusion in fact means multiplying it with the time step Δt_D and the diffusion coefficient \mathcal{K}_4 , then take the product as a correction term for the normal wind. To check what the effect is, we perform the following two calculations:

- (I) Apply the discrete divergence operator to the correction term of the normal wind, yielding

$$\operatorname{div}(-\Delta t_D \mathcal{K}_4 \nabla_d^4 \mathbf{v})_i = -\Delta t_D \mathcal{K}_4 24^2 l^{-3} (-1)^\delta H(\mathbf{v})_i - \Delta t_D \mathcal{K}_4 \operatorname{div}(\nabla^4 \mathbf{v})_i + \dots \quad (2.46)$$

For the regular planar mesh considered here, the length of the dual and primal edges are linked by $\hat{l} = l/\sqrt{3}$; In addition, from Eqn. (2.27) we know the leading error in divergence is

$$\mathbb{E}_{div,1} = (-1)^\delta l H(\mathbf{v})_i . \quad (2.47)$$

Thus (2.46) can be further manipulated into

$$\operatorname{div}(-\Delta t_D \mathcal{K}_4 \nabla_d^4 \mathbf{v})_i = -\Delta t_D \mathcal{K}_4 \left(\frac{\sqrt{8}}{\hat{l}} \right)^4 \mathbb{E}_{div,1} - \Delta t_D \mathcal{K}_4 [\nabla^4 (\nabla \cdot \mathbf{v})]_i + \dots \quad (2.48)$$

This indicate that in addition to the "correct" diffusion we want to have (i.e., the second term on the right-hand side of Eqn. (2.48)), the discrete vector Laplacian introduces a correction term which removes – at least to some extent – the leading error in divergence (i.e., the checkerboard pattern). Furthermore, if the coefficient \mathcal{K}_4 is calculated from a parameter τ^* by

$$\mathcal{K}_4 := \frac{1}{\tau^*} \left(\frac{\hat{l}}{\sqrt{8}} \right)^4 , \quad (2.49)$$

then the quantity $\Delta t_D/\tau^*$ equals the fraction of the checkerboard that can be removed after one time step.

- (II) As already mentioned, in the adiabatic part of the governing equations, the divergence operator is used in calculating the change in mass in each grid cell. The leading error in the approximated mass flux divergence is (cf. Eqn. (2.35))

$$\mathbb{E}_{md,1} = \underbrace{(-1)^\delta l [h H(\mathbf{v})]_i}_{\mathbb{E}_{md,1a}} + \underbrace{(-1)^\delta l [Q(\mathbf{v}, h)]_i}_{\mathbb{E}_{md,1b}} \quad (2.50)$$

$$=: \mathbb{E}_{md,1a} + \mathbb{E}_{md,1b} . \quad (2.51)$$

Similar to the derivation in (I), we find that the velocity diffusion lead to a correction term in the mass flux divergence of the form

$$\operatorname{div}(-\Delta t_D \mathcal{K}_4 (\nabla_d^4 \mathbf{v}) \tilde{h})_i = -\Delta t_D \mathcal{K}_4 \left(\frac{\sqrt{8}}{\hat{l}} \right)^4 \mathbb{E}_{md,1a} - \Delta t_D \mathcal{K}_4 [\nabla^4 (\nabla \cdot \mathbf{v} h)]_i + \dots \quad (2.52)$$

Thus the leading error in the fourth-order vector Laplacian also helps removing the checkerboard in the divergence of the mass flux.

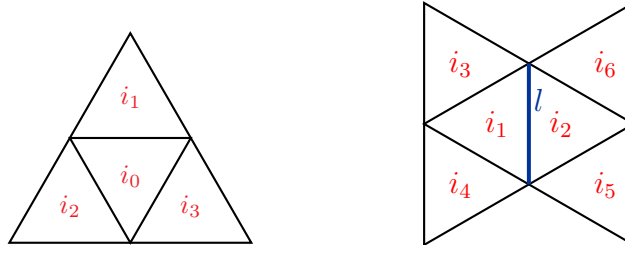


Fig. 2.10: Left: Stencil of the four-cell smoothing schemes designed to remove the first-order truncation error of the discrete divergence operator. Right: Stencil of the normal gradient operator that is consistent with the smoothed divergence. See text for the details.

Regarding the thermodynamic equation, it has been observed in the idealized tests that the $\nabla_d^4 T$ does help stabilize the ICOHDC, even though this discrete operator does not converge to its differential counterpart. The actual effect of the leading error in the discrete fourth-order scalar Laplacian is not yet clear.

2.3.6 Reducing the grid-scale noise in divergence

Among the results obtained from the truncation error analysis, the most unexpected and important part is the leading error of the discrete divergence operator which introduces grid-scale noise into the model. If the accuracy of the divergence operator can be increased to second-order, not only will the noise level be reduced, but the nonconvergence problem of the hyper-Laplace operators will be solve as well.

Conservative smoothing

On the regular planar grid, the simplest way to remove the checkerboard in divergence without introducing new variables is to add a four-cell smoothing to the original formula. The resulting divergence operator can be written as

$$\overline{(\operatorname{div}(\mathbf{v}))_0}^{s1} := \frac{1}{6A_0} \left(3 \operatorname{div}(\mathbf{v})_0 A_0 + \sum_{j=1,2,3} \operatorname{div}(\mathbf{v})_j A_j \right). \quad (2.53)$$

Here the subscript 0 denotes the target cell, while $j = 1, 2, 3$ denote the three neighbouring triangles sharing an edge with cell 0 (see the left panel of Fig. 2.10). This smoothing enlarges the stencil of divergence computation from a single triangle to the four neighbouring cells.

The modified operator can also be interpreted as first calculating the momentum fluxes over the three rhombuses $i_0 i_1$, $i_0 i_2$ and $i_0 i_3$, assigning the arithmetic mean to the shared triangle and then scale the flux according to the area of the target triangle. Since each rhombus consists of two primal cells, the upward- and downward-pointing triangles are coupled together. From this viewpoint, we can define another smoothing method:

$$\overline{(\operatorname{div}(\mathbf{v}))_0}^{s2} := \frac{1}{3} \sum_{j=1,2,3} \frac{\operatorname{div}(\mathbf{v})_0 A_0 + \operatorname{div}(\mathbf{v})_j A_j}{A_0 + A_j}, \quad (2.54)$$

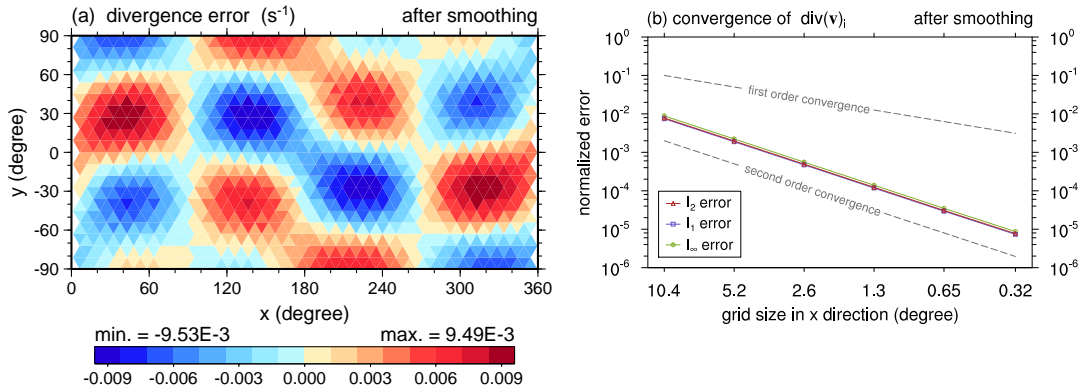


Fig. 2.11: Divergence calculated with the original formula (2.6) combined with the four-cell smoothing defined by Eqn. (2.53). Since the calculations are performed on regular triangular grids on the plane (cf. Section 2.3.3), Eqn. (2.53) is equivalent to Eqn. (2.54). Analytical expressions of the vector field used in the test are given in Eqn. (2.31).

which assigns the mean divergence (instead of momentum flux) of the three rhombuses to the shared triangle. The two smoothing schemes (2.53) and (2.54) are equivalent when all the triangular cells have the same area. In a non-uniform grid, the coefficients associated to the four triangles in Fig. 2.10 (left panel) are slightly different. The second scheme is conceptually better, because it takes the form of area-weighted averaging which is also used in the vertical discretization of the hydrostatic dynamical core (see next chapter, Sec 3.3).

For the regular planar grid considered in this section, it can be proven that the truncation error of the modified divergence operators is

$$\overline{(\text{div}(\mathbf{v})_0)^s} = D_0 + \frac{5l^2}{96} (\nabla^2 D)_0 + O(l^3). \quad (2.55)$$

The modified divergence becomes second-order accurate. An example demonstrating the effect of the smoothing is shown in Fig. 2.11, which can be compared with the results given by the original operator in Fig. 2.9, and the true solution in Fig. 2.7d. Furthermore, both Eqn. (2.53) and (2.54) ensure vanishing of the global integral of the divergence, thus guarantee the conservation of total mass.

The consistent normal gradient operator

Another point worth mentioning is, if either of the aforementioned smoothing scheme is included as part of the discrete divergence operator, the relationship

$$\int_A \varrho (\nabla \cdot \mathbf{v}) dA = - \int_A (\nabla \varrho) \cdot \mathbf{v} dA \quad (2.56)$$

will not hold any longer, unless the discrete normal gradient operator is also modified. For the smoothing scheme (2.53), we need to enlarge the stencil of the gradient operator to the right panel in Fig. 2.10 and change the definition of the discrete normal gradient into

$$\text{grad}_n(\varrho)_l^* := \frac{1}{6\hat{l}} \left[\frac{3\varrho_{i_2} + (\varrho_{i_1} + \varrho_{i_5} + \varrho_{i_6})}{6} - \frac{3\varrho_{i_1} + (\varrho_{i_2} + \varrho_{i_3} + \varrho_{i_4})}{6} \right]. \quad (2.57)$$

This can be interpreted as first smoothing the scalar ϱ in the same way as in Eqn. (2.53) but without the area weights, and then applying the original normal gradient operator (Eqn. (2.8)). If scheme Eqn. (2.54) is used for divergence, the normal gradient needs to be changed into

$$\text{grad}_n(\varrho)_l^{**} := \text{grad}_n(\bar{\varrho}^{s2})_l, \quad (2.58)$$

which means applying the same area-weighted smoothing as Eqn. (2.54) to the scalar function before using the original gradient operator. The symmetry between Eqns. (2.54) and (2.58) can be regarded as another indication that this pair of modified operators are more appropriate than Eqns. (2.53) and (2.57).

The modified gradient operators (2.57) and (2.58) are both second-order accurate on the regular planar grid. The potential disadvantage is that if one retains the idea of constructing higher order derivatives using the div, curl and grad_n as building blocks, the resulting formulae will be considerably more complex than the current ones. On the other hand, the Laplace operators constructed from the modified divergence and gradient operators will be consistent with the continuous counterparts and second-order accurate.

2.4 Impact of the irregularity of the spherical triangular grid

In the previous section the truncation error of the horizontal differencing operators has been discussed in the idealized context of the regular planar grid. On such a grid, not only all the triangles are of the same size and shape, but the orthogonality and bisection relationships are also strictly satisfied. This is no longer true on a spherical grid. In the ICON models, the orthogonality and the bisection relationships between the primal and dual edges have been used in an essential way in defining the horizontal differencing operators. In order to retain these properties in the spherical grid, the Heikes and Randall (1995b) grid optimization algorithm has been employed (cf. Section 2.1.3). Two aspects that have not been discussed so far in this chapter are the inequality of the grid spacing, and the distortion of the shape of the triangles.

2.4.1 Inequality of the grid spacing

Although the use of the icosahedral grid has dramatically improved the homogeneity of the grid size comparing to the traditional latitude-longitude grid, once the subdivision of the icosahedron starts, differences in cell areas and edge lengths occur. As an example, Fig. 2.12 displays the global distribution of the normalized primal and dual edge lengths, as well as the areas associated to triangle faces and edges, of the R2B3 grid without optimization. The grid at the same resolution but optimized using the Heikes-Randall algorithm is depicted in Fig. 2.13. The differences in the primal edge length and cell area are moderate. In contrast, changes in the dual edge length can exceed a factor of two near the icosahedron edges, especially near the corners of the original icosahedron. Because of this strong inequality, any explicit or implicit assumption of equal grid spacing in the discrete model will lead to inaccuracies. The horizontal diffusion coefficient is an example that has been noticed during the development of the 3D dynamical core described in this thesis.

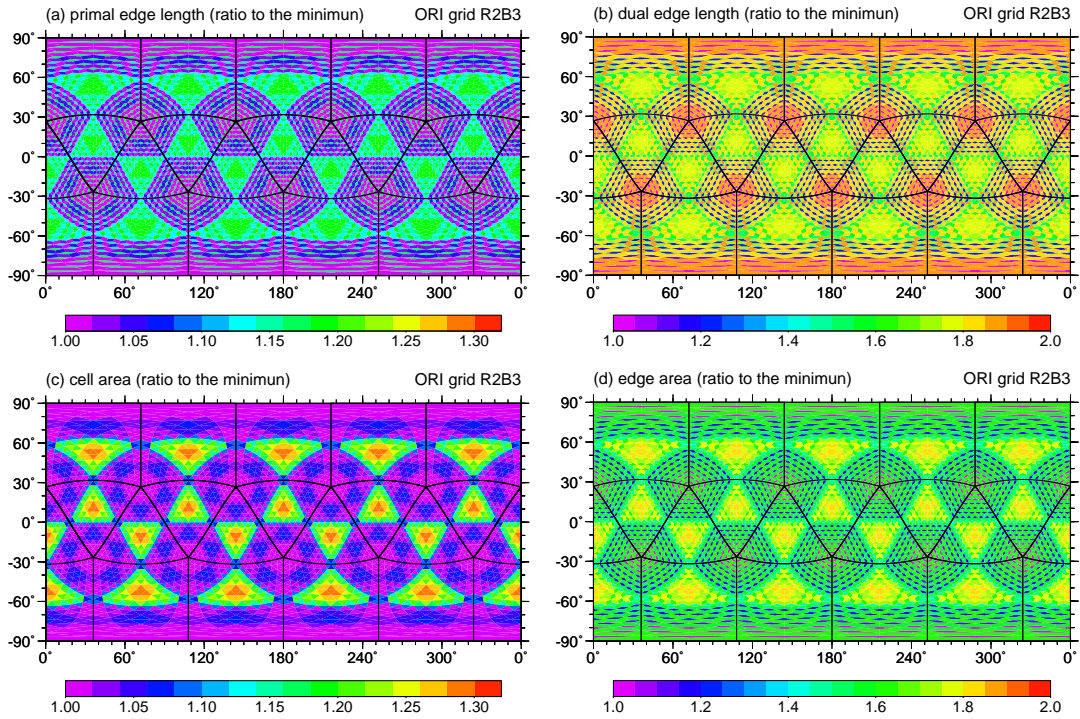


Fig. 2.12: Inequality of the edge lengths and cell areas on the spherical triangular grid obtained by subdividing the icosahedron using the root division $n_r = 2$ and 3 subsequent bisections. The quantities shown are (a) the primal edge length and (b) the dual edge length, scaled by the corresponding shortest length; (c) the triangle area and (d) the area associated to each edge, again scaled by the corresponding minima. The black lines indicate the edges of the icosahedron.

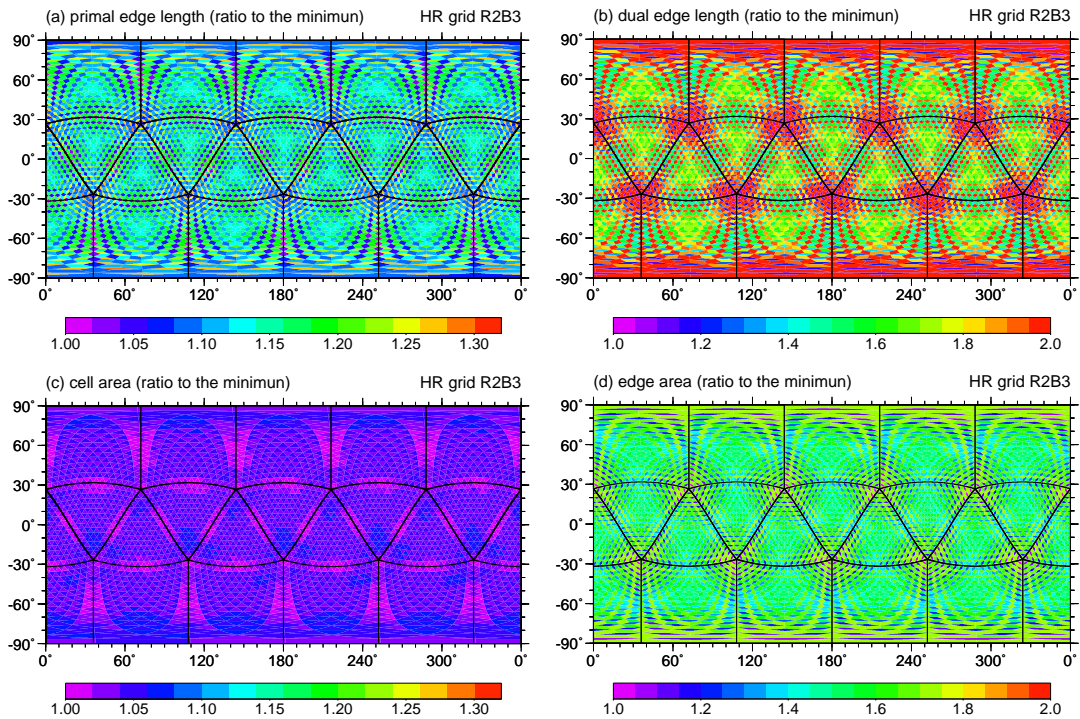


Fig. 2.13: As in Fig. 2.12 but after applying the Heikes-Randall grid optimization algorithm.

In Section 2.3.5 it has been found that the discrete vector Laplacian provides a mechanism of removing the checkerboard noise in divergence, and the magnitude of the compensating term is related to the horizontal grid spacing (see Eqn. (2.48)). In the ICON shallow water model, the horizontal diffusion coefficient \mathcal{K}_4 is calculated from the minimum dual edge length \hat{l}_{min} and the user-specified damping time τ^* according to the formula

$$\mathcal{K}_4 = \frac{1}{\tau^*} \left(\frac{\hat{l}_{min}}{\pi} \right)^4. \quad (2.59)$$

The motivation for using π in Eqn. (2.59) probably originated from other applications of the numerical diffusion (cf. Appendix C, especially Eqns.(C.8) and (C.14)). Using this diffusion coefficient, Eqn. (2.48) can be rewritten as

$$\text{div}(-\Delta t_D \mathcal{K}_4 \nabla_d^4 \mathbf{v})_i \approx -0.657 \frac{\Delta t_D}{\tau^*} \left(\frac{\hat{l}_{min}}{\hat{l}} \right)^4 \mathbb{E}_{div,1} - \Delta t_D \mathcal{K}_4 [\nabla^4 (\nabla \cdot \mathbf{v})]_i + \dots \quad (2.60)$$

When constructing the 3D dynamical core, the first implementation followed the ICOSWM and used Eqn. (2.59). It was then observed in the numerical experiments (cf. Chapter 4) that one had to choose very short damping time to ensure that the integration did not blow up within a few model days. In the baroclinic wave test (Section 4.5), when the parameter $\Delta t_D/\tau^*$ was gradually increased to about 10, the simulation could proceed up to around day 20, and correctly reproduced the life cycle of the baroclinic vortices. Further increase of the parameter, e.g., to 15, led to numerical instability within 2 model days.

A possible explanation for this behaviour is the following: First, it is necessary to choose the coefficient \mathcal{K}_4 such that the grid-scale noise introduced by the divergence operator is suppressed to a significant extent. Second, because the same coefficient \mathcal{K}_4 is used for the whole computational domain despite the differences in the edge length, the value of \mathcal{K}_4 has to be sufficiently large so that the grid-scale noise can be well suppressed even for the largest cells (longest edges); Third, when the compensating effect is enhanced, the strength of the second term on the right-hand side of Eqn. (2.60), the numerical diffusion, is enhanced simultaneously. When the coefficient \mathcal{K}_4 exceeds a certain limit, the diffusion process itself can no longer be sufficiently resolved by the selected time step, and will introduce another source of numerical instability.

Inspired by Eqn. (2.49), we use a location dependent coefficient for the velocity diffusion in the hydrostatic dynamical core defined as

$$(\mathcal{K}_4)_{\mathbf{v}} := \frac{1}{\tau^*} \left(\frac{l \hat{l}}{8\sqrt{3}} \right)^2. \quad (2.61)$$

As for the temperature diffusion, the coefficient is computed as

$$(\mathcal{K}_4)_T := \frac{1}{\tau^*} \left(\frac{A_i}{6\sqrt{3}} \right)^2, \quad (2.62)$$

where A_i is the area of the triangular cell associated to the temperature points. Using the coefficients (2.61) and (2.62), the hydrostatic dynamical core becomes reasonably stable. Even the idealized climate simulation (cf. Section 4.6) can be finished without stability problem. In the numerical experiments presented in Chapter 4, the typical value of the parameter $\Delta t_D/\tau^*$ is between 0.5 and 1.33.

2.4.2 Deformation of the triangular cells

In Section 2.3.6 we have discussed the possibility of improving the accuracy of the divergence operator by adding a four-cell smoothing. On a regular planar grid, the smoothing schemes proposed are able to remove the first-order error in divergence completely, and raise the accuracy to second-order (Fig. 2.11). When applied to the spherical grid, it is observed that although over most of the triangles the errors are reduced by at least one order of magnitude, large values remain along some of the icosahedron edges (Fig. 2.14, a-c). This must not have been caused by the change in the size of the triangles, because Fig. 2.13c shows that the Heikes-Randall optimization leads to almost equal areas (which explains the similarity between panels (b) and (c) of Fig. 2.14).

Consider the case of a planar triangle of arbitrary shape, as depicted in Fig. 2.15. It can be verified that the divergence calculated using Eqn. (2.6) can be expressed as

$$\operatorname{div}(\mathbf{v})_i = (\nabla \cdot \mathbf{v})_o + \frac{r \sin \alpha}{2} \left(\frac{\partial^2 u}{\partial x^2} \right)_o + (-1)^\delta \frac{r}{4} H^*(\mathbf{v})_o + \mathcal{O}(r^2) , \quad (2.63)$$

where

$$H^*(\mathbf{v}) := 2(\cos \alpha - \cos \beta) \left(\frac{\partial^2 u}{\partial x \partial y} \right) + \frac{\sin^2 \beta}{\cos \alpha + \cos \beta} \left(\frac{\partial^2 v}{\partial x^2} \right) + (\cos \alpha - 3 \cos \beta) \left(\frac{\partial^2 v}{\partial y^2} \right) . \quad (2.64)$$

The third term on the right-hand side of Eqn. (2.63) is a generalization of the leading error of the divergence operator in Eqn. (2.27). The second term reveals that the deformation of a triangular cell introduces an additional first-order error term.

When the icosahedron is recursively subdivided, the resulting triangular cells near the center of the original icosahedron faces suffer little from the change in shape, whilst the deformation gradually increase towards the icosahedron edges. The triangles along an icosahedron edge belonging to adjacent icosahedron faces can be distorted to extents that differ considerably. Therefore when the four-cell smoothing is applied, the deformation error can not be effectively removed, leaving large errors in the approximated divergence along the icosahedron edges. Experiments have shown that the use of the spring dynamics optimization (Tomita *et al.*, 2001) can enforce smoother transition of the grid properties, thus leading to some improvements compared to the errors shown in Fig. 2.14b,c. Nevertheless, the twelve corners of the icosahedron remain a problem. To solve the divergence problem, we probably need to either design another smoothing scheme that is orthogonal to Eqn. (2.53) and (2.54), or construct a more sophisticated divergence operator which can also handle significantly distorted triangles.

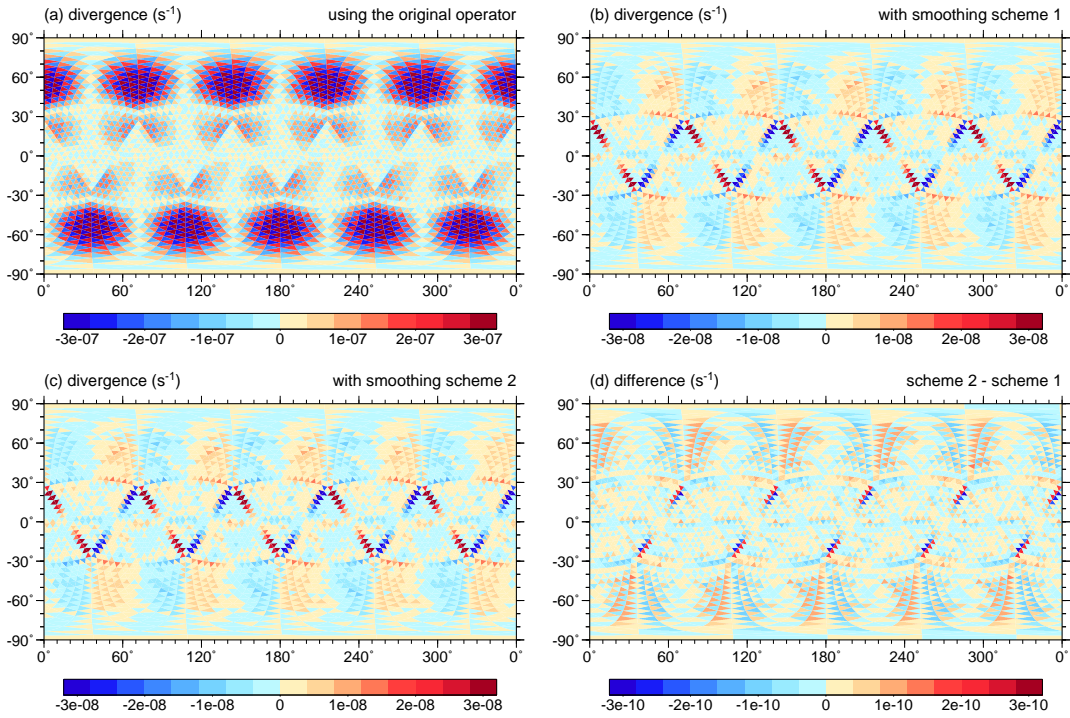


Fig. 2.14: The approximated divergence of an analytically prescribed smooth flow, calculated by (a) the discrete divergence operator defined by Eqn. (2.6), (b) the modified divergence operator Eqn. (2.53), and (c) Eqn. (2.54), on the Heikes-Randall optimized grid at resolution R2B3. Panel (d) shows the differences between (b) and (c). The prescribed flow field is the Rossby-Haurwitz wave of wavenumber 5 (see Eqns. (4.3) and (4.4) in Section 4.2.2), which is nondivergent. The purpose of choosing this wavenumber instead of the standard wavenumber 4 is to match the quasi-periodicity of the optimized icosahedral grid in the zonal direction.

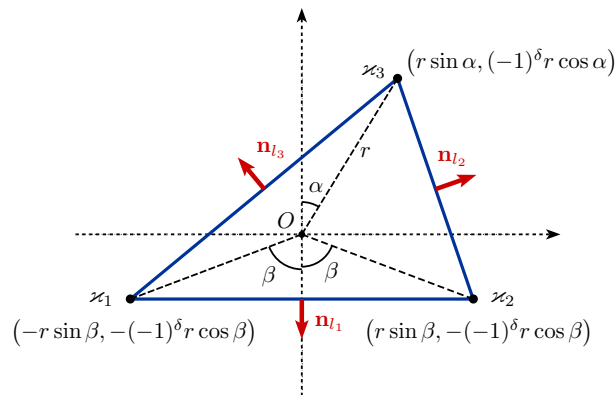


Fig. 2.15: An arbitrarily shaped triangular cell on the plane. Here r denotes the radius of the circumcircle of the triangle. δ indicates the orientation of the triangle in the Cartesian coordinate, which is defined in Fig. 2.4 on page 18.

Chapter 3

Discrete formulation of the icosahedral hydrostatic dynamical core

This chapter describes the discrete formulation of the icosahedral hydrostatic dynamical core (ICOHDC) which represents the adiabatic dynamics of the atmosphere in the spherical coordinate. Section 3.1 introduces the terrain-following vertical coordinate and the arrangement of the discrete variables in the 3D grid system; Section 3.2 gives an overview of the discrete formulation of the governing equations, followed by the details about the spatial discretization in Sections 3.3 to 3.8, as well as the time integration schemes in Section 3.9.

3.1 The hybrid vertical coordinate and the 3D grid system

In the first chapter the primitive equations have been introduced in a generic vertical coordinate η that depends on pressure and its surface value, and satisfies the following requirements:

- η is a monotonic function of pressure;
- Its values at the upper and lower boundaries are $\eta = 0$ and $\eta = 1$, respectively;
- There is no vertical motion in the η coordinate at the upper and lower boundaries, i.e., $\dot{\eta} = 0$ when $\eta = 0$ or $\eta = 1$.

Eqns. (1.3) – (1.6) can be manipulated into the following form which is the starting point of the spatial discretization:

$$\frac{\partial \mathbf{v}}{\partial t} = -(f + \xi) \mathbf{k} \times \mathbf{v} - \nabla K - \dot{\eta} \frac{\partial p}{\partial \eta} \frac{\partial \mathbf{v}}{\partial p} - \frac{R_d T}{p} \nabla p - \nabla \phi \quad (3.1)$$

$$\frac{\partial T}{\partial t} = -\mathbf{v} \cdot \nabla T - \dot{\eta} \frac{\partial p}{\partial \eta} \frac{\partial T}{\partial p} + \frac{1}{C_p} \left[\frac{R_d T}{p} \mathbf{v} \cdot \nabla p + \frac{R_d T}{p} \left(\frac{\partial p}{\partial t} + \dot{\eta} \frac{\partial p}{\partial \eta} \right) \right] \quad (3.2)$$

$$\frac{\partial p_s}{\partial t} = - \int_0^1 \nabla \cdot \left(\mathbf{v} \frac{\partial p}{\partial \eta} \right) d\eta \quad (3.3)$$

$$\dot{\eta} \frac{\partial p}{\partial \eta} = - \int_0^\eta \nabla \cdot \left(\mathbf{v} \frac{\partial p}{\partial \eta} \right) d\eta - \frac{\partial p}{\partial p_s} \frac{\partial p_s}{\partial t} \quad (3.4)$$

$$\phi = - \int_0^\eta R_d T \ln p \, d\eta \quad (3.5)$$

Note that if we further substitute Eqn. (3.4) for $\dot{\eta} \frac{\partial p}{\partial \eta}$ in the velocity and temperature equations, the resulting formulation will have η only appearing in vertical derivatives. Therefore when a finite-difference method is applied for the vertical discretization, the equation set can be solved without an explicit definition of η . The only requirement is that $\frac{\partial p}{\partial p_s}$ and p must be determined.

Simmons and Strüfing (1981) introduced a hybrid coordinate (the "coordinate 4" in their report) which is implicitly defined by the expression

$$p_{k+1/2} = A_{k+1/2} + B_{k+1/2} p_s, \quad k = 0, 1, \dots, NLEV, \quad (3.6)$$

in which $NLEV$ is the total number of vertical layers. † $A_{k+1/2}$ and $B_{k+1/2}$ are parameters independent of horizontal location, whose values effectively define pressure of the interfaces between model layers (known as the "half levels") as well as the derivative

$$\left(\frac{\partial p}{\partial p_s} \right)_{k+1/2} = B_{k+1/2}. \quad (3.7)$$

The values of $A_{k+1/2}$ and $B_{k+1/2}$ corresponding to the L19 and L31 grids are listed in Tab. 3.1, together with the corresponding pressure values assuming $p_s=1000$ hPa (truncated at two digits after the decimal point). Near the Earth's surface, $A_{k+1/2}$ equals zero and the interfaces are pure sigma levels; near the model top, $B_{k+1/2}$ equals zero and the interfaces coincide with isobaric surfaces. The layers in between form a smooth transition.

The grid staggering in the vertical direction follows Lorenz (1960). The horizontal wind and temperature are carried at "full levels" which are defined as

$$p_k = \frac{1}{2} \left(p_{k-1/2} + p_{k+1/2} \right). \quad (3.8)$$

The vertical velocity $\dot{\eta}$ is diagnosed on half-levels. The pressure thickness of the k -th model layer is given by

$$\Delta p_k = p_{k+1/2} - p_{k-1/2}. \quad (3.9)$$

[†]The original formula in Simmons and Strüfing (1981) was $p_{k+1/2} = A_{k+1/2} p_0 + B_{k+1/2} p_s$ with p_0 being 1013.2 hPa. In ECHAM5 this constant has the value 1013.25 hPa and is incorporated in $A_{k+1/2}$. In the ICOHDC the ECHAM5 formula is used, although for most of the idealized tests in Chapter 4, we have followed the suggestion of Jablonowski *et al.* (2008) and taken $p_0=1000$ hPa.

Tab. 3.1: Vertical coordinate parameters A and B of the 19- and 31-layer ECHAM5 model, and the corresponding pressure values (in hPa) when $p_s=1000$ hPa.

k	$A_{k+1/2}$	$B_{k+1/2}$	$p_{k+1/2}$	$A_{k+1/2}$	$B_{k+1/2}$	$p_{k+1/2}$
0	0.000000	0.0000000000	0.00	0.00000000	0.00000000	0.00
1	2000.000000	0.0000000000	20.00	2000.00000000	0.00000000	20.00
2	4000.000000	0.0000000000	40.00	4000.00000000	0.00000000	40.00
3	6046.110595	0.0003389933	60.80	6000.00000000	0.00000000	60.00
4	8267.927560	0.0033571866	86.04	8000.00000000	0.00000000	80.00
5	10609.513232	0.0130700434	119.17	9976.13671875	0.00039086	100.15
6	12851.100169	0.0340771467	162.59	11820.53906250	0.00291970	121.13
7	14698.498086	0.0706498323	217.63	13431.39453125	0.00919413	143.51
8	15861.125180	0.1259166826	284.53	14736.35546875	0.02031916	167.68
9	16116.236610	0.2011954093	362.36	15689.20703125	0.03697486	193.87
10	15356.924115	0.2955196487	449.09	16266.60937500	0.05948764	222.15
11	13621.460403	0.4054091989	541.62	16465.00390625	0.08789498	252.55
12	11101.561987	0.5249322235	635.95	16297.62109375	0.12200361	284.98
13	8127.144155	0.6461079479	727.38	15791.59765625	0.16144150	319.36
14	5125.141747	0.7596983769	810.95	14985.26953125	0.20570326	355.56
15	2549.969411	0.8564375573	881.94	13925.51953125	0.25418860	393.44
16	783.195032	0.9287469142	936.58	12665.29296875	0.30623537	432.89
17	0.000000	0.9729851852	972.99	11261.23046875	0.36114502	473.76
18	0.000000	0.9922814815	992.28	9771.40625000	0.41820228	515.92
19	0.000000	1.0000000000	1000.00	8253.21093750	0.47668815	559.22
20				6761.33984375	0.53588659	603.50
21				5345.91406250	0.59508425	648.54
22				4050.71777344	0.65356457	694.07
23				2911.56933594	0.71059442	739.71
24				1954.80517578	0.76540524	784.95
25				1195.88989258	0.81716698	829.13
26				638.14892578	0.86495584	871.34
27				271.62646484	0.90771586	910.43
28				72.06358337	0.94421321	944.93
29				0.00000000	0.97298521	972.99
30				0.00000000	0.99228150	992.28
31				0.00000000	1.00000000	1000.00

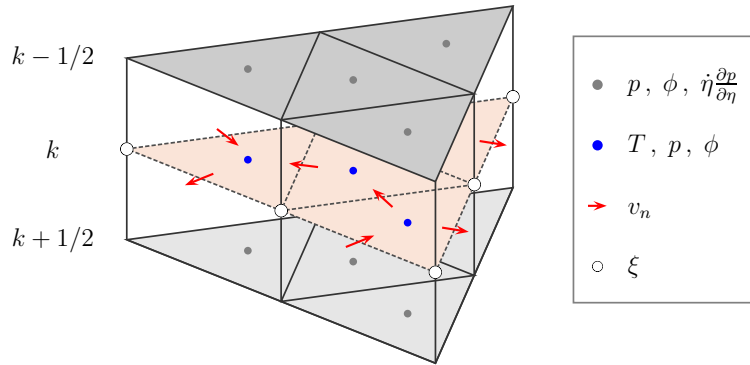


Fig. 3.1: Arrangement of the prognostic and diagnostic variables in the icosahedral hydrostatic dynamical core. See the text for details.

Combining the triangular C-grid and the Lorenz coordinate, we arrange the discrete variables in the ICOHDC as follows:

- Surface pressure is predicted at triangle centers and denoted by the symbol p_{s_i} ;
- Temperature is predicted at triangle centres on full-levels and denoted by $T_{i,k}$;
- The component of the horizontal wind normal to edge l is predicted at edge midpoints on full-levels and denoted by $v_{n_{l,k}}$;
- Geopotential is diagnosed at triangle centres on both half- and full-vertical levels, denoted by the symbols $\phi_{i,k+\frac{1}{2}}$ and $\phi_{i,k}$, respectively;
- For the vertical velocity in the η coordinate, we diagnose the quantity $\eta \frac{\partial p}{\partial \eta}$ at triangle centres on half-levels;
- Relative vorticity is diagnosed on full levels at vertices of the triangular cells, represented by the symbol $\xi_{\mathcal{X},k}$.

The staggered 3D grid system is depicted in Fig. 3.1.

3.2 Overview of the discrete formulation

As already mentioned in the introduction, the hydrostatic dynamical core developed in this thesis can be seen as a combination of the horizontal discretization used in the ICON shallow water model and the vertical discretization used by the dynamical core of ECHAM5. So as to clarify the similarities and differences between the two dynamical cores, we first briefly summarize the main features of the numerical schemes used in ECHAM5.

The dynamical core of ECHAM5 originated from the operational forecast model cycle 36 of the European Centre for Medium-range Weather Forecasts (ECMWF). The prognostic variables include vorticity, divergence, temperature, and logarithm of the surface pressure.

The horizontal discretization is carried out with the spectral transform method using triangular truncation (Hoskins and Simmons, 1975; Roeckner *et al.*, 2003); The generalized pressure-based terrain-following vertical coordinate is used in the vertical (Simmons and Strüfing, 1981).

In the standard model version for tropospheric applications, the uppermost computational level is located at 10 hPa. A second-order energy and angular momentum conserving scheme (Simmons and Burridge, 1981; Simmons and Strüfing, 1981) is employed for the grid-point calculations including the vertical differencing and nonlinear terms in the governing equations. Following the work by Simmons and Chen (1991), a reference temperature profile is introduced in the computation of the pressure gradient force, so as to reduce numerical errors near steep topography.

The time integration is based on the leapfrog method. Following Robert *et al.* (1972), a semi-implicit scheme is used for divergence, temperature and surface pressure. In addition, semi-implicit treatment for the zonal advection terms in the vorticity equation is employed following the work of Robert (1981, 1982). The growth of spurious computational modes caused by the leapfrog time integration method is inhibited by the Asselin (1972) filter.

The horizontal diffusion scheme takes the form of scale-selective hyper-viscosity applied to vorticity, divergence and temperature. To avoid spurious wave reflection at the upper boundary, the damping is enhanced in the top layers by decreasing the order of the hyper-Laplace operator. A detailed description of the horizontal diffusion scheme can be found in Roeckner *et al.* (2003) and in Appendix B of Wan *et al.* (2008).

After this brief overview of the dynamical core of ECHAM5, we now come to the new dynamical core established on the spherical triangular grid, which we refer to as the ICOHDC. With the help of Eqns. (3.1) – (3.4), the discrete formulation of the ICOHDC can be summarized as follows:

For the surface pressure equation (3.3), a flux-form discretization is applied to each model layer using the discrete divergence operator, followed by the sum over all layers (Section 3.4). To discretize the vorticity flux term $(f + \xi) \mathbf{k} \times \mathbf{v}$ in the velocity equation (3.1), the wind component tangential to each edge is reconstructed from the normal component (Section 3.5). The horizontal gradient of kinetic energy (Section 3.5) and geopotential (Section 3.7) are direct applications of the normal gradient operator. The aforementioned parts closely resemble the ICON shallow water model.

The vertical advection of momentum and temperature are calculated by the conservative discretization scheme of Simmons and Burridge (1981) (Section 3.6.1). The horizontal advection of temperature uses a generalized energy-conserving formulation (Section 3.6.2).

The computation of the pressure gradient term $\frac{R_d T}{p} \nabla p$ and the adiabatic heating terms follows the idea of Simmons and Burridge (1981) (Sections 3.7 and 3.8). The original scheme ensures angular momentum conservation on the latitude-longitude. On the triangular grid, this is generalized such that for any closed path on the sphere consisting of dual edges, the vertically integrated circulation is conserved. This property is beneficial for avoiding spurious vorticity production.

As for time integration, the leapfrog scheme and the Asselin filter are implemented (Section 3.9.1) together with the semi-implicit treatment of gravity waves (Sections 3.9.2 and 3.9.3) as discussed in Simmons and Burridge (1981). Note that following ECHAM5, the semi-implicit scheme uses a constant reference temperature.

Regarding the horizontal diffusion, spectral transform models benefit from the fact that the

spherical harmonics are the eigenfunctions of the Laplace operator, thus they can easily employ hyper-viscosity of very high order with almost no additional cost. Since the new dynamical core is constructed with finite difference method, this convenience no longer exists, and we choose to use the fourth-order diffusion. The same strength of damping is used for all vertical levels.

The following sections describe in detail the spatial discretization and the time stepping schemes.

3.3 Horizontal interpolation of scalar and vector fields

Because of the C-type grid staggering, horizontal interpolation is needed for calculating fluxes at cell boundaries and advection terms at cell centers. In the ICOHDC, area-weighted averaging is used for the interpolation of scalar variables, while radial basis functions are employed in reconstructing the horizontal wind vector (Baudisch *et al.*, 2006, see also Appendix D of this thesis for a brief introduction).

Using the notation listed in Tab. 2.3 on page 13, the area associated to a generic triangular cell i and edge l can be expressed as

$$A_i = \sum_{l \in \mathcal{E}(i)} A_{i,l} \quad (3.10)$$

$$A_l = \sum_{j=1,2} A_{i(l,j),l} \quad (3.11)$$

where

$$A_{i,l} := \frac{\widehat{MV} \cdot l}{2}, \quad (3.12)$$

and \widehat{MV} is the great circle distance between the center of cell i and the midpoint of edge l (Fig. 3.2). On the sphere Eqn. (3.12) is an approximation, but it is consistent with the discrete version of the formula for integration by parts (cf. Eqn. (2.10)). The edge-to-cell and cell-to-edge averaging of scalar variables are defined as

$$\bar{\varrho}_i := \sum_{l \in \mathcal{E}(i)} \frac{A_{i,l}}{A_i} \varrho_l, \quad \text{and} \quad (3.13)$$

$$\check{\varrho}_l := \sum_{j=1,2} \frac{A_{i(l,j)}}{A_l} \varrho_{i(l,j)}, \quad (3.14)$$

respectively.

Radial basis functions (RBFs) are used for reconstructing the horizontal wind vector from its normal component at the midpoint of edges. When the velocity information is needed at other locations, or at the edge midpoints but in the tangential direction, the full vector field is first reconstructed at triangle centers with the RBF algorithm and then interpolated in the 3D Cartesian coordinate to the location where it is needed. Projection to a certain direction follows if needed. A brief introduction to the RBF interpolation is provided in Appendix D.

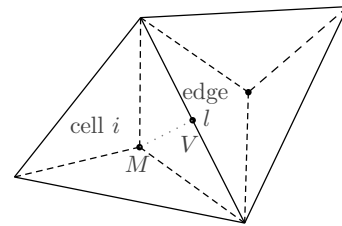


Fig. 3.2: A schematic showing the area-weighted averaging of scalar variables.

3.4 The continuity equation

Using the divergence operator defined in Chapter 2 and a simple central-difference in the vertical direction, the continuity equation (1.5) of cell i in the k -th vertical layer can be spatially discretized as

$$\frac{\partial p_{i,k+1/2}}{\partial t} - \frac{\partial p_{i,k-1/2}}{\partial t} + \text{div}(\mathbf{v}\Delta p)_{i,k} + \left(\dot{\eta} \frac{\partial p}{\partial \eta} \right)_{i,k+1/2} - \left(\dot{\eta} \frac{\partial p}{\partial \eta} \right)_{i,k-1/2} = 0. \quad (3.15)$$

This flux-form formulation ensures conservation of the total air mass. Taking a sum of Eqn. (3.15) over the whole vertical column, the tendency of the surface pressure can be obtained as

$$\frac{\partial p_{si}}{\partial t} = - \sum_{j=1}^{NLEV} \text{div}(\mathbf{v}\Delta p)_{i,j}, \quad (3.16)$$

which is the discrete counterpart of Eqn. (3.3). Accordingly, the vertical velocity equation in the discrete model reads

$$\left(\dot{\eta} \frac{\partial p}{\partial \eta} \right)_{i,k+1/2} = - \sum_{j=1}^k \text{div}(\mathbf{v}\Delta p)_{i,j} - B_{k+1/2} \frac{\partial p_{si}}{\partial t}. \quad (3.17)$$

The mass flux divergence of each grid cell is calculated by

$$\text{div}(\mathbf{v}\Delta p)_{i,k} = \frac{1}{A_i} \sum_{l \in \mathcal{E}(i)} v_{n_{l,k}} \Delta \check{p}_{l,k} (\mathbf{N}_l \cdot \mathbf{n}_{i,l}) l, \quad (3.18)$$

where $\Delta \check{p}_{l,k}$ is the layer thickness interpolated to edge l from the two neighbouring mass points using Eqn. (3.14).

3.5 Vorticity flux and kinetic energy gradient

For the governing equations of the atmospheric motion, we have chosen the so-called "vector invariant" form of the velocity equation (i.e., Eqns. (1.3) and (3.1)) to represent the hydrodynamics of the atmosphere. Compared with the momentum advection form that reads

$$\frac{\partial u}{\partial t} = f v - \mathbf{v} \cdot \nabla u + \frac{uv \tan \varphi}{a} - \dot{\eta} \frac{\partial u}{\partial \eta} - \frac{R_d T}{p} \frac{\partial p}{a \cos \varphi \partial \lambda} - \frac{\partial \phi}{a \cos \varphi \partial \lambda}, \quad (3.19)$$

$$\frac{\partial v}{\partial t} = -f u - \mathbf{v} \cdot \nabla v - \frac{u^2 \tan \varphi}{a} - \dot{\eta} \frac{\partial v}{\partial \eta} - \frac{R_d T}{p} \frac{\partial p}{a \partial \varphi} - \frac{\partial \phi}{a \partial \varphi}, \quad (3.20)$$

the vector invariant form represents the nonlinear advection as absolute vorticity flux and kinetic energy gradient. Information about the geometry is implicitly contained in the areas and lengths of the volumes used to discretize the model. Explicit calculation of the metric terms is thus avoided. For the normal direction of a generic edge l , the terms that need discretization are $(f + \xi) v_{\tau_{k,l}}$ and $-\nabla K \cdot \mathbf{N}_l$.

From the point of view of fluid dynamics, vorticity flux changes the direction of the flow but has no effect on kinetic energy; The term $-\nabla K$ leads to redistribution of kinetic energy over

different locations, but does not affect its global integral. To preserve these properties in the numerical model, one has to make sure that the following two equalities

$$\sum_{l \in S} \Delta \check{p}_{l,k} v_{n_{l,k}} \left[(f + \xi) v_\tau \right]_{l,k} A_l = 0 \quad (3.21)$$

$$\sum_{l \in S} \Delta \check{p}_{l,k} v_{n_{l,k}} \left[\nabla K \cdot \mathbf{N}_l \right]_{l,k} 2A_l + \sum_{i \in S} K_{i,k} \operatorname{div}(\mathbf{v} \Delta p)_{i,k} A_i = 0 \quad (3.22)$$

are satisfied, where S denotes the spherical domain. [†] If the mass flux divergence is calculated by Eqn. (3.18), then Eqn. (3.22) can be automatically fulfilled as long as the kinetic energy gradient is computed by

$$\left[\nabla K \cdot \mathbf{N}_l \right]_{l,k} = \operatorname{grad}_n(K)_l = \frac{K_{i(l,2)} - K_{i(l,1)}}{l}. \quad (3.23)$$

The cell-based kinetic energy $K_{i,k}$ can be obtained either from the reconstructed wind vector \mathbf{v}^* as

$$K_{i,k}^* := \frac{\mathbf{v}_{i,k}^* \cdot \mathbf{v}_{i,k}^*}{2}, \quad (3.24)$$

or interpolated from the edge-based normal velocity as

$$\bar{K}_{i,k} := \sum_{l \in \mathcal{E}(i)} \frac{A_{i,l}}{A_i} v_{n_{l,k}}^2. \quad (3.25)$$

To fulfill Eqn. (3.21), one can follow Bonaventura and Ringler (2005) and calculate the vorticity flux by

$$\left[(f + \xi) v_\tau \right]_{l,k} = \sum_{l' \in \mathcal{E}(l)} \left(v_{n_{l',k}} \widetilde{(f + \xi)}_{i(l,l'),k} \frac{A_{l'} \Delta p_{l',k}}{2A_{i(l,l')} \Delta p_{i(l,l'),k}} \right) \mathbf{T}_l \cdot \mathbf{N}_{l'}. \quad (3.26)$$

The summation in (3.26) is done over the other four edges that are associated to the two neighbouring triangles of edge l (Fig. 3.3). $i(l, l')$ is the triangle that has both l and l' as edges. The key feature that makes this formula energy conserving is, when multiplied by $(v_{n_{l,k}} \Delta p_{l,k} A_l)$, the expression in the right-hand-side parentheses become invariant to the exchange of l and l' but the inner product changes its sign. As to the absolute vorticity $(f + \xi)$ at cell centers, the choice of formulation does not affect the conservation property of Eqn. (3.26). One can obtain it by, for example, taking the arithmetic average of the absolute vorticity at the three vertices.

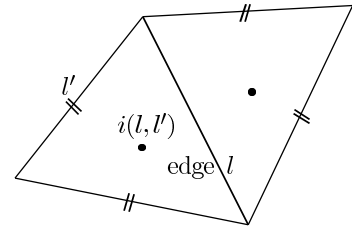


Fig. 3.3: Stencil of the energy conserving discretization of the vorticity flux (cf. Eqn. (3.26)).

[†]Note that there is a factor 2 before A_l in Eqn. (3.22). This is necessary because – as discussed in the text below Eqn. (2.10) on page 15 – only the normal velocity and the normal component of the kinetic energy gradient are included in the calculation of the vector inner product. This factor will appear again later, implicitly in Eqns. (3.25) and (3.59), and explicitly in Eqn. (3.57).

An alternative discretization scheme for the vorticity flux that does not satisfy Eqn. (3.21) but is used as the default option in the ICON shallow water model takes the form

$$\left[(f + \xi) v_\tau \right]_{l,k} = \overline{(f + \xi)}_{l,k}^e v_{\tau_{l,k}}^* \quad (3.27)$$

Here the notation $\overline{(\)}_l^e$ denotes the simple arithmetic average of values at the two vertices of edge l . The tangential velocity $v_{\tau_l}^*$ is obtained by first reconstructing the full wind vector at triangle centers, interpolating to edge centres and then project to the normal direction. The argument of Bonaventura and Ringler (2005) for using this formula is that taking the discrete curl of (3.27) yields a consistent discretization of the relative vorticity equation for the dual cells. In the numerical experiments discussed in Chapter 4, this local calculation is used.

3.6 Advection of momentum and temperature

Like the vorticity flux and kinetic energy terms, the role of the other advection terms in the momentum and temperature equations – from the point of view of the energy budget – is the spatial re-distribution of energy. To avoid spurious energy sources or sinks, the vertical advection of momentum and temperature as well as the horizontal advection of temperature need to be discretized in a way that is consistent with the continuity equation.

3.6.1 Vertical advection

Simmons and Burridge (1981) and Simmons and Strüfing (1981) suggested calculating the vertical advection of a variable ψ by

$$\left(\dot{\eta} \frac{\partial \psi}{\partial \eta} \right)_k = \frac{1}{2\Delta p_k} \left\{ \left(\dot{\eta} \frac{\partial p}{\partial \eta} \right)_{k+1/2} (\psi_{k+1} - \psi_k) + \left(\dot{\eta} \frac{\partial p}{\partial \eta} \right)_{k-1/2} (\psi_k - \psi_{k-1}) \right\}, \quad (3.28)$$

which recovers the relationships

$$\int_{\eta_1}^{\eta_2} \left(\dot{\eta} \frac{\partial \psi}{\partial \eta} \right) \frac{\partial p}{\partial \eta} d\eta + \int_{\eta_1}^{\eta_2} \psi \frac{\partial}{\partial \eta} \left(\dot{\eta} \frac{\partial p}{\partial \eta} \right) d\eta = \int_{\eta_1}^{\eta_2} \frac{\partial}{\partial \eta} \left(\psi \dot{\eta} \frac{\partial p}{\partial \eta} \right) d\eta \quad (3.29)$$

$$\int_{\eta_1}^{\eta_2} \psi \left(\dot{\eta} \frac{\partial \psi}{\partial \eta} \right) \frac{\partial p}{\partial \eta} d\eta + \int_{\eta_1}^{\eta_2} \frac{1}{2} \psi^2 \frac{\partial}{\partial \eta} \left(\dot{\eta} \frac{\partial p}{\partial \eta} \right) d\eta = \int_{\eta_1}^{\eta_2} \frac{\partial}{\partial \eta} \left(\frac{1}{2} \psi^2 \dot{\eta} \frac{\partial p}{\partial \eta} \right) d\eta \quad (3.30)$$

in the discrete model.

Application of formula (3.28) to temperature is straightforward, for which the vertical velocity $\left(\dot{\eta} \frac{\partial p}{\partial \eta} \right)_{i,k+1/2}$ is obtained from Eqn. (3.17). For the momentum advection, both the layer thickness and the vertical velocity at edge midpoints are interpolated from the neighbouring mass point using the area-weighted average (3.14).

3.6.2 Horizontal advection of temperature

The temperature advection term $-\mathbf{v} \cdot \nabla T$ has no counterpart in the shallow water model and has to be treated with care. In ECHAM5, it is simply calculated according to its definition as

$$\left[-\mathbf{v} \cdot \nabla T \right]_{i,j,k} = -\frac{u_{i,j,k}}{a \sin \varphi_j} \left(\frac{\partial T}{\partial \lambda} \right)_{i,j,k} - \frac{v_{i,j,k}}{a} \left(\frac{\partial T}{\partial \varphi} \right)_{i,j,k} \quad (3.31)$$

in which i, j, k are the grid point indices in the longitudinal, latitudinal and vertical directions, respectively. The partial derivatives of temperature are provided directly by the spectral transform method which does not guarantee energy conservation. In the ECMWF grid-point forecast model (Simmons and Strüfing, 1981; Burridge and Haseler, 1977) the discretization scheme reads

$$\left[-\mathbf{v} \cdot \nabla T \right]_{i,j,k} = \frac{-1}{\Delta p_{i,j,k} a \sin \varphi_j} \left(\overline{\Delta p_k^\lambda} u_k \partial_\lambda T_k + \overline{\Delta p_k^\varphi} v_k \sin \varphi \partial_\varphi T_k \right)_{i,j}, \quad (3.32)$$

in which $\overline{(\)}^\lambda$ and ∂_λ are the well-known averaging and differencing operators in the longitudinal direction:

$$\left(\overline{\psi}^\lambda \right)_{i,j} := \frac{1}{2} (\psi_{i+1/2,j} + \psi_{i-1/2,j}), \quad (\partial_\lambda \psi)_{i,j} := \frac{1}{\Delta \lambda} (\psi_{i+1/2,j} - \psi_{i-1/2,j}). \quad (3.33)$$

The corresponding operators in the latitudinal direction are defined in a similar way. It can be verified that formula (3.32) does not cause spurious sources and sinks in the internal energy. For the ICOHDC, one needs to find out how (3.32) can be adapted for the triangular C-grid.

If we go back to the primitive equations in differential form and recall how the internal energy equation is derived, the key point which leads to the conclusion that horizontal advection does not affect the global integral of internal energy is that the sum of the advection multiplied by the pseudo-density $\frac{\partial p}{\partial \eta}$ and the horizontal mass flux divergence multiplied by temperature gives

$$\frac{\partial p}{\partial \eta} (-\mathbf{v} \cdot \nabla T) - T \nabla \cdot \left(\mathbf{v} \frac{\partial p}{\partial \eta} \right) = -\nabla \cdot \left(\mathbf{v} \frac{\partial p}{\partial \eta} T \right). \quad (3.34)$$

The right-hand side vanishes when the global integral is taken. Eqn. (3.34) can be recovered automatically in the ICOHDC if the horizontal temperature advection at cell i in layer k is discretized as

$$(\mathbf{v} \cdot \nabla T)_{i,k} = \frac{1}{\Delta p_{i,k}} \left[\text{div}(\mathbf{v} \Delta p T)_{i,k} - T_{i,k} \text{div}(\mathbf{v} \Delta p)_{i,k} \right], \quad (3.35)$$

which is the discrete analogue of

$$\mathbf{v} \cdot \nabla T = \left(\frac{\partial p}{\partial \eta} \right)^{-1} \left[\nabla \cdot \left(\mathbf{v} \frac{\partial p}{\partial \eta} T \right) - T \nabla \cdot \left(\mathbf{v} \frac{\partial p}{\partial \eta} \right) \right]. \quad (3.36)$$

The mass flux divergence in Eqn. (3.35) is taken directly from the discrete continuity equation; The heat flux divergence is calculated similarly by

$$\text{div}(\mathbf{v} T \Delta p)_{i,k} = \frac{1}{A_i} \sum_{l \in \mathcal{E}(i)} v_{n_{l,k}} \check{T}_{l,k} \Delta \check{p}_{l,k} (\mathbf{N}_l \cdot \mathbf{n}_{i,l}) \quad (3.37)$$

in which $\check{T}_{l,k}$, like $\Delta \check{p}_{l,k}$, is obtained by the area-weighted cell-to-edge interpolation.

If we regard the divergence operator (2.6) as a generic formulation for any arbitrarily-shaped convex polygon, then Eqn. (3.35) is the corresponding conservative formulation for discretizing the temperature advection. For example, on a latitude-longitude C-grid, each grid cell has four edges whose normal direction coincide with the coordinate lines. When the grid is evenly spaced in both directions, the cell-to-edge interpolation defined by Eqn. (3.14) reduces to simple arithmetic average, and formula (3.35) reduces exactly to scheme (3.32) in the ECMWF grid-point model. In the one-dimensional case, the boundaries of a grid cell collapse to the two

end points and the divergence degrades to a simple central difference. One can use the idea of Eqn. (3.36) and discretize the vertical advection in a similar way from

$$\dot{\eta} \frac{\partial T}{\partial \eta} = \left(\frac{\partial p}{\partial \eta} \right)^{-1} \left[\frac{\partial}{\partial \eta} \left(\dot{\eta} \frac{\partial p}{\partial \eta} T \right) - T \frac{\partial}{\partial \eta} \left(\dot{\eta} \frac{\partial p}{\partial \eta} \right) \right]. \quad (3.38)$$

By using the central difference for computing the vertical derivative and the arithmetic mean for calculating the temperature at layer interfaces, the discrete scheme (3.28) is recovered.

3.7 Hydrostatic equation and pressure gradient force

Special attention needs to be paid when discretizing the pressure gradient force, because of the following considerations:

1. In the continuous form, the pressure gradient force generates no circulation of vertically integrated momentum along a contour of the surface topography (Arakawa and Suarez, 1983). This property has an important effect on the vorticity field of the atmospheric flow. The pressure gradient force is given by $-\nabla_p \phi$ in the pressure coordinate. In the generalized η -coordinate of the ICOHDC presented in this thesis, it can be rewritten as

$$-\nabla_p \phi = -\nabla_\eta \phi + \frac{\partial \phi}{\partial p} \nabla_\eta p = - \left(\frac{\partial p}{\partial \eta} \right)^{-1} \left[(\nabla_\eta \phi) \frac{\partial p}{\partial \eta} - \frac{\partial \phi}{\partial \eta} \nabla_\eta p \right] \quad (3.39)$$

$$= - \left(\frac{\partial p}{\partial \eta} \right)^{-1} \left[\nabla_\eta \left(\phi \frac{\partial p}{\partial \eta} \right) - \frac{\partial}{\partial \eta} (\phi \nabla_\eta p) \right]. \quad (3.40)$$

Taking the mass-weighted vertical integral of (3.40) yields

$$- \int_{\eta_S}^{\eta_T} (\nabla_p \phi) \frac{\partial p}{\partial \eta} d\eta = -\nabla_\eta \left(\int_{\eta_S}^{\eta_T} \phi \frac{\partial p}{\partial \eta} d\eta \right) + \phi_S \nabla_\eta p_S. \quad (3.41)$$

The first term on the right-hand side of (3.41) is a gradient vector. The line integral of its tangential component along an arbitrary closed curve on the sphere vanishes. Retaining this property in the discrete model can help avoid spurious sources or sinks of the vertically integrated vorticity. It is also beneficial for the angular momentum budget since (3.41) leads to the conservation of angular momentum when the closed line is chosen to be the latitude circle.

2. In the terrain-following vertical coordinate, the pressure gradient force takes the form of two large-in-magnitude terms with opposite sign near steep mountains, i.e.,

$$\mathcal{O}(-\nabla_p \phi) \ll \mathcal{O}(-\nabla_\eta \phi) \approx \mathcal{O} \left(\frac{\partial \phi}{\partial p} \nabla_\eta p \right). \quad (3.42)$$

The numerical approximation of the pressure gradient term is therefore subject to large errors in these areas. The resulting horizontal wind tendency further causes erroneous divergence and vertical motion, which then may lead to large errors in the local circulation and precipitation in an AGCM.

Numerous methods have been developed in the past to take into account either or both aspects, among which the approaches by Simmons and Burridge (1981) and Arakawa and Suarez (1983) have been widely adopted in AGCMs.

The scheme of Simmons and Burridge (1981) conserves angular momentum on the latitude-longitude grid by ensuring

$$\sum_{k=1}^{NLEV} \left[\nabla \phi_k + \left(\frac{R_d T}{p} \nabla p \right)_k \right] \Delta p_k = \sum_{k=1}^{NLEV} \nabla (\phi_k \Delta p_k) - \phi_s \nabla p_s . \quad (3.43)$$

Derivation of the discrete pressure gradient force starts from discretizing the hydrostatic equation at mass points in the grid system. In the ICOHDC, we use

$$\phi_{i,k+1/2} - \phi_{i,k-1/2} = -R_d T_{i,k} \ln \left(\frac{p_{i,k+1/2}}{p_{i,k-1/2}} \right) \quad \text{for } k \geq 2 . \quad (3.44)$$

A discrete vertical integration of this equation gives the value of geopotential at the half levels:

$$\phi_{i,k+1/2} = \phi_{si} + \sum_{j=k+1}^{NLEV} R_d T_{i,j} \ln \left(\frac{p_{i,j+1/2}}{p_{i,j-1/2}} \right) \quad \text{for } k \geq 1 . \quad (3.45)$$

Full level values are calculated from

$$\phi_{i,k} = \phi_{i,k+1/2} + \alpha_{i,k} R_d T_{i,k} \quad \text{for } k \geq 1 , \quad (3.46)$$

where the coefficient α_k is defined as

$$\alpha_{i,k} = \begin{cases} \ln 2 , & \text{for } k = 1 ; \\ 1 - \frac{p_{i,k-1/2}}{\Delta p_{i,k}} \ln \left(\frac{p_{i,k+1/2}}{p_{i,k-1/2}} \right) , & \text{for } k > 1 . \end{cases} \quad (3.47)$$

The geopotential part of the pressure gradient force is computed as

$$\left(\nabla \phi \right)_{l,k} \cdot \mathbf{N}_l = \frac{\phi_{i(l,2),k} - \phi_{i(l,1),k}}{\hat{l}} \quad (3.48)$$

at velocity points.

Following the procedures detailed in Appendix A of Simmons and Strüfing (1981), the analogue of the Simmons and Burridge (1981) formulation of the $\frac{R_d T}{p} \nabla p$ term on the triangular C-grid can be derived as

$$\left(\frac{R_d T}{p} \nabla p \right)_{l,k} \cdot \mathbf{N}_l = \frac{R_d}{\Delta \tilde{p}_{l,k}} \left[\overline{\overline{(T_k)_l}} \Delta B_k + C_k \left(\frac{T_k}{\Delta p_k} \ln \frac{p_{k+1/2}}{p_{k-1/2}} \right)_l \right] \text{grad}_n(p_s)_l , \quad (3.49)$$

in which the parameter C_k is defined as

$$C_k = A_{k+1/2} B_{k-1/2} - A_{k-1/2} B_{k+1/2} , \quad (3.50)$$

and the notation $\overline{\overline{(\)}_l}$ denotes a linear interpolation

$$\overline{\overline{\psi}}_l := \frac{A_{i(l,2),l}}{A_l} \psi_{i(l,1)} + \frac{A_{i(l,1),l}}{A_l} \psi_{i(l,2)} . \quad (3.51)$$

Note that this interpolation is different from the cell-to-edge averaging defined by Eqn. (3.14) because there is a swap of the interpolation coefficients assigned to the two neighbouring mass points. Formula (3.49) can be compared with the ECHAM5 formulation

$$\left(\frac{R_d T}{p} \nabla p \right)_k = \frac{R_d T_k}{\Delta p_k} \left\{ \Delta B_k + C_k \frac{1}{\Delta p_k} \left(\ln \frac{p_{k+1/2}}{p_{k-1/2}} \right) \right\} \nabla p_s, \quad (3.52)$$

which is computed on an unstaggered grid with the surface pressure gradient provided by the spectral discretization. While the scheme in ECHAM5 ensures conservation of the zonally and vertically integrated angular momentum, formula (3.49) conserves the vertically integrated circulation along any closed grid line consisting of edges of the dual cells.

As Simmons and Burridge (1981) have pointed out, the formulation of the pressure gradient force above implies that the full-level values of pressure are given by

$$p_k = \begin{cases} \frac{1}{2} \Delta p_1, & \text{for } k = 1; \\ \exp \left[\frac{1}{\Delta p_k} (p_{k+1/2} \ln p_{k+1/2} - p_{k-1/2} \ln p_{k-1/2}) - 1 \right], & \text{for } k > 1. \end{cases} \quad (3.53)$$

However, with the ECHAM5 model, little difference has been detected in numerical experiments performed using formulae (3.53) and (3.8). Following ECHAM5, the ICOHDC uses the simpler formula (3.8).

3.8 Adiabatic heating

In the continuous case, the kinetic energy equation and potential energy equation can be obtained from the velocity equation, the thermodynamic equation, and the continuity equation:

$$\frac{\partial}{\partial t} \left(K \frac{\partial p}{\partial \eta} \right) + \nabla \cdot \left(\mathbf{v} K \frac{\partial p}{\partial \eta} \right) + \frac{\partial}{\partial \eta} \left(\dot{\eta} K \frac{\partial p}{\partial \eta} \right) = \frac{\partial p}{\partial \eta} \mathbf{v} \cdot \left(-\frac{R_d T}{p} \nabla p \right) + \frac{\partial p}{\partial \eta} \mathbf{v} \cdot (-\nabla \phi) \quad (3.54)$$

$$\frac{\partial}{\partial t} \left(C_p T \frac{\partial p}{\partial \eta} \right) + \nabla \cdot \left(\mathbf{v} C_p T \frac{\partial p}{\partial \eta} \right) + \frac{\partial}{\partial \eta} \left(\dot{\eta} C_p T \frac{\partial p}{\partial \eta} \right) = \frac{\partial p}{\partial \eta} \frac{R_d T}{p} (\mathbf{v} \cdot \nabla p) + \frac{\partial p}{\partial \eta} \frac{R_d T}{p} \left(\frac{\partial p}{\partial t} + \dot{\eta} \frac{\partial p}{\partial \eta} \right) \quad (3.55)$$

Using the hydrostatic equation, continuity equation, and the chain rule of differentiation, the last term in the potential energy equation can be further manipulated into the form

$$\begin{aligned} \frac{\partial p}{\partial \eta} \frac{R_d T}{p} \left(\frac{\partial p}{\partial t} + \dot{\eta} \frac{\partial p}{\partial \eta} \right) &= -\frac{\partial \phi}{\partial \eta} \left(\frac{\partial p}{\partial t} + \dot{\eta} \frac{\partial p}{\partial \eta} \right) \\ &= -\frac{\partial}{\partial \eta} \left[\phi \left(\frac{\partial p}{\partial t} + \dot{\eta} \frac{\partial p}{\partial \eta} \right) \right] + \phi \frac{\partial}{\partial \eta} \left(\frac{\partial p}{\partial t} + \dot{\eta} \frac{\partial p}{\partial \eta} \right) \\ &= \frac{\partial}{\partial \eta} \left[\phi \int_0^\eta \nabla \cdot \left(\mathbf{v} \frac{\partial p}{\partial \eta} \right) \right] - \phi \nabla \cdot \left(\frac{\partial p}{\partial \eta} \mathbf{v} \right) \end{aligned} \quad (3.56)$$

The spatial gradient terms on the left-hand side of the energy equations originate from the vorticity flux, kinetic energy gradient and the advection terms in Eqns. (3.1) and (3.2) which have already been discussed in Sections 3.5 and 3.6. Terms on the right-hand come from the

pressure gradient force in the velocity equation and the adiabatic heating term in the temperature equation. They describe the conversion of energy between different forms. The formulation of the pressure gradient force in the icosahedral dynamical core has been determined in the previous section. In this section the schemes for computing the adiabatic heating are derived based on the work of Simmons and Burridge (1981).

In the continuous case the first terms on the right-hand side of Eqn. (3.54) and (3.55) cancel exactly. In the ICOHDC, however, this can only be achieved when taking the global integral because the horizontal grid is staggered. Using Eqn. (3.49) we discretize the term $\left(\frac{R_d T}{p} \mathbf{v} \cdot \nabla p\right)$ by

$$\left(\frac{R_d T}{p} \mathbf{v} \cdot \nabla p\right)_{i,k} = \frac{1}{A_i \Delta p_{i,k}} \sum_{l \in \mathcal{E}(i)} \left[\left(\frac{R_d T}{p} \nabla p\right)_{l,k} \cdot \mathbf{N}_l \right] u_{l,k} \Delta \check{p}_{l,k} 2A_{i,l} . \quad (3.57)$$

The discretization of the second part of the adiabatic heating term, $\frac{R_d T}{p} \left(\frac{\partial p}{\partial t} + \dot{\eta} \frac{\partial p}{\partial \eta}\right)$, is based on Eqn. (3.56). Approximate the vertical derivative outside the square brackets in (3.56) by central differencing, and the vertical integral by discrete sum. Then substitute Eqns. (3.18), (3.45) and (3.46) for the mass flux divergence and the values of geopotential on half- and full-levels, respectively. These steps yield the formula

$$\left[\frac{R_d T}{p} \left(\frac{\partial p}{\partial t} + \dot{\eta} \frac{\partial p}{\partial \eta}\right) \right]_{i,k} = -\frac{R_d T_{i,k}}{\Delta p_{i,k}} \left[\ln \left(\frac{p_{i,k+1/2}}{p_{i,k-1/2}}\right) + \alpha_{i,k} \operatorname{div}(\mathbf{v} \Delta p)_{i,k} \right] , \quad (3.58)$$

in which $\alpha_{i,k}$ is defined by Eqn. (3.47).

It can be proven that if the vorticity flux in the velocity equation is calculate by expression (3.26), the discretization schemes described in Sections 3.4 – 3.8 ensure conservation of total energy in the sense that

$$\frac{\partial}{\partial t} \frac{1}{g} \left\{ \sum_i \phi_{si} p_{si} A_i + \sum_{k=1}^{NLEV} \left[\sum_l \left(v_{n_l,k}^2 \Delta \check{p}_{l,k} A_l \right) + \sum_i \left(C_p T_{i,k} \Delta p_{i,k} A_i \right) \right] \right\} = 0 \quad (3.59)$$

holds if the temporal derivative is not discretized.

3.9 Time integration

The time integration in the ICOHDC features the leap-frog scheme, a time filter and an optional semi-implicit treatment for gravity waves. For completeness, this section first briefly introduces the general formulation of the explicit scheme and the basic idea of the semi-implicit scheme. The application to the ICOHDC is described thereafter.

3.9.1 Leap-frog scheme with Asselin filter

The leapfrog time stepping scheme for solving the equation

$$\frac{\partial \psi}{\partial t} = F(\psi) \quad (3.60)$$

is given by

$$\psi_{expl}^{n+1} = \psi^{n-1} + 2 \Delta t F(\psi^n) . \quad (3.61)$$

Here the superscripts denote time steps that are evenly distributed with interval Δt . The leapfrog scheme is explicit and requires only one function evaluation (i.e., $F(\psi^n)$) per time step. Both the physical and computational modes of the solution are neutral for the oscillation equation. The disadvantage is the undamped computational mode. In the case of a nonlinear problem, the computational mode slowly amplifies and generates an instability known as the "time splitting problem".

To control the computational mode, Asselin (1972) suggested incorporating an approximate second-derivative time filter into the integration cycle. After each leapfrog time step

$$\psi^{n+1} = \psi_f^{n-1} + 2\Delta t F(\psi^n), \quad (3.62)$$

the following filter is applied:

$$\psi_f^n = \psi^n + \epsilon_f \left(\psi_f^{n-1} - 2\psi^n + \psi^{n+1} \right). \quad (3.63)$$

Here the variable ψ with a subscript f is the filtered quantity. As in ECHAM5, the filtering coefficient $\epsilon_f = 0.1$ is used in the ICOHDC.

3.9.2 The basic idea of the semi-implicit approach

According to their typical time scales, the atmospheric motions can be categorized into two types: fast processes related to gravity waves, and slow processes like advection. The gravity waves are energetically weak, but their existence leads to a very stringent constraint on the time interval for stability reasons. The use of fully implicit schemes can significantly improve the stability of the time integration, but results in the need to deal with a nonlinear algebraic equation at each step which must be solved with iterative techniques. In numerical weather prediction and climate modelling, it has become a common practice to use semi-implicit schemes, i.e., employ implicit schemes for the linear part of the fast processes and explicit schemes for all the other terms. Assume the forcing term in equation (3.60) can be split into the fast and linear part F_{fl} and the slow and/or nonlinear part F_{sn} . A semi-implicit scheme can be formally written as

$$\left(\frac{\partial \psi}{\partial t} \right)^n = \frac{1}{2} \left[\theta F_{fl}^{n+1} + (2 - \theta) F_{fl}^{n-1} \right] + F_{sn}^n, \quad (3.64)$$

where θ is the weight of the implicitly evaluated forcing. Further manipulation of (3.64) gives

$$\begin{aligned} \left(\frac{\partial \psi}{\partial t} \right)^n &= \frac{1}{2} \left[\theta F_{fl}^{n+1} + (2 - \theta) F_{fl}^{n-1} - 2F_{fl}^n \right] + \underbrace{(F_{fl}^n + F_{sn}^n)}_{F^n} \\ &=: \underbrace{\frac{1}{2} \Delta_{tt}^\theta F_{fl}}_{\text{implicit}} + F^n. \end{aligned} \quad (3.65)$$

Combining (3.65) with an explicit scheme, we get

$$\left(\frac{\partial \psi}{\partial t} \right)^n = (1 - \epsilon_i) F^n + \epsilon_i \left(F^n + \frac{1}{2} \Delta_{tt}^\theta F_{fl} \right) = F^n + \frac{1}{2} \epsilon_i \Delta_{tt}^\theta F_{fl}, \quad (3.66)$$

in which ϵ_i is the implicitness parameter having its value between 0 and 1. The use of the centered differencing for the time derivative on the left-hand side of Eqn. (3.66) eventually

yields

$$\begin{aligned}\psi^{n+1} &= \psi^{n-1} + 2 \Delta t F^n + \epsilon_i \Delta t \Delta_{tt}^\theta F_{fl} \\ &= \psi_{expl}^{n+1} + \epsilon_i \Delta t \Delta_{tt}^\theta F_{fl}\end{aligned}\quad (3.67)$$

Here ψ_{expl}^{n+1} is the prediction given by scheme (3.61), and the term $\epsilon_i \Delta_{tt}^\theta F_{fl}$ is usually called the semi-implicit correction.

3.9.3 Application of the semi-implicit scheme in the hydrostatic dynamical core

Following the notation in Simmons and Burridge (1981), we use column vectors to denote variables defined at all the vertical layers in the same horizontal location, i.e.,

$$\mathbf{v} = (v_1, v_2, \dots, v_{NLEV})^T, \quad (3.68)$$

$$\mathbf{T} = (T_1, T_2, \dots, T_{NLEV})^T, \quad (3.69)$$

$$\mathbf{D} = (D_1, D_2, \dots, D_{NLEV})^T. \quad (3.70)$$

Here D denotes divergence. The superscript T means matrix transpose. Taking an isothermal reference state

$$\mathbf{v}^r = 0, \quad T^r = 300 \text{ K}, \quad p_s^r = 800 \text{ hPa}, \quad \phi_s^r = 0, \quad (3.71)$$

and linearizing the gravity wave related terms

$$F(\mathbf{v})_{fl} = -\frac{R_d T}{p} \nabla p - \nabla \phi, \quad (3.72)$$

$$F(T)_{fl} = \frac{R_d T}{C_p p} \frac{dp}{dt}, \quad (3.73)$$

$$F(p_s)_{fl} = -\int_0^1 \nabla \cdot \left(\mathbf{v} \frac{\partial p}{\partial \eta} \right) d\eta, \quad (3.74)$$

one can derive the semi-implicit leap-frog scheme for normal velocity, temperature and surface pressure in the following vector form:

$$\mathbf{v}^{n+1} = (\mathbf{v})_{expl}^{n+1} - \epsilon_i \Delta t \nabla \left(\gamma \Delta_{tt}^\theta \mathbf{T} + \mathbf{h} \Delta_{tt}^\theta p_s \right), \quad (3.75)$$

$$\mathbf{T}^{n+1} = (\mathbf{T})_{expl}^{n+1} - \epsilon_i \Delta t \tau \Delta_{tt}^\theta \mathbf{D}, \quad (3.76)$$

$$p_s^{n+1} = (p_s)_{expl}^{n+1} - \epsilon_i \Delta t \nu \cdot \Delta_{tt}^\theta \mathbf{D}. \quad (3.77)$$

The constant matrices $\underline{\gamma}$, $\underline{\tau}$, and vectors \mathbf{h} , $\boldsymbol{\nu}$ are defined as

$$\left(\underline{\gamma}\right)_{kj} := \begin{cases} 0 & \text{for } j < k \\ R_d \alpha_k^r & \text{for } j = k \\ R_d \ln \left(\frac{p_{j+1/2}^r}{p_{j-1/2}^r} \right) & \text{for } j > k \end{cases} \quad (3.78)$$

$$\left(\underline{\tau}\right)_{kj} := \frac{\Delta p_j^r}{\Delta p_k^r} \frac{T^r}{C_p} \left(\underline{\gamma}\right)_{jk} \quad (3.79)$$

$$\boldsymbol{\nu} := (\Delta p_1^r, \Delta p_2^r, \dots, \Delta p_{NLEV}^r)^T \quad (3.80)$$

$$\mathbf{h} := \frac{R_d T^r}{p_s^r} (1, 1, \dots, 1)_{NLEV \times 1}^T \quad (3.81)$$

Note that Eqns. (3.78) – (3.81) are in fact a simplified version of the formulae in the appendix of Simmons and Burridge (1981), because in the ICOHDC we have followed ECHAM5 and chosen an isothermal reference state, whilst the reference temperature was vertical level dependent in Simmons and Burridge (1981).

Define a constant matrix

$$\underline{\mathbf{B}} := \underline{\gamma} \underline{\tau} + \mathbf{h} \boldsymbol{\nu}^T \quad (3.82)$$

and the notation

$$\Delta_{tt,expl}^\theta \psi := \theta \psi_{expl}^{n+1} + (2 - \theta) \psi^{n-1} - 2\psi^n \quad (3.83)$$

Use $\underline{\mathbf{I}}$ to denote the $NLEV \times NLEV$ identity matrix. From Eqns.(3.75) – (3.77) the temporally discretized divergence equation can be obtained:

$$\left[\underline{\mathbf{I}} - (\epsilon_i \theta \Delta t)^2 \nabla^2 \underline{\mathbf{B}} \right] \Delta_{tt}^\theta \mathbf{D} = \Delta_{tt,expl}^\theta \mathbf{D} - \epsilon_i \theta \Delta t \nabla^2 \left(\underline{\gamma} \Delta_{tt,expl}^\theta \mathbf{T} + \mathbf{h} \Delta_{tt,expl}^\theta p_s \right) \quad (3.84)$$

The semi-implicit time integration scheme applied in the hydrostatic model can then be described as the following algorithm:

1. Use the explicit leap-frog scheme to obtain $(v_n)_{expl}^{n+1}$, T_{expl}^{n+1} and $(p_s)_{expl}^{n+1}$;
2. Solve Eqn. (3.84) for $\Delta_{tt}^\theta D$;
3. Substitute $\Delta_{tt}^\theta D$ into Eqns. (3.76) and (3.77) to update temperature and surface pressure;
4. Substitute the newly obtained T^{n+1} and p_s^{n+1} into Eqn. (3.75) to get the normal velocity at the new time step;
5. Apply the Asselin filter to v_n , T and p_s at time level n ;
6. Switch the time indices: $n \rightarrow n - 1$, $n + 1 \rightarrow n$; Go to step 1.

3.9.4 Solving the divergence equation

The divergence equation (3.84) appears to be a linear algebraic equation of $NLEV$ unknowns (corresponding to the $NLEV$ vertical layers at the same horizontal location). In a finite-difference model like the ICOHDC, the Laplace operator ∇^2 has to be discretized, which results in the coupling of individual vertical columns with their neighbouring columns. The divergence equation thus becomes a 3D Helmholtz equation. Due to efficiency reasons, a common practice in solving this equation is to decompose it into $NLEV$ 2D equations using the eigenvectors of the matrix \mathbf{B} . Furthermore, making use of the fact that the eigenvalues of \mathbf{B} are the squares of the gravity wave phase speeds, only a few of these 2D equations that are associated with fast waves are solved, and the others ignored. Solutions of the 2D equations are re-coupled subsequently, again using the eigenvectors of \mathbf{B} , to get $\Delta_{tt}^\theta D$ at each grid point of the 3D grid system.

In the ICOHDC we have implemented two options for solving the divergence equation. The first option follows the idea above and solves only the decoupled modes of phase speed higher than 30 m s^{-1} . This is referred to as "the semi-implicit scheme with 2D solver" or simply "the SI-2D scheme" in the model evaluation in Chapter 4. The second option is to solve directly the 3D Helmholtz equation, which is referred to as the "SI-3D scheme". In both cases, the generalized minimal residual method (GMRES, Saad and Schultz, 1986) is used for solving the algebraic equation(s). The comparison between the two options is discussed in the next chapter.

Chapter 4

Evaluation of the hydrostatic dynamical core

In this chapter the icosahedral hydrostatic dynamical core is evaluated by carrying out idealized numerical experiments that represent basic mechanisms of atmospheric dynamics. The purpose of the evaluation is to find out whether convergence of the numerical solution with respect to horizontal resolution can be achieved by using the numerical schemes described in the previous chapters. Parameterizations of the diabatic processes in the atmosphere, such as radiation, convection, formation of clouds and precipitation, are currently excluded.

4.1 Introduction

The eventual purpose of developing atmospheric dynamical cores is to use them for operational weather prediction and atmospheric research. These realistic applications require in addition mathematical representations of various diabatic processes. Diabatic processes usually have much smaller spatial scales compared to the typical grid size of the AGCMs, and hence have to be parameterized. Conventionally, the parameterized parts of an AGCM is referred to as the "physics", while the adiabatic fluid motions represented by the dynamical core are called the "dynamics", although fluid dynamics is in fact a branch of physics, and the "physics" part of GCMs and couple GCM systems has been extended so as to include chemistry and aerosol microphysics in atmospheric models, and biogeochemistry in ocean models.

Interactions between the dynamics and the physics in an AGCM are very complex and highly nonlinear. Quite often, when one component in a model is modified, unexpected responses of some other components appear, and it is not always easy to find out why. Even when the only change is the spatial resolution, one usually has to adjust some of the empirical parameters in the parameterization schemes so as to achieve optimal model performance in realistic applications. In the case of the ICON atmospheric model, switching from the latitude-longitude grid to

the quasi-uniform triangular grid leads to different resolution changes in different geographical locations, especially in the zonal direction. This probably will have considerable impact on the parameterizations, and consequently on the simulated global circulation. In this thesis, model evaluation is restricted to idealized tests of fluid dynamics. The coupling of the dynamics with the parameterizations and the simulation of realistic atmospheric states are topics of future work.

Although the uncertainties associated with parameterizations are avoided, the evaluation of 3D dynamical cores is still not straightforward. This is mainly due to the fact that the general analytical solution of the primitive equations is not known. Compared to the widely applied standard test suite of the shallow water model (Williamson *et al.*, 1992, hereafter W92) and the commonly used test cases for 2D nonhydrostatic slice models (e.g., Durran and Klemp, 1983; Robert, 1992; Schär *et al.*, 2002), benchmark experiments for the global hydrostatic dynamical cores are less well established. In this chapter the performance of the ICON hydrostatic atmospheric dynamical core is assessed in four groups of test cases.

The evaluation starts from simulating the Rossby-Haurwitz waves which closely resemble the wave-like patterns that are frequently observed in the middle and upper troposphere. Subsequently a Rossby wave train induced by an isolated mountain in the westerly flow is simulated, following the experimental design proposed by Jablonowski *et al.* (2008). Both tests are essentially barotropic, and can be considered as 3D extensions of the most widely applied shallow water test cases in the W92 test suite. Through these experiments the model's behaviour is evaluated in barotropically stable and unstable conditions.

Regarding the baroclinic dynamics, Polvani *et al.* (2004), Lin (2004), and Jablonowski and Williamson (2006a,b) have performed similar experiments, in which the evolution of baroclinic vortices was simulated. In the studies by Polvani *et al.* (2004) and Lin (2004), only the horizontal wind field was analytically specified at the initial time step. Numerical computations were needed to obtain the initial temperature field. In contrast, Jablonowski and Williamson (2006a,b) unambiguously defined the initial conditions by analytical expressions, and provided reference results from four dynamical cores using different numerical methods and covering a wide range of horizontal resolutions. In this chapter, we follow the proposal of Jablonowski and Williamson (2006a,b) to assess the convergence property of the numerical solutions produced by the ICOHDC.

For the three test cases mentioned above, the physical constants involved in the dry dynamical core are set to the values proposed by Jablonowski *et al.* (2008) (see the column "NCAR ASP 2008" in Tab. 4.1). Regarding the vertical grid, the L31 configuration of the ECHAM5 model is used in stead of the L26 grid suggested by Jablonowski *et al.* (2008). This is because the same L31 grid will be employed in climate simulations when the ICOHDC has been combined with physics parameterizations. Testing the ICOHDC in the L31 configuration can thus provide useful information for later applications of the new dynamical core.

After the three deterministic test cases, we follow the proposal of Held and Suarez (1994) and carry out an idealized climate simulation, in which the dry dynamical core is driven by analytically specified forcings. In addition to evaluating the ability of the ICOHDC to reproduce the idealized zonal mean climate, this experiment also demonstrates the long-term numerical

Tab. 4.1: Common physical constants used in the adiabatic test cases.

physical quantity	symbol and unit	NCAR ASP 2008	ECHAM5
parameter of the hybrid vertical coordinate	p_0 (hPa)	1000	1013.25
gravitational acceleration	g (m s ⁻²)	9.80616	9.80665
the Earth's radius	a (km)	6371.229	6371
the Earth's angular velocity	Ω (10 ⁻⁵ s ⁻¹)	7.29212	7.292
ideal gas constant for dry air	R_d (J kg ⁻¹ K ⁻¹)	287.04	287.05
specific heat of dry air at constant pressure	C_p (J kg ⁻¹ K ⁻¹)	1004.64	1005.46

stability of the ICOHDC. For the Held-Suarez test, the physical constants are set to their default values used in the ECHAM5 model, so as to facilitate comparison with results obtained earlier from the spectral model.

As already mentioned, a general analytical solution of the governing equations of the hydrostatic atmosphere is not known. Intercomparison between different models is thus necessary. In this chapter we take the spectral transform dynamical core of ECHAM5 as the reference model. It has been known for a long time in the atmospheric modelling community that with a fixed degrees of freedom, the spectral transform method gives more accurate results than the other methods when the simulated flow is relatively smooth. In the experiments performed here, no grid scale forcing or discontinuous initial condition is involved. Therefore the high-resolution results from the dynamical core of ECHAM5 are considered as reference solutions.

So far the ECHAM5 model has been employed in applications covering a wide range of horizontal and vertical resolutions (see, e.g., Roeckner *et al.*, 2006). In this chapter, we run the dynamical core at the vertical resolution L31, and horizontal resolutions ranging from T42 to T319 (Tab. 4.2). Ideally, experiments with the ICOHDC should be performed at similar resolutions. However, due to the technical status of the source code and the current limitation in computing resources, we have only obtained results till resolution R2B5 (64 km spacing between neighbouring mass points) in the deterministic test cases, and R2B4 (127 km) in the idealized climate test. The triangular grids used in this chapter are listed in Tab. 4.3. The time steps corresponding to each resolution of the ECHAM5 model and that of the ICOHDC are shown in Tabs. 4.4 and 4.5.

Tab. 4.2: Grid spacing of the Gaussian grid at various resolutions. All the resolutions listed here are used in the model evaluation in Chapter 4.

truncation	number of spherical harmonics	number of Gaussian latitudes	zonal grid spacing			
			in degrees	in kilometers at different latitudes		
				equator	45°	60°
T42	946	64	2.81°	312.75 km	221.15 km	156.37 km
T63	2080	96	1.88°	208.50 km	147.43 km	104.25 km
T85	3741	128	1.41°	156.37 km	110.57 km	78.19 km
T106	5778	160	1.12°	125.10 km	88.46 km	62.55 km
T159	12880	240	0.75°	83.40 km	58.97 km	41.70 km
T255	32896	384	0.47°	52.12 km	36.86 km	26.06 km
T319	51360	480	0.38°	41.70 km	29.49 km	20.85 km

Tab. 4.3: Grid spacing of the spherical triangular grid. n_r denotes the number of equal arcs each icosahedron edge is divided into during the root division. n_b stands for the number of subsequent bisections. The dual edge length is the great circle arc distance between two neighbouring triangle centers. The arc lengths listed here can be regarded roughly as the mean value on the sphere.

(n_r, n_b)	number of triangular cells	dual edge length		number of primal edges	primal edge length	
		in degrees	in km		in degrees	in km
(2, 2)	1280	4.58°	509.07 km	1920	7.93°	881.74 km
(2, 3)	5120	2.29°	254.54 km	7680	3.96°	440.87 km
(5, 2)	8000	1.83°	203.63 km	12000	3.17°	352.69 km
(3, 3)	11520	1.53°	169.69 km	17280	2.64°	293.91 km
(2, 4)	20480	1.14°	127.27 km	30720	1.98°	220.43 km
(3, 4)	46080	0.76°	84.85 km	69120	1.32°	146.96 km
(2, 5)	81920	0.57°	63.63 km	122880	0.99°	110.22 km

Tab. 4.4: Default time steps of the full ECHAM5 model at various resolutions. These are also the values used in the model evaluation in this chapter.

resolution	T42	T63	T85	T106	T159	T255	T319
time step (in seconds)	1200	720	480	360	240	150	150

Tab. 4.5: Time steps used in the idealized experiments performed with the ICOHDC.

resolution	R2B2	R2B3	R5B2	R3B3	R2B4	R3B4	R2B5
time step (in seconds)	2400	1200	900	720	600	360	300

4.2 Rossby-Haurwitz wave

In the middle and upper troposphere the atmospheric flow usually features relatively smooth wave-shaped patterns. Rossby (1939) first studied the dynamics of these waves using the non-divergent barotropic vorticity equation. Taking into account the latitudinal variation of the Coriolis parameter, he deduced non-trivial analytical solution to the equation on the β -plane, which is later referred to as the Rossby wave. Haurwitz (1940) generalized Rossby's work and used spherical harmonics to derive the equivalent solutions on the sphere. His solution is now known as the Rossby-Haurwitz wave. It has been an important topic in atmospheric dynamics to study the interaction between this type of waves and other flow motions. In this section we first briefly introduce the main conclusions drawn in the theoretical and numerical studies on this topic, and review the history of using the Rossby-Haurwitz wave in testing dynamical cores. The numerical experiments performed in this thesis are then described and the results discussed.

4.2.1 Rossby-Haurwitz wave and barotropic instability

In the nondivergent barotropic atmosphere, the Rossby-Haurwitz (hereafter RH) wave component corresponding to the spherical harmonic Y_n^m propagates in the zonal direction with the angular velocity

$$\nu = \Omega_0 - \frac{2(\Omega_0 + \Omega)}{n(n+1)}. \quad (4.1)$$

Here Ω_0 is the angular velocity of the superrotating background flow and Ω denotes the Earth's rotation velocity. A single wave component retains the same shape and amplitude as it propagates. The linear combination of any arbitrary number of RH wave components is also an exact solution to the nondivergent barotropic vorticity equation.

Although the RH wave is neutral by itself, instability can be triggered by perturbations if the wave is sufficiently strong or the wavenumber sufficiently large (Lorenz, 1972; Hoskins, 1973; Baines, 1976). Hoskins (1973) investigated the case of the perturbations being a single planetary wave and a zonal flow. He showed that in the RH wave family Y_{m+1}^m , components of $m \leq 5$ are relatively stable, while those of larger wavenumbers can break down very quickly. Baines (1976) examined the triad interaction and found that RH wave components of total wavenumber greater than 3 can be unstable when the amplitude is large.

An important point to note is that the "usual" concept of barotropic instability as formulated by Kuo (1949) is concerned with the stability of a zonal flow to infinitesimal wave perturbations and the transformation of kinetic energy from the mean flow to the eddies. In contrast, when the RH wave breaks down, its energy mostly feeds into the zonal flow instead of into even larger wavenumbers. This is the reverse process compared to Kuo's (1949) work, and has been noticed in the stability analysis in Lorenz (1972), Hoskins (1973) and Baines (1976), among others. Barotropic instability of the RH wave is thus considered an important mechanism for producing jet streams. The formation of jet-like currents through barotropic instability has also been simulated by Kreiss and Oliger (1972) and Dunst and Roeckner (1975), in which numerical shallow water models were initialized with the RH wave of wavenumber 6 and 8, respectively. Although there was only one RH wave component at the initial step, the divergence

associated with the free surface provided perturbations to the wave. Due to the relatively large wavenumber, these perturbations amplified very quickly, leading to dramatic changes of the flow patterns within a few model days.

4.2.2 Rossby-Haurwitz wave as a test case

The use of the RH wave for testing numerical methods applied in atmospheric models can be traced back to the work of Phillips (1959). The initial velocity field was defined via the stream function

$$\psi(\lambda, \varphi) := -a^2 \Omega_0 \sin \varphi + a^2 \Omega_m \cos^m \varphi \sin \varphi \cos m\lambda, \quad (4.2)$$

where a is the Earth's radius and Ω_m a constant determining the amplitude of the wave. Eqn. (4.2) is a superposition of a solid body rotation and the RH wave component Y_{m+1}^m . The phase speed of the wave can be calculated from Eqn. (4.1).

The horizontal wind components can be derived from (4.2):

$$u(\lambda, \varphi) = a \Omega_0 \cos \varphi + a \Omega_m (m \sin^2 \varphi - \cos^2 \varphi) \cos^{m-1} \varphi \cos m\lambda, \quad (4.3)$$

$$v(\lambda, \varphi) = -a m \Omega_m \cos^{m-1} \varphi \sin \varphi \sin m\lambda. \quad (4.4)$$

The vorticity of the flow is

$$\xi(\lambda, \varphi) = 2 \Omega_0 \sin \varphi - (m+1)(m+2) \Omega_m \sin \varphi \cos^m \varphi \cos m\lambda. \quad (4.5)$$

The geopotential perturbation is given by

$$\phi'(\lambda, \varphi) := a^2 A_\phi + a^2 B_\phi \cos m\lambda + a^2 C_\phi \cos 2m\lambda, \quad (4.6)$$

where

$$A_\phi(\varphi) := \frac{\Omega_0(2\Omega + \Omega_0)}{2} \cos^2 \varphi + \frac{\Omega_m^2}{4} \cos^{2m} \varphi \left[(m+1) \cos^2 \varphi + (2m^2 - m - 2) - \frac{2m^2}{\cos^2 \varphi} \right],$$

$$B_\phi(\varphi) := \frac{2(\Omega + \Omega_0)\Omega_m}{(m+1)(m+2)} \cos^m \varphi [(m^2 + 2m + 2) - (m+1)^2 \cos^2 \varphi],$$

$$C_\phi(\varphi) := \frac{\Omega_m^2}{4} \cos^{2m} \varphi [(m+1) \cos^2 \varphi - (m+2)].$$

This set of expressions were adopted in the W92 shallow water test suite. The proposed amplitude parameters were $\Omega_0 = \Omega_m = 50 \text{ m s}^{-1}/a$ ($= 7.848 \times 10^{-6} \text{ s}^{-1}$). The resulting geopotential perturbation and relative vorticity are shown in Fig. 4.1 for the case of zonal wavenumber 4.

We emphasize that the neutral propagation of the RH wave can only be guaranteed in a nondivergent barotropic model. This wave is not an exact solution of the unfiltered shallow water model or the primitive equations. Considering that the accuracy of a numerical solution is much more straightforward to assess for a stable flow than for an unstable one, Williamson *et al.* (1992) proposed using zonal wavenumber 4 ($m = 4$). A reference solution from a high-resolution spectral model was provided for quantitative comparison (Williamson *et al.*, 1992; Jakob *et al.*, 1993). Now the RH wavenumber 4 is considered a benchmark test and regarded

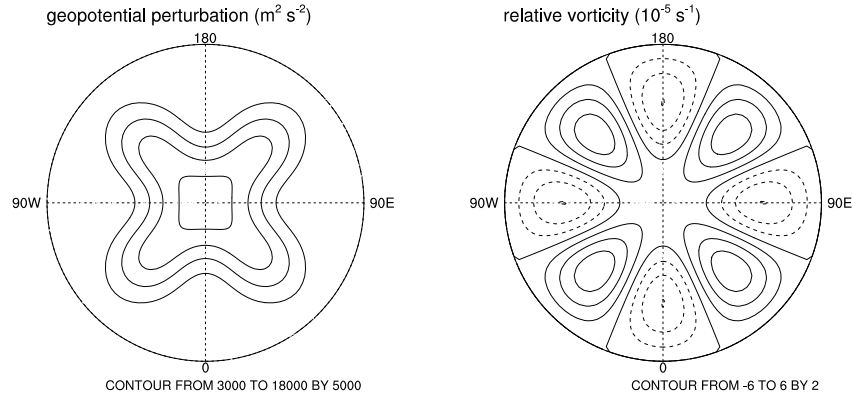


Fig. 4.1: Geopotential perturbation (left) and relative vorticity (right) corresponding to Rossby-Haurwitz wavenumber 4 with $\Omega_0 = \Omega_m = 50 \text{ m s}^{-1}/a$. A polar stereographic map projection is used. The North Pole is at the center of each panel, and the outer circle is the equator. In the right panel, negative values are indicated by dashed contours.

as one of the most dynamically interesting cases in the W92 test suite. Besides numerous publications documenting new models, some in-depth discussions about the numerical solutions have also been presented (e.g. Bates *et al.*, 1995; Thuburn and Li, 2000).

Beyond the application in the one-layer shallow water models, Monaco and Williams (1975) carried out a series of experiments using the RH wave as the initial condition to evaluate a two-layer hydrostatic model. The expressions they used for the initial wind and geopotential were essentially the same as in Phillips (1959), although there was a phase shift:

$$[m\lambda]_{Monaco(1975)} = [m\lambda]_{Phillips(1959)} + \frac{\pi}{2}. \quad (4.7)$$

As for the thermodynamic state, the NACA standard atmosphere in Haltiner and Martin (1957) was used to define the temperature profile:

$$T := T_N - \gamma_N z^* = 288 - 0.0065 z^*. \quad (4.8)$$

Here z^* should be interpreted as the equivalent height of a hydrostatic atmosphere (instead of the geopotential height) which is defined as

$$z^* := \frac{T_N}{\gamma_N} \left[1 - \left(\frac{p}{p_N} \right)^{\frac{\gamma_N R_d}{g}} \right], \quad \text{with} \quad (4.9)$$

$$p_N := 101325 \text{ Pa}. \quad (4.10)$$

Equations (4.8) – (4.10) effectively define a barotropic state whose temperature and pressure are related by the following equality:

$$T = T_N \left(\frac{p}{p_N} \right)^{\frac{\gamma_N R_d}{g}}. \quad (4.11)$$

Under the assumption that the Earth's surface is flat and that Eqn. (4.6) is the geopotential at $p = p_N$, the initial condition of the surface pressure can be derived using (4.11) and the

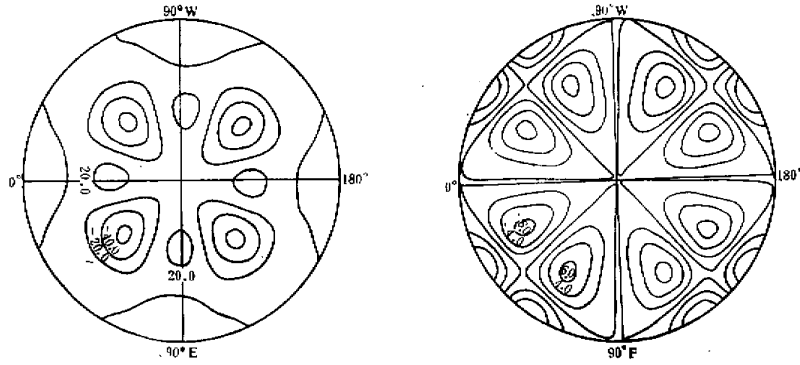


Fig. 4.2: The first-order correction of the geopotential height (left, unit: m) and divergence (right, unit 10^{-7} s^{-1}) obtained by Zhang *et al.* (1986) for the Rossby-Haurwitz wavenumber 4.

hydrostatic equation:

$$p_s(\lambda, \varphi) = p_N \left(1 + \frac{\gamma_N}{g T_N} \phi' \right)^{\frac{g}{\gamma_N R_d}}. \quad (4.12)$$

The formulae of Monaco and Williams (1975) were employed later by Giraldo and Rosmond (2004) in the evaluation of a hydrostatic spectral element model. Following the suggestion from Williams, they used the parameters $\Omega_m = 50 \text{ m s}^{-1}/(ma)$ and $\Omega_0 = 20 \text{ m s}^{-1}/a$ (F. X. Giraldo, personal communication).

Another effort in using the RH wave as a test case was made by Zhang *et al.* (1986) and Zhang *et al.* (1987). Based on the perturbation theory, scale analysis was applied to the baroclinic primitive equations on the sphere. Under the assumptions of weak baroclinicity and weak compressibility for large-scale low-speed flow, they derived the zeroth- and first-order approximations of the governing equations. It was shown that the wave pattern defined by Phillips (1959) was the analytical solution to the zeroth-order problem. An iterative algorithm was then developed to calculate the first-order correction (cf. Fig. 4.2) in a numerical way. Zhang *et al.* (1987) showed that in their two-level finite difference model, the integrations initialized using the first-order approximation exhibited significantly less deformation of the initial wave.

In this thesis, we choose the RH wave as a test case for the icosahedral dynamical core mainly because the wave is an important conceptual model of atmospheric dynamics, and the smoothness of the flow pattern in space and time renders the RH wave a good tool for the initial debugging of the model source code. In principle it is possible to follow Zhang *et al.* (1986) and generalize their work for the primitive equations in a hybrid p - σ coordinate. However, the outcome will still be an approximation rather than the exact solution. Therefore we use the formulae from Monaco and Williams (1975) in this thesis. In order to make our results directly comparable to those of other models obtained during the NCAR ASP 2008 Summer Colloquium (Jablonowski *et al.*, 2008), the reference pressure p_N in Eqn. (4.10) is set to 955 hPa. By choosing different combinations of the zonal wavenumber m and the amplitude parameters Ω_0 and Ω_m , we simulate both the steady wave propagation and the formation of jet streams.

Regarding the horizontal resolution, T85 is used by the dynamical core of ECHAM5, since experiences have shown that numerical solutions of idealized tests given by this dynamical core converge at T85L31 (see, e.g., Wan *et al.* (2008)). The zonal grid size of the T85 Gaussian grid

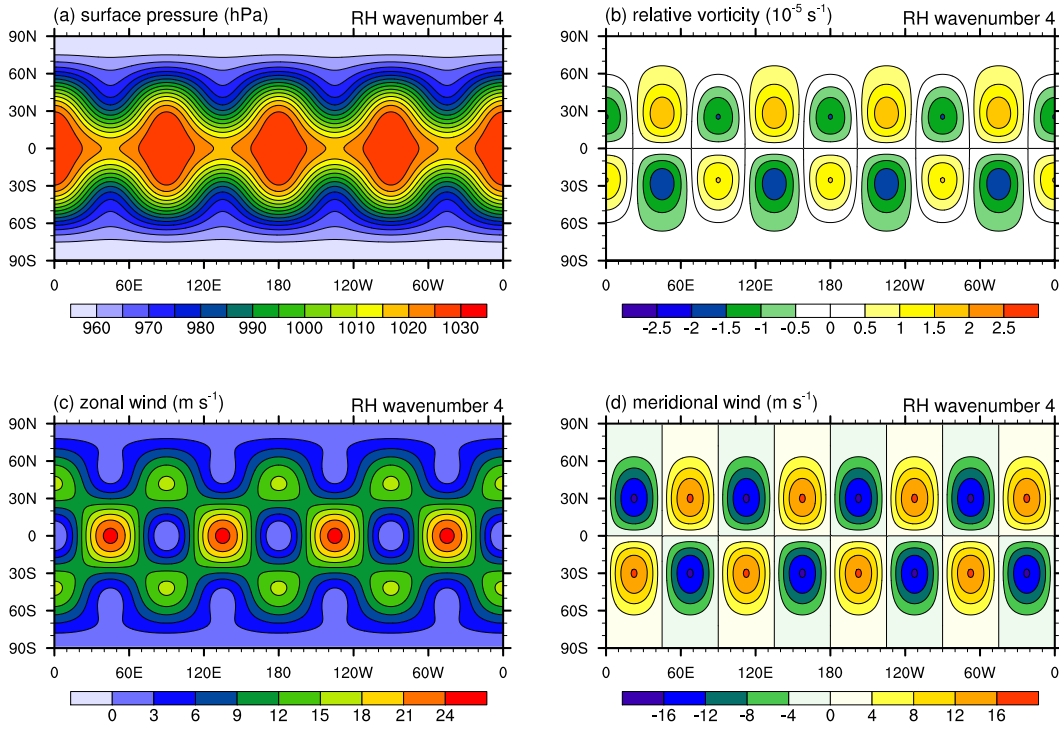


Fig. 4.3: Initial conditions of the 3D Rossby-Haurwitz wavenumber 4 experiment performed in this thesis. The initial atmospheric state is nondivergent and barotropic.

ranges from about 156 km at the equator to 78 km at 60° latitudes. According to these numbers, we choose the R2B4 triangular grid for the experiments with the ICOHDC. On the R2B4 grid, the distance between neighbouring mass points ranges from 80 km to 181 km, with the average being about 127 km. All simulations are performed using the L31 hybrid vertical grid described in Section 3.1 (cf. Tab. 3.1 on page 37).

4.2.3 The steady propagation of wavenumber four

As the first step we simulate a case in which the RH wave does not experience much change in its shape on the time scale of a month. In order to ensure dynamical stability of the RH wave, we choose a small zonal wavenumber ($m=4$) and relatively small amplitude ($\Omega_m = \Omega_0 = 50 \text{ m s}^{-1}/(4a)$). The resulting initial conditions are depicted in Fig. 4.3. Both dynamical cores are integrated for 90 model days and have not encountered any numerical stability problem.

The simulated 500 hPa geopotential height in the Northern Hemisphere is shown in Fig. 4.4 for days 1, 10 and 60. In both simulations, the wave pattern is well preserved, although a slight decrease in the wave amplitude is detectable at day 60. The simulated angular velocity of the RH wave is approximately $-14^\circ \text{ day}^{-1}$ in ECHAM5. (Negative value means westward propagation.) In the ICOHDC simulation the wave moves slightly slower, but the difference is less than 0.1° per day. In both models the westward propagation is slower than the theoretically predicted speed of $-15^\circ \text{ day}^{-1}$ that is valid for the nondivergent barotropic vorticity equation. This discrepancy is qualitatively consistent with the well-known fact that the presence of divergence in the barotropic atmosphere slows down the progression of the flow pattern, especially for small wavenumbers

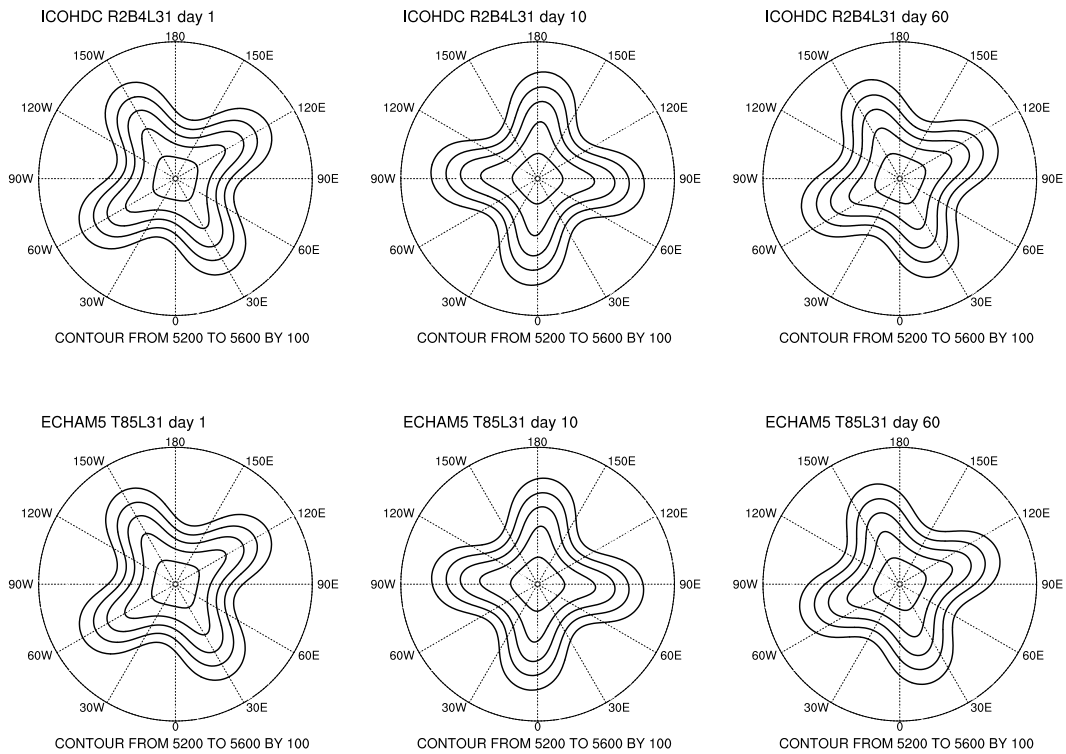


Fig. 4.4: Snapshots of the 500 hPa geopotential height at days 1, 30 and 60. The top row shows the ICOHDC results at R2B4L31 resolution with the diffusion parameter $\Delta t_D / \tau^* = 1.0$; The bottom row shows the simulation performed with the dynamical core of ECHAM5 at T85L31 resolution using the default horizontal diffusion parameters. The contour plots are drawn using the polar stereographic projection. The North Pole is at the center of the map, and the outer circle is the equator.

(Phillips, 1959). The derivations in Zhang *et al.* (1986) have shown that compared to the zeroth-order approximation of the theoretical phase speed, the first-order correction is of the opposite sign.

It is worth noting that in the model evaluation we do not take the length of the period before the breakdown of the initial wave as a performance metric. Theoretical studies have already shown that the RH wave is subject to dynamical instability. Although wavenumber 4 is commonly believed to be stable, in long enough (more than 30 days) integrations the numerical solutions are strongly sensitive to small perturbations in the initial conditions and to the truncation and roundoff errors which can project onto the dynamical instability (Hoskins, 1973; Thuburn and Li, 2000). On the other hand, the first 15 days of the flow evolution are commonly considered as a dynamically stable period. In Figs. 4.5 and 4.6 we present snapshots of the atmospheric state at day 15 simulated by the two hydrostatic dynamical cores.

The first impression from the intercomparison is that the two models produce very similar results. [†] Compared to the initial state (Fig. 4.3) the pattern in the surface pressure experiences

[†]Note that in this chapter, all the color-shaded contour plots of the ICOHDC results are drawn directly on the triangular grid, and shown with the cylindrical equidistance projection. The visualization is performed using the NCAR Command Language (www.ncl.ucar.edu). Due to the inherent property of the plotting software, the panels showing the ICOHDC results in the hemispherical or global domain usually have two or three corners unfilled, or

little change (Fig. 4.5, first row). In the wind fields (Fig. 4.5, third and fourth rows) and the relative vorticity (Fig. 4.6, first row), a northwest/southeast tilt of the wave is clearly detectable. In fact in both models the direction of the troughs and ridges in, e.g., surface pressure and geopotential height keeps oscillating during the integration with a period of about 8 days. A similar model behaviour has been mentioned by Hoskins (1973).

Nonlinear interactions between the wave and the zonal flow as well as numerical errors gradually introduce new motions in the model. Weak baroclinicity appears (Fig. 4.6, third row). The originally nondivergent flow also develops divergence near the equator. The divergence eventually grows to large magnitude and distorts the flow pattern in the low latitudes. From 30° poleward, the wavenumber 4 pattern in wind and vorticity is preserved for more than 50 days, while the surface pressure and geopotential height fields remain smooth until the end of the 90-day simulations.

4.2.4 A dynamically unstable case

As the next step, we compare ICOHDC with ECHAM5 in the simulation of jet stream formation. The initial conditions are again defined by the formulae in Section 4.2.2, but now with zonal wavenumber 8. Considering that the large amplitude of the RH wave is a source of dynamical instability whilst the westerly zonal flow provides stabilization (Hoskins, 1973), we increase the amplitude of the RH wave by a factor of two (i.e., $\Omega_m = 50 \text{ m s}^{-1}/(2a)$) and decrease the strength of the zonal flow to one half (i.e., $\Omega_0 = 50 \text{ m s}^{-1}/(8a)$).

As can be seen from the surface pressure plots in Fig. 4.7, dramatic changes happen to the flow pattern, and the initial wave breaks down within 10 days. At 30° latitudes, the pressure gradient points in the east-west direction at the initial step, while by day 7 it has already turned into the meridional direction.

In this experiment differences between the two models are much more evident. In contrast to the spectral transform model which always retains the symmetry about the equator, the icosahedral model already produces some asymmetry in the flow at day 7. Differences between panels (c) and (g) of Fig. 4.7 clearly reflect the features of the horizontal grids and numerical methods used in these two models. As predicted by the barotropic instability theory, both models eventually reach a state dominated by westerly flow, with one jet stream in each hemisphere.

There is an interesting point worth mentioning here. Given the property of the icosahedral triangular grid, one would think that the ICOHDC is not particularly good at simulating zonal flows. This expectation seems confirmed by the second and third rows of Fig. 4.7. However, as the integrations continue further, the two models finally reach quasi-equilibrium states that are extremely similar. This is probably related to the fact that the zonal state depicted by panels (d) and (h) of Fig. 4.7 is in fact a stable equilibrium. Although in the early days of the simulation, numerical errors in the ICOHDC interact more strongly with the initial wave than in the spectral model, the energy of the newly generated perturbations eventually transforms into the zonal flow as a result of the dominating dynamical process.

filled with unexpected colors (see, e.g., the left panels in Fig. 4.5). This is not a problem of the ICOHDC results. These incorrectly filled corners will disappear if, for example, the polar stereographic projection is used.

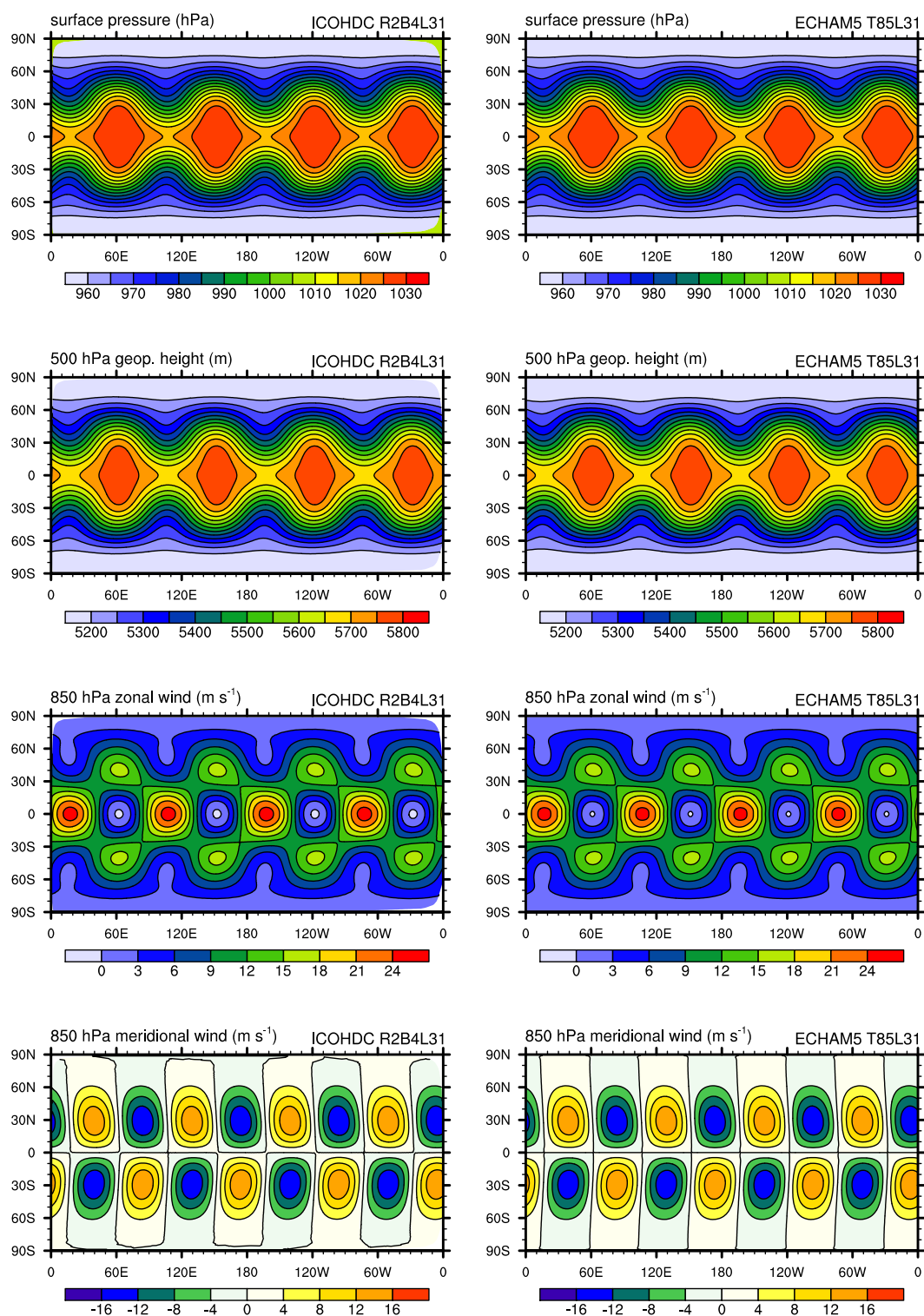


Fig. 4.5: Snapshots of the atmospheric state at day 15 simulated by the ICOHDC (left column) and the dynamical core of ECHAM5 (right column) in the Rossby-Haurwitz wavenumber 4 experiment.

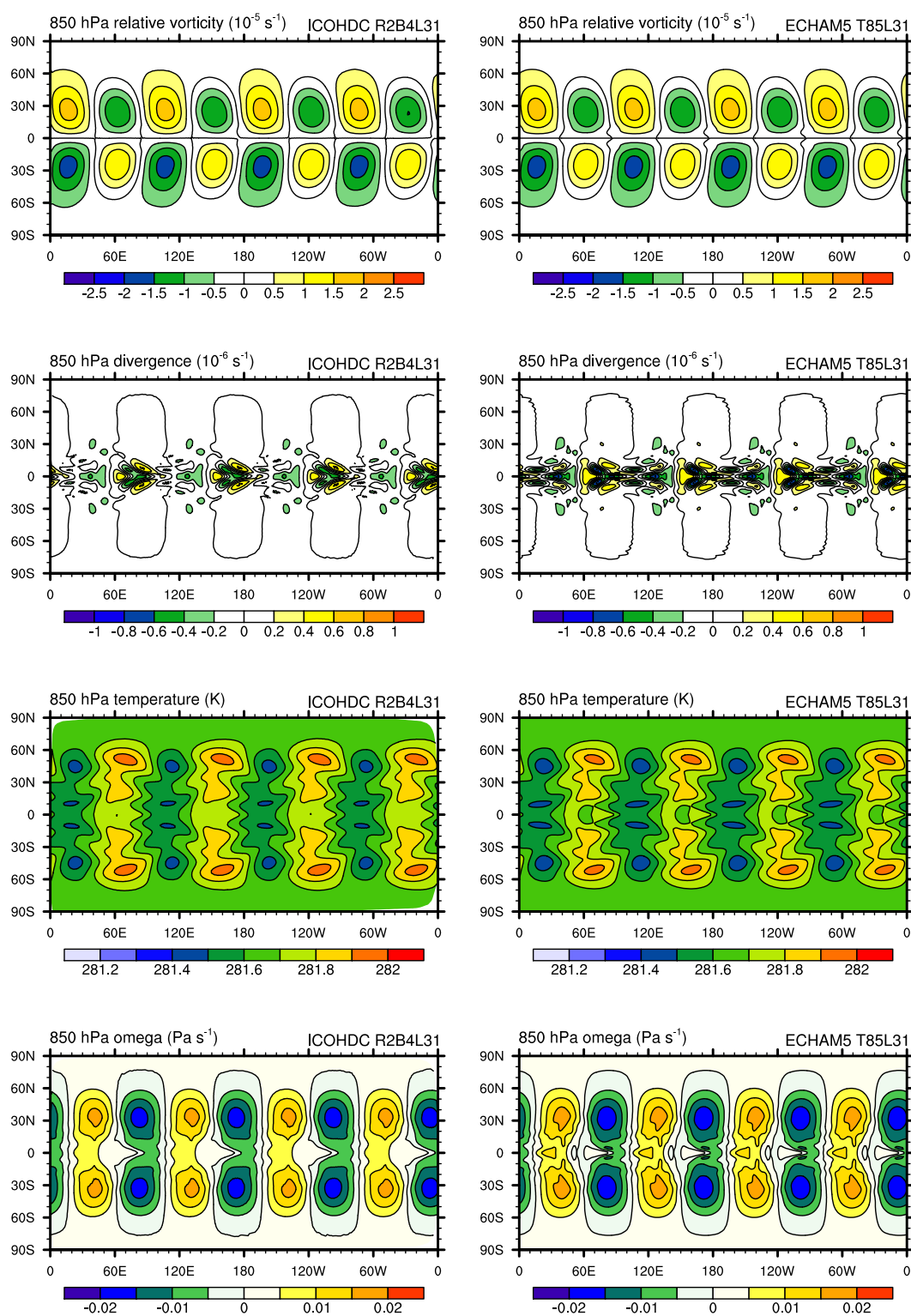


Fig. 4.6: Fig. 4.5 continued.

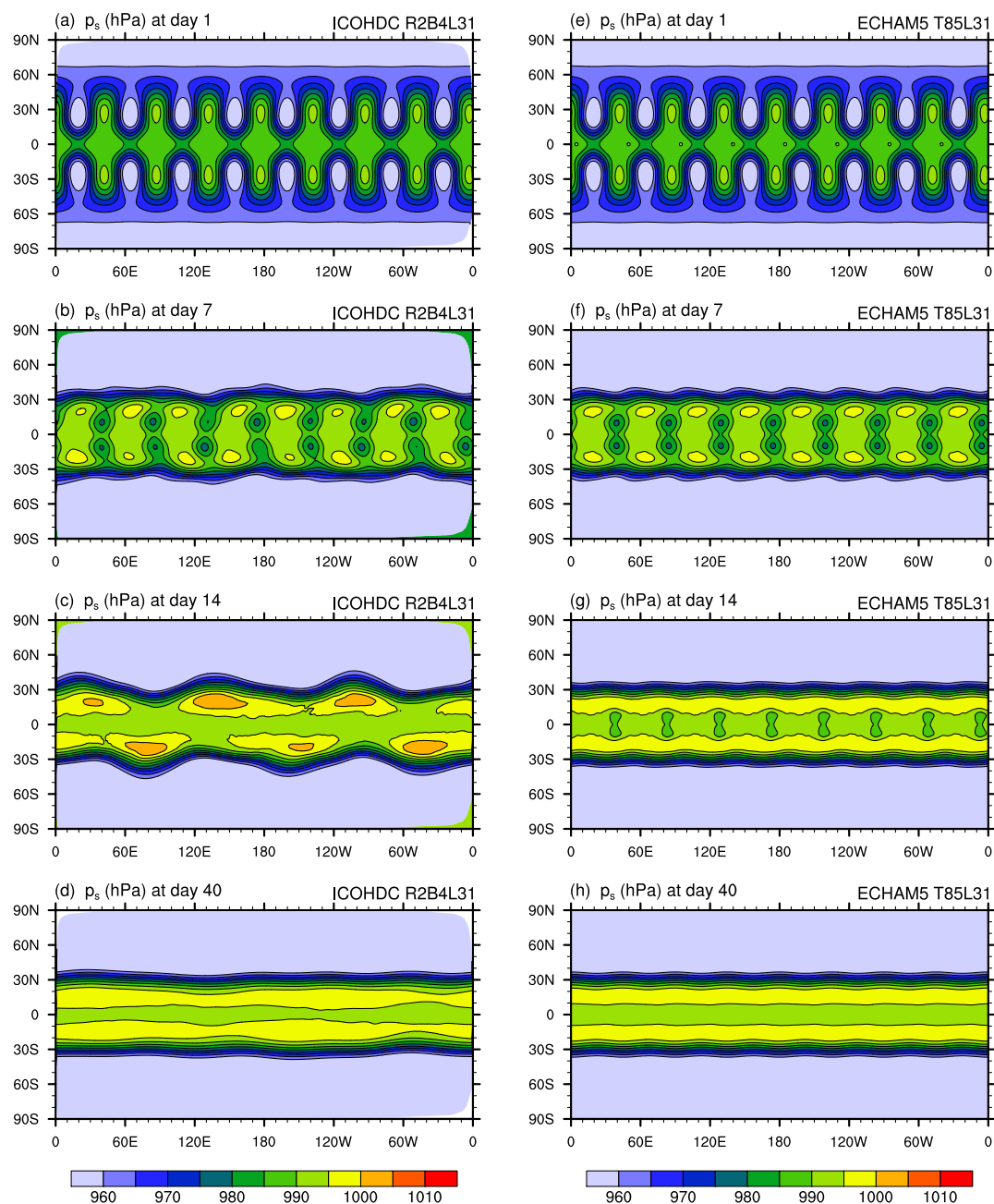


Fig. 4.7: Evolution of the surface pressure in the Rossby-Haurwitz wavenumber 8 experiment. The left column shows results from the ICOHDC. The right column is the simulation with the dynamical core of the ECHAM5 model.

4.3 Mountain-induced Rossby wave train

The simulations performed in the previous section focused on how a particular family of large-scale waves travel in the atmosphere and how they transform into other forms of motion. A closely related question is what leads to the formation of large-scale waves in the atmosphere. The theory of atmospheric energy dispersion developed by Rossby (1945) and Yeh (1949) described how a stationary source of vorticity in a simple westerly flow on the β -plane can give rise to a succession of troughs and ridges. This theory was refined by Hoskins *et al.* (1977) who took into account the Earth's sphericity and more realistic patterns of the zonal flow. Vorticity anomaly can be introduced in many ways, among which the orographic forcing is a particularly important one which has attracted a lot of attention.

The test case in this section closely resembles one of the numerical experiments performed in the early studies on the influence of orography on the large-scale atmospheric flow (e.g., Grose and Hoskins, 1979; Hoskins and Karoly, 1981). Following the proposal of Jablonowski *et al.* (2008), the initial conditions of the simulation feature an isothermal atmosphere of $T_0 := 288$ K, rotating at a constant angular velocity on all vertical levels. The initial wind field is given by

$$\begin{cases} u(\lambda, \varphi, \eta) & := u_0 \cos \varphi, \\ v(\lambda, \varphi, \eta) & := 0, \end{cases} \quad (4.13)$$

with a maximum wind speed of $u_0 := 20$ m s⁻¹. The flow is nondivergent, and the relative vorticity is

$$\xi(\lambda, \varphi, \eta) = \frac{2u_0}{a} \sin \varphi. \quad (4.14)$$

Under the assumption that there is no orography and that the surface pressure at the South Pole (and at the North Pole as well) is $p_{sp} := 930$ hPa, the surface pressure field that is in balance with the zonal flow can be derived:

$$(p_s)_b = p_{sp} \exp\left(-\frac{u_0(0.5u_0 + \Omega a)}{R_d T_0}\right). \quad (4.15)$$

Eqns. (4.13) and (4.15) together with the isothermal state form an analytical solution to the primitive equations.

So as to provide a vorticity source and trigger the waves, an idealized mountain is introduced in the Northern Hemisphere. The center of the mountain is located at $\lambda_c := \frac{\pi}{2}$, $\varphi_c := \frac{\pi}{6}$. The surface geopotential takes the form

$$\phi_s(\lambda, \varphi) = g z_s := g h_0 \exp\left[-\left(\frac{r}{d}\right)^2\right]. \quad (4.16)$$

Here the horizontal scale d is set to 1500 km, and the peak height h_0 2000 m. r denotes the great circle distance to the mountain center, which can be calculated by

$$r(\lambda, \varphi) = a \arccos\left[\sin \varphi_c \sin \varphi + \cos \varphi_c \cos \varphi \cos(\lambda - \lambda_c)\right]. \quad (4.17)$$

Instead of Eqn. (4.15) Jablonowski *et al.* (2008) proposed initializing the surface pressure field with

$$p_s := p_{sp} \exp\left(-\frac{u_0(0.5u_0 + \Omega a)}{R_d T_0} - \frac{\phi_s}{R_d T_0}\right). \quad (4.18)$$

This modified formula ensures that the initial tendency of the horizontal wind is zero since the pressure gradient force vanishes. The evolution of the flow starts from changes in the surface pressure.

The numerical experiment is performed with the ICOHDC at horizontal resolutions R2B4 and R2B5, and with the spectral dynamical core at spectral truncations T85 and T106. The pair of lower resolutions are the same as in the previous section, while the R2B5 and T106 resolutions are used as a supplement for assessing the convergence of the numerical solutions. All simulations use the same L31 vertical grid. The length of the time integration is 30 model days, as suggested by Jablonowski *et al.* (2008). The simulated 700 hPa relative vorticity and geopotential height at the higher resolutions (R2B5 and T106) are displayed in Figs. 4.8 and 4.9. The existence of the mountain in the super-rotational zonal flow introduces a source of negative relative vorticity in the upslope region and positive vorticity in the downslope region, which then induce a train of waves downstream of the mountain. Although the background flow is zonally symmetric, the wave train exhibits an evident equatorial propagation, and the downstream vorticity centers feature a strong northeast-southwest tilt. Hoskins *et al.* (1977) showed that this is caused by the meridional gradient of the β parameter [†] associated with the sphericity of the Earth. At day 5 the forerunner of the wave has already passed the antipodean point of the mountain center and returned to the Northern Hemisphere. In the geopotential height field, the trough on the lee side of the mountain keeps deepening until a cut-off low is formed (see the third and fourth rows in Fig. 4.9). After day 10 the wave train in the vorticity field is strongly affected by nonlinear interactions and dissipation. The disturbance is dissipated and distorted before returning to the vorticity source. Strong small-scale perturbations start to develop to the east of the mountain. In the longitude-pressure cross-section of the vertical velocity at 45° N at day 25 (Fig. 4.10), gravity waves have been generated and are propagating in the vertical direction.

The whole process of the generation, propagation and dissipation of the Rossby wave has been reproduced by both models. Although there are small differences in the details of the snapshots, there is no systematic discrepancies. The two sets of results are extremely similar.

The simulations at lower resolutions are shown in Figs. 4.11 and 4.12. The T85 and T106 solutions from the spectral model are hardly distinguishable in the vorticity field (Figs. 4.8 and 4.12, the right columns), while the vertical motions associated to gravity waves are slightly weaker in the T85 run (Figs. 4.10 and 4.11, the right panels). As for the ICOHDC simulation at R2B4, the propagation and dissipation of the Rossby wave is equally well represented compared to the other three simulations. On the other hand, the filament structures in the vorticity field (e.g., at day 10 near 50° N) and the gravity waves (Fig. 4.11 left panel) are less well resolved. These results suggest that in this test case, solutions from the spectral dynamical core converge at resolution T85, while in the ICOHDC convergence is not achieved before R2B5.

[†] $\beta = df/d\varphi$, i.e., the change of the Coriolis parameter with latitude.

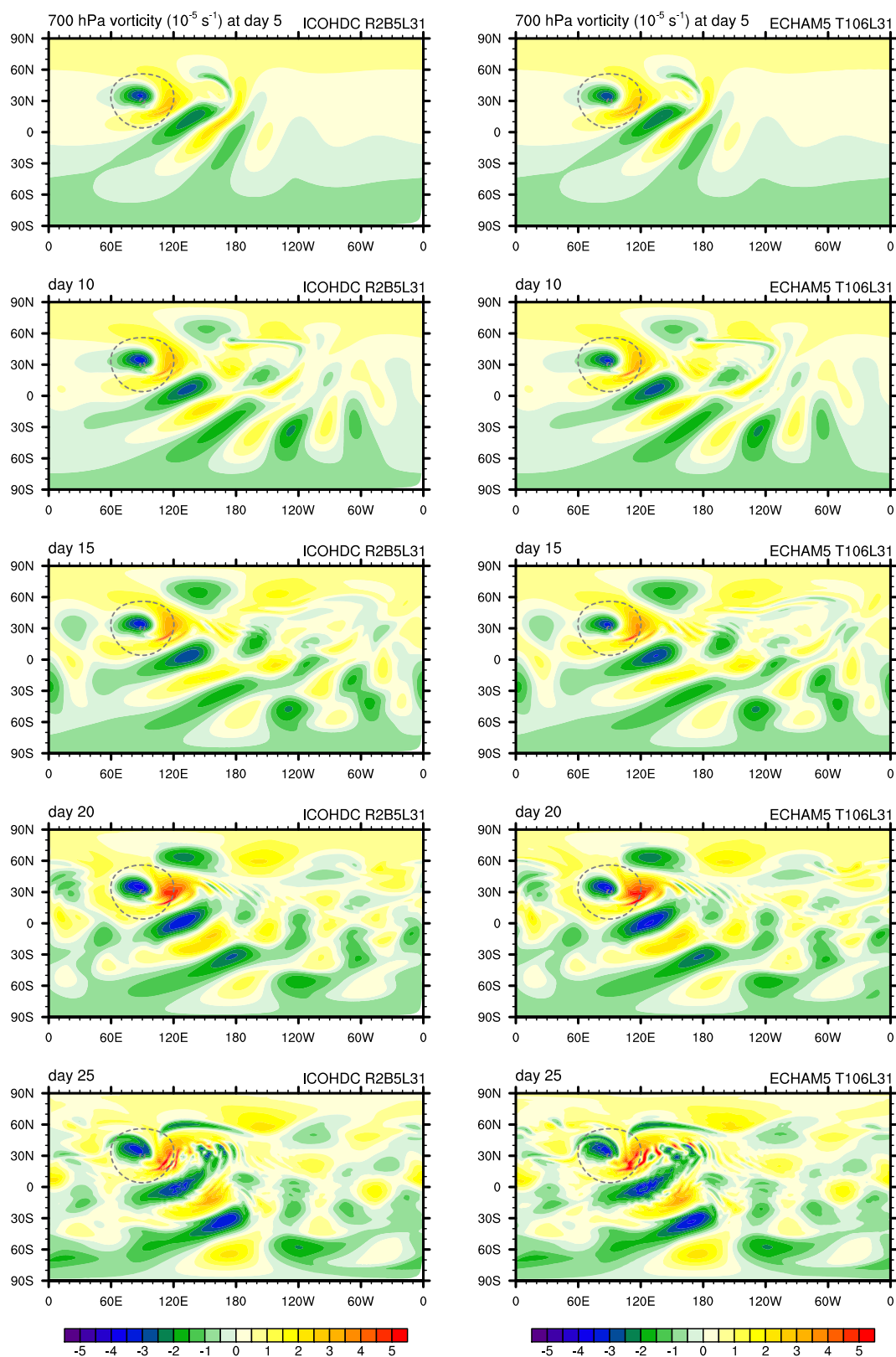


Fig. 4.8: Evolution of the 700 hPa relative vorticity in the test case of the mountain-induced Rossby wave train. The left column shows results from the icosahedral hydrostatic dynamical core at R2B5L31 resolution. The right column is the simulation with the dynamical core of ECHAM5 at T106L31 resolution.

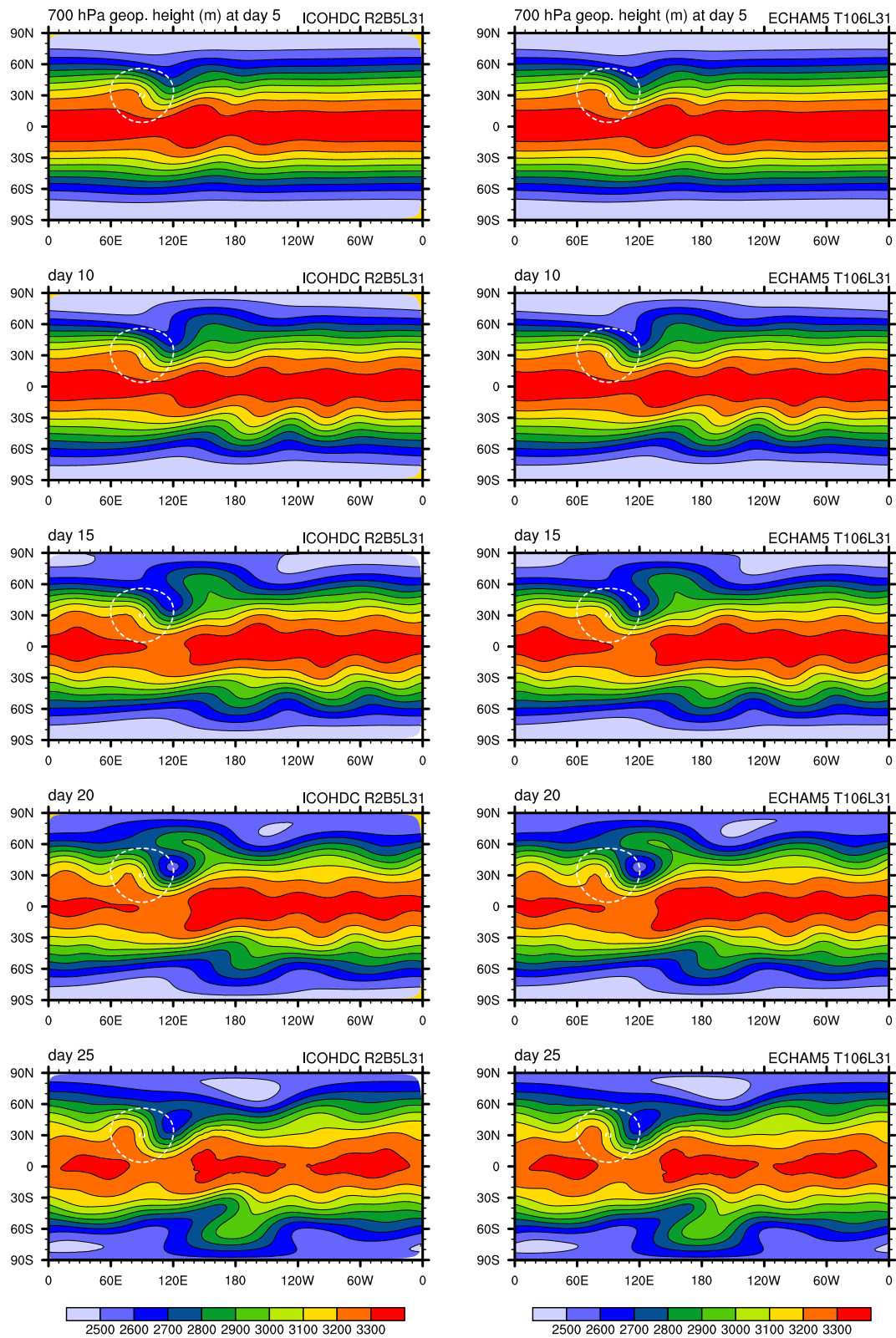


Fig. 4.9: As in Fig. 4.8 but showing the geopotential height at 700 hPa.

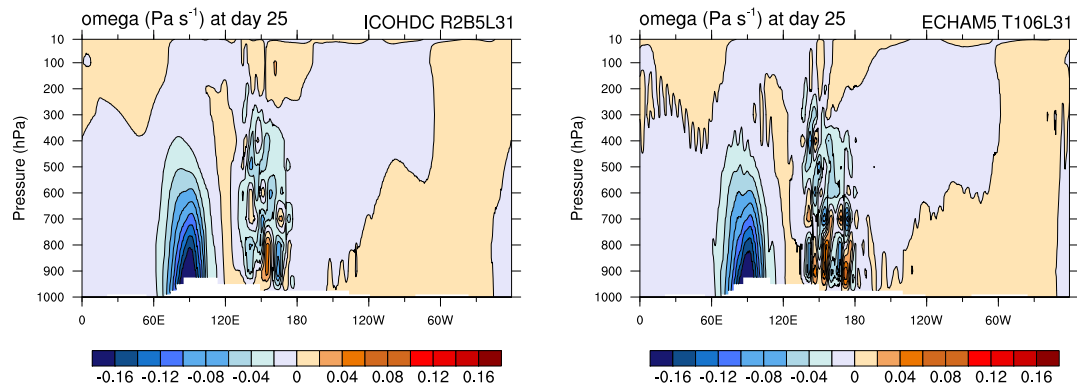


Fig. 4.10: Pressure-latitude cross section of the vertical velocity at 45° N, simulated by the ICOHDC at R2B5L31 resolution (left) and by the dynamical core of ECHAM5 at T106L31 resolution.

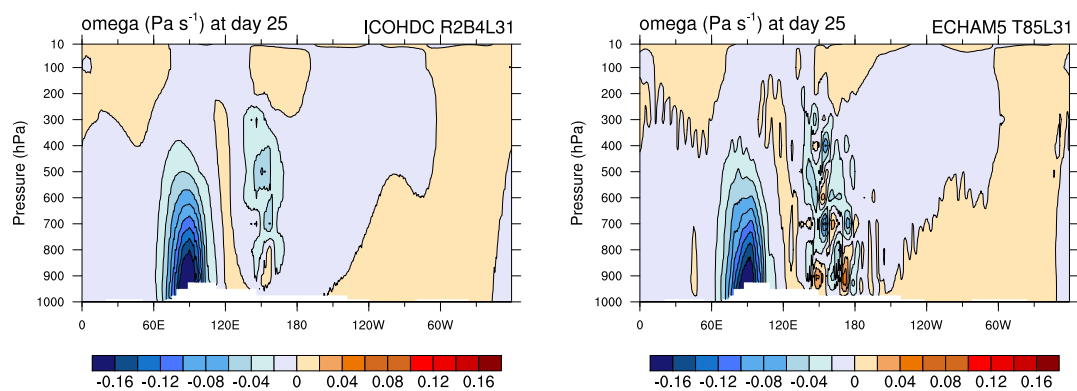


Fig. 4.11: As in Fig. 4.10, but the resolutions are R2B4L31 for the ICOHDC and T85L31 for the dynamical core of ECHAM5.

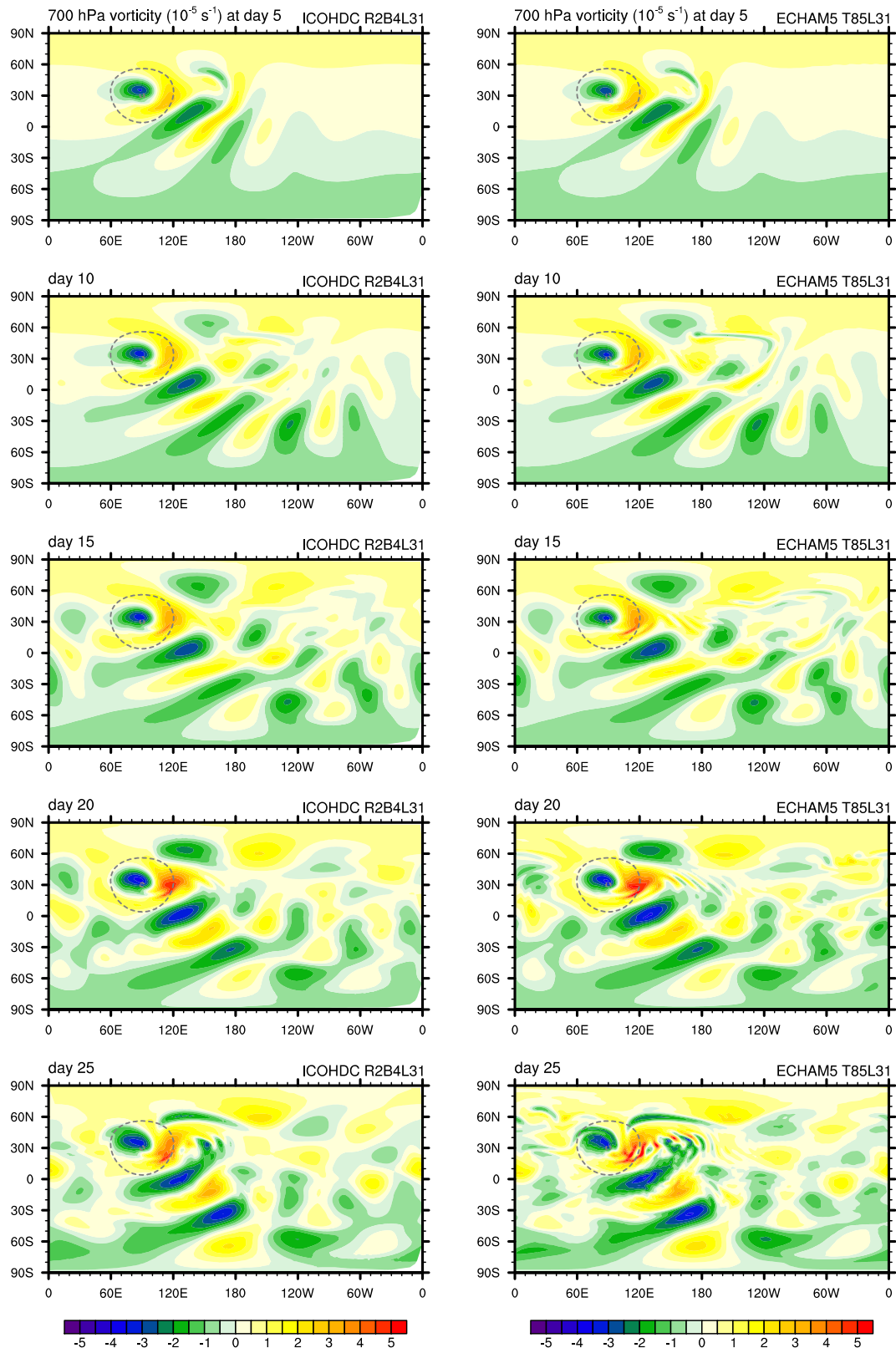


Fig. 4.12: As in Fig. 4.8 but the resolutions are R2B4L31 for the ICOHDC and T85L31 for the dynamical core of ECHAM5.

4.4 Jablonowski-Williamson steady state test

The test case proposed by Jablonowski and Williamson (2006a,b, hereafter JW06) is the first one in literature that provides a non-trivial analytical steady state solution to the primitive equations. The complete test case consists of two steps: In the first step, the dynamical core is initialized with the balanced initial conditions and integrated for 30 model days at various horizontal resolutions. The degradation of the steady state is measured by error norms. This stringent test serves as an assessment tool for the algorithmic design of the numerical scheme and its horizontal grid. In the second step of the test, a perturbation in the horizontal wind is introduced to the balanced state, which triggers the evolution of a baroclinic wave in the Northern Hemisphere. In this section the steady state test is performed. The second step is discussed in the next section.

4.4.1 Initial conditions and diagnostics

The initial state is zonally symmetric and comprised of constant surface pressure $p_s := 10^5$ Pa, a quasi-realistic temperature distribution, and a westerly jet in the mid-latitudes of each hemisphere. The analytical expressions are given in spherical coordinates (λ, φ, η) where $\lambda \in [0, 2\pi]$ stands for the longitude, $\varphi \in [-\pi/2, \pi/2]$ denotes the latitude, and η denotes the vertical coordinate. In the hybrid vertical coordinate used in this thesis, under the condition that the parameter p_0 (cf. the footnote on page 36 and Tab. 4.1 on page 55) and the surface pressure have the same value, values of η on the full-levels can be defined as

$$\eta_k := \frac{A_{k-1/2} + A_{k+1/2}}{2p_0} + \frac{B_{k-1/2} + B_{k+1/2}}{2}. \quad (4.19)$$

Let the symbol η_v denote an auxiliary variable

$$\eta_v := \frac{\pi}{2} (\eta - \eta_0) \quad (4.20)$$

with $\eta_0 := 0.252$. The zonal wind is defined as

$$u(\lambda, \varphi, \eta) := u_0 \cos^{\frac{3}{2}} \eta_v \sin^2 2\varphi. \quad (4.21)$$

with the maximum wind u_0 set to 35 m s^{-1} . The meridional wind vanishes. This flow field is divergence-free, and the relative vorticity is given by

$$\xi(\lambda, \varphi, \eta) = -\frac{4u_0}{a} \cos^{\frac{3}{2}} \eta_v \sin \varphi \cos \varphi (2 - 5 \sin^2 \varphi). \quad (4.22)$$

The temperature field is defined as

$$\begin{aligned} T(\lambda, \varphi, \eta) := & \frac{3\pi \eta u_0}{4R_d} \sin \eta_v \cos^{\frac{1}{2}} \eta_v \left\{ 2u_0 \cos^{\frac{3}{2}} \eta_v \left[-2 \sin^6 \varphi \left(\cos^2 \varphi + \frac{1}{3} \right) + \frac{10}{63} \right] \right. \\ & \left. + a\Omega \left[\frac{8}{5} \cos^3 \varphi \left(\sin^2 \varphi + \frac{2}{3} \right) - \frac{\pi}{4} \right] \right\} + \bar{T}(\eta), \end{aligned} \quad (4.23)$$

where

$$\bar{T}(\eta) := \begin{cases} T_0 \eta^{R_d \Gamma / g}, & \text{for } \eta \in [\eta_t, \eta_s] \\ T_0 \eta^{R_d \Gamma / g} + \Delta T (\eta_t - \eta)^5, & \text{for } \eta \in [0, \eta_t] \end{cases} \quad (4.24)$$

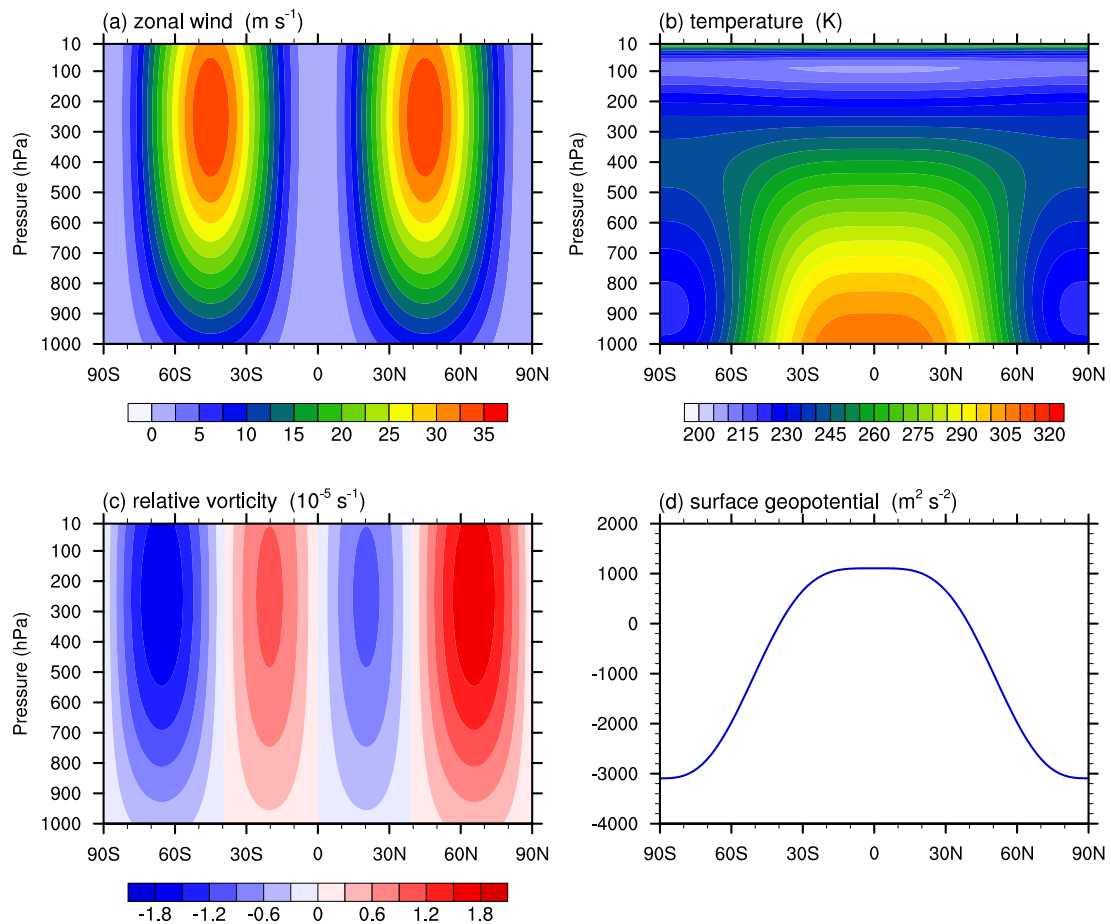


Fig. 4.13: Meridional cross-sections depicting the zonally symmetric initial conditions of the Jablonowski-Williamson steady state test: (a) zonal wind; (b) temperature, (c) relative vorticity, (d) surface geopotential. The meridional wind is zero by design, and the flow field is divergence-free.

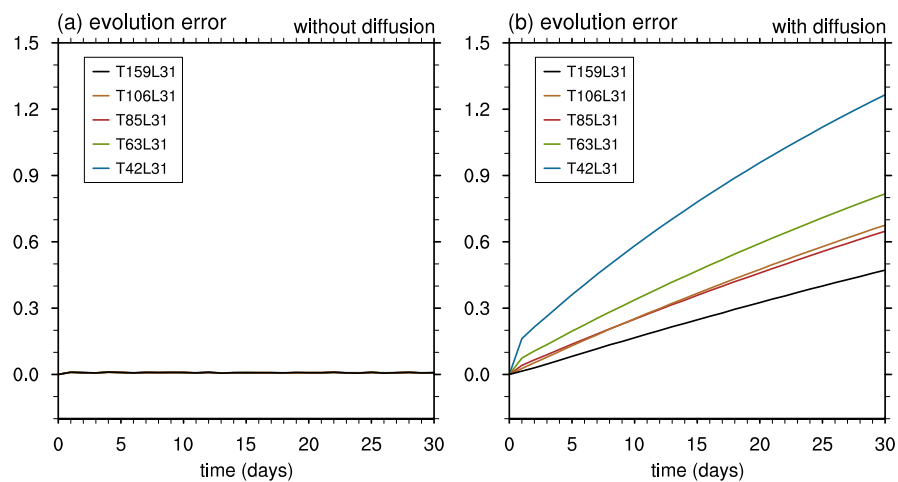


Fig. 4.14: The evolution error (cf. Eqn. (4.28)) of the simulated atmospheric state in the Jablonowski-Williamson steady state test performed with the dynamical core of ECHAM5 at various resolutions. The left panel shows the results obtained without horizontal diffusion, and the right panel with the default diffusion setup.

and

$$\eta_s := 1, \quad \eta_t := 0.2, \quad \Gamma := 0.005 \text{ K m}^{-1}, \quad T_0 := 288 \text{ K}, \quad \Delta T := 4.8 \times 10^5 \text{ K}. \quad (4.25)$$

For the hydrostatic dynamical cores, the initial state is completed by the surface geopotential

$$\begin{aligned} \phi_s(\lambda, \varphi) := & u_0 \cos^{\frac{3}{2}} \left[\frac{\pi}{2} (\eta_s - \eta_0) \right] \left\{ u_0 \cos^{\frac{3}{2}} \left[\frac{\pi}{2} (\eta_s - \eta_0) \right] \left[-2 \sin^6 \varphi \left(\cos^2 \varphi + \frac{1}{3} \right) + \frac{10}{63} \right] \right. \\ & \left. + a \Omega \left[\frac{8}{5} \cos^3 \varphi \left(\sin^2 \varphi + \frac{2}{3} \right) - \frac{\pi}{4} \right] \right\}. \end{aligned} \quad (4.26)$$

Meridional cross-sections depicting the initial state are presented in Fig. 4.13.

It can be verified that the initial conditions defined above are a steady solution to the primitive equations. The main aim of the analysis of model results is to quantify the evolution of the numerical error. According to the specifications of JW06, two error norms are calculated from the daily model output to assess the degradation of the numerical solution:

- the symmetry deviation:

$$l_2 \left(u(t) - \bar{u}^\lambda(t) \right) := \left\{ \frac{1}{4\pi} \int_0^1 \int_{-\frac{\pi}{2}}^{\frac{\pi}{2}} \int_0^{2\pi} \left[u(\lambda, \varphi, \eta, t) - \bar{u}^\lambda(\varphi, \eta, t) \right]^2 \cos \varphi \, d\lambda \, d\varphi \, d\eta \right\}^{\frac{1}{2}}; \quad (4.27)$$

- the evolution error:

$$l_2 \left(\bar{u}^\lambda(t) - \bar{u}^\lambda(t=0) \right) := \left\{ \frac{1}{2} \int_0^1 \int_{-\frac{\pi}{2}}^{\frac{\pi}{2}} \left[\bar{u}^\lambda(\varphi, \eta, t) - \bar{u}^\lambda(\varphi, \eta, t=0) \right]^2 \cos \varphi \, d\varphi \, d\eta \right\}^{\frac{1}{2}}. \quad (4.28)$$

Here \bar{u}^λ stands for the zonally averaged zonal wind.

4.4.2 Results from the spectral dynamical core

With the dynamical core of ECHAM5 it is possible to run this test without horizontal diffusion. Additionally, due to the property of the spectral transform algorithm and the insignificance of the round-off error in this model, the zonal symmetry of the atmospheric state is precisely preserved throughout the 30-day integration. After an initial adjustment in the first model day, the circulation experiences no significant degradation, as can be seen in the degradation error (Fig. 4.14 left panel) and in the snapshot of the surface pressure (Fig. 4.15, left column). When the horizontal diffusion is applied, the model state deviates slowly from the initial state, but the zonal symmetry is always preserved (Figs. 4.14 and 4.15, right panels).

4.4.3 Experiments with the ICOHDC

With the new dynamical core ICOHDC, time integrations without horizontal diffusion can not remain stable for longer than a few days. In this test case, the horizontal diffusion is applied with the parameter $\Delta t_D / \tau^* = 1$ (cf. Section 2.3.5). The horizontal resolutions investigated include R2B2, R2B3, and R2B4. The vertical resolution is L31 as in the previous sections.

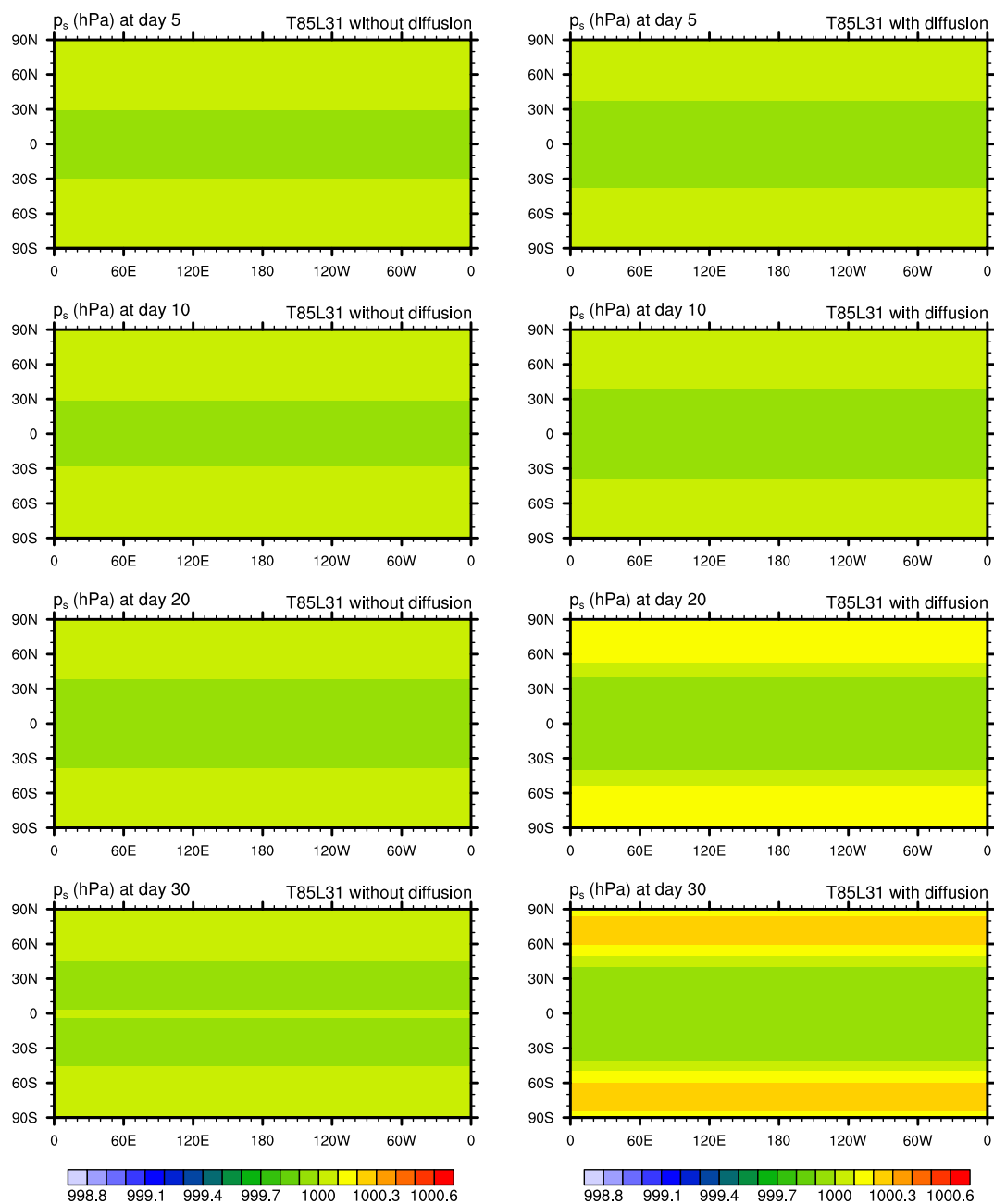


Fig. 4.15: Snapshots of surface pressure at days 5, 10, 20 and 30 simulated by the dynamical core of ECHAM5 in the Jablonowski-Williamson steady state test. The left column shows the results obtained without horizontal diffusion, and the right column with the default diffusion setup. Both simulations are performed at T85L31 resolution.

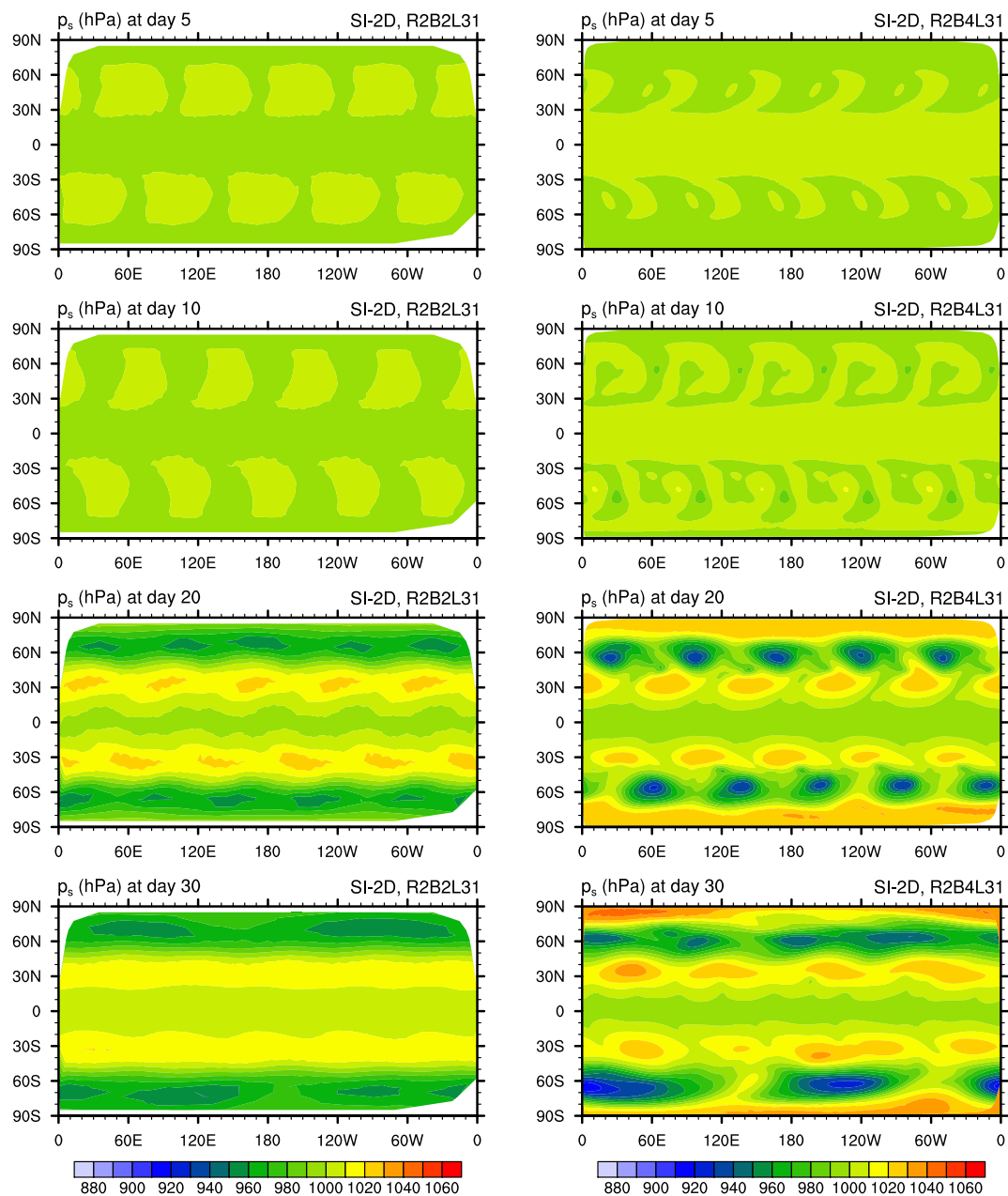


Fig. 4.16: Snapshots of surface pressure at days 5, 10, 20 and 30 simulated by the ICOHDC in the Jablonowski-Williamson steady state test case at resolutions R2B2 (left) and R2B4 (right). Both experiments were carried out with 31 vertical levels, using the semi-implicit time stepping scheme with 2D solver, and the original divergence operator defined by Eqn. (2.6).

In addition to assessing the model's behaviour at different horizontal resolutions, the sensitivity of the simulations to some other factors are also investigated, including the grid optimization, the 2D versus 3D semi-implicit time stepping scheme, and the smoothing applied to the divergence operator.

Evolution of the circulation

Fig. 4.16 shows snapshots of the surface pressure on selected days at horizontal resolutions R2B2 and R2B4. Both simulations are carried out using the original divergence operator and the SI-2D time stepping scheme. Considering the inherent structure of the triangular grid used in the ICOHDC and the dynamically unstable nature of the initial state, we expect deviation from the zonal symmetry develop to a significant extent. This is indeed what happens. At day 5 the wavenumber 5 structure related to the icosahedron is already clearly detectable (Fig. 4.16, first row). These perturbations amplify till 15 to 20 days after the initialization (depending on the resolution), and gradually dissipates thereafter. At day 30 the circulation has reach a quasi-equilibrium state, with high pressure systems near 30° latitudes and low pressure systems in higher latitudes (Fig. 4.16). When the resolution increases, the asymmetric signal develops stronger and dissipates more slowly (Fig. 4.16, bottom right). The latitudinal locations of the high and low pressure belts also change slightly.

The evolution of the numerical error is depicted in Fig. 4.17 by the symmetry deviation (Eqn. (4.27)) and the degradation of the zonal mean zonal wind (Eqn. (4.28)). Till day 5 the flow has not yet deviated much from the initial state. Between day 5 and day 10 the redistribution of mass happens mainly in the zonal direction. Although the symmetry degrades, the zonal mean wind is still similar to the initial state; after day 10 the perturbations start developing exponentially and matures around day 17. During this fast-developing phase, strong meridional transport of momentum and mass takes place, and the zonal mean wind deviates quickly from the earlier state. After about 25 days the atmospheric state reaches a quasi-equilibrium regime.

Effect of the grid optimization

In the third and fourth rows in Fig. 4.16 the zonal structure shows some deviation from an exact zonal wavenumber 5 pattern. This is caused by the specific implementation of the Heikes and Randall (1995b) grid optimization algorithm in the ICON models (see Section 2.1.3). When the original icosahedral grid is used in the experiments, the results display an exact periodicity in the zonal direction, as well as symmetry about the equator if one of the hemispheres is rotated by 36° in the east-west direction. Two examples are provided in Appendix E (see Figs. E.1 and E.2).

Sensitivity to the numerical schemes

Additional ICOHDC simulations have been performed using the modified divergence operators discussed in Section 2.3.6. Since the two schemes (see Eqns. (2.53) and (2.54)) are equivalent on a grid of equally-sized cells, and also produce very similar results on the ICON grid, we present here only the results obtained with the *s2* smoothing scheme (i.e., Eqn. (2.54)).

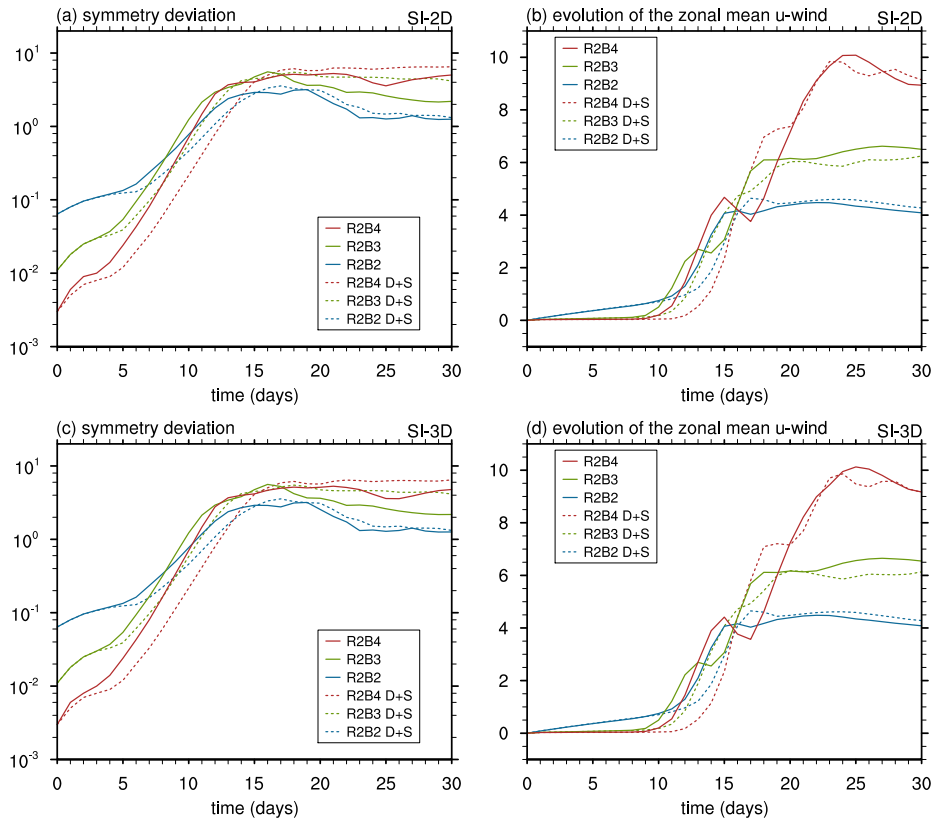


Fig. 4.17: The symmetry deviation (left column, cf. Eqn. (4.27)) and the evolution of the zonal mean zonal wind (right column, cf. Eqn. (4.28)) of the ICOHDC simulations in the Jablonowski-Williamson steady test at various resolutions. The upper panels show the results obtained with the semi-implicit time stepping scheme using the 2D linear solver; the lower panels correspond to the integrations using the 3D solver. Different resolutions are indicated by different colors. The solid curves correspond to simulations performed with the original divergence operator, and the dashed curves correspond to the runs using the modified divergence operator defined by Eqn. (2.54) (indicated by "D+S" in the legends).

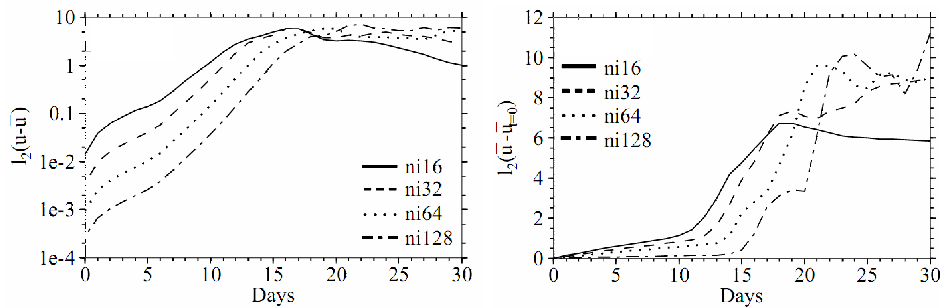


Fig. 4.18: The symmetry deviation (left) and the evolution of the zonal mean zonal wind (right) in the Jablonowski-Williamson steady test performed with the dynamical core of the GME model at various resolutions. Both panels are taken from Jablonowski and Williamson (2006b) with the authors' permission.

The symmetry deviation and evolution error of the zonal wind in the simulations performed with the modified divergence operator are shown by dotted lines in Fig. 4.17a,b. The first impression one gets is that qualitatively the evolution of the numerical errors is the same as with the original operator. This is probably related to the inherent properties of the horizontal grid. In the GME model which uses very similar grid generation algorithm but different numerical schemes, the error norm curves appear to be similar to our results (Fig. 4.18). On the other hand, Fig. 4.17a,b also reveals that in the evolution phase of this test case, the numerical errors associated to the simulations using the modified divergence operator are evidently smaller than those produced by the original operator, and the reductions in the errors become more significant as the horizontal resolution increases.

Regarding the time stepping scheme, the results obtained with the 3D solver are hardly distinguishable from those with the 2D solver, especially at lower resolutions (R2B2 and R2B3) and in the first 20 days. Visual comparison of the surface pressure snapshots also confirms this (not shown). During the experiments with the ICOHDC it has been noticed that the simulations using the 3D solver typically cost 50% to 150% more CPU time than the runs at the same resolution but using the 2D solver. The SI-2D scheme is thus a more cost-effective choice.

4.5 Jablonowski-Williamson baroclinic wave test

The second step of the Jablonowski-Williamson test case focuses on the evolution of an idealized baroclinic wave in the Northern Hemisphere over a short time period of 10 days. As detailed in JW06, the definition of the initial state in Section 4.4 guarantees static, inertial and symmetric stability, but is unstable with respect to baroclinic and barotropic instability mechanisms. Evolution of the baroclinic wave is triggered by an initial perturbation in the zonal wind field which is of relatively large scale but small magnitude:

$$u'(\lambda, \varphi, \eta) := u_p \exp\left[-\left(\frac{r}{\mathcal{R}}\right)^2\right], \quad (4.29)$$

with the radius $\mathcal{R}:=a/10$ and the maximum amplitude $u_p:=1 \text{ m s}^{-1}$. The great circle distance r is given by

$$r = a \arccos[\sin \varphi_c \sin \varphi + \cos \varphi_c \cos \varphi \cos(\lambda - \lambda_c)]. \quad (4.30)$$

The perturbation u' is centered at $(\lambda_c, \varphi_c):=(\pi/9, 2\pi/9)$, as shown in Fig. 4.19a, and superposed on the zonal wind on all vertical levels. The corresponding perturbations on initial divergence and vorticity are given by analytical expressions in JW06 and depicted in Fig. 4.19b and c. The simulation length is 30 days as in the steady state test.

4.5.1 Reference solution from the dynamical core of ECHAM5

The phenomenon simulated in the baroclinic wave test represents one of the most important mechanisms in the atmospheric dynamics. This process is highly nonlinear, and can not be described by an analytical solution even though the initial conditions are unambiguously defined in JW06. Model intercomparison is thus necessary for identifying the reference solution.

In addition to defining the test case, JW06 carried out numerical experiments with different models at various resolutions. The test case was applied to a spectral transform dynamical core at resolutions from T21 to T340, a semi-Lagrangian model at the same resolutions, a finite volume dynamical core using regular latitude-longitude meshes of grid size $4^\circ(\text{latitude}) \times 5^\circ(\text{longitude})$ to $0.25^\circ \times 0.3125^\circ$, and the dynamical core of GME from resolution ni16 to ni256 (corresponding to R2B3 and R2B7 of the ICON grid, respectively). A clear trend of convergence with respect to horizontal resolution was observed in all the four models. The simulation at the highest resolution of each dynamical core was identified as the reference solution of that particular model. Since the four reference solutions closely resemble each other, a consensus can be regarded as achieved about the basic characteristics of this test case. On the other hand, because the basic state in this test case is dynamically unstable, the differences in the numerical schemes used in the models also project onto the model states and grow with time, as does the imposed initial perturbation. The highest-resolution solutions from the four dynamical cores thus differ from each other in many small details.

Based on these results, JW06 have estimated the uncertainty of the reference solutions using

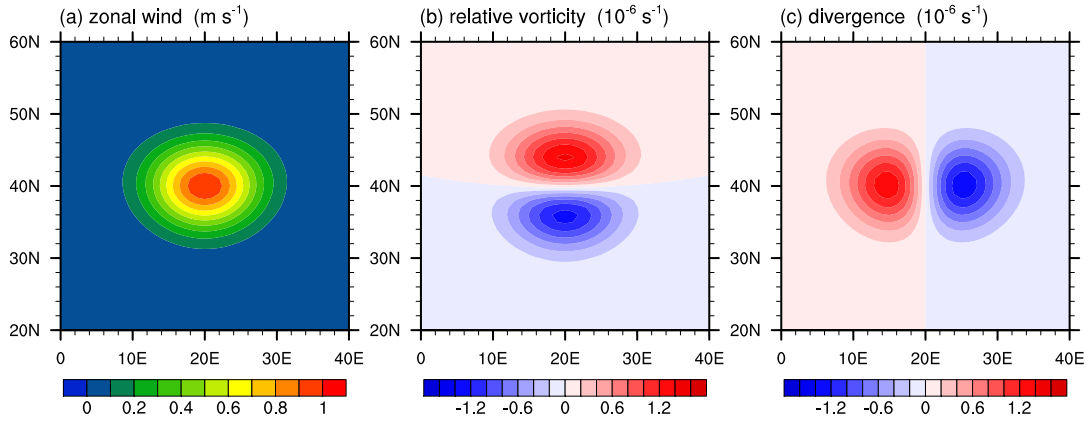


Fig. 4.19: The initial perturbation of (a) zonal wind, (b) relative vorticity, and (c) divergence in the Jablonowski-Williamson baroclinic wave test. The perturbation is added to the balanced initial state in Fig. 4.13 throughout the vertical domain of the model atmosphere, so as to trigger the evolution of the baroclinic wave.

the l_1 , l_2 and l_∞ difference norms of the surface pressure, which are defined as

$$l_1(p_s(t)) := \frac{1}{4\pi} \int_{-\frac{\pi}{2}}^{\frac{\pi}{2}} \int_0^{2\pi} |p_{s_1}(\lambda, \varphi, t) - p_{s_2}(\lambda, \varphi, t)| \cos \varphi \, d\lambda \, d\varphi, \quad (4.31)$$

$$l_2(p_s(t)) := \left\{ \frac{1}{4\pi} \int_{-\frac{\pi}{2}}^{\frac{\pi}{2}} \int_0^{2\pi} [p_{s_1}(\lambda, \varphi, t) - p_{s_2}(\lambda, \varphi, t)]^2 \cos \varphi \, d\lambda \, d\varphi \right\}^{\frac{1}{2}}, \quad (4.32)$$

$$l_\infty(p_s(t)) := \max_{\text{all } \lambda, \varphi} |p_{s_1}(\lambda, \varphi, t) - p_{s_2}(\lambda, \varphi, t)|. \quad (4.33)$$

The difference norms were calculated at each model day for

1. solutions from different dynamical cores at their highest resolution used in the test;
2. solutions from different dynamical cores at their second highest resolution;
3. solution from one dynamical core at its highest resolution and that from another dynamical core at its second highest resolution.

Each possible combination of two solutions gives a curve of a difference norm against time. It turned out that these curves showed similar magnitude and shape. The maximum of all curves was taken as the estimate of the uncertainty associated to the reference solutions in the surface pressure field (JW06).

In the study presented in this thesis, the baroclinic wave test is applied first to the spectral transform dynamical core of ECHAM5 as a preparation step for the evaluation of the ICOHDC. Experiments are carried out at resolutions T42, T63, T85, T106, T159, T255 and T319, always with 31 vertical layers. [†] Fig. 4.20 shows the l_1 , l_2 and l_∞ norms of the surface pressure difference between these simulations and the reference solution from the spectral dynamical core used in JW06. It can be seen that at lower resolutions (T42 and T63), the differences

[†]These resolutions are chosen because they have been used in climate simulations with the full ECHAM5 model.

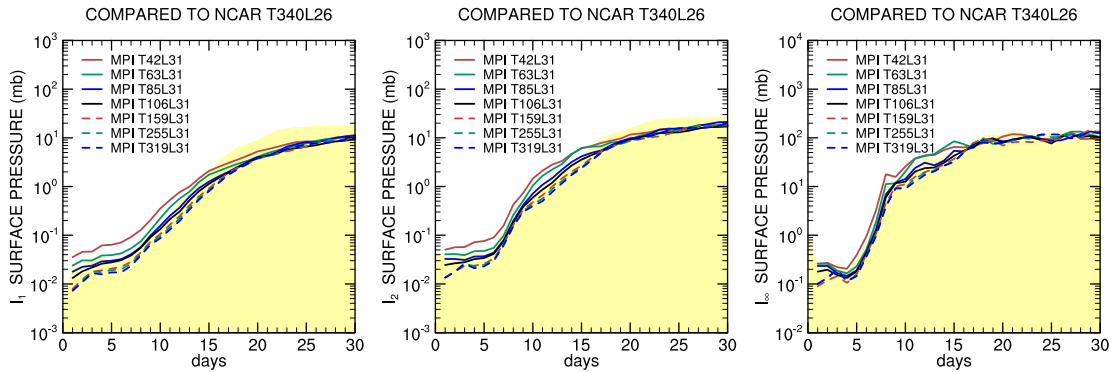


Fig. 4.20: The l_1 (left), l_2 (middle) and l_∞ (right) norms of the surface pressure difference between the simulations with the dynamical core of ECHAM5 (denoted by "MPI" in the legends) at various resolutions and the T340L26 solution from the spectral transform dynamical core used in Jablonowski and Williamson (2006a,b) (denoted by "NCAR" in the title of each panel). The ECHAM5 experiments were performed during the preparation of this thesis. The computation of the error norms and the making of this figure were kindly conducted by Dr. David L. Williamson from the National Center for Atmospheric Research.

between the ECHAM5 simulation and the T340L26 solution from JW06 are clearly outside the uncertainty range, especially in the first 15 days. In contrast, the ECHAM5 simulations at T159L31, T255L31 and T319L31 are sufficiently close to the T340L26 solution from JW06, for the difference curves lie well under the uncertainty estimate. In other words, the T159L31, T255L31 and T319L31 simulations from ECHAM5 have the same quality as any of the reference solutions in JW06. It is thus a justified choice to use the ECHAM5 results at T319L31 as the reference solution in this section when the performance of the ICOHDC is evaluated.

The evolution of the baroclinic wave in the ECHAM5 T319L31 simulation is depicted in Figs. 4.21 and 4.22 by snapshots of the surface pressure, 850 hPa temperature and 850 hPa relative vorticity in the Northern Hemisphere at days 4, 6, 7, 8 and 10. The evolution of the circulation is slow in the first 4 days. After that, weak high and low pressure systems become clearly visible, which correspond to the weak wave patterns in temperature and vorticity. Dramatic amplification of the baroclinic wave starts in day 7. The high and low pressure systems intensify quickly; By day 8 sharp gradients have formed in temperature and vorticity, and the peaks of the wave have started wrapping around. The wave reaches its mature stage at day 9 (see the last row in Fig. 4.24 and the bottom right panel in Fig. 4.26). By this time, well defined vorticies appear to be the most distinct feature in the temperature and vorticity plots. At day 10 the wave starts breaking down. Closed cells of warm air can be seen in the bottom right panel of Fig. 4.21.

Fig. 4.21 presented here can be directly compared with Figs. 5.1 – 5.4 in Jablonowski and Williamson (2006b), which shows the simulations from the four dynamical cores used therein. We point out here that the ECHAM5 results are very similar to the converged solutions in JW06, not only in terms of the global measures (i.e., the difference norms in Fig. 4.20), but also in the characteristics of the spatial pattern of the atmospheric flow and its evolution. This further confirms that the T319L31 simulation is a sufficiently good reference solution.

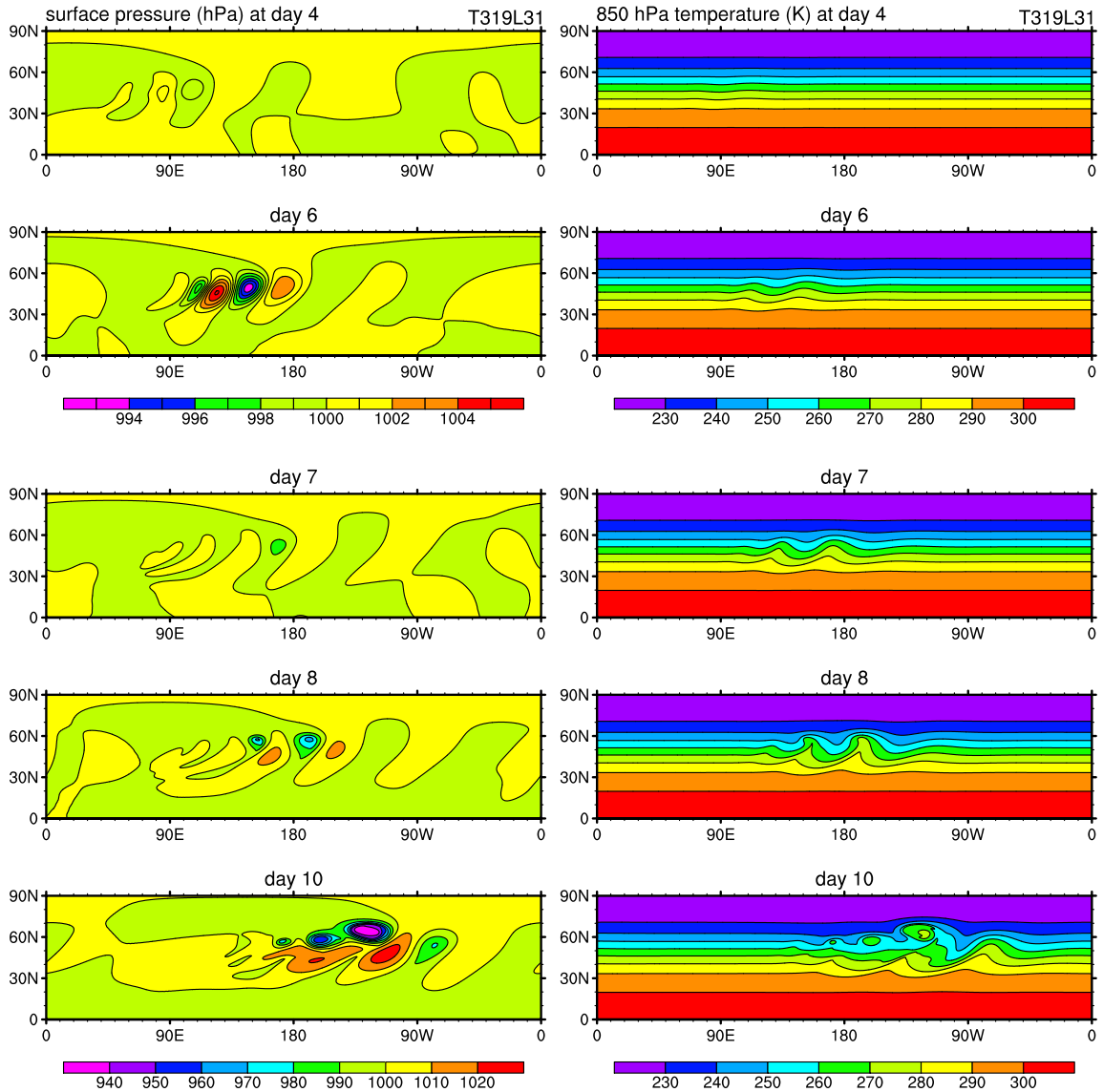


Fig. 4.21: Evolution of the surface pressure (left) and 850 hPa temperature (right) in the Jablonowski-Williamson baroclinic wave test performed with the dynamical core of ECHAM5 at resolution T319L31. The choices of color scale and contour interval follow Jablonowski and Williamson (2006b).

4.5.2 Experiments with the ICOHDC

The baroclinic wave test with the ICOHDC is performed not only at the three horizontal resolutions used in the steady state test (i.e., root 2 with 2 to 4 subsequent bisections), but also at R5B2, R3B3, R3B4 and R2B5 (cf. Tab. 4.5 on page 56). This is meant to provide smooth and small steps of reduction in the horizontal grid size, so as to allow for identifying equivalent resolutions of the ICOHDC and the ECHAM5 dynamical core by assessing the quality of the solutions. The vertical resolution is again fixed at L31.

In the previous section it has been observed that the simulations performed using the SI-3D scheme show little difference from those using the SI-2D scheme, but cost considerably more CPU time. Therefore in the baroclinic wave test, all the experiments are carried out using only

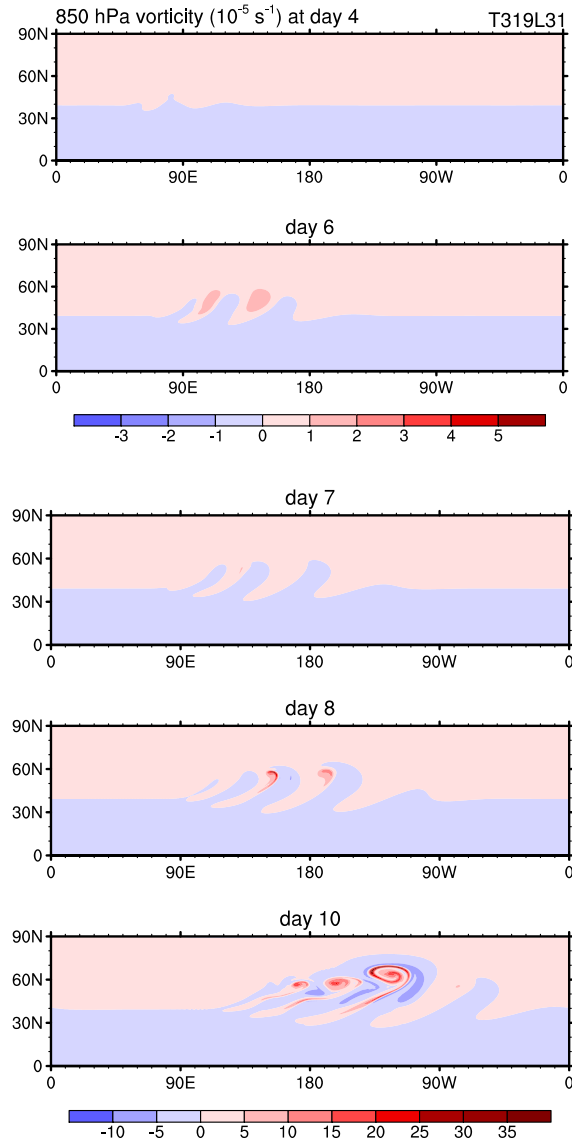


Fig. 4.22: Evolution of the 850 hPa relative vorticity in the Jablonowski-Williamson baroclinic wave test performed with the dynamical core of ECHAM5 at resolution T319L31.

the SI-2D scheme. Regarding the divergence operator, both the original definition (Eqn. (2.6)) and a modified version (Eqn. (2.54)) are tested.

The evolution of the Northern Hemisphere surface pressure and 850 hPa temperature simulated at resolution R2B5L31 with the modified divergence operator is depicted in Fig. 4.23. Compared to the reference solution in Fig. 4.21, this simulation has captured the main features of the flow at each of the displayed time instants. The slow rate of change in the first 6 days and the subsequent exponential intensification of the high and low pressure systems are correctly simulated. The amplification of the wave in temperature is also well represented. The location and strength of the fronts at day 10 and the formation of closed cells of warm air mass agree well with the reference solution. The experiment performed at the same resolution but using the original divergence operator will be discussed later.

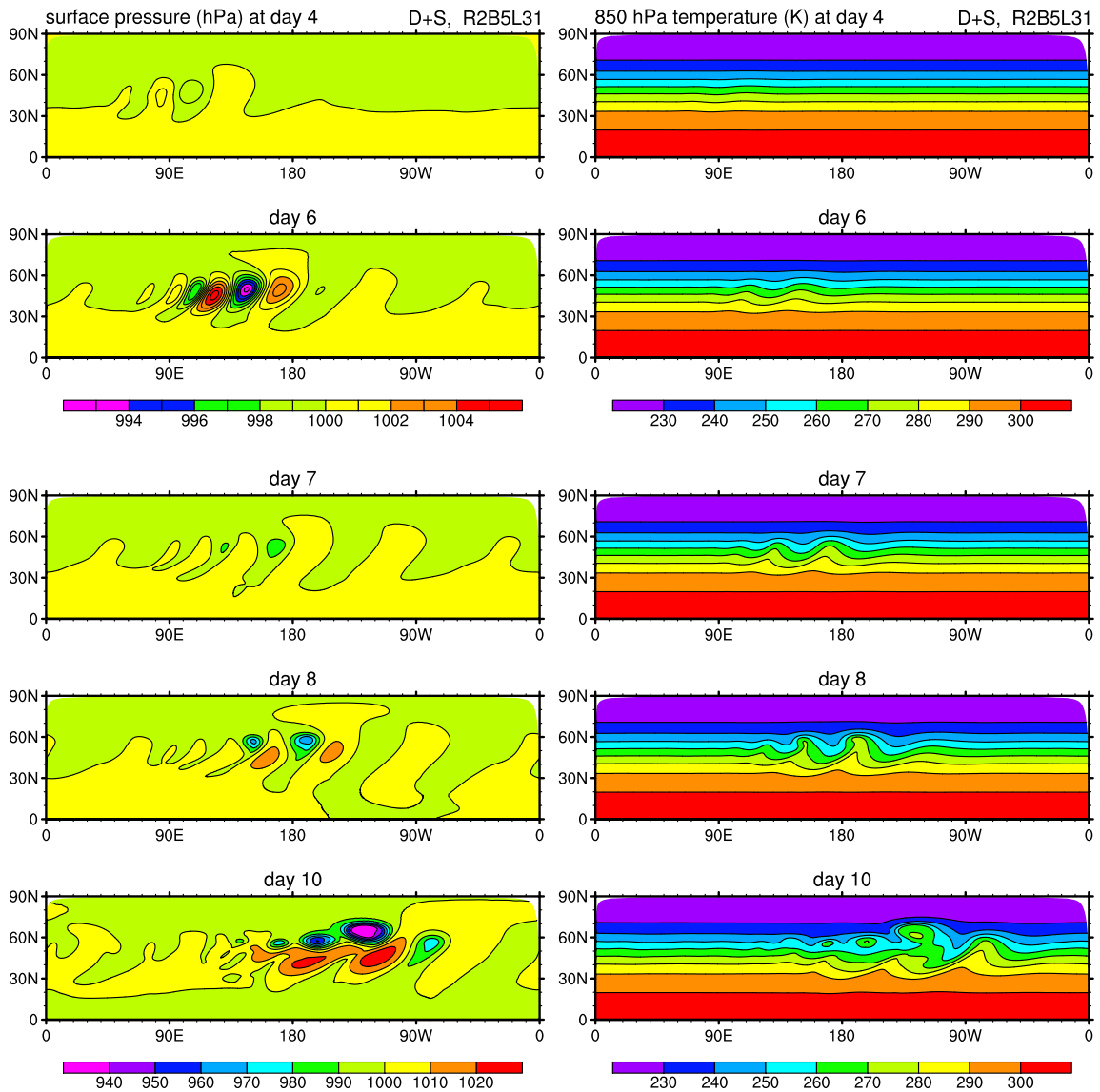


Fig. 4.23: As in Fig. 4.21 but simulated with the ICOHDC at resolution R2B5L31 using the modified divergence operator defined by Eqn. (2.54). The horizontal diffusion coefficient used is $\Delta t_D/\tau^* = 1$.

In contrast to R2B5, the experiments at the R2B2 resolution do not produce meaningful results. After one model day, the perturbation superposed on the zonal wind at the initial time step has already decreased to an amplitude similar to the errors introduced by the spatial discretization (not shown). The snapshots of surface pressure and 850 hPa temperature of the subsequent days are not considerably different from those obtained in the steady state test at the same resolution. Only when the magnitude of the initial wind perturbation is increased by a factor of 2, can the resulting high and low pressure systems be clearly distinguished from the numerical noise at day 6. When the initial perturbation is further increased to $u_p = 5 \text{ m s}^{-1}$, the simulated surface pressure distribution at day 10 starts to vaguely show some similarities to the high-resolution results. It can therefore be concluded that the R2B2 resolution, with a characteristic grid size of 510 km between mass points and 880 km between vorticity points, is

not sufficient for simulating the synoptic scale vortices.

In the following we follow JW06, and investigate the sensitivity of the numerical solution to the horizontal resolution by comparing the simulated circulation at day 9. The integrations performed with the modified divergence operator (Eqn. (2.54)) are used as an example. Subsequently the effect of using the four-cell stencil in computing the divergence is discussed.

4.5.3 Sensitivity of the numerical solution to horizontal resolution

In Figs. 4.24 and 4.25 the surface pressure and 850 hPa temperature of day 9 simulated by the spectral dynamical core and the ICOHDC are shown at various resolutions. The ICOHDC simulation at R2B2 is not shown because, as already mentioned, this resolution is not sufficient to represent the synoptic-scale process in investigation. For the ICOHDC (Fig. 4.25) the characteristic distance between neighbouring mass points (cf. Tab. 4.3 on page 56) is indicated in each panel to facilitate comparison with the spectral model. For the spectral dynamical core, the numbers indicated in the parentheses in Fig. 4.24 are the zonal spacing of the corresponding Gaussian grids at 60°N , where the center of the baroclinic vortices are located. The comparison of the dual edge length of the ICON grid and the zonal spacing of the Gaussian grid makes sense, because they are directly related to the accuracy of the discretized nonlinear terms in the governing equations. According to this comparison, half of the ICON grids in Fig. 4.25 are coarser than the lowest resolution (T42) of the ECHAM5 simulations; The finest ICON grid used here (i.e., R2B5) has a grid size comparable to the zonal spacing of the T106 Gaussian grid at 60°N . As stated in the first section of this chapter, simulations from the ICOHDC at higher resolutions are not yet available due to technical reasons, and will be the task of future work.

In the results from the spectral model, the most prominent features associated to the lower resolutions are the "spectral ringing" in the surface pressure and the less well resolved filament of warm air near 145°W (see the temperature plots). The first mature low pressure system (the one at 150°W) is weaker at lower resolutions. Regarding the ICOHDC results, the strength of the depression at 150°W at R2B4 (127 km) is similar to that of the T42 (156 km) simulation. The use of finite difference discretization in the ICOHDC avoids the spectral noise in the surface pressure field, but brings in error in the phase speed of the baroclinic wave. At resolutions R2B4 (127 km) and lower (Fig. 4.25, first to fourth rows), the westward propagation of the high and low pressure systems are evidently slower than in the reference solution (Fig. 4.24, bottom left). This can be more clearly detected in the relative vorticity field by comparing Figs. 4.26 and 4.27. It should be pointed out that the phase error is not a peculiar problem of the ICOHDC, but a typical feature of models that utilize the finite difference method. Moreover, as the resolution increases, the ICOHDC simulations converge quickly. At R2B5 (64 km), the phase error is no longer evident. Judging from the shape and the magnitude of the baroclinic vortices (Figs. 4.26 and 4.27), we conclude that the solution from the ICOHDC at R2B5 (64 km) resolution is of comparable quality as the T106 (63 km) simulation from the spectral model. In JW06 it has been suggested that the convergence property of the numerical solutions should be quantitatively assessed using the difference norms defined by Eqns. (4.31) – (4.33). Since the ICOHDC simulations at resolutions higher than R2B5 are currently not available, we leave this task to future work.

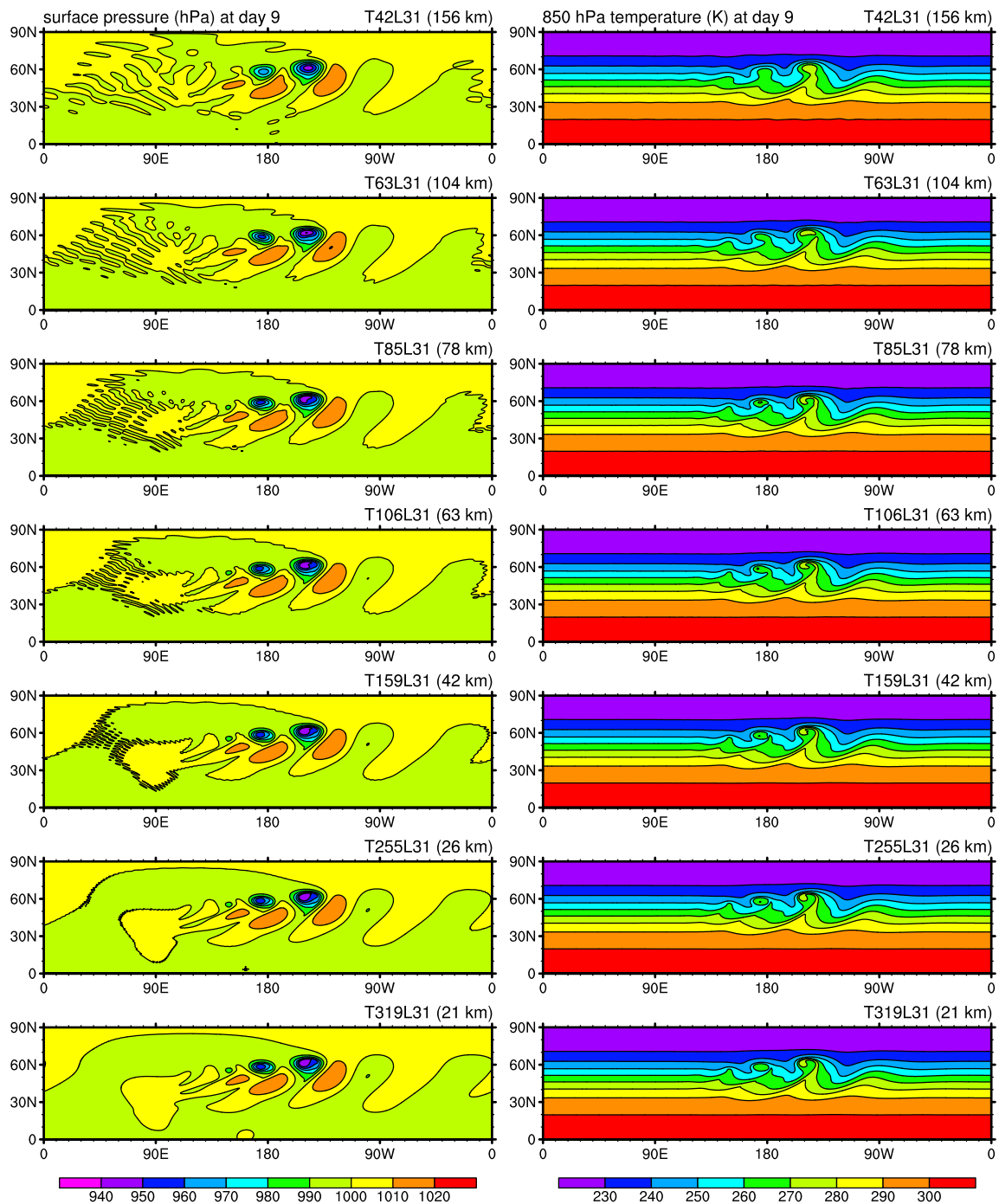


Fig. 4.24: Snapshots of the surface pressure (left) and 850 hPa temperature (right) in the Northern Hemisphere simulated by the dynamical core of ECHAM5 at various horizontal resolutions. The zonal grid sizes at 60°N on the corresponding Gaussian grids are indicated in the top right corner of each panel.

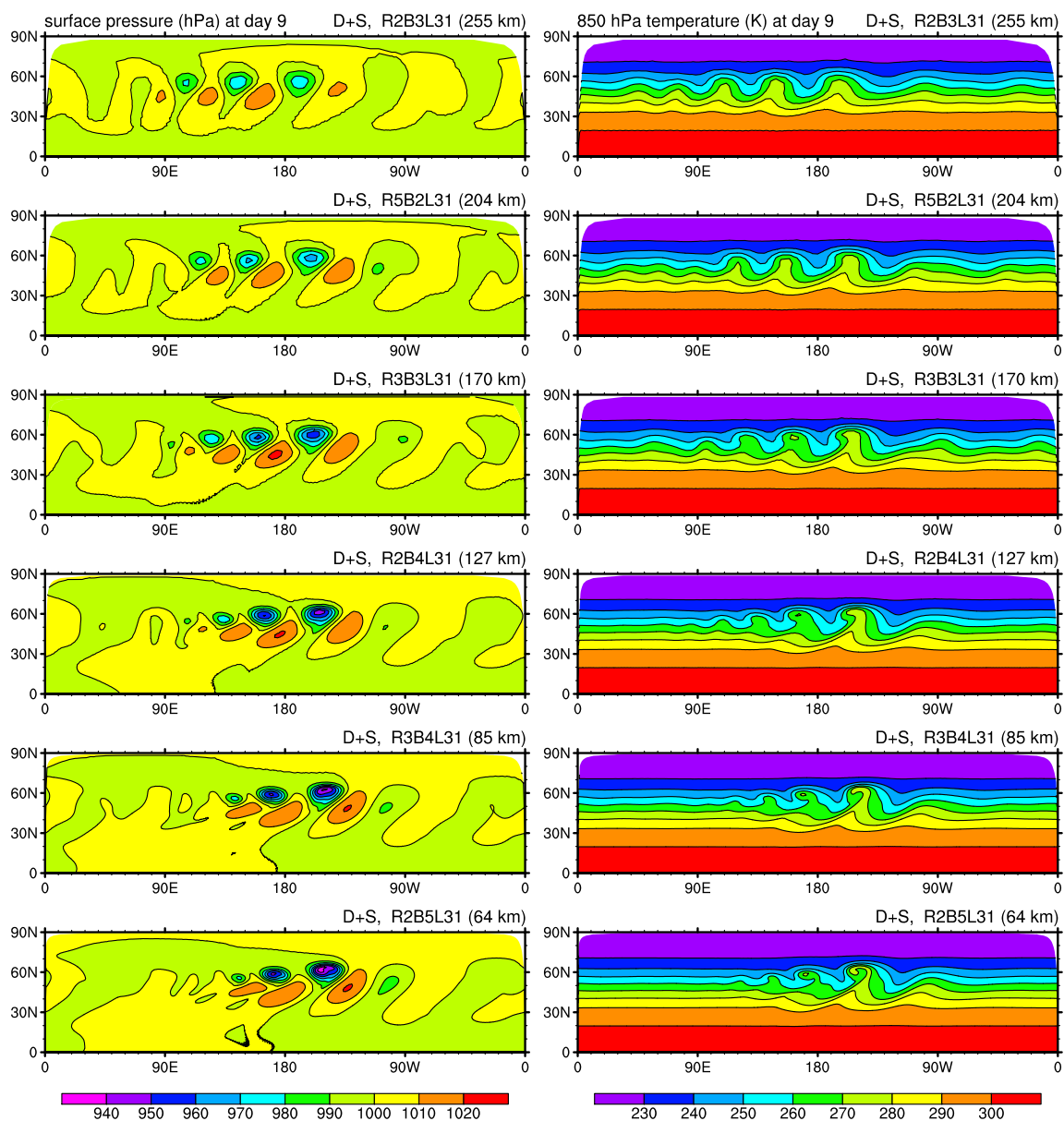


Fig. 4.25: As in Fig. 4.24 but simulated with the ICOHDC. The characteristic distance between neighbouring mass points (cf. Tab. 4.3 on page 56) are indicated in the top right corner of each panel. In these simulations the modified divergence operator defined by Eqn. (2.54) is used. The horizontal diffusion parameter $\Delta t_D / \tau^*$ has the value 1.

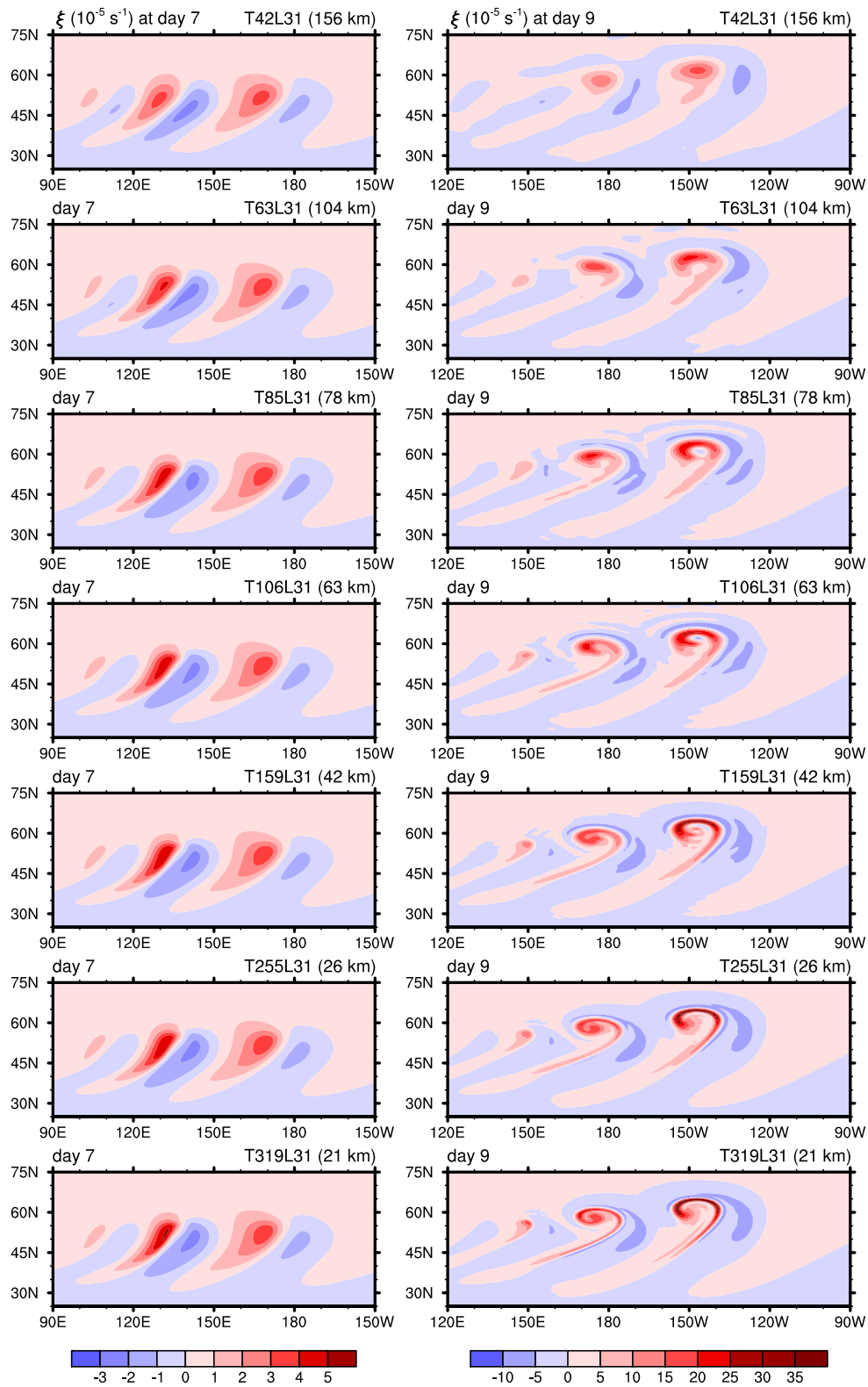


Fig. 4.26: Snapshots of the 850 hPa relative vorticity at day 7 and day 9 simulated by the dynamical core of ECHAM5 at various horizontal resolutions.

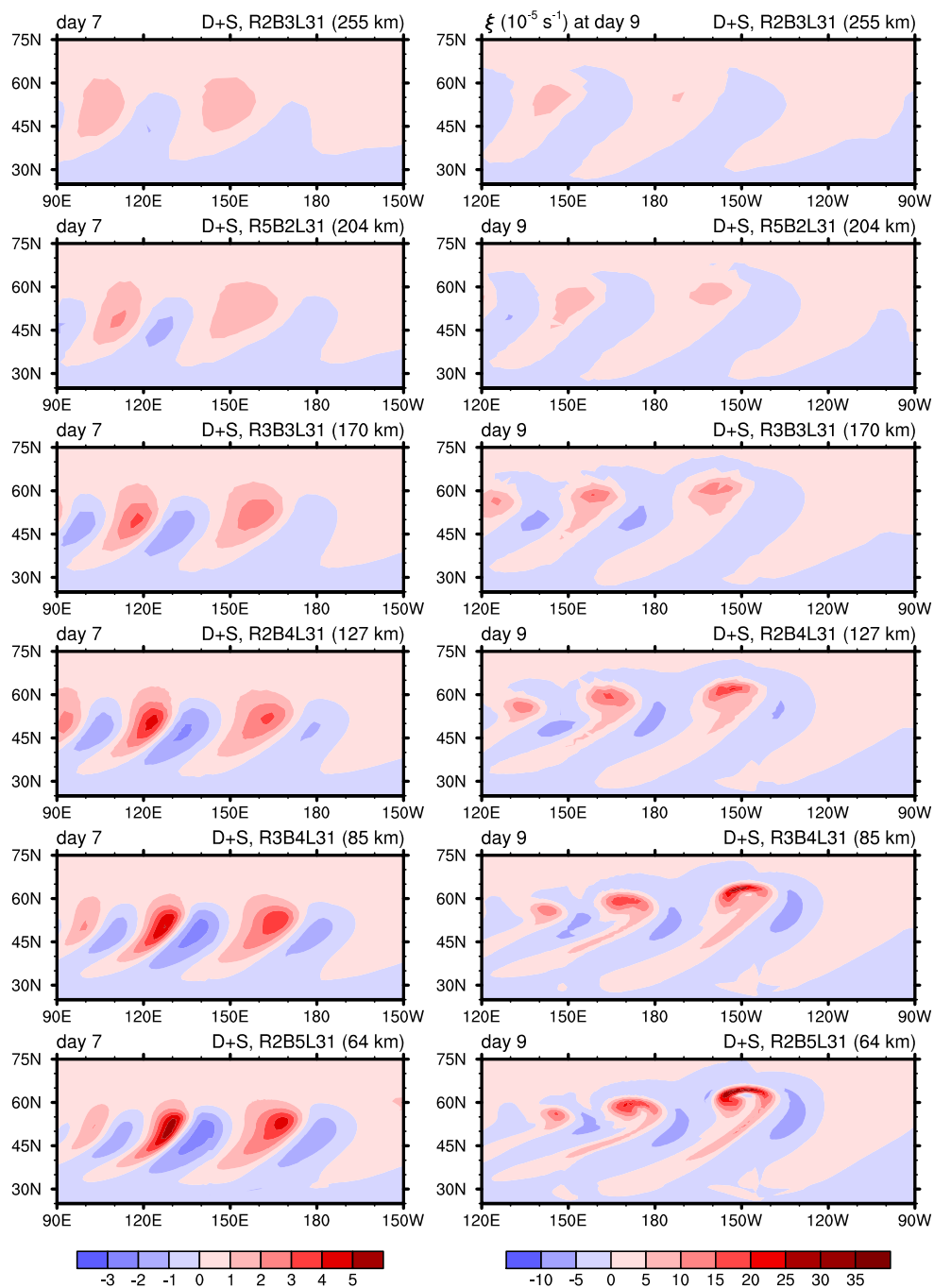


Fig. 4.27: As in Fig. 4.26 but with the ICOHDC. The choices of the divergence operator and the horizontal diffusion parameter are the same as described in Fig. 4.25.

4.5.4 Impact of the modification in the divergence operator

Now we compare the two groups of simulations performed using the original divergence operator (Eqn. (2.6)) and a modified version (Eqn. (2.54)). As already mentioned, all the results shown in Figs. 4.23, 4.25 and 4.27 are obtained with the modified operator and the horizontal diffusion parameter $\Delta t_D/\tau^* = 1$. For the integrations using the original operator, the same parameter works for resolutions up to R3B4, while for R2B5 it is necessary to increase the value to at least $4/3$ so as to avoid numerical instability.

The comparison of Figs. 4.28 – 4.29 with Figs. 4.25 and 4.27 indicates that on the whole, the two groups of experiments produce similar results. As the horizontal grid size decreases, both groups show an evident trend of convergence towards the reference solution. On the other hand, differences are still clearly detectable. In the plots of surface pressure and relative vorticity, it can be seen that at the two lowest resolutions (R2B3 and R5B2), the baroclinic waves simulated with the modified divergence operator are slightly weaker than those using the original operator; in contrast, from R2B4 on, the high and low pressure systems and the corresponding vortices become stronger than the counterparts in the group using the original operator.

A possible explanation is that the impact of the modification in the divergence operator is twofold. First, the use of a larger stencil leads to a decrease in the effective resolution; meanwhile, the modified operator has a higher order of accuracy, and does not generate grid-scale noise. The baroclinic vortices simulated in this test case have a horizontal scale of 1000 – 1500 km. A computational mesh with grid spacing larger than 200 km can only resolve the vortices in a very crude way. Within this resolution range, the effective grid size is the main factor that determines the quality of the solution. The coarsening of the effective resolution due to the smoothing in divergence plays an important role, and results in less well resolved baroclinic waves. When the grid size is decreased to 150 km or smaller, the large-scale vortices can be relatively well resolved on the computational mesh. The diffusivity of the numerical schemes now becomes a more important factor, which affects the strength of the simulated vortices. Even though the same horizontal diffusion parameter is used for both groups of simulations at most of the resolutions shown in the figures, the integrations using the original divergence operator has stronger small scale noise in the flow. A close look into the results reveals that, in this case, the damping imposed on velocity by the horizontal diffusion is significantly stronger than in the simulation which uses the modified divergence operator. The simulation performed with the original divergence operator is therefore more diffusive. This can be seen from the fact that in the bottom right panel of Fig. 4.28, the filament of warm air near 145°W is thicker than in Fig. 4.25. The positive vorticity centers at day 7 are also weaker when using the original operator (Fig. 4.29 bottom left, compared to Fig. 4.27 bottom left). At day 9 (Fig. 4.29, right column), the vortex centered at 150°W develops stronger when the resolution increases from R3B4 to R2B5, but its shape stays more or less unchanged, and the decrease of the vorticity value near the center of the vortex is not as strong as in Figs. 4.27 and 4.26. This makes this simulation more similar to the run in the same group but with lower resolution (R3B4) than compared to the higher resolution results from the spectral model.

In order to find out whether the stronger diffusivity is simply caused by increasing the

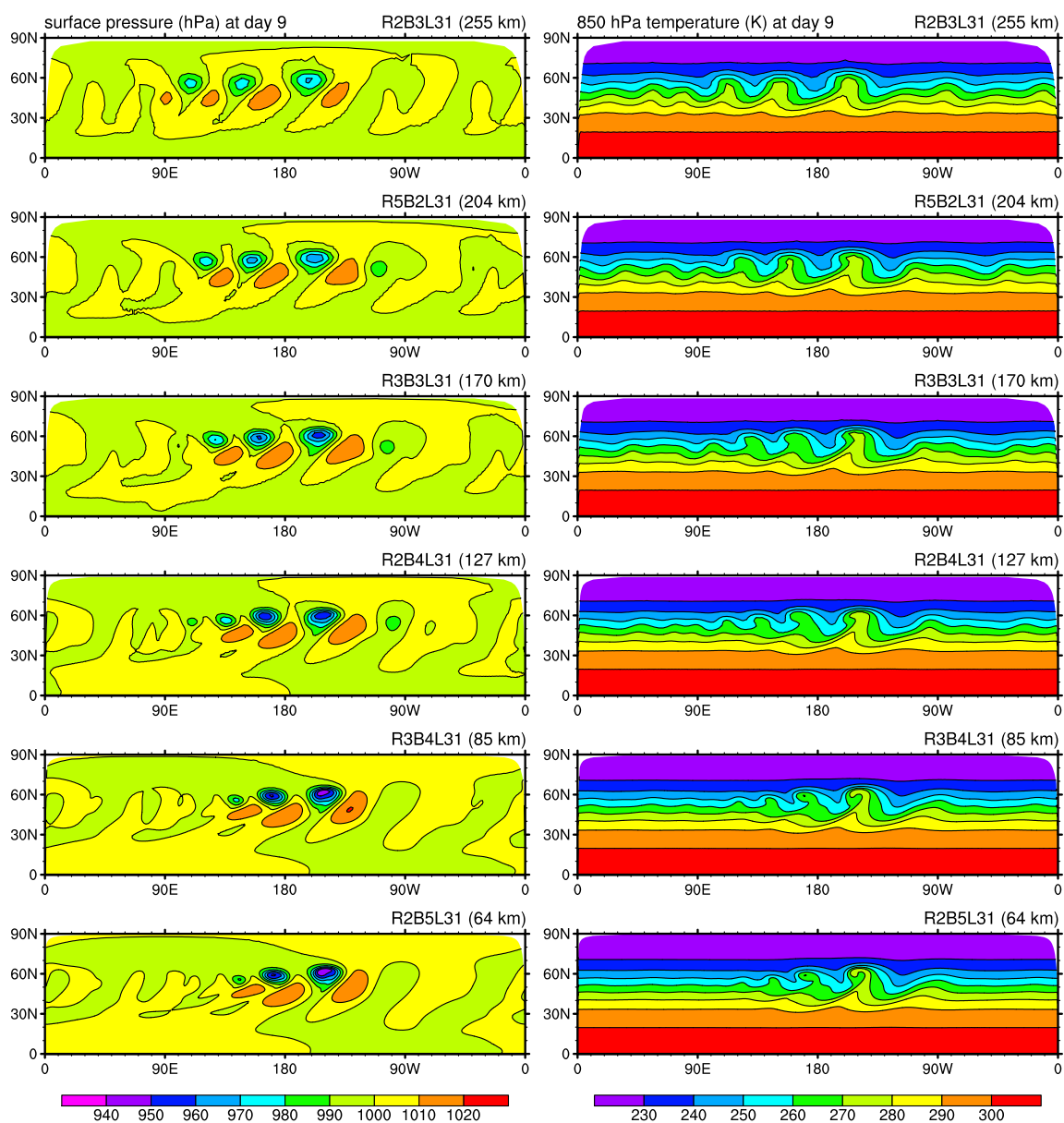


Fig. 4.28: As in Fig. 4.24 but simulated with the ICOHDC using original divergence operator (Eqn. (2.6)). The horizontal diffusion parameter $\Delta t_D/\tau^*$ is $4/3$ in the R2B5 simulation (i.e., the one with the highest resolution), and 1 in the other experiments.

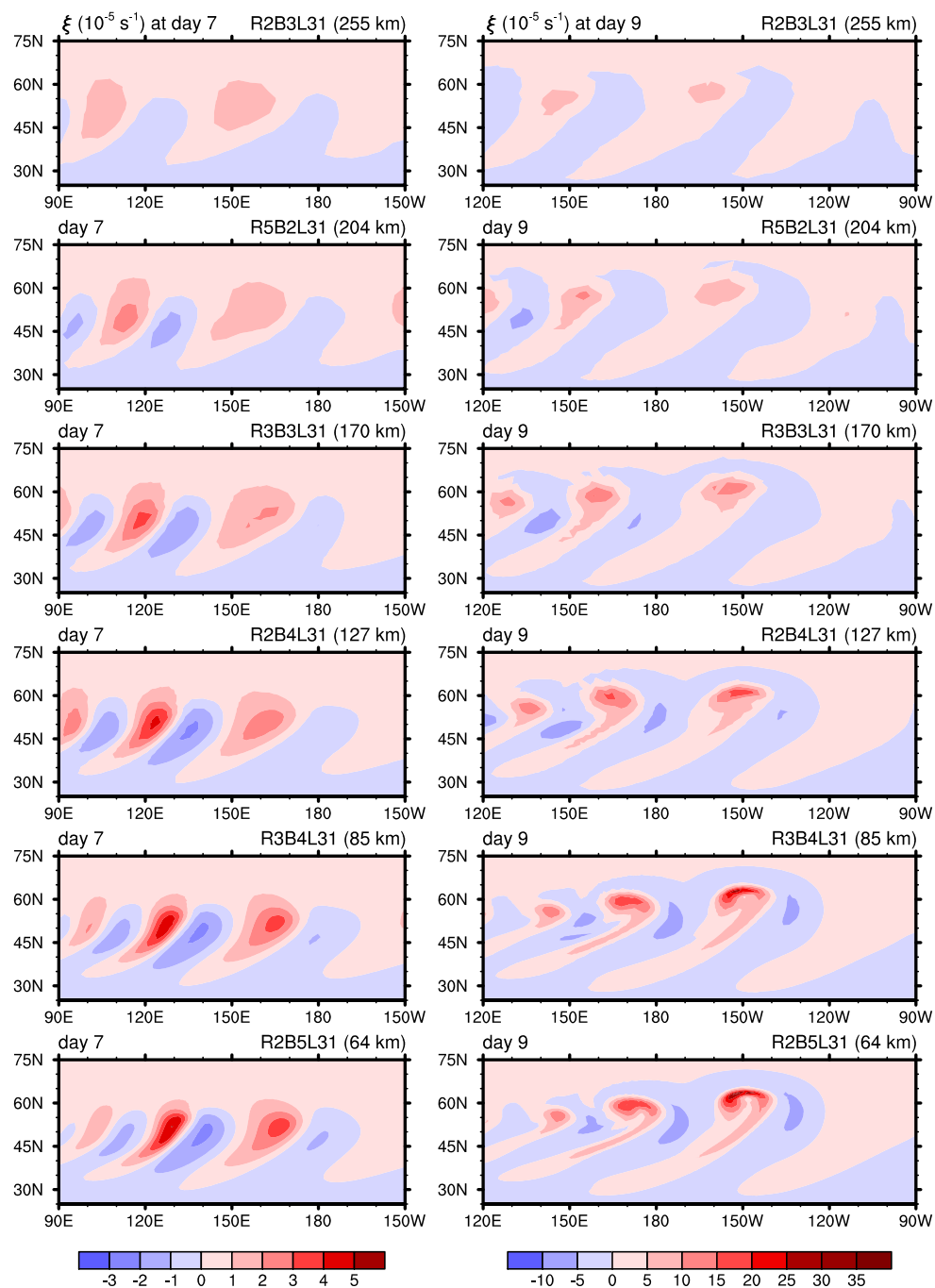


Fig. 4.29: As in Fig. 4.26 but with the ICOHDC. The choices of the divergence operator and the horizontal diffusion parameter are the same as described in Fig. 4.28.

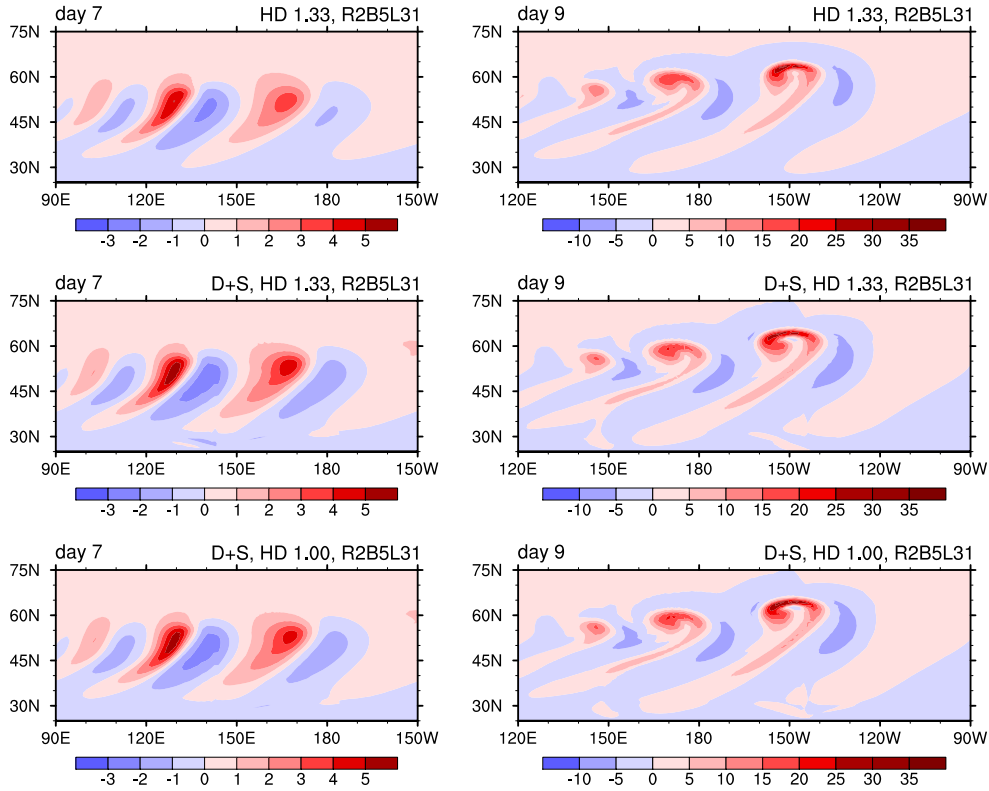


Fig. 4.30: Simulated 850 hPa relative vorticity (unit: 10^{-5} s^{-1}) at day 7 and day 9 with the ICOHDC at the R2B5L31 resolution. The first row shows results obtained using the original divergence operator and horizontal diffusion parameter $\Delta t_D/\tau^* = 4/3$; The second row corresponds to the integration using the modified divergence operator (2.54) and $\Delta t_D/\tau^* = 4/3$; The simulation displayed in the third row uses the same modified divergence operator, but $\Delta t_D/\tau^* = 1$. The first and third rows are the same as the bottom panels of Figs. 4.29 and 4.27, respectively.

diffusion parameter $\Delta t_D/\tau^*$ from 1 to $4/3$ (which is necessary for the sake of numerical stability), we performed another simulation at the same resolution (R2B5) using the modified divergence operator, but with $\Delta t_D/\tau^* = 4/3$. The results from this run are shown in the second row of Fig. 4.30. The increased diffusion coefficient does lead to a slight decrease in the strength of the vortex near 150°W at day 9 (Fig. 4.30, middle and bottom rows), but the effect is very weak, and this simulation is still clearly distinguishable from the results produced using the same diffusion coefficient but the original divergence operator (i.e., Fig. 4.30, first row).

It is true that on the whole the simulations performed with and without the divergence smoothing are similar, and even at resolution R2B5 the differences are not dramatic. However, we do see a trend of more evident differences at higher resolutions. The R2B5 simulation using the modified divergence operator seems to agree better with the reference resolution. It is possible that when the grid size is further decreased, the simulation performed using the original operator will need an even large diffusion parameter, and the difference between the two groups of experiments will become even more evident. This speculation needs to be verified in the future.

4.6 Held-Suarez test

All the numerical experiments performed in the previous sections are short-term deterministic cases, or, in other words, NWP-like tests. For climate research, the typical length of a simulation is much longer. In principle one could assess the numerical stability of the ICOHDC by extending the short experiments to, e.g., a few years of model time. However, after the first few days or months (depending on the test case chosen), the atmospheric motion will be dominated by the dissipation process, which is not a particularly challenging task from the point of view of numerical discretization. The results obtained will not be really suggestive for climate applications of the model, either.

Held and Suarez (1994, hereafter HS94) proposed a benchmark calculation in which the dry dynamical core is driven towards a quasi-equilibrium state by idealized linear forcing. The diabatic processes in the atmosphere are highly simplified, and parameterized as Newtonian relaxation of the temperature field to a prescribed zonally symmetric state. The impact of the boundary-layer processes on atmospheric circulation is represented as Rayleigh damping on the horizontal wind in the near-surface layers. The Held-Suarez test case is simple by design, but forces the dynamical core to produce tropospheric circulations that are reasonably realistic in many aspects. Since proposed, this test case has been widely applied in evaluating newly developed AGCM dynamical cores (e.g., Jablonowski, 1998; Ringler *et al.*, 2000), in assessing the convergence of numerical schemes with respect to vertical and horizontal resolution (Boer and Denis, 1997; Williamson *et al.*, 1998), as well as to help explain results obtained by full AGCMs (e.g., Pope and Stratton, 2002). In this section we carry out the Held-Suarez test with the ICOHDC and compare the results with the reference solutions provided by the dynamical core of ECHAM5.

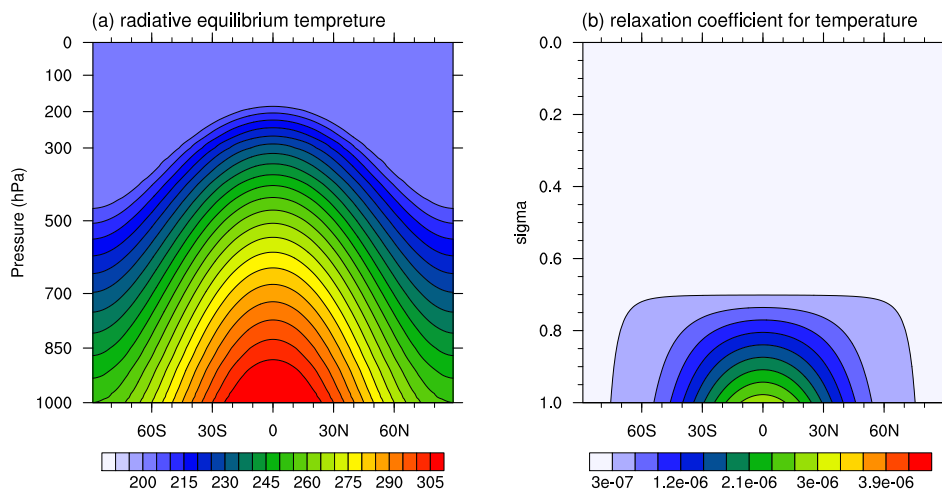


Fig. 4.31: The prescribed radiative equilibrium temperature (left, unit: K) and the temperature relaxation coefficient (right) in the Held-Suarez test.

4.6.1 Test specification

In the Held-Suarez test the dry dynamical core is integrated without topography or land-sea contrast. The forcing imposed on the atmospheric motion is specified as follows:

$$\frac{\partial \mathbf{v}}{\partial t} = \dots - k_v(\sigma) \mathbf{v}, \quad (4.34)$$

$$\frac{\partial T}{\partial t} = \dots - k_T(\varphi, \sigma) [T - T_{eq}(\varphi, p)], \quad (4.35)$$

in which

$$\sigma := p/p_s, \quad (4.36)$$

$$T_{eq} := \max \left\{ 200K, \left[315 - (\Delta T)_y \sin^2 \varphi - (\Delta \theta)_z \log \left(\frac{p}{p_0} \right) \cos^2 \varphi \right] \left(\frac{p}{p_0} \right)^\kappa \right\}, \quad (4.37)$$

$$k_T := k_a + (k_s - k_a) \max \left(0, \frac{\sigma - \sigma_b}{1 - \sigma_b} \right) \cos^4 \varphi, \quad (4.38)$$

$$k_v := k_f \max \left(0, \frac{\sigma - \sigma_b}{1 - \sigma_b} \right). \quad (4.39)$$

The constants involved are

$$\begin{aligned} k_f &:= 1 \text{ day}^{-1}, & k_a &:= 1/40 \text{ day}^{-1}, & k_s &:= 1/4 \text{ day}^{-1}, \\ \sigma_b &:= 0.7, & (\Delta T)_y &:= 60K, & (\Delta \theta)_y &:= 60K, \\ \kappa &:= \frac{R_d}{C_p} = \frac{2}{7}. \end{aligned}$$

Distributions of the radiative equilibrium temperature T_{eq} and the temperature relaxation coefficient k_T are shown in Fig. 4.31. HS94 suggested performing the integration for 1200 days and calculating long-term statistics from the last 1000 days. The statistics commonly shown in the literature include the time average of the horizontal wind and temperature, temperature variance, eddy kinetic energy, and the meridional heat and momentum fluxes caused by eddy activities. The latter three are defined as

$$\text{eddy kinetic energy} : \quad \frac{1}{2} \overline{(u')^2 + (v')^2}, \quad (4.40)$$

$$\text{eddy heat flux} : \quad \overline{v' T'}, \quad (4.41)$$

$$\text{eddy momentum flux} : \quad \overline{v' u'}, \quad (4.42)$$

respectively. In this section we use the notation $\overline{\psi}$ to denote the time average of a physical quantity ψ , and ψ' the perturbation with respect to the time average.

In the literature the Held-Suarez test case has been implemented in different ways for different purposes. Usually the proposal in HS94, namely obtaining the model climate from the last 1000 days of a 1200-day integration, is adopted, while shorter integrations are used in some other studies (e.g., Ringler *et al.*, 2000). Boer and Denis (1997) and Jablonowski (1998) subdivided one 1200-day integration to shorter periods so as to get independent realizations for their analysis.

4.6.2 Reference solution from the spectral model

In order to obtain a good understanding of this test case and provide reference solutions for the ICOHDC, a series of experiments are carried out using the dynamical core of ECHAM5. Detailed analysis of the results can be found in Wan *et al.* (2008). Here we only summarize the main findings:

- In the simulations performed following the HS94 proposal, it is observed that the main features of the idealized climate simulated by ECHAM5 are in good agreement with those shown in HS94 and many other studies. Although no analytical solution is known to the this test case, this agreement can be considered as an indication that the performance of ECHAM5 is reliable.
- Ultra-long integrations of 22000 days are performed at T42L19 and T85L31 resolutions. It is found that the internal variability of this test case leads to fluctuations at time scales as long as thousands of days. The 1000-day statistics thus have inherent variations, leading to some extent of uncertainty when these statistics are utilized to quantitatively assess the convergence property of the solutions.
- One of the main purpose of the work in Wan *et al.* (2008) was to investigate the sensitivity of the solutions produced by the dynamical core of ECHAM5 to the spatial resolution. In order to distinguish the effect of changed resolution from the fluctuations caused by the internal variability, the ensemble technique is employed in experiments at resolutions ranging from T31 to T159 with 16 to 81 vertical levels. From a practical point of view, it is computationally expensive to produce ensembles of 1200-day integrations. Since analyses indicate that the 100-day statistics can represent well the climate state in this test case, we decide to obtain an ensemble by performing 10 integrations of 300 days. Each integration starts from an isothermal state at rest, with random noise added to vorticity and divergence (which are prognostic variables of the spectral transform dynamical core). The first 200 days are discarded as spin-up phase, and the climate state is calculated over the third 100 days. Ensemble averages at different resolutions are then calculated and compared. The significance of differences between results at different resolutions is assessed by the Kolmogorov-Smirnov test (cf. Press *et al.*, 1992, 1996), the Mann-Whitney test (von Storch and Zwiers, 2001, page 117) and the Student's *t*-test (von Storch and Zwiers, 2001, pages 111 – 113). A clear trend of convergence is observed. The simulation at the T85L31 resolution is found to be a sufficiently good solution in this test case.

4.6.3 Experiments with the ICOHDC

The experience obtained in the Held-Suarez test with ECHAM5 has indicated that it is not at all straightforward to assess the convergence property of the simulated climate state. In addition, the need for ensembles further increases the demand for the CPU time. Due to technical reasons, it is not yet possible to conduct the ensemble experiments with the new dynamical core at very high resolution. In this section, results from the ICOHDC are presented only at resolutions

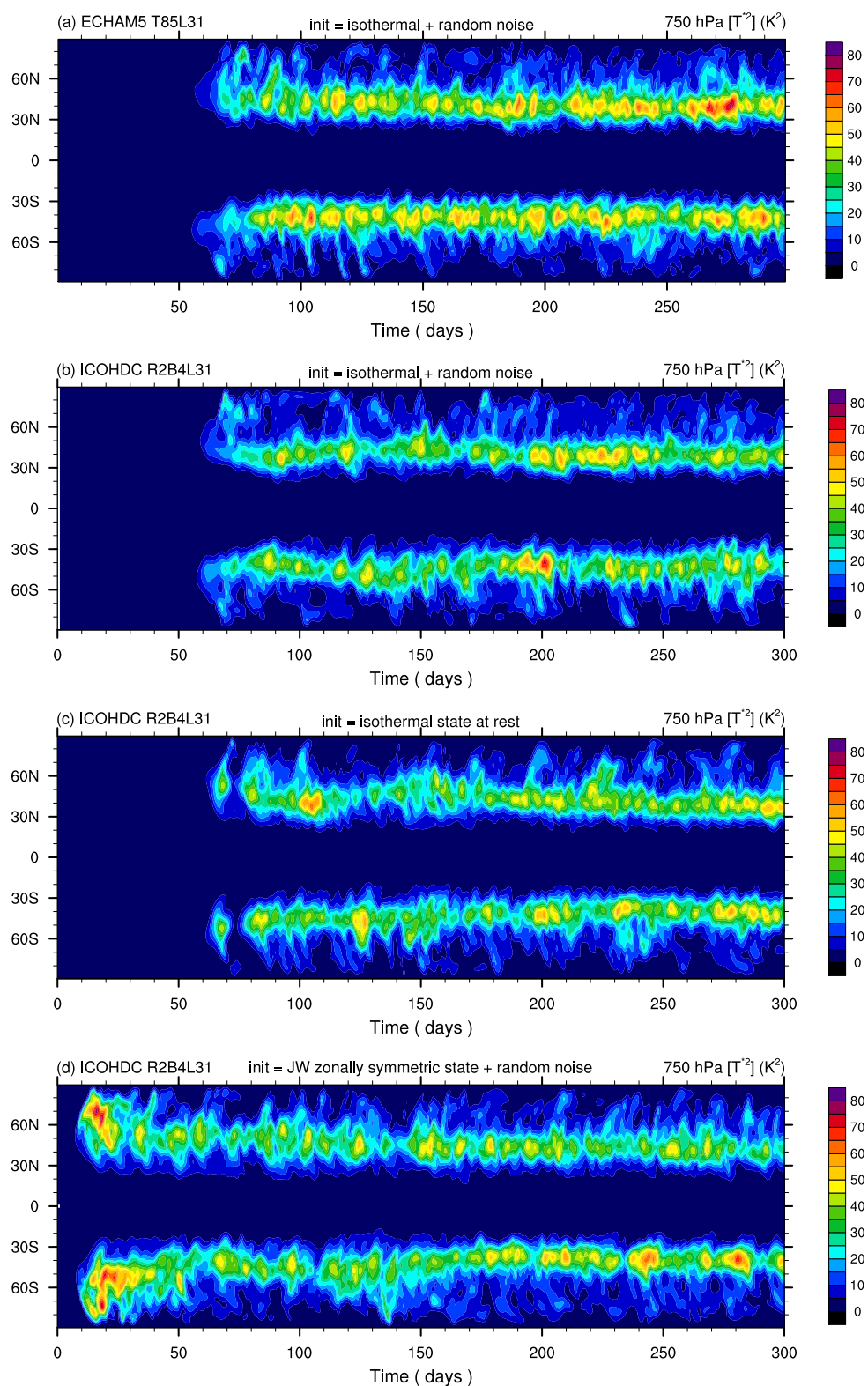


Fig. 4.32: Evolution of the atmospheric circulation in the Held-Suarez test as depicted by the zonal variance of temperature in the lower troposphere. Panel (a) shows the result produced by the spectral dynamical core of ECHAM5. (b)-(d) are simulations with the ICOHDC. The resolutions and initial conditions of the integrations are indicated in the text above each panel.

R2B3L31 and R2B4L31. We focus on a qualitative comparison of these results to the reference solution from the spectral model. The quantitative assessment of the convergence property has to be left to future work.

Similar to the ensemble experiments with ECHAM5, the integrations are initialized using an isothermal state ($T:=300$ K) at rest. Random noise within the range of $[-0.5, 0.5]$ [†] is added to the normal wind at the initial step to obtain independent realizations. The evolution of the atmospheric circulation is depicted in Fig. 4.32 by the zonal variance of temperature in the lower troposphere. Panel (a) shows one member of the T85L31 ensemble of ECHAM5, and panel (b) an example from the ICOHDC ensemble at R2B4L31. In the first 50 model days the zonal variance stays at a very low level. After day 60, the perturbations experience a dramatic amplification and the circulation transforms quickly to another regime. By day 100, a quasi-equilibrium state has been reached in all the tropospheric layers (not shown), characterized by strong eddy activity in the mid-latitudes. The transitions of the circulation simulated by the two dynamical cores are very similar.

In the Jablonowski-Williamson steady state test it has been shown that in the ICOHDC the numerical error associated with the horizontal grid and discretization schemes can trigger baroclinic instability, and lead to the breakdown of a zonally symmetric unstable initial state. In contrast, the dynamical core of ECHAM5 retains the axisymmetry of the circulation to machine precision. The same distinction is observed in the Held-Suarez test. Fig. 4.32c shows an integration with the ICOHDC without random initial perturbation. Although the atmospheric state between day 60 and day 80 is slightly different from that in panel (b), the main feature of the evolution is the same. As for the spectral dynamical core, in the absence of initial perturbation, the prescribed forcing drives the circulation into another equilibrium characterized by zonal symmetry and a Hadley cell type circulation (Fig. 4.33). Therefore for the spectral model, the random noise added to the initial conditions not only ensures the independency of the ensemble members, but also provides asymmetry in the model state, which is necessary for this model to evolve to the expected equilibrium.

The last panel in Fig. 4.32 depicts another integration with the ICOHDC, which is initialized with the zonally symmetric state of the Jablonowski-Williamson steady state test, and additional random perturbation in the wind field. Due to the unstable background, the noise grows quite fast. Before day 10 there is already significant zonal variance in temperature. Note that this time scale is similar to that observed in the Jablonowski-Williamson test. This indicates that the initial evolution of the circulation in this test case is controlled both by the prescribed forcing and by the characteristics of the background state of the model atmosphere.

In all the panels of Fig. 4.32, the simulation reaches the quasi-equilibrium within 100 model days. In order to ensure that the subsequent analysis are not affected by the spin-up period, we use the last 100 days of each simulation for calculating the statistics. Furthermore, in order to make the simulations directly comparable to the results from ECHAM5, all the physical constants, including the parameter p_0 of the hybrid vertical coordinate, are exactly the same as in ECHAM5 (cf. Tab. 4.1 on page 55).

[†]Including -0.5 but excluding 0.5, due to the inherent property of the Fortran random number generator.

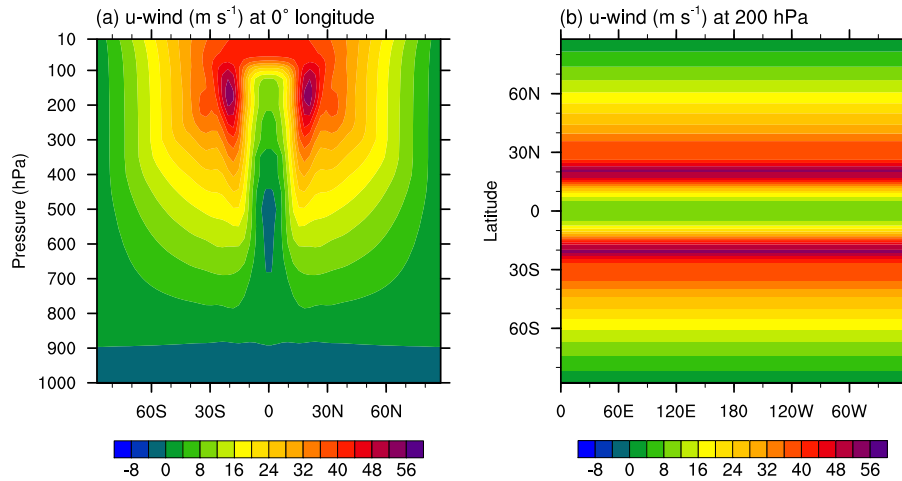


Fig. 4.33: Snapshots of the zonal wind at day 1200 in a simulation with the dynamical core of ECHAM5 starting from an isothermal state at rest. (a) pressure-latitude cross section at 0° longitude; (b) horizontal distribution at 200 hPa.

4.6.4 The simulated climate state

Fig. 4.34 shows the ensemble average of the 100-day climate simulated by the ICOHDC at R2B4L31 resolution. We first make a qualitative comparison with the reference solution from the spectral model (Fig. 4.35).

The most important dynamical mechanism in this test case is the baroclinic wave activity and the eddy-meanflow interaction. Eddy activities cause strong poleward heat transport (Fig. 4.34d), which reduces the meridional temperature gradient compared to the prescribed radiative equilibrium (cf. Fig. 4.31a). The meridional transport of the angular momentum converges in the mid-latitude regions, and forms a single westerly jet in each hemisphere (Fig. 4.34a). The core regions of the jets are located around 250 hPa. The maximum time- and zonal-mean zonal wind is about 30 m s^{-1} . Easterlies appear in the equatorial and polar lower atmosphere, as well as in the tropics near the model top. Note that in the equatorial region, the zonal wind simulated by the dynamical core of ECHAM5 shows a closed cell of easterly wind near $\eta = 0.1$. In the ICOHDC simulation the easterly wind increase all the way from $\eta = 0.2$ to the model top. This discrepancy is caused by the differences in the horizontal diffusion schemes in the two models. As already mentioned, in the ICOHDC the fourth-order hyper-Laplacian is used for all the vertical layers. In ECHAM5 the order is decreased near the model top to avoid spurious wave reflection in the full AGCM. Sensitivity experiments reveal that if the decrease of diffusion order is removed, ECHAM5 also produces strengthening easterly wind towards the upper boundary (not shown). On the other hand, the circulation in the troposphere is not affected.

The baroclinic wave activities concentrate in the middle latitudes, as depicted by the transient eddy kinetic energy and the temperature variance (Fig. 4.34e,f). The single maximum of eddy kinetic energy in each hemisphere appears at 250 hPa near 45° latitude, close to the core region of the westerly jet. Easterlies in the tropics show little variance. In each hemisphere, the maximum temperature variance appears near the Earth's surface, and extends upward and poleward. A second maximum of smaller magnitude occurs near the tropopause. These features of

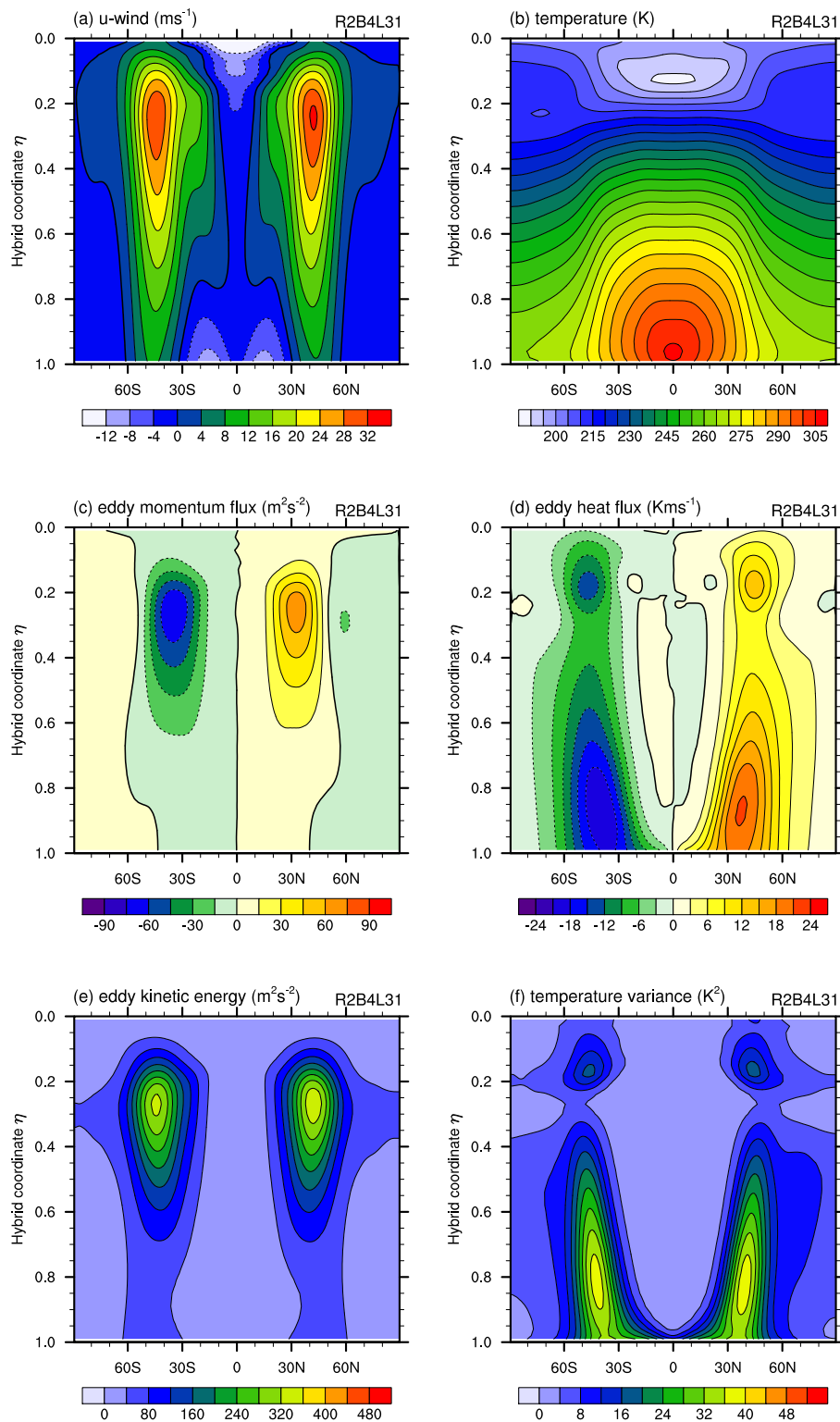


Fig. 4.34: The zonal mean climate state simulated by the ICOHDC in the Held-Suarez test at R2B4L31 resolution. The quantities shown are the ensemble means of 10 independent integrations. Each ensemble member starts from an isothermal state at rest, with random noise added to the normal wind field.

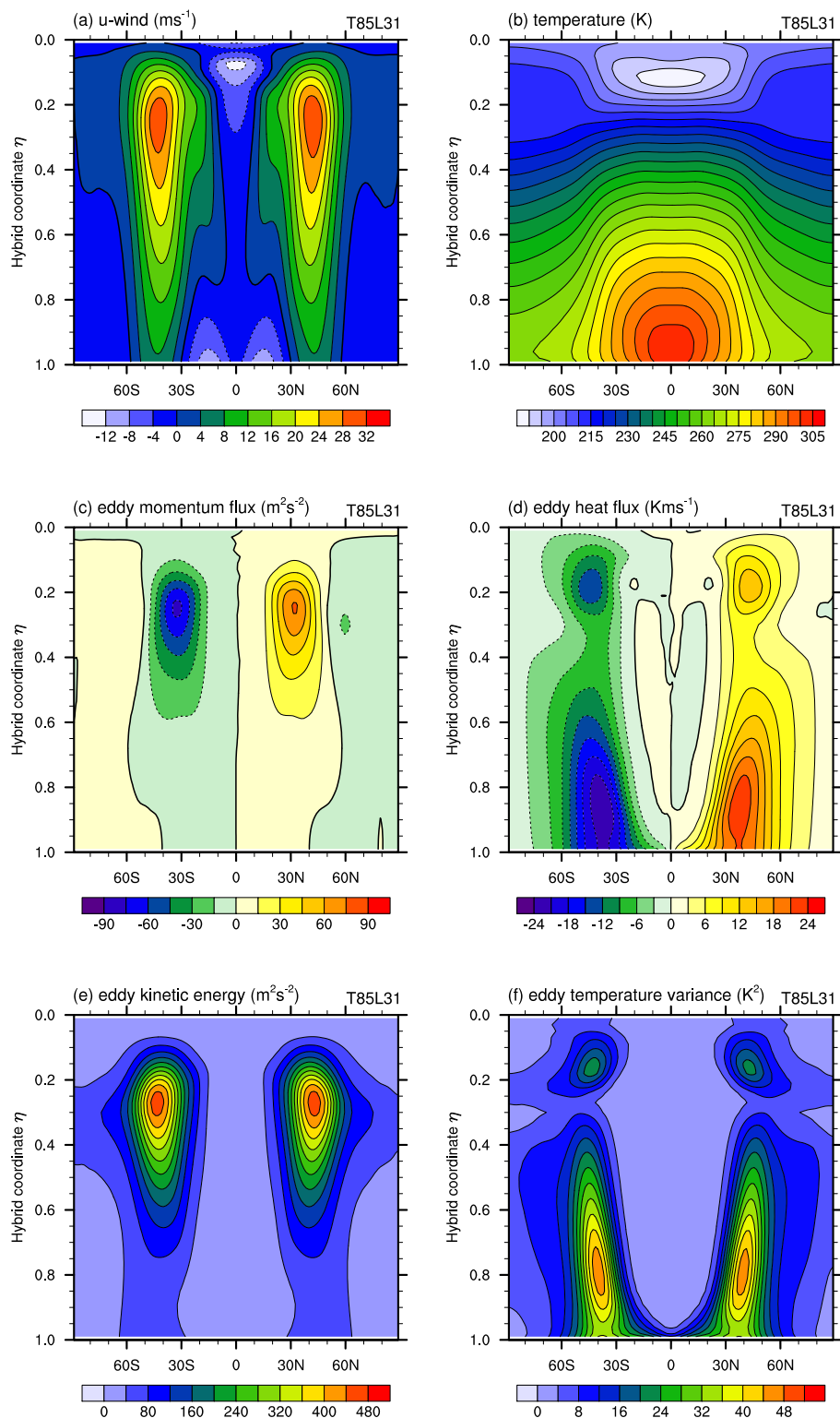


Fig. 4.35: As in Fig. 4.34 but simulated by the dynamical core of ECHAM5 at T85L31 resolution. The integrations start from an isothermal state at rest, with random noise added to vorticity and divergence.

the simulated zonal mean climate in Fig. 4.34 agree well with the reference solution in Fig. 4.35. The characteristic patterns closely resemble those simulated by ECHAM5. Meanwhile, we also see that the amplitude of the eddy kinetic energy and the temperature variance in the ICOHDC simulation (Fig. 4.34e,f) is smaller than in the ECHAM5 simulation. This point will be picked up again in the next subsection.

The results presented so far in this section are obtained using the original divergence operator. Two additional ensembles are obtained using the modified divergence operator (2.54), at resolutions R2B3L31 and R2B4L31. It turns out that at least for these two resolutions, the simulated zonal mean climate is not sensitive to the choice of the operator. Only marginal differences are observed between each pair of ensemble averages of the same resolution (not shown). These differences are not significant compared with the relatively strong internal variability in this test case.

4.6.5 Sensitivity to horizontal resolution

The differences between the two ICOHDC ensembles of different horizontal resolutions are displayed in Fig. 4.36. Both groups of experiments are performed using the original divergence operator. Roughly speaking, the increase of the horizontal resolution from R2B3 to R2B4 corresponds to a decrease of the mean grid size from about 255 km to 127 km between mass points. The eddy activities dramatically enhance with resolution (Fig. 4.36e,f), leading to stronger poleward transport of heat and angular momentum (Fig. 4.36d,c). Since these enhancements mainly happen in the middle latitudes where the baroclinic eddies are most active, the convergence zones of the momentum- and heat-flux shift poleward, resulting in a poleward displacement of the westerly jets and considerable warming at high latitudes (Fig. 4.36a,b). These changes with resolution are qualitatively the same as those observed in ECHAM5 (Fig. 4.37).

One point worth noting is that although from R2B3 to R2B4 the grid size is reduced only by one half, the resulting changes in the second-order statistics are considerably larger than those seen between the T31 and T106 ensembles from the spectral dynamical core. This indicates that the solutions given by the icosahedral model converge fast at low and medium resolutions.

Despite the qualitative similarities between the results from the two dynamical cores, there are also clear discrepancies. The most evident one is the considerably weaker eddy variances in the ICOHDC. On the one hand, in the ICOHDC simulation at R2B4 the maximum temperature variances in the lower troposphere are located near 800 hPa rather than at the Earth's surface (Fig. 4.34f). In ECHAM5 this feature is associated to resolutions T42 and higher (Wan *et al.*, 2008). On the other hand, the temperature variance and the eddy kinetic energy in the R2B4 simulation of the ICOHDC are not much stronger than the ECHAM5 result at T31, and clearly weaker than in the T42 simulation (cf. Figs. E.4 and E.5 in Appendix E). It is not yet clear what the reason is. The inherent properties of the finite difference methods employed in the icosahedral dynamical core may play a role. It should be noted that in the Jablonowski-Williamson baroclinic wave test, we see significant improvements in the ICOHDC simulations when the horizontal resolution is increased from R2B4 to R2B5. The same is probably true for the Held-Suarez test. This speculation needs to be verified in the future when the R2B5 ensemble simulations become available.

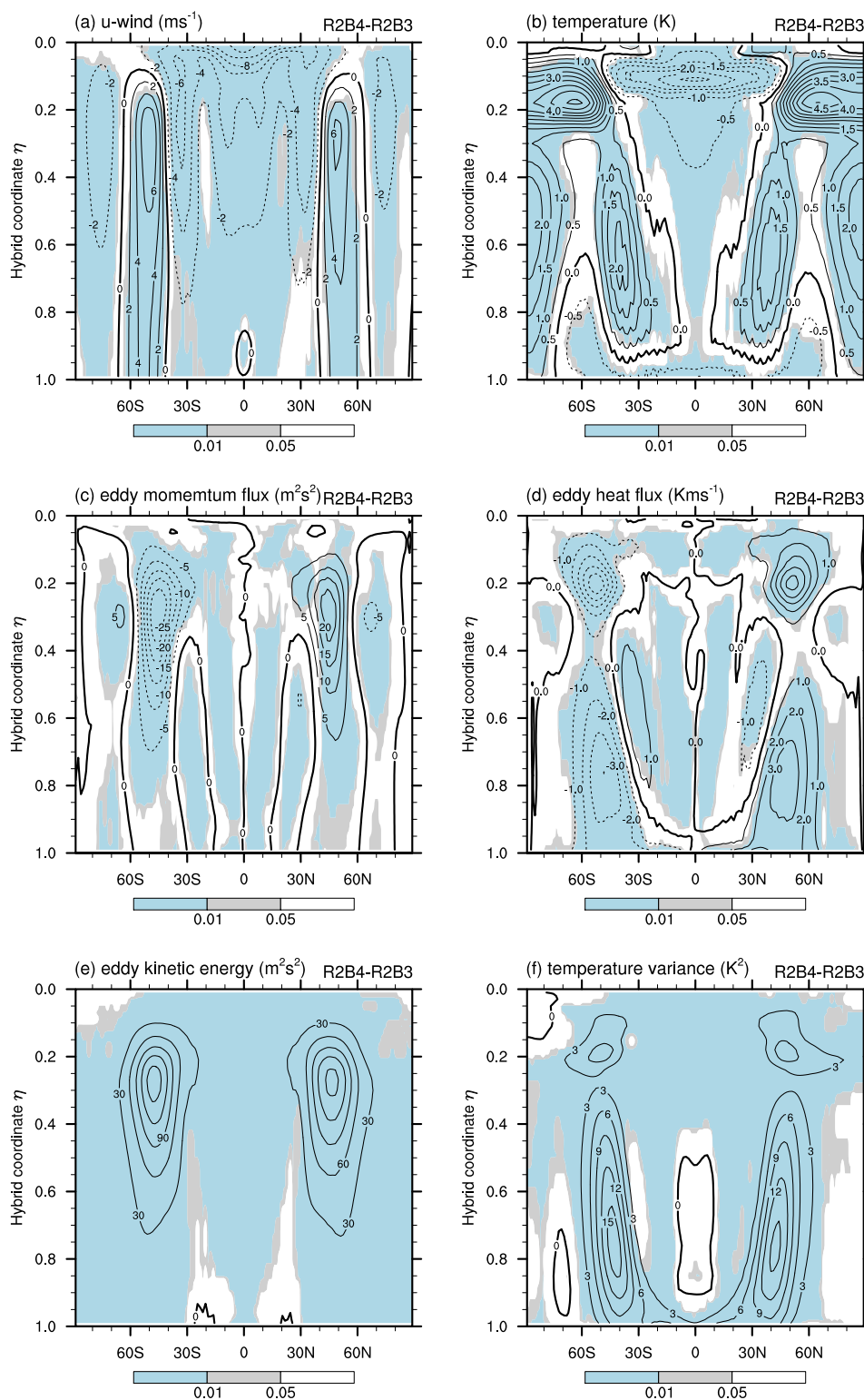


Fig. 4.36: Differences of the zonal mean climate simulated by the ICOHDC at R2B4L31 and R2B3L31 resolutions. The black contours display the differences between the ensemble means. Negative values are indicated by dashed lines. The color shading shows the regions in which the differences are judged to be statistically significant by the Kolmogorov-Smirnov test.

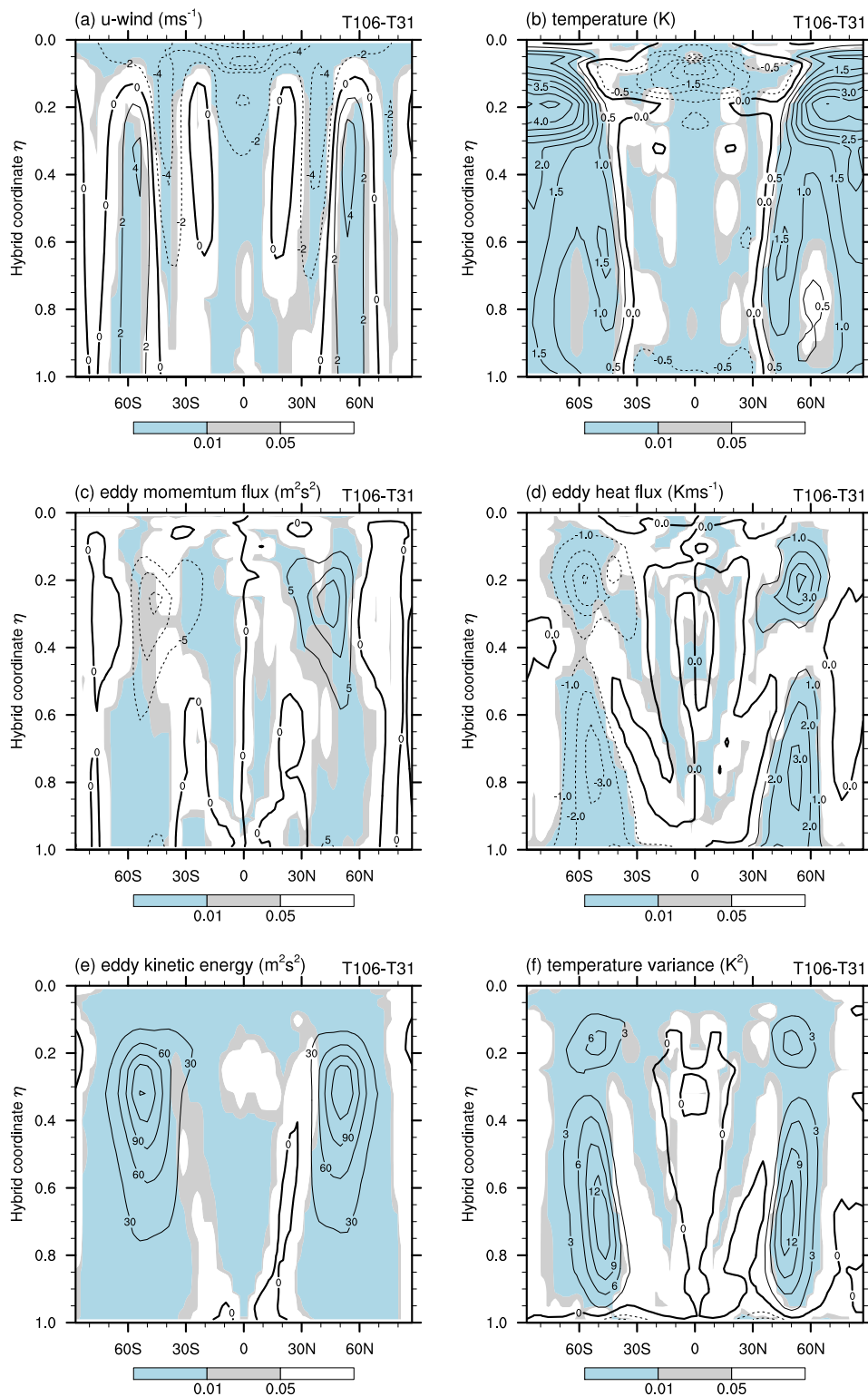


Fig. 4.37: As in Fig. 4.36 but showing the differences between the ECHAM5 simulations at T106L19 and T31L19 resolutions.

Chapter 5

Summary and outlook

5.1 Summary

In this thesis a hydrostatic atmospheric dynamical core is established on the spherical triangular grid. This work is carried out within the framework of the ICON project which was initiated by the Max Planck Institute for Meteorology and the German Weather Service with the aim of developing high-resolution new dynamical cores for climate research and numerical weather forecast. Prior to this thesis, the horizontal grid and basic differencing operators have been defined, and a two-dimensional shallow water model developed. This work takes a step forward by extending the 2D testbed to a 3D hydrostatic dynamical core, and compares its performance with the well-established spectral transform dynamical core of the ECHAM5 model. The main purpose of this work is twofold: first, to perform further testing and gain deeper understanding about the properties of the horizontal grid and differencing schemes; second, to establish a hydrostatic dynamical core of reasonable performance, which can serve as the central part of a full AGCM and be used later in climate research.

The work starts with a theoretical analysis of the truncation errors associated with the horizontal differencing operators, carried out in the context of a regular planar grid consisting of equilateral triangles. From this analysis, it is found that in contrast to the second-order accuracy of the gradient and curl operators, the discrete divergence operator – defined over a triangular cell according to the Gauss’s theorem – is only first-order accurate. The leading error changes its sign with the orientation of the triangle, causing grid-scale noise in the numerical model. This is a direct consequence of the anisotropy of the triangles and the specific scheme used for the divergence calculation.

In the ICON 2D testbed, spatial derivatives of the second and higher order (e.g., the Laplacian and hyper-Laplacian) are approximated by combining the basic operators (i.e., divergence, gradient and curl). Because of the first-order error in divergence, the approximated vector Laplacian does not converge to its continuous counterpart. The positive consequence is, when this approximated Laplacian is used in the horizontal diffusion scheme, its leading error has the effect of reducing the checkerboard noise in the divergence field. The compensation between the leading errors of two different operators is an artifact in the numerical model. In order to effectively suppress the grid-scale noise, one needs to specify a sufficiently large scaling pa-

parameter for the discrete Laplacian. The side effect is that the strength of the true diffusion is fixed at the same time. We thus no longer have the freedom of choosing the diffusion coefficient independently, for example for using weaker diffusion to avoid over-damping of the dynamically meaningful signal.

So as to remove this artifact and obtain consistent discretization schemes for the high-order derivatives, possible modifications of the discrete divergence operator are discussed. The proposed modifications can be interpreted as supplementing the original divergence operator with a four-cell smoothing, still following the principle of the Gauss's theorem. In effect the stencil of the divergence calculation is enlarged from a single triangle to four triangles. The two opposite orientations of the triangles are hence coupled together. On the regular planar grid, the modified divergence operators are second-order accurate, and meanwhile guarantee mass conservation. The Laplace operators constructed from the modified divergence operator converge to their continuous counterparts, and become also second-order accurate. On the spherical triangular grid which is not strictly regular, the proposed smoothing schemes still work well in the regions where the changes in the geometric properties of the grid cells are relatively smooth. Near the icosahedron edges, the triangles are distorted to different extents and in different directions. The discretization error caused by the deformation then stands out. We have not yet found a satisfactory algorithm that efficiently removes this deformation error and meanwhile retains the desired conservation properties.

After the truncation error analysis, the horizontal differencing operators are combined with the vertical and temporal discretization schemes of Simmons and Burridge (1981) to establish a 3D hydrostatic dynamical core. These schemes were originally designed for the latitude-longitude mesh. To use them on the triangular grid, adaptations are made. The conservation of angular momentum in Simmons and Burridge (1981) is generalized such that the vertically integrated circulation vanishes over any closed path composed of the dual edges. This property is beneficial for avoiding spurious generation of vorticity in the discrete model. Furthermore, the horizontal advection of temperature is discretized in a flux form, which guarantees the conservation of total energy.

The time integration in the ICOHDC features the leapfrog scheme with the Asselin filter, and an optional semi-implicit correction for gravity waves. The Helmholtz equation resulting from the semi-implicit treatment is solved either directly with a 3D linear solver, or first decomposed into 2D systems and then solved separately. Numerical experiments show that these two versions produce solutions of equal quality, while the 2D solver costs considerably less CPU time.

The performance of the new dynamical core is evaluated in a series of idealized experiments, in which important mechanisms of the atmospheric dynamics are simulated. Since the purpose is to test the numerical schemes employed in the dynamical core, the parameterizations of diabatic processes, such as radiative transfer, convection and cloud formation, are not included at this stage. Realistic boundary conditions such as orography and land-sea contrast are also excluded in this thesis.

The model evaluation starts from two test cases representing the barotropic dynamics of the atmosphere, namely the Rossby-Haurwitz wave and the mountain induced Rossby wave. These two experiments are 3D extensions of widely used 2D test cases which have also been used

in testing the ICON shallow water model. Considering the fact that the simulated dynamical processes are essentially nondivergent, and that the ICON shallow water model has performed well in these tests, the 3D experiments are carried out first using the original divergence operator.

The Rossby-Haurwitz wave is a conceptual model resembling the wave-like patterns constantly observed in the middle and upper troposphere. With a relatively small amplitude, the RH wavenumber 4 is expected to propagate steadily in the zonal direction without significant changes in shape and magnitude. At R2B4 resolution (i.e., 127 km grid size between neighbouring mass points), the stably propagating wave is well simulated by the ICOHDC. There is no evident deformation of the wave. The relative phase difference between the ICOHDC simulation and the reference solution from the spectral model is less than 1%.

In addition to the widely applied wavenumber 4 test case, simulations are also carried out in a dynamically unstable case, in which the wavenumber 8 breaks down within a few model days, and a westerly jet forms in each hemisphere near 30° latitude. In contrast to the general expectation that the inherent structure of the triangular grid is not particularly suitable for simulating zonal flows, the ICOHDC is able to reproduce the transformation of energy from the wave to the zonal flow. This suggests that the ICOHDC is able to correctly represent the barotropic instability which is an important mechanism in the atmospheric dynamics.

The second test case performed is the Rossby wave induced by an isolated mountain in the westerly flow, reflecting the influence of orography on the large-scale atmospheric circulation. At resolution R2B4, the ICOHDC simulation already captures the key features of the Rossby wave, although some small-scale structures caused by the nonlinearity of the atmospheric motion differ slightly from the reference solution provided by the spectral model. When the resolution is increased to R2B5 (i.e., 64 km grid size between neighbouring mass points), the ICOHDC simulation becomes hardly distinguishable from the reference solution. Convergence with respect to horizontal resolution is achieved in this test case at R2B5.

The results from the barotropic test cases indicate that the extension of the 2D testbed to a 3D model has not brought in any numerical or technical error. In the simulations of the quasi-horizontal nondivergent processes, the performance of the ICOHDC is equivalently good as the ICON shallow water model. This sounds trivial. However, from the point of view of model development, the ability of the 3D dynamical core to handle barotropic test cases provides a solid basis for more complex applications.

Using the aforementioned two test cases the modified divergence operators are also tested. The simulated surface pressure, horizontal wind and geopotential fields are similar to the experiments with the original divergence operator, while in the relative vorticity – which is a highly sensitive field – disturbances are observed. On the spherical grid, the smoothing applied to divergence removes the checkerboard noise, whilst the numerical errors related to the deformation of the triangle cells remain and stand out. These errors are fixed to certain locations, thus introduce continuous forcing on the large scale flow. On the one hand, this indicates that further improvement in the divergence calculation on the irregular grid is probably beneficial. On the other hand, in realistic weather forecast and climate simulations, all kinds of disturbances introduced by the complex surface conditions and subgrid-scale processes are probably much stronger, and thus will overwhelm the deformation errors in the discrete divergence operator. In

fact, in the idealized baroclinic tests that are performed subsequently, the icosahedron corners already become almost invisible in the simulated atmospheric state.

The baroclinic test cases carried out in this thesis include two deterministic experiments and one idealized climate simulation. In the Jablonowski-Williamson steady state test, it is observed that the ICOHDC can not retain the strict zonal symmetry of a flow for a long time if the flow is dynamically unstable. Given the inherent properties of the horizontal grid and the discretization schemes, this result is fully consistent with expectation. The barotropically and baroclinically unstable nature of the prescribed zonal state is a key point in this test case. In the realistic climate simulations and operational weather forecast, such an axisymmetric unstable state can not occur on the global scale or persist long in the existence of the strongly non-zonal external forcings.

The evolution of a large-scale perturbation in an unstable flow is simulated in the Jablonowski-Williamson baroclinic wave test, which eventually leads to the formation of cyclone-like structures. Integrations with the ICOHDC are performed at various resolutions so as to investigate the sensitivity of the numerical solutions to the horizontal grid size. It is found that the R2B2 grid, with typically 510 km spacing between mass points and 880 km between vorticity points, is not sufficient for simulating the synoptic-scale vortices. As the resolution increases, results given by the ICOHDC improve significantly. A clear trend of convergence is observed. At the R2B5 resolution (i.e., 64 km grid size between mass points), the performance of the ICOHDC becomes clearly comparable to the spectral transform dynamical core of the ECHAM5 model. The life cycle of the baroclinic vortices is correctly represented. The sharp gradient in temperature, and the shape, strength and phase speed of the vortices are all well simulated.

In these two tests it is also noticed that the use of the modified divergence operators is beneficial. In the steady state test, the degradation of the zonal flow is slower, suggesting that the numerical errors are of smaller magnitude; In the baroclinic wave test, although the smoothing applied to the divergence leads to a slight decrease of the effective resolution, the reduction of numerical noise shows positive effect in medium- and high-resolution simulations. The integrations performed with the smoothing tend to be more stable and less diffusive.

As a supplement to the deterministic experiments, idealized climate simulations are carried out following the proposal by Held and Suarez (1994). The ensemble technique is employed so as to facilitate the quantitative assessment of the convergence of the numerical solutions. Forced by prescribed linear forcing, the model atmosphere reaches a quasi-realistic equilibrium state. Already at the R2B3 (255 km) and R2B4 (157 km) resolutions, the ICOHDC can reasonably represent the key features of the idealized climate. The simulated strength and location of the westerly jets, as well as the characteristic patterns of the meridional heat and momentum transport, agree well with the reference solution from the spectral dynamical core and the published results from other models. In addition, the ICOHDC integrations have not displayed any numerical stability problem in the idealized climate simulation.

The highlights of the work presented in this thesis are summarized as follows:

- A new hydrostatic atmospheric dynamical core has been established. Although some other modelling groups have also employed icosahedral grids in their AGCMs, the ICOHDC is unique in that the discretization schemes are constructed on the staggered triangular grid

which is an analog of the widely used Arakawa C-grid. The new dynamical core has now reached a mature state. It has demonstrated encouraging performance in the idealized experiments, and forms a good basis for a full AGCM. The ICOHDC was presented and run at the NCAR ASP 2008 Summer Colloquium on Numerical Techniques for Global Atmospheric Models.

- The truncation error analysis performed during this study has provided a deeper insight of the properties of the horizontal grid and discrete operators, which were defined for the ICON development before this study. This analysis not only has helped in understanding the behaviours of the 2D ICON shallow water model and the ICOHDC, but also provides useful information for further work, for example the development of nonhydrostatic models.
- Regarding the idealized experiments, this work has proposed a clear specification of the 3D Rossby-Haurwitz wave test. Although the Rossby-Haurwitz wavenumber 4 has already been widely applied as a benchmark test for 2D models, the 3D extension was not formally defined in the literature, and inaccuracies exist in some earlier publications. In this work the choices of the formulation, the related parameters and the reasoning behind them are explicitly stated. This proposal has been adopted by Jablonowski *et al.* (2008) and used in the NCAR ASP 2008 Summer Colloquium. Furthermore, the breakdown of the Rossby-Haurwitz wave of wavenumber 8 is used for the first time as a test case in the evaluation of 3D dynamical cores.
- During the numerical experiments, the inherent properties of the Held-Suarez test have been investigated in detail. The internal variability is analyzed, and the ensemble technique is proposed which reduces the uncertainty associated with the assessment of the convergence properties of the numerical solutions. This makes a contribution to the understanding and application of the Held-Suarez test in general.

5.2 Outlook

Due to the technical status of the source code and the current limitations in the computational resources, the idealized experiments with the new dynamical core are performed only up to resolution R2B5 in the deterministic test cases, and R2B4 in the Held-Suarez test. This seems sufficient for the barotropic tests, since convergence has clearly been achieved. For the baroclinic tests, however, it will be useful to perform simulations at higher resolutions.

For the Jablonowski-Williamson baroclinic wave test, experience with the ECHAM5 model shows that the convergence with respect to horizontal resolution is achieved at T85, in the sense that the differences between the T85 solution and the reference one have fallen below the estimated uncertainty limit. The results presented in this thesis indicate that the ICOHDC simulations at R2B5 are of similar quality to the T106 result from ECHAM5. By inference, the R2B5 results probably have also converged. To verify this, we will need to perform an ICOHDC simulation at R2B6 (32 km) or R2B7 (16 km) resolution, and calculate the difference norms according to the suggestions by Jablonowski and Williamson (2006a,b). A further prerequisite

for this convergence assessment is a high-accuracy algorithm for interpolating scalar variables from the ICON grid at one resolution to another, or from the ICON grids to latitude-longitude grids. The radial basis functions (RBFs) are probably a good choice.

In the Held-Suarez test, it has been noticed that the R2B3 and R2B4 simulations from the ICOHDC have weaker eddy activities than the T85 results from the spectral model. One possible explanation is that the ICOHDC simulations have not yet converged at such resolutions. Given that the increase of the resolution from R2B3 to R2B4 has led to significant improvement in the results, we expect further enhanced eddy activities at higher resolutions. Experiments at resolutions R2B5 and R2B6 are planned.

Regarding the numerical schemes, we have proposed some modifications for the horizontal discretization, so as to get rid of the checkerboard noise in divergence, and to obtain consistent discretization schemes for the high-order spatial derivatives. The proposed smoothing schemes work very well on regular grids, but suffer from the irregularity of the spherical grid which is most pronounced near the edges and vertices of the icosahedron. In the barotropic test cases, the modified divergence operators have introduced undesirable disturbances to the numerical solutions. One may thus wonder whether these modifications make sense at all. Two points are worth mentioning here:

First, in our experiments it is clear that as the test cases get more complex, the detrimental effect of the modified operator decreases and eventually disappears. In fact the degradation of the results only appears in the cases when the atmospheric flow is essentially nondivergent. In the baroclinic test cases, the unwanted disturbances are not evident. In the Jablonowski-Williamson vortex test – which is the most relevant case for the mid-latitude weather and climate – we do see that as the resolution increases, the integrations performed with the modified divergence operator tend to be more stable and less diffusive. It is natural to speculate that when the grid size is further reduced, the benefit of using the modified operator will become more evident. We plan to verify this point when simulations at higher resolutions become available.

Second, the numerical experiments performed in this thesis have by no means covered all the important dynamical processes in the atmosphere. The eventual aim of developing a new dynamical core is to use it in more realistic climate simulations and in the operational weather forecast. In such applications, atmospheric motions appear on a wide spectrum of spatial and temporal scales, and interact strongly with each other. Many diabatic processes, e.g., the cumulus convection, are directly connected to the divergent component of the atmospheric flow. It is not yet known how the original divergence operator and the modified versions will behave in such situations.

The next development step will be the coupling of the ICOHDC with physics parameterizations. The resulting new AGCM will be tested at typical time scales and spatial resolutions of realistic and quasi-realistic climate simulations and weather forecast. Further evaluation of the numerical schemes will be carried out in the context of sophisticated physical forcing. These experiments will also provide first experiences in realistic model applications.

Appendix A

The primitive equations: assumptions and conservation properties

The first decision to make in the process of building up an atmospheric general circulation model is the form of the equations that determine the atmospheric motions. The Eulerian representation of fluid flow is considered here, which means observing the fluid at fixed positions. We start from an inertial coordinate system and make the following basic assumptions:

1. The atmosphere can be viewed as a continuous fluid and ideal gas;
2. There is no external source or sink of mass.

Applying Newton's second law of motion and the first law of thermodynamics to the atmosphere, we can derive the governing equations as

$$\frac{\hat{D}\mathbf{v}_3}{Dt} = -\frac{1}{\rho}\hat{\nabla}_3 p + \mathbf{g}^* + \mathbf{F}_v \quad (\text{A.1})$$

$$C_v \frac{\hat{D}T}{Dt} + p \frac{\hat{D}\alpha}{Dt} = F_h + F_d \quad (\text{A.2})$$

$$\frac{\hat{D}\rho}{Dt} + \rho \hat{\nabla}_3 \cdot \mathbf{v}_3 = 0 \quad (\text{A.3})$$

$$p = \rho RT . \quad (\text{A.4})$$

The symbols used in these equations are explained in Table A.1. The terrestrial gravitation \mathbf{g}^* is given by

$$\mathbf{g}^* = \frac{GM}{d^3} \mathbf{d} \quad (\text{A.5})$$

in which G and M are the universal gravitational constant and the mass of the Earth, respectively. \mathbf{d} is the distance vector pointing to the Earth's centre.

As the second step, we set up a global spherical coordinate fixed to the Earth. At each location in this system, a local spherical coordinate is also established, with the z -axis aligned

Tab. A.1: List of symbols used in the governing equations of the atmosphere.

symbol	quantity	unit
$\frac{\hat{D}}{\hat{D}t}$	material derivative in inertial coordinate	s^{-1}
$\hat{\nabla}_3$	3D spatial derivative in inertial coordinate	m^{-1}
∇	2D horizontal derivative along the tangent plane of the sphere	m^{-1}
η	hybrid vertical coordinate	-
\mathbf{k}	unit vector pointing upward	-
\mathbf{v}_3	3D velocity vector	$m s^{-1}$
\mathbf{v}	2D velocity vector in the tangent plane of the sphere	$m s^{-1}$
K	kinetic energy per unit mass ($K := \frac{1}{2}\mathbf{v}\cdot\mathbf{v}$)	$m^2 s^{-2}$
ξ	vertical component of relative vorticity ($\xi := \mathbf{k}\cdot(\nabla\times\mathbf{v})$)	s^{-1}
$\dot{\eta}$	vertical velocity in the η -coordinate	s^{-1}
T	temperature	K
T_v	virtual temperature	K
p	pressure	Pa
p_s	pressure at the Earth's surface	Pa
ϕ	geopotential	$m^2 s^{-2}$
ρ	density	$kg m^{-3}$
f	Coriolis coefficient ($f := 2\Omega \sin \varphi$. φ is latitude.)	s^{-1}
α_ρ	specific volume ($\alpha_\rho := 1/\rho$)	$m^3 kg^{-1}$
C_v	specific heat capacity at constant volume	$J kg^{-1} K^{-1}$
C_p	specific heat capacity of dry air under constant pressure	$J kg^{-1} K^{-1}$
R	gas constant of air (i.e. the universal gas constant divided by the molar mass of air)	$J kg^{-1} K^{-1}$
R_d	gas constant of dry air	$J kg^{-1} K^{-1}$
\mathbf{g}^*	terrestrial gravitation	$kg m s^{-2}$
\mathbf{F}_v	force of friction per unit mass	$kg m s^{-2}$
F_h	heating rate	$J kg^{-1} K^{-1} s^{-1}$
F_d	dissipation rate	$J kg^{-1} K^{-1} s^{-1}$

with the outgoing radial direction of the global coordinate (defined as "upward"). Furthermore, we assume

1. The only motion of the Earth that renders it an accelerated reference body is the rotation about its polar axis. This rotation has a constant angular velocity Ω determined by the sidereal day.
2. The apparent vertical direction, as revealed by a plumb-line at rest with respect to the Earth, coincides with the z -axis of the local spherical coordinate.
3. The atmosphere is a shallow fluid. The characteristic scale of its vertical dimension is far less than its horizontal scale and the Earth's mean radius.
4. The atmosphere is a hydrostatic fluid. The vertical component of the pressure gradient force is balanced by the apparent gravity force. The latter is defined as the composite of the terrestrial gravitation and the centrifugal force caused by the Earth's rotation.
5. Magnitude of the gravitational acceleration \mathbf{g} can be used as a constant.
6. We consider the atmosphere as nonviscous. The friction terms are ignored.

Use a generic pressure-based terrain-following coordinate $\eta(p, p_s)$ in the vertical direction, where η is a monotonic function of pressure p , and depends also on the surface pressure p_s in such a way that

$$\eta(0, p_s) = 0 \quad \text{and} \quad \eta(p_s, p_s) = 1$$

With all the assumptions above, the differential form of the governing equations of the atmosphere can be derived following Kasahara (1974) as:

$$\frac{\partial \mathbf{v}}{\partial t} = -(f + \xi) \mathbf{k} \times \mathbf{v} - \nabla K - \dot{\eta} \frac{\partial \mathbf{v}}{\partial \eta} - \frac{R_d T_v}{p} \nabla p - \nabla \phi \quad (\text{A.6})$$

$$\frac{\partial T}{\partial t} = -\mathbf{v} \cdot \nabla T - \dot{\eta} \frac{\partial T}{\partial \eta} + \frac{R_d T_v}{C_p} \frac{dp}{dt} \quad (\text{A.7})$$

$$\frac{\partial}{\partial t} \left(\frac{\partial p}{\partial \eta} \right) = -\nabla \cdot \left(\mathbf{v} \frac{\partial p}{\partial \eta} \right) - \frac{\partial}{\partial \eta} \left(\dot{\eta} \frac{\partial p}{\partial \eta} \right) \quad (\text{A.8})$$

$$0 = \frac{\partial \phi}{\partial \eta} + \frac{R_d T_v}{p} \frac{\partial p}{\partial \eta}. \quad (\text{A.9})$$

The newly introduced symbols are also listed in Table A.1. This set of equations are usually referred to as the primitive equations in the area of atmospheric dynamics.

By integrating the continuity equation (A.8) using the boundary conditions $\dot{\eta} = 0$ at $\eta = 0$ and $\eta = 1$, the following expressions can be obtained:

$$\frac{\partial p_s}{\partial t} = - \int_0^1 \nabla \cdot \left(\mathbf{v} \frac{\partial p}{\partial \eta} \right) d\eta \quad (\text{A.10})$$

$$\dot{\eta} \frac{\partial p}{\partial \eta} = - \int_0^\eta \nabla \cdot \left(\mathbf{v} \frac{\partial p}{\partial \eta} \right) d\eta - \frac{\partial p}{\partial t} \quad (\text{A.11})$$

(A.6)-(A.11) are the equations that are numerically solved by the dynamical core discussed in this thesis.

The hydrostatic governing equations (1.3)-(1.6) have the following conservation properties:

Conservation of total energy

The kinetic energy equation and potential energy equation can be derived from the momentum, thermodynamic, and hydrostatic equations as

$$\frac{\partial}{\partial t} \left(K \frac{\partial p}{\partial \eta} \right) + \nabla \cdot \left(\vec{V} K \frac{\partial p}{\partial \eta} \right) + \frac{\partial}{\partial \eta} \left(\dot{\eta} K \frac{\partial p}{\partial \eta} \right) = \vec{V} \cdot \left(-\frac{R_d T}{p} \nabla p - \nabla \phi \right) \frac{\partial p}{\partial \eta} \quad (\text{A.12})$$

and

$$\frac{\partial}{\partial t} \left(C_p T \frac{\partial p}{\partial \eta} \right) + \nabla \cdot \left(\vec{V} C_p T \frac{\partial p}{\partial \eta} \right) + \frac{\partial}{\partial \eta} \left(\dot{\eta} C_p T \frac{\partial p}{\partial \eta} \right) = \frac{R_d T}{p} \left(\vec{V} \cdot \nabla p + \frac{\partial p}{\partial t} + \dot{\eta} \frac{\partial p}{\partial \eta} \right) \frac{\partial p}{\partial \eta}. \quad (\text{A.13})$$

The spatial flux divergence terms on the l.h.s. of (A.12) and (A.13) lead to redistribution of kinetic and potential energy at different locations. They vanish when the global integral is taken. The r.h.s. terms cause conversion of energy between different forms.

Manipulation of the r.h.s. of (A.13) gives

$$\begin{aligned} \frac{\partial p}{\partial \eta} \frac{R_d T}{p} \left(\frac{\partial p}{\partial t} + \dot{\eta} \frac{\partial p}{\partial \eta} \right) &= -\frac{\partial \phi}{\partial \eta} \left(\frac{\partial p}{\partial t} + \dot{\eta} \frac{\partial p}{\partial \eta} \right) \\ &= -\frac{\partial}{\partial \eta} \left[\phi \left(\frac{\partial p}{\partial t} + \dot{\eta} \frac{\partial p}{\partial \eta} \right) \right] + \phi \frac{\partial}{\partial \eta} \left(\frac{\partial p}{\partial t} + \dot{\eta} \frac{\partial p}{\partial \eta} \right) \\ &= -\frac{\partial}{\partial \eta} \left[\phi \left(\frac{\partial p}{\partial t} + \dot{\eta} \frac{\partial p}{\partial \eta} \right) \right] - \phi \nabla \cdot \left(\frac{\partial p}{\partial \eta} \vec{V} \right) \end{aligned} \quad (\text{A.14})$$

Combine (A.12), (A.13) and (A.14) and take the vertical and global integral, it can be proven that

$$\frac{d}{dt} \left\{ \int_A \frac{1}{g} \left[\phi_s p_s + \int_0^1 (K + C_p T) \frac{\partial p}{\partial \eta} d\eta \right] dA \right\} = 0 \quad (\text{A.15})$$

which is the conservation of total energy of the atmosphere.

Conservation of the angular momentum

The pressure gradient force can be re-written as

$$-\nabla_\eta \phi + \frac{\partial \phi}{\partial p} \nabla_\eta p = -\frac{1}{\frac{\partial p}{\partial \eta}} \left[(\nabla_\eta \phi) \frac{\partial p}{\partial \eta} - \frac{\partial \phi}{\partial \eta} \nabla_\eta p \right] \quad (\text{A.16})$$

$$= -\frac{1}{\frac{\partial p}{\partial \eta}} \left[\nabla_\eta \left(\phi \frac{\partial p}{\partial \eta} \right) - \frac{\partial}{\partial \eta} (\phi \nabla_\eta p) \right] \quad (\text{A.17})$$

$$= \frac{1}{\frac{\partial p}{\partial \eta}} \left[\nabla_\eta \left(p \frac{\partial \phi}{\partial \eta} \right) - \frac{\partial}{\partial \eta} (p \nabla_\eta \phi) \right] \quad (\text{A.18})$$

Under the assumption that the upper boundary of the vertical coordinate η has constant pressure, the mass-weighted vertical integral of expressions (A.17) and (A.18) gives

$$\int_{\eta_S}^{\eta_T} \left(-\nabla_\eta \phi + \frac{\partial \phi}{\partial p} \nabla_\eta p \right) \frac{\partial p}{\partial \eta} d\eta = -\nabla_\eta \left(\int_{\eta_S}^{\eta_T} \phi \frac{\partial p}{\partial \eta} d\eta \right) + \phi_S \nabla_\eta p_S \quad (\text{A.19})$$

$$= \nabla_\eta \left(\int_{\eta_S}^{\eta_T} p \frac{\partial \phi}{\partial \eta} d\eta + p_T \phi_T \right) - p_S \nabla_\eta \phi_S \quad (\text{A.20})$$

The first terms on the right-hand-side of (A.19) and (A.20) are gradient vectors. The line integral of the tangential component along an arbitrary closed curve on the sphere vanishes. When the line integral is taken around a latitude circle, we get the conservation of the angular momentum in the absence of mountain torque.

Appendix B

Derivation of the truncation error of the horizontal differencing operators

B.1 Taylor expansion of the edge average

Consider a segment of a line on the x - y plane that can be described by parametric equations as

$$\begin{cases} x = x(s) := \alpha_x s + \beta_x \\ y = y(s) := \alpha_y s + \beta_y \end{cases}, \quad s \in (s_a, s_b). \quad (\text{B.1})$$

with $\alpha_x, \alpha_y, \beta_x$ and β_y being constants. For a generic differentiable function ψ , its average over the segment can be expressed using the Taylor expansion as

$$\begin{aligned} \bar{\psi}^e &= \frac{1}{s_b - s_a} \int_{s_a}^{s_b} \psi [x(s), y(s)] ds \\ &= \frac{1}{s_b - s_a} \int_{s_a}^{s_b} \left[\psi_o + \left(\frac{\partial \psi}{\partial s} \right)_o s + \left(\frac{\partial^2 \psi}{\partial s^2} \right)_o \frac{s^2}{2} + \left(\frac{\partial^3 \psi}{\partial s^3} \right)_o \frac{s^3}{6} + \left(\frac{\partial^4 \psi}{\partial s^4} \right)_o \frac{s^4}{24} + \mathcal{O}(s^5) \right] ds \\ &= \psi_o + \left(\frac{\partial \psi}{\partial s} \right)_o \frac{s_b + s_a}{2} + \left(\frac{\partial^2 \psi}{\partial s^2} \right)_o \frac{s_b^3 - s_a^3}{6(s_b - s_a)} + \left(\frac{\partial^3 \psi}{\partial s^3} \right)_o \frac{s_b^4 - s_a^4}{24(s_b - s_a)} + \left(\frac{\partial^4 \psi}{\partial s^4} \right)_o \frac{s_b^5 - s_a^5}{120(s_b - s_a)} \\ &\quad + \mathcal{O}[(s_b - s_a)^5], \end{aligned}$$

in which the subscript o denotes the reference point $s=0$.

Assume the length of the segment is l , i.e. $s_b - s_a = l$. If the reference point coincides with s_a , we have

$$\bar{\psi}^e = \psi_a + \frac{l}{2} \left(\frac{\partial \psi}{\partial s} \right)_a + \frac{l^2}{6} \left(\frac{\partial^2 \psi}{\partial s^2} \right)_a + \frac{l^3}{24} \left(\frac{\partial^3 \psi}{\partial s^3} \right)_a + \frac{l^4}{120} \left(\frac{\partial^4 \psi}{\partial s^4} \right)_a + \mathcal{O}(l^5). \quad (\text{B.2})$$

When the midpoint of the segment is taken as the reference point, we get

$$\bar{\psi}^e = \psi_o + \frac{l^2}{24} \left(\frac{\partial^2 \psi}{\partial s^2} \right)_o + \frac{l^4}{1920} \left(\frac{\partial^4 \psi}{\partial s^4} \right)_o + \mathcal{O}(l^6). \quad (\text{B.3})$$

The directional derivatives in Eqns. (B.2) and (B.3) can be calculated according to the chain rule of differentiation by using the following formula:

$$\frac{\partial^m \varrho}{\partial s^m} = \left(\alpha_x \frac{\partial}{\partial x} + \alpha_y \frac{\partial}{\partial y} \right)^m \varrho. \quad (\text{B.4})$$

B.2 Truncation error of the normal gradient operator

The normal gradient of a scalar function is defined at the midpoint of a triangle edge, calculated by taking the difference of the scalar values associated to the two neighbouring mass points (O_1 and O_2 in Fig. B.1), and then dividing by the distance between the two cell centers. In the planar grid considered in this section, if the values at the mass points are viewed as pointwise evaluation of the considered scalar function, the normal gradient operator is nothing else than a simple central difference, and thus a second-order approximation to the pointwise value of the true derivative at the velocity point:

$$\text{grad}_n(\varrho)_o = \left(\frac{\partial \varrho}{\partial n} \right)_o + \frac{l^2}{72} \left(\frac{\partial^3 \varrho}{\partial n^3} \right)_o + \mathcal{O}(l^4). \quad (\text{B.5})$$

If one takes the viewpoint that the normal gradient operates on the average of ϱ over the triangles, the order of accuracy can be obtained by first applying Eqn. (2.24) to the two neighbouring triangles and then substituting for the corresponding symbols in Eqn. (2.8). This yields

$$\begin{aligned} \text{grad}_n(\overline{\varrho}^i)_o &= \frac{\sqrt{3}}{l} \left\{ (\varrho_{o_2} - \varrho_{o_1}) + \frac{l^2}{48} \left[(\nabla^2 \varrho)_{o_2} - (\nabla^2 \varrho)_{o_1} \right] - (-1)^{\delta_{o_2}} \frac{\sqrt{3} l^3}{720} \left[G(\varrho)_{o_2} + G(\varrho)_{o_1} \right] \right. \\ &\quad \left. + \frac{l^4}{5760} \left[(\nabla^4 \varrho)_{o_2} - (\nabla^4 \varrho)_{o_1} \right] + \mathcal{O}(l^5) \right\}, \end{aligned}$$

in which the function G is the same as in Eqn. (2.25). Expanding the evaluations at O_1 and O_2 about the point O and using the relationships

$$\frac{\partial}{\partial x} = \frac{\partial}{\partial \tau}, \quad \frac{\partial}{\partial y} = -\frac{\partial}{\partial n}$$

we obtain

$$\text{grad}_n(\overline{\varrho}^i)_o = \left(\frac{\partial \varrho}{\partial n} \right)_o + \frac{l^2}{80} \left(\frac{\partial^3 \varrho}{\partial \tau^2 \partial n} + 3 \frac{\partial^3 \varrho}{\partial n^3} \right)_o + \mathcal{O}(l^4). \quad (\text{B.6})$$

This indicates that when applied to cell averages, the normal gradient operator is also second order if the aim is to approximate the pointwise derivative. Furthermore, from Eqn. (2.23) we

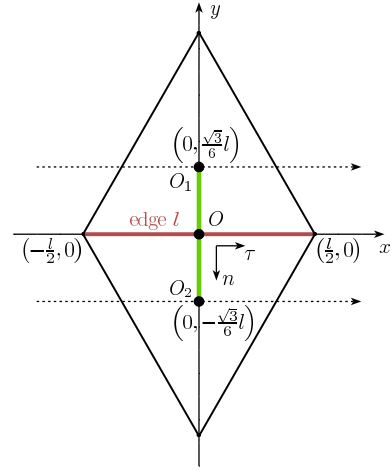


Fig. B.1: Stencil of the normal gradient operator.

have

$$\overline{\left(\frac{\partial \rho}{\partial n}\right)}^e = \left(\frac{\partial \rho}{\partial n}\right)_o + \frac{l^2}{24} \left(\frac{\partial^3 \rho}{\partial \tau^2 n}\right)_o + \mathcal{O}(l^4). \quad (\text{B.7})$$

Thus when approximating the edge average, the normal gradient calculated from cell averages is also second-order.

B.3 Truncation error of the curl operator

The discrete curl operator (2.7) (page 15) is defined at triangle vertices which coincide with the center of the dual hexagonal cells. It operates on the edge-based normal component of a vector field. For compactness of the formulation, use the symbol ξ to denote the relative vorticity $\mathbf{k} \cdot (\nabla \times \mathbf{v})$.

When the operand is a pointwise value

If the operand has a pointwise nature, it can be directly expanded as the Taylor series with respect to the dual cell center, yielding

$$\text{curl}(\mathbf{v}) = \xi_o + \frac{l^2}{32} (\nabla^2 \xi)_o + \mathcal{O}(l^4). \quad (\text{B.8})$$

According to Eqn. (2.26) the analytical solution of the relative vorticity averaged over the dual cell can be expressed as

$$\overline{\overline{\xi}}^\varkappa = \xi_o + \frac{5l^2}{144} (\nabla^2 \xi)_o + \mathcal{O}(l^4). \quad (\text{B.9})$$

Comparing Eqn.(B.8) and (B.9) reveals that the former is a second-order approximation both to the pointwise value at triangle vertices and to the average over the dual cells.

When the operand is the averaged normal velocity

Now we derive the truncation error of the discrete curl in the case that the operand is the average of a vector field over triangle edges.

For the stencil depicted in Fig. 2.6, the six primal edges sharing vertex \varkappa can be expressed with parametric equations in Tab. B.1, in which $s = 0$ correspond to the vertex \varkappa and $s = l$ corresponds to the other end of each edge. The truncation error of the curl operator can be derived via the following steps:

1. Calculate the average of vector \mathbf{v} over a generic primal edge l associated to vertex \varkappa . According to Eqn. (B.2),

$$\overline{\mathbf{v}}^e = \mathbf{v}_o + \frac{l}{2} \left(\frac{\partial \mathbf{v}}{\partial s}\right)_o + \frac{l^2}{6} \left(\frac{\partial^2 \mathbf{v}}{\partial s^2}\right)_o + \frac{l^3}{24} \left(\frac{\partial^3 \mathbf{v}}{\partial s^3}\right)_o + \mathcal{O}(l^4). \quad (\text{B.10})$$

2. Apply (B.10) to all six primal edges and use the directional derivatives listed in Tab. B.1 to get

$$\begin{aligned}\bar{\mathbf{v}}^{l_1} &= \mathbf{v}_o + \frac{l}{4} \left(\frac{\partial \mathbf{v}}{\partial x} - \sqrt{3} \frac{\partial \mathbf{v}}{\partial y} \right)_o + \frac{l^2}{24} \left(\frac{\partial^2 \mathbf{v}}{\partial x^2} - 2\sqrt{3} \frac{\partial^2 \mathbf{v}}{\partial x \partial y} + 3 \frac{\partial^2 \mathbf{v}}{\partial y^2} \right)_o \\ &\quad + \frac{l^3}{192} \left(\frac{\partial^3 \mathbf{v}}{\partial x^3} - 3\sqrt{3} \frac{\partial^3 \mathbf{v}}{\partial x^2 \partial y} + 9 \frac{\partial^3 \mathbf{v}}{\partial x \partial y^2} - 3\sqrt{3} \frac{\partial^3 \mathbf{v}}{\partial y^3} \right)_o + \mathcal{O}(l^4)\end{aligned}\quad (\text{B.11})$$

$$\bar{\mathbf{v}}^{l_2} = \mathbf{v}_o + \frac{l}{2} \left(\frac{\partial \mathbf{v}}{\partial x} \right)_o + \frac{l^2}{6} \left(\frac{\partial^2 \mathbf{v}}{\partial x^2} \right)_o + \frac{l^3}{24} \left(\frac{\partial^3 \mathbf{v}}{\partial x^3} \right)_o + \mathcal{O}(l^4)\quad (\text{B.12})$$

$$\begin{aligned}\bar{\mathbf{v}}^{l_3} &= \mathbf{v}_o + \frac{l}{4} \left(\frac{\partial \mathbf{v}}{\partial x} + \sqrt{3} \frac{\partial \mathbf{v}}{\partial y} \right)_o + \frac{l^2}{24} \left(\frac{\partial^2 \mathbf{v}}{\partial x^2} + 2\sqrt{3} \frac{\partial^2 \mathbf{v}}{\partial x \partial y} + 3 \frac{\partial^2 \mathbf{v}}{\partial y^2} \right)_o \\ &\quad + \frac{l^3}{192} \left(\frac{\partial^3 \mathbf{v}}{\partial x^3} + 3\sqrt{3} \frac{\partial^3 \mathbf{v}}{\partial x^2 \partial y} + 9 \frac{\partial^3 \mathbf{v}}{\partial x \partial y^2} + 3\sqrt{3} \frac{\partial^3 \mathbf{v}}{\partial y^3} \right)_o + \mathcal{O}(l^4)\end{aligned}\quad (\text{B.13})$$

$$\begin{aligned}\bar{\mathbf{v}}^{l_4} &= \mathbf{v}_o + \frac{l}{4} \left(-\frac{\partial \mathbf{v}}{\partial x} + \sqrt{3} \frac{\partial \mathbf{v}}{\partial y} \right)_o + \frac{l^2}{24} \left(\frac{\partial^2 \mathbf{v}}{\partial x^2} - 2\sqrt{3} \frac{\partial^2 \mathbf{v}}{\partial x \partial y} + 3 \frac{\partial^2 \mathbf{v}}{\partial y^2} \right)_o \\ &\quad + \frac{l^3}{192} \left(-\frac{\partial^3 \mathbf{v}}{\partial x^3} + 3\sqrt{3} \frac{\partial^3 \mathbf{v}}{\partial x^2 \partial y} - 9 \frac{\partial^3 \mathbf{v}}{\partial x \partial y^2} + 3\sqrt{3} \frac{\partial^3 \mathbf{v}}{\partial y^3} \right)_o + \mathcal{O}(l^4)\end{aligned}\quad (\text{B.14})$$

$$\bar{\mathbf{v}}^{l_5} = \mathbf{v}_o - \frac{l}{2} \left(\frac{\partial \mathbf{v}}{\partial x} \right)_o + \frac{l^2}{6} \left(\frac{\partial^2 \mathbf{v}}{\partial x^2} \right)_o - \frac{l^3}{24} \left(\frac{\partial^3 \mathbf{v}}{\partial x^3} \right)_o + \mathcal{O}(l^4)\quad (\text{B.15})$$

$$\begin{aligned}\bar{\mathbf{v}}^{l_6} &= \mathbf{v}_o + \frac{l}{4} \left(-\frac{\partial \mathbf{v}}{\partial x} - \sqrt{3} \frac{\partial \mathbf{v}}{\partial y} \right)_o + \frac{l^2}{24} \left(\frac{\partial^2 \mathbf{v}}{\partial x^2} + 2\sqrt{3} \frac{\partial^2 \mathbf{v}}{\partial x \partial y} + 3 \frac{\partial^2 \mathbf{v}}{\partial y^2} \right)_o \\ &\quad + \frac{l^3}{192} \left(-\frac{\partial^3 \mathbf{v}}{\partial x^3} - 3\sqrt{3} \frac{\partial^3 \mathbf{v}}{\partial x^2 \partial y} - 9 \frac{\partial^3 \mathbf{v}}{\partial x \partial y^2} - 3\sqrt{3} \frac{\partial^3 \mathbf{v}}{\partial y^3} \right)_o + \mathcal{O}(l^4)\end{aligned}\quad (\text{B.16})$$

3. Calculate the component of $\bar{\mathbf{v}}^e$ that is tangential to the dual edge \hat{l} and points to the counterclockwise direction of the boundary of the dual cell \varkappa :

$$\bar{\mathbf{v}}^{l_j} \cdot \mathbf{t}_{\varkappa, \hat{l}_j} \quad (j = 1, \dots, 6).$$

The value of $\mathbf{t}_{\varkappa, \hat{l}}$ at each edge is labeled in Fig. 2.6 on page 18.

4. Compute the summation

$$\left(\frac{\sqrt{3}}{2} l^2 \right)^{-1} \frac{l}{\sqrt{3}} \sum_{j=1}^6 \bar{\mathbf{v}}^{l_j} \cdot \mathbf{t}_{\varkappa, \hat{l}_j}.$$

It turns out that because of the symmetry of the hexagon, all the zeroth- and second-order terms in (B.11) – (B.16) cancel out, finally resulting in

$$\text{curl}(\bar{\mathbf{v}}^e) = \xi_o + \frac{l^2}{16} (\nabla^2 \xi)_o + \mathcal{O}(l^4). \quad (\text{B.17})$$

Tab. B.1: The parametric equations and directional derivatives of the primal edges in Fig. 2.6 on page 18. Here ψ can be either a scalar function or a vector field. s ranges from 0 at \varkappa (the vertex shared by all the six primal edges in Fig. 2.6) to l at the other end of each edge.

primal edge	parametric equations	directional derivative		
		first-order	second-order	third-order
l_1	$x = \frac{s}{2}, y = -\frac{\sqrt{3}}{2}s$	$\frac{\partial\psi}{\partial s} = \frac{1}{2}\frac{\partial\psi}{\partial x} - \frac{\sqrt{3}}{2}\frac{\partial\psi}{\partial y}$	$\frac{\partial^2\psi}{\partial s^2} = \frac{1}{4}\left(\frac{\partial^2\psi}{\partial x^2} - 2\sqrt{3}\frac{\partial^2\psi}{\partial x\partial y} + 3\frac{\partial^2\psi}{\partial y^2}\right)$	$\frac{\partial^3\psi}{\partial s^3} = \frac{1}{8}\left(\frac{\partial^3\psi}{\partial x^3} - 3\sqrt{3}\frac{\partial^3\psi}{\partial x^2\partial y} + 9\frac{\partial^3\psi}{\partial x\partial y^2} - 3\sqrt{3}\frac{\partial^3\psi}{\partial y^3}\right)$
l_2	$x = s, y = 0$	$\frac{\partial\psi}{\partial s} = \frac{\partial\psi}{\partial x}$	$\frac{\partial^2\psi}{\partial s^2} = \frac{\partial^2\psi}{\partial x^2}$	$\frac{\partial^3\psi}{\partial s^3} = \frac{\partial^3\psi}{\partial x^3}$
l_3	$x = \frac{s}{2}, y = \frac{\sqrt{3}}{2}s$	$\frac{\partial\psi}{\partial s} = \frac{1}{2}\frac{\partial\psi}{\partial x} + \frac{\sqrt{3}}{2}\frac{\partial\psi}{\partial y}$	$\frac{\partial^2\psi}{\partial s^2} = \frac{1}{4}\left(\frac{\partial^2\psi}{\partial x^2} + 2\sqrt{3}\frac{\partial^2\psi}{\partial x\partial y} + 3\frac{\partial^2\psi}{\partial y^2}\right)$	$\frac{\partial^3\psi}{\partial s^3} = \frac{1}{8}\left(\frac{\partial^3\psi}{\partial x^3} + 3\sqrt{3}\frac{\partial^3\psi}{\partial x^2\partial y} + 9\frac{\partial^3\psi}{\partial x\partial y^2} + 3\sqrt{3}\frac{\partial^3\psi}{\partial y^3}\right)$
l_4	$x = -\frac{s}{2}, y = \frac{\sqrt{3}}{2}s$	$\frac{\partial\psi}{\partial s} = -\frac{1}{2}\frac{\partial\psi}{\partial x} + \frac{\sqrt{3}}{2}\frac{\partial\psi}{\partial y}$	$\frac{\partial^2\psi}{\partial s^2} = \frac{1}{4}\left(\frac{\partial^2\psi}{\partial x^2} - 2\sqrt{3}\frac{\partial^2\psi}{\partial x\partial y} + 3\frac{\partial^2\psi}{\partial y^2}\right)$	$\frac{\partial^3\psi}{\partial s^3} = \frac{1}{8}\left(-\frac{\partial^3\psi}{\partial x^3} + 3\sqrt{3}\frac{\partial^3\psi}{\partial x^2\partial y} - 9\frac{\partial^3\psi}{\partial x\partial y^2} + 3\sqrt{3}\frac{\partial^3\psi}{\partial y^3}\right)$
l_5	$x = -s, y = 0$	$\frac{\partial\psi}{\partial s} = -\frac{\partial\psi}{\partial x}$	$\frac{\partial^2\psi}{\partial s^2} = \frac{\partial^2\psi}{\partial x^2}$	$\frac{\partial^3\psi}{\partial s^3} = -\frac{\partial^3\psi}{\partial x^3}$
l_6	$x = -\frac{s}{2}, y = -\frac{\sqrt{3}}{2}s$	$\frac{\partial\psi}{\partial s} = -\frac{1}{2}\frac{\partial\psi}{\partial x} - \frac{\sqrt{3}}{2}\frac{\partial\psi}{\partial y}$	$\frac{\partial^2\psi}{\partial s^2} = \frac{1}{4}\left(\frac{\partial^2\psi}{\partial x^2} + 2\sqrt{3}\frac{\partial^2\psi}{\partial x\partial y} + 3\frac{\partial^2\psi}{\partial y^2}\right)$	$\frac{\partial^3\psi}{\partial s^3} = \frac{1}{8}\left(-\frac{\partial^3\psi}{\partial x^3} - 3\sqrt{3}\frac{\partial^3\psi}{\partial x^2\partial y} - 9\frac{\partial^3\psi}{\partial x\partial y^2} - 3\sqrt{3}\frac{\partial^3\psi}{\partial y^3}\right)$

Equations (B.8), (B.9) and (B.17) reveal that, although there exist different possible interpretations, the curl operator defined by Eqn. (2.7) on page 15 is always second-order accurate on a uniform planar grid.

B.4 Truncation error of the divergence operator

The divergence operator defined by formula (2.6) is a direct application of the Gauss's theorem in the two-dimensional case. When the quantity v_{n_i} in the summation symbol in Eqn. (2.6) represents accurately the flux through the corresponding triangle edge, or in other words, the normal component of the vector in formula (2.6) represents the average normal velocity along the edge, this formula gives the accurate average divergence over the triangular cell. Moreover, using Eqn. (2.24) on page 19, the average divergence can be expressed as

$$\overline{\overline{D}}^i = D_o + \frac{l^2}{48} (\nabla^2 D)_o + \mathcal{O}(l^3) \quad \text{with} \quad D := \nabla \cdot \mathbf{v} , \quad (\text{B.18})$$

indicating that the cell average is a second-order approximation to the pointwise value at the center of the triangle.

On the other hand, one can assume that the quantity v_{n_i} represents the pointwise value of the normal velocity component at the edge centers. For the stencil depicted by Fig. 2.5 on page 18, this means

$$\mathbf{v}_{l_1} = \mathbf{v} \left(0, -(-1)^\delta \frac{\sqrt{3}}{6} l \right), \quad \mathbf{v}_{l_2} = \mathbf{v} \left(\frac{l}{4}, (-1)^\delta \frac{\sqrt{3}}{12} l \right), \quad \mathbf{v}_{l_3} = \mathbf{v} \left(-\frac{l}{4}, (-1)^\delta \frac{\sqrt{3}}{12} l \right)$$

Direct Taylor expansion with respect to the triangle center yields

$$\begin{aligned} \operatorname{div}(\mathbf{v})_i &= \left(\frac{\sqrt{3}l^2}{4} \right)^{-1} l \sum_{j=1}^3 \mathbf{v}_{l_j} \cdot \mathbf{n}_j \\ &= D_o + (-1)^\delta l H(\mathbf{v})_o + \frac{l^2}{96} (\nabla^2 D)_o + (-1)^\delta l^3 F(\mathbf{v})_o + \mathcal{O}(l^4) , \end{aligned} \quad (\text{B.19})$$

in which

$$H(\mathbf{v}) := \frac{\sqrt{3}}{24} \left(2 \frac{\partial^2 u}{\partial x \partial y} + \frac{\partial^2 v}{\partial x^2} - \frac{\partial^2 v}{\partial y^2} \right) , \quad (\text{B.20})$$

$$F(\mathbf{v}) := \frac{\sqrt{3}}{2^9 3^3} \left(12 \frac{\partial^4 u}{\partial x^3 \partial y} + 2 \frac{\partial^4 u}{\partial x \partial y^3} + 3 \frac{\partial^4 v}{\partial x^4} + 6 \frac{\partial^4 v}{\partial x^2 \partial y^2} - 5 \frac{\partial^4 v}{\partial y^4} \right) . \quad (\text{B.21})$$

Expression (B.19) is clearly a first-order approximation both to the pointwise divergence at the triangle center and to the cell average (see Eqn. (B.18)).

Eqn. (B.19) can also be interpreted in another way with the average viewpoint for the operand. Note that according to Eqn. (2.23), the midpoint value at an edge is a second-order approximation to the edge average, therefore Eqn. (B.19) can also be understood as when the flux through the edges is approximated to the second-order, the divergence operator (2.6) gives a first-order approximation to the average divergence over triangles.

Now consider a more general case by assuming the average velocity along triangle edges are numerically approximated to m -th order ($m > 0$) and used as the operand of the divergence operator. Consider again the stencil depicted in Fig. 2.4. Using Eqn. (B.3) in Section B.1, we assume the approximated average velocity can be expressed using the Taylor series about the midpoint (denoted by o_l) as

$$\bar{\mathbf{v}}_d^e = \bar{\mathbf{v}}^e + \gamma l^m \left(\alpha_x \frac{\partial}{\partial x} + \alpha_y \frac{\partial}{\partial y} \right)^m \mathbf{v}_{o_l} + \mathcal{O}(l^{m+1}) \quad (\text{B.22})$$

For a regular grid we can further assume the average at all the edges are approximated in the same way, thus γ is the same constant. Applying the discrete divergence operator (2.6) to Eqn. (B.22) yields

$$\text{div}(\bar{\mathbf{v}}_d^e) = \text{div}(\bar{\mathbf{v}}^e) + \gamma l^m \text{div} \left[\left(\alpha_x \frac{\partial}{\partial x} + \alpha_y \frac{\partial}{\partial y} \right)^m \mathbf{v} \right] + \text{h.o.t.} \quad (\text{B.23})$$

The acronym "h.o.t." stands for "higher order terms". The Gauss's theorem states that the first term on the right-hand side of (B.23) gives the accurate average divergence over the triangular cell. Consequently the truncation error is solely determined by the second term on the right-hand side.

According to the chain rule of differentiation and the binomial theorem,

$$\left(\alpha_x \frac{\partial}{\partial x} + \alpha_y \frac{\partial}{\partial y} \right)^m \mathbf{v}_o = \sum_{j=0}^m C_m^j \alpha_x^{m-j} \alpha_y^j \left(\frac{\partial^m \mathbf{v}}{\partial x^{m-j} \partial y^j} \right)_o. \quad (\text{B.24})$$

Here

$$C_m^j := \frac{m!}{j!(m-j)!} \quad (\text{B.25})$$

is the binomial coefficient and $m!$ denotes the factorial of m . In the local Cartesian coordinate depicted in Fig. 2.4, the parameters α_x , α_y and the outward normal unit vector \mathbf{n}_l at each edge have the following values:

$$\begin{aligned} \text{edge } l_1 : \quad & \alpha_{x_1} = 1, \quad \alpha_{y_1} = 0, \quad \mathbf{n}_{l_1} = (0, -(-1)^\delta); \\ \text{edge } l_2 : \quad & \alpha_{x_2} = -\frac{1}{2}, \quad \alpha_{y_2} = (-1)^\delta \frac{\sqrt{3}}{2}, \quad \mathbf{n}_{l_2} = \left(\frac{\sqrt{3}}{2}, (-1)^\delta \frac{1}{2} \right); \\ \text{edge } l_3 : \quad & \alpha_{x_3} = \frac{1}{2}, \quad \alpha_{y_3} = (-1)^\delta \frac{\sqrt{3}}{2}, \quad \mathbf{n}_{l_3} = \left(-\frac{\sqrt{3}}{2}, (-1)^\delta \frac{1}{2} \right). \end{aligned}$$

Using these values, we can further expand Eqn. (B.24) for each individual edge:

$$\begin{aligned} \left(\alpha_{x_1} \frac{\partial}{\partial x} + \alpha_{y_1} \frac{\partial}{\partial y} \right)^m \mathbf{v}_{o_1} &= \left(\frac{\partial^m \mathbf{v}}{\partial x^m} \right)_{o_1}, \\ \left(\alpha_{x_2} \frac{\partial}{\partial x} + \alpha_{y_2} \frac{\partial}{\partial y} \right)^m \mathbf{v}_{o_2} &= \frac{(-1)^m}{2^m} \left(\frac{\partial^m \mathbf{v}}{\partial x^m} \right)_{o_2} + \sum_{j=1}^m (-1)^{m-j} [(-1)^\delta]^j \frac{\sqrt{3}^j C_m^j}{2^m} \left(\frac{\partial^m \mathbf{v}}{\partial x^{m-j} \partial y^j} \right)_{o_2}, \\ \left(\alpha_{x_3} \frac{\partial}{\partial x} + \alpha_{y_3} \frac{\partial}{\partial y} \right)^m \mathbf{v}_{o_3} &= \frac{1}{2^m} \left(\frac{\partial^m \mathbf{v}}{\partial x^m} \right)_{o_3} + \sum_{j=1}^m [(-1)^\delta]^j \frac{\sqrt{3}^j C_m^j}{2^m} \left(\frac{\partial^m \mathbf{v}}{\partial x^{m-j} \partial y^j} \right)_{o_3}. \end{aligned}$$

Now calculate the second term on the right-hand side of Eqn. (B.23) :

$$\begin{aligned}
& \gamma l^m \operatorname{div} \left[\left(\alpha_x \frac{\partial}{\partial x} + \alpha_y \frac{\partial}{\partial y} \right)^m \mathbf{v} \right] = \frac{4\gamma l^{m-1}}{\sqrt{3}} \sum_{k=1}^3 \mathbf{n}_{l_k} \cdot \left(\alpha_{x_k} \frac{\partial}{\partial x} + \alpha_{y_k} \frac{\partial}{\partial y} \right)^m \mathbf{v}_{o_k} \\
& = \gamma \frac{l^{m-1}}{2^{m-1}} \left[(-1)^m \left(\frac{\partial^m u}{\partial x^m} \right)_{o_2} - \left(\frac{\partial^m u}{\partial x^m} \right)_{o_3} \right] \\
& \quad + \gamma \frac{l^{m-1}}{2^{m-1}} \frac{(-1)^\delta}{\sqrt{3}} \left[-2^{m+1} \left(\frac{\partial^m v}{\partial x^m} \right)_{o_1} + \left(\frac{\partial^m v}{\partial x^m} \right)_{o_2} + \left(\frac{\partial^m v}{\partial x^m} \right)_{o_3} \right] \\
& \quad + \gamma \frac{l^{m-1}}{2^{m-1}} \sum_{j=1}^m \sqrt{3^j} C_m^j \left[(-1)^\delta \right]^j \left[(-1)^{m-j} \left(\frac{\partial^m u}{\partial x^{m-j} \partial y^j} \right)_{o_2} - \left(\frac{\partial^m u}{\partial x^{m-j} \partial y^j} \right)_{o_3} \right] \\
& \quad + \frac{\gamma}{\sqrt{3}} \frac{l^{m-1}}{2^{m-1}} \sum_{j=1}^m \sqrt{3^j} C_m^j \left[(-1)^\delta \right]^{j+1} \left[(-1)^{m-j} \left(\frac{\partial^m v}{\partial x^{m-j} \partial y^j} \right)_{o_2} + \left(\frac{\partial^m v}{\partial x^{m-j} \partial y^j} \right)_{o_3} \right]. \quad (\text{B.26})
\end{aligned}$$

For a generic differentiable function $\psi(x, y)$,

$$\begin{aligned}
\psi_{o_2} + \psi_{o_3} &= 2\psi_o + \mathcal{O}(l), \\
\psi_{o_2} - \psi_{o_3} &= \mathcal{O}(l), \\
-2^{m+1}\psi_{o_1} + \psi_{o_2} + \psi_{o_3} &= -2(2^m - 1)\psi_o + \mathcal{O}(l), \\
-2^{m+1}\psi_{o_1} - \psi_{o_2} + \psi_{o_3} &= -2^{m+1}\psi_o + \mathcal{O}(l).
\end{aligned}$$

Thus Eqn. (B.26) continues as

$$\gamma l^m \operatorname{div} \left[\left(\alpha_x \frac{\partial}{\partial x} + \alpha_y \frac{\partial}{\partial y} \right)^m \mathbf{v} \right] = \begin{cases} l^{m-1} [M(\mathbf{v}) + (-1)^\delta N(\mathbf{v})]_o + \mathcal{O}(l^m), & m = 1, 3, 5, \dots \\ l^{m-1} (-1)^\delta M^*(\mathbf{v})_o + \mathcal{O}(l^m), & m = 2, 4, 6, \dots \end{cases} \quad (\text{B.27})$$

where

$$\begin{aligned}
M(\mathbf{v}) &:= \frac{\gamma}{2^{m-2}} \left[\sum_{j=1}^{m/2} \sqrt{3^{2j-2}} \left(-\frac{3 C_m^{2j} \partial^m u}{\partial x^{m-2j} \partial y^{2j}} + \frac{C_m^{2j-1} \partial^m v}{\partial x^{m-(2j-1)} \partial y^{2j-1}} \right) - \frac{\partial^m u}{\partial x^m} \right], \\
M^*(\mathbf{v}) &:= \frac{\gamma}{2^{m-2}} \left[\sum_{j=1}^{m/2} \sqrt{3^{2j-1}} \left(-\frac{C_m^{2j-1} \partial^m u}{\partial x^{m-(2j-1)} \partial y^{2j-1}} + \frac{C_m^{2j} \partial^m v}{\partial x^{m-2j} \partial y^{2j}} \right) - \frac{\sqrt{3}(2^m - 1)}{3} \frac{\partial^m v}{\partial x^m} \right], \\
N(\mathbf{v}) &:= -\frac{4\sqrt{3}\gamma}{3} \frac{\partial^m v}{\partial x^m}.
\end{aligned}$$

Substituting Eqn. (B.27) into Eqn. (B.23), we get

$$\operatorname{div}(\bar{\mathbf{v}}_d^e) = \begin{cases} \operatorname{div}(\bar{\mathbf{v}}^e) + l^{m-1} [M(\mathbf{v}) + (-1)^\delta N(\mathbf{v})]_o + \mathcal{O}(l^m), & m = 1, 3, 5, \dots \\ \operatorname{div}(\bar{\mathbf{v}}^e) + (-1)^\delta l^{m-1} M^*(\mathbf{v})_o + \mathcal{O}(l^m), & m = 2, 4, 6, \dots \end{cases} \quad (\text{B.28})$$

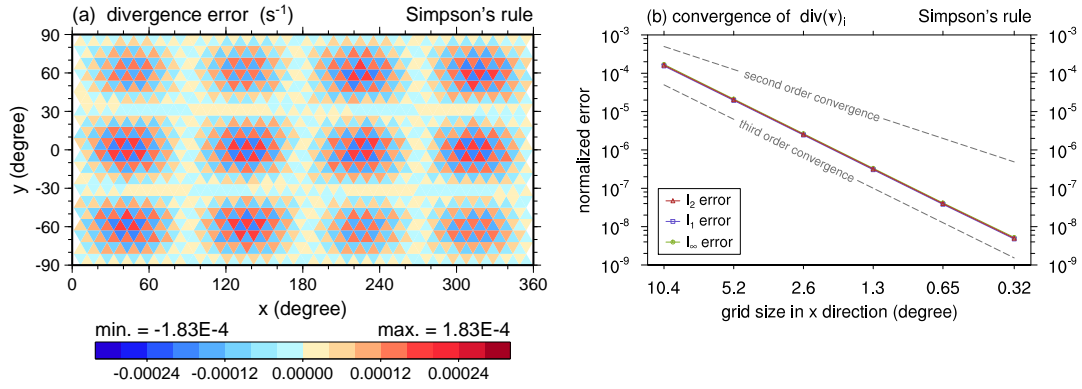


Fig. B.2: As in the first row of Fig. 2.9 on page 24, but with the average velocity at triangle edges calculated according to the Simpson's rule (cf. Eqn. (B.29)).

If the aim is to use this expression approximate the average divergence over a triangle, the first term on the right-hand side gives the exact solution and the remaining terms are the discretization error. We can thus conclude that

- The accuracy of the approximated average divergence is one order lower than that of the edge-mean velocity, and
- When the order of accuracy of the divergence is an odd number, the sign of the leading error depends on the orientation of the triangle; when order is an even number, part of the leading error also has an alternating sign.

The case of Eqn. (B.19) and the numerical calculations performed in Section 2.3.3 (see Figs. 2.7 – 2.9) can be regarded as a special instance of $m = 2$. As another example, we repeat the numerical calculation but approximate the edge average using the Simpson's rule:

$$\bar{\mathbf{v}}_d^e := \frac{1}{6} \left[\mathbf{v} \left(-\frac{l}{2} \right) + 4 \mathbf{v} (0) + \mathbf{v} \left(\frac{l}{2} \right) \right] = \bar{\mathbf{v}}^e + \mathcal{O} (l^4) . \quad (\text{B.29})$$

The resulting $\text{div}(\bar{\mathbf{v}}_d^e)$ of the test function (2.31) is shown in Fig. (B.2), where we see third-order convergence and the alternating sign of the absolute error. Both are consistent with the conclusions itemized above.

B.5 The cell-averaged divergence of a particular vector field

Assume a two-dimensional vector field is defined in the Cartesian coordinate as

$$\begin{cases} u(x, y) := \frac{1}{4} \sqrt{\frac{105}{2\pi}} \cos 2x \cos^2 y \sin y \\ v(x, y) := -\frac{1}{2} \sqrt{\frac{15}{2\pi}} \cos x \cos y \sin y . \end{cases}$$

This section derives the formula for the divergence of this vector averaged over a generic triangular cell depicted in Fig. 2.4. The two parts of the divergence, i.e. $\partial u / \partial x$ and $\partial v / \partial y$, are dealt with separately.

The $\partial u/\partial x$ part

$$\begin{aligned}
& \left(\frac{\sqrt{3}l^2}{4} \right)^{-1} \iint \frac{\partial u}{\partial x} dx dy \\
&= \frac{(-1)^\delta}{l^2} \sqrt{\frac{35}{2\pi}} \int_{y_o - (-1)^\delta \frac{\sqrt{3}}{6} l}^{y_o + (-1)^\delta \frac{\sqrt{3}}{3} l} u(x, y) \Big|_{x=\mathcal{X}_3(y)}^{x=\mathcal{X}_2(y)} dy \\
&= \frac{(-1)^\delta}{l^2} \sqrt{\frac{35}{2\pi}} \int_{y_o - (-1)^\delta \frac{\sqrt{3}}{6} l}^{y_o + (-1)^\delta \frac{\sqrt{3}}{3} l} \cos^2 y \sin y \left\{ \cos \left[2\mathcal{X}_2(y) \right] - \cos \left[2\mathcal{X}_3(y) \right] \right\} dy \\
&= \frac{(-1)^\delta}{l^2} \sqrt{\frac{35}{2\pi}} \int_{y_o - (-1)^\delta \frac{\sqrt{3}}{6} l}^{y_o + (-1)^\delta \frac{\sqrt{3}}{3} l} 2 \sin 2x_o \cos^2 y \sin y \sin 2 \left[(-1)^\delta \frac{\sqrt{3}}{3} (y - y_o) - \frac{l}{3} \right] dy
\end{aligned} \tag{B.30}$$

For arbitrary real numbers α ($\neq 0$) and β ,

$$\begin{aligned}
& \int \cos^2 y \sin y \sin(\alpha y + \beta) dy \\
&= \frac{1}{9 - \alpha^2} \left\{ \frac{1}{1 - \alpha^2} \left[\alpha(3 - \alpha^2) \cos(\alpha y + \beta) \sin y - 2\alpha^2 \sin(\alpha y + \beta) \cos y \right] \right. \\
&\quad \left. - \alpha \cos(\alpha y + \beta) \sin^3 y - 3 \sin(\alpha y + \beta) \cos^3 y \right\} .
\end{aligned}$$

Now let

$$\alpha = (-1)^\delta \frac{2\sqrt{3}}{3}, \quad \beta = -2 \left[(-1)^\delta y_o + \frac{l}{3} \right] .$$

The lower and upper integration limit in (B.30) correspond to $\alpha y + \beta = -l$ and $\alpha y + \beta = 0$, respectively. Therefore

$$\begin{aligned}
& \left(\frac{\sqrt{3}l^2}{4} \right)^{-1} \iint \frac{\partial u}{\partial x} dx dy \\
&= \frac{\sqrt{70}}{23\sqrt{\pi}l^2} \sin 2x_o \left[10\sqrt{3} (\sin y_{\mathcal{X}_3} - \cos l \sin y_{\mathcal{X}_2}) - (-1)^\delta 24 \sin l \cos y_{\mathcal{X}_2} \right. \\
&\quad \left. + 2\sqrt{3} (\sin^3 y_{\mathcal{X}_3} - \cos l \sin^3 y_{\mathcal{X}_2}) + (-1)^\delta 9 \sin l \cos^3 y_{\mathcal{X}_2} \right] \tag{B.31}
\end{aligned}$$

The $\partial v/\partial y$ part

Using the integration formula

$$\int \cos x \sin(\alpha x + \beta) dx = \frac{1}{1 - \alpha^2} \left[\sin(\alpha x + \beta) \sin x + \alpha \cos(\alpha x + \beta) \cos x \right]$$

it can be verified that

$$\begin{aligned}
 & \left(\frac{\sqrt{3}l^2}{4} \right)^{-1} \iint \frac{\partial v}{\partial y} dx dy \\
 &= \frac{-(-1)^\delta}{l^2} \sqrt{\frac{10}{\pi}} \left[\int_{x_o - \frac{l}{2}}^{x_o} v(x, y) \Big|_{y=\mathcal{Y}_1(x)}^{y=\mathcal{Y}_3(x)} dy + \int_{x_o}^{x_o + \frac{l}{2}} v(x, y) \Big|_{y=\mathcal{Y}_1(x)}^{y=\mathcal{Y}_2(x)} dy \right] \\
 &= \frac{-(-1)^\delta}{l^2} \sqrt{\frac{5}{2\pi}} \left\{ \int_{x_o - \frac{l}{2}}^{x_o} \cos x \sin [2\mathcal{Y}_3(x)] dy + \int_{x_o}^{x_o + \frac{l}{2}} \cos x \sin [2\mathcal{Y}_2(x)] dy \right. \\
 &\quad \left. - \int_{x_o - \frac{l}{2}}^{x_o + \frac{l}{2}} \cos x \sin 2 \left[y_o - (-1)^\delta \frac{\sqrt{3}}{6} l \right] dy \right\} \\
 &= \frac{1}{11l^2} \sqrt{\frac{5}{2\pi}} \left[2\sqrt{3} \left(2 \cos 2y_{\varkappa_3} \cos x_{\varkappa_3} - \cos 2y_{\varkappa_2} \cos x_{\varkappa_2} - \cos 2y_{\varkappa_1} \cos x_{\varkappa_1} \right) \right. \\
 &\quad \left. + (-1)^\delta 12 \left(\sin 2y_{\varkappa_2} \sin x_{\varkappa_2} - \sin 2y_{\varkappa_1} \sin x_{\varkappa_1} \right) \right] \quad (\text{B.32})
 \end{aligned}$$

Summation of the Eqns. (B.31) and (B.32) gives the average divergence over the triangle.

B.6 Truncation error of the scalar Laplacian

In the ICON models the discrete scalar Laplacian is defined as

$$(\nabla_d^2 \varrho)_i := \text{div} \left[\text{grad}_n(\varrho) \right]_i . \quad (\text{B.33})$$

On a regular triangular grid on the plane this is equivalent to

$$(\nabla_d^2 \varrho)_o = \frac{4}{l^2} (\varrho_1 + \varrho_2 + \varrho_3 - 3\varrho_o) \quad (\text{B.34})$$

for the stencil depicted in Fig. B.3. Note that in the figure the symbol δ_o indicates the orientation of the target triangle O to which the value of $\nabla_d^2 \varrho$ is associated. If ϱ_j ($j = 0, 1, 2, 3$) in Eqn. (B.34) are understood as pointwise function evaluation at cell centers, one can apply the Taylor expansion to Eqn. (B.34) to obtain

$$(\nabla_d^2 \varrho)_o = (\nabla^2 \varrho)_o + (-1)^{\delta_o} \frac{\sqrt{3}l}{6} G(\varrho)_o + \frac{l^2}{48} (\nabla^4 \varrho)_o + \mathcal{O}(l^3) . \quad (\text{B.35})$$

$G(\varrho)$ here is the same as that defined by Eqn. (2.25).

Regarding the average viewpoint of the operand, we can first calculate the cell average using Eqn. (2.24) for all the four triangles in Fig. B.3, and then expand the function evaluation at O_1 ,

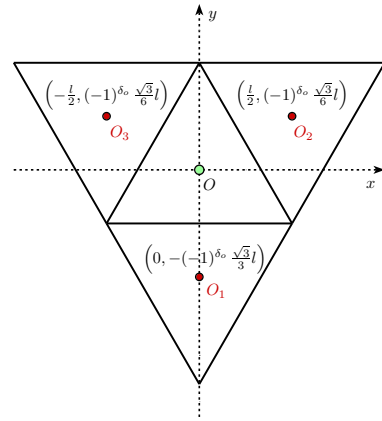


Fig. B.3: Stencil of the discrete scalar Laplacian $\nabla_d^2 \varrho$.

O_2 and O_3 about the origin O . Keeping in mind that the three surrounding triangles point to the direction opposite to the target triangle, we find

$$\left[\nabla_d^2 \left(\overline{\overline{\varrho}}^i \right) \right]_o = (\nabla^2 \varrho)_o + (-1)^{\delta_o} \frac{\sqrt{3}l}{5} G(\varrho)_o + \frac{l^2}{24} (\nabla^4 \varrho)_o + \mathcal{O}(l^3) . \quad (\text{B.36})$$

Note that the right-hand sides of (B.35) and (B.36) have the same structure and only differs in the coefficients. They are both first-order approximation to $(\nabla^2 \varrho)_o$ (i.e., pointwise value at cell center).

Furthermore, in the continuous case, we have

$$\overline{\overline{(\nabla^2 \varrho)}}^i = (\nabla^2 \varrho)_o + \frac{l^2}{48} (\nabla^4 \varrho)_o + \mathcal{O}(l^3) . \quad (\text{B.37})$$

Thus Eqn. (B.35) – (B.37) reveal that regardless of the viewpoints chosen for the operand and the outcome of the operator, the discrete scalar Laplacian is always first-order and the sign of the leading error depends on the orientation of the triangle at which the Laplacian is approximated.

The discrete fourth-order hyper-Laplacian of scalar ϱ in the ICON shallow water model is defined as

$$\nabla_d^4 \varrho := \nabla_d^2 (\nabla_d^2 \varrho) . \quad (\text{B.38})$$

Substituting expression (B.35) for ϱ in Eqn. (B.34) yields

$$(\nabla_d^4 \varrho)_o = \frac{4}{l^2} \left[\sum_{j=1,3} (\nabla_d^2 \varrho)_j - 3 (\nabla_d^2 \varrho)_o \right] \quad (\text{B.39})$$

$$\begin{aligned} &= \frac{4}{l^2} \underbrace{\left(\sum_{j=1}^3 (\nabla^2 \varrho)_j - 3 (\nabla^2 \varrho)_o \right)}_{\text{T1}} - \underbrace{(-1)^{\delta_b} \frac{2\sqrt{3}}{3l} \left(\sum_{j=1,3} G_j + 3 G_o \right)}_{\text{T2}} \\ &\quad + \frac{l^2}{48} \cdot \frac{4}{l^2} \underbrace{\left(\sum_{j=1}^3 (\nabla^4 \varrho)_j - 3 (\nabla^4 \varrho)_o \right)}_{\text{T3}} + \mathcal{O}(l^3) . \end{aligned} \quad (\text{B.40})$$

According to Eqn. (B.35),

$$\text{T1} = (\nabla^4 \varrho)_o + \mathcal{O}(l) , \quad (\text{B.41})$$

$$\text{T3} = \frac{l^2}{48} \left[(\nabla^6 \varrho)_o + \mathcal{O}(l) \right] = \mathcal{O}(l^2) . \quad (\text{B.42})$$

The term T2 has a plus sign instead of minus in the parentheses, for which the Taylor expansion about the origin O gives

$$\text{T2} = (-1)^{\delta_b} \frac{2\sqrt{3}}{3l} \left[6G(\varrho)_o + \mathcal{O}(l^2) \right] , \quad (\text{B.43})$$

thus (B.40) continues as

$$\nabla_d^4 \varrho = (\nabla^4 \varrho)_o - (-1)^{\delta_b} 4\sqrt{3} l^{-1} G(\varrho)_o + \mathcal{O}(l) . \quad (\text{B.44})$$

To derive the truncation error of $\nabla_d^4 \bar{\varrho}^i$, one can follow the same steps and use (B.37) to obtain

$$\nabla_d^4 (\bar{\varrho}^i) = \frac{4}{l^2} \left\{ \sum_{j=1}^3 [\nabla_d^2 (\bar{\varrho}^i)]_j - 3 [\nabla_d^2 (\bar{\varrho}^i)]_o \right\} \quad (\text{B.45})$$

$$= (\nabla^4 \varrho)_o - (-1)^{\delta} \frac{24\sqrt{3}}{5} l^{-1} G(\varrho)_o + \mathcal{O}(l). \quad (\text{B.46})$$

Eqns. (B.44) and (B.45) are clearly of order -1, either comparing to $(\nabla^4 \varrho)_o$ (the pointwise value) or with respect to $\overline{\overline{(\nabla^4 \varrho)^i}}$ (the cell average). In other words, there are nonconverging approximations to the desired hyper-Laplacian.

As verification of these derivations, numerical calculations are performed using the test function

$$\varrho := Y_3^2(x, y) = \frac{1}{4} \sqrt{\frac{105}{2\pi}} \cos 2x \cos^2 y \sin y. \quad (\text{B.47})$$

For simplicity, we take a pure pointwise viewpoint and check the expressions (B.35) and (B.44) only. The results (Fig. B.4) indicate a first-order convergence for $\nabla_d^2 \varrho$ and order -1 for $\nabla_d^4 \varrho$, which confirms the formal derivations.

B.7 Truncation error of the vector Laplacian

In the ICON shallow water model the discrete vector Laplacian is defined at midpoints of triangle edges. The projection onto the normal direction of an edge l is calculated by

$$(\nabla_d^2 \mathbf{v})_l \cdot \mathbf{N}_l := \text{grad}_n [\text{div}(\mathbf{v})]_l - \text{grad}_\tau [\text{curl}(\mathbf{v})]_l. \quad (\text{B.48})$$

To find out the truncation error of this operator, we analyze the two parts on the right-hand side of Eqn. (B.48) separately and consider the stencil depicted in Fig. B.5.

First consider the tangential gradient of the curl. The relative vorticity ξ ($:= \mathbf{k} \cdot (\nabla \times \mathbf{v})$) approximated at vertices $\varkappa(l, 1)$ and $\varkappa(l, 2)$ are second-order accurate regardless of the viewpoint chosen (cf. Eqn. (B.8) on page 120 and Eqn. (B.17) on page 121). Its tangential gradient at the center of the primal edge l is therefore also second-order:

$$\text{grad}_\tau [\text{curl}(\mathbf{v})]_l = \left(\frac{\partial \xi}{\partial \tau} \right)_o + \frac{l^2}{96} \left[\frac{\partial}{\partial \tau} \left(7 \frac{\partial^2 \xi}{\partial \tau^2} + 3 \frac{\partial^2 \xi}{\partial n^2} \right) \right]_o + \mathcal{O}(l^4), \quad (\text{B.49})$$

$$\text{grad}_\tau [\text{curl}(\bar{\mathbf{v}}^e)]_l = \left(\frac{\partial \xi}{\partial \tau} \right)_o + \frac{l^2}{48} \left[\frac{\partial}{\partial \tau} \left(5 \frac{\partial^2 \xi}{\partial \tau^2} + 3 \frac{\partial^2 \xi}{\partial n^2} \right) \right]_o + \mathcal{O}(l^4). \quad (\text{B.50})$$

Regarding the normal gradient of divergence, we distinguish the following two cases:

1. Assume the calculation starts from the exact average velocity over each triangle edge, yielding the exact average divergence over the triangle cells. One can directly apply Eqn. (B.6) to divergence D ($:= \nabla \cdot \mathbf{v}$) and obtain

$$\text{grad}_n [\text{div}(\bar{\mathbf{v}}^e)]_o = \left(\frac{\partial D}{\partial n} \right)_o + \frac{l^2}{80} \left(\frac{\partial^3 D}{\partial \tau^2 n} + 3 \frac{\partial^3 D}{\partial n^3} \right)_o + \mathcal{O}(l^4). \quad (\text{B.51})$$

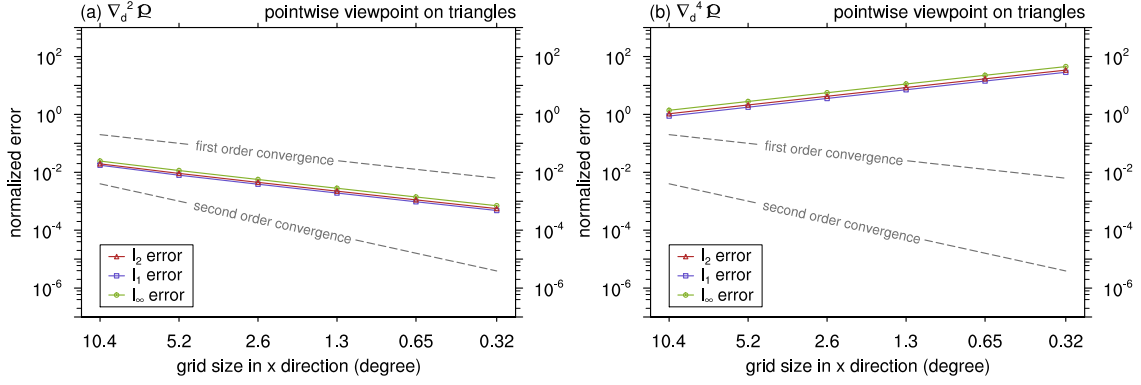


Fig. B.4: Normalized errors of the scalar Laplace operators $\nabla_d^2 \rho$ and $\nabla_d^4 \rho$ operating on pointwise values. The analytical expression of the test function ρ is given in Eqn. (B.47). The numerical calculations are performed on the triangular grid shown in Fig. 2.8.

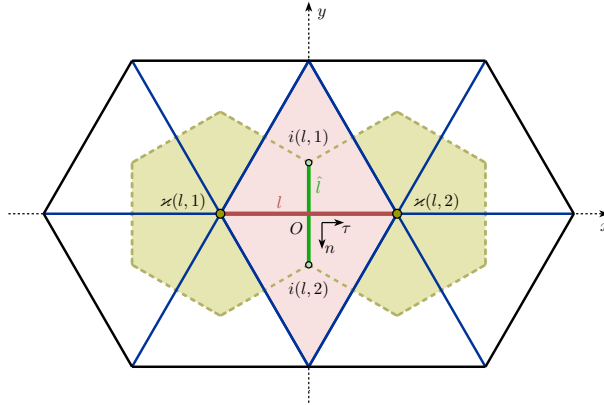


Fig. B.5: Stencil of the vector Laplacian $\nabla_d^2 \mathbf{v}$.

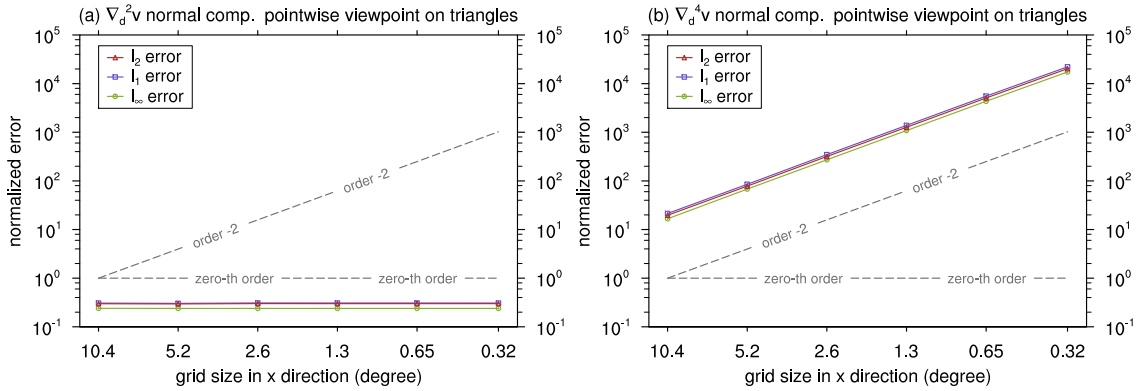


Fig. B.6: Normalized errors of the vector Laplace operators $\nabla_d^2 \mathbf{v}$ and $\nabla_d^4 \mathbf{v}$ operating on pointwise values. The analytical expression of the test function \mathbf{v} is given by Eqn. (2.31). The numerical calculations are performed on the triangular grid shown in Fig. 2.8.

2. Suppose we take the ICOSWM viewpoint (see the last paragraph in Section 2.3.2) and regard the \mathbf{v} in Eqn. (B.48) as the pointwise value. First use Eqn. (B.19) on page 123 to get the approximated divergence for the primal cells $i(l,1)$ and $i(l,2)$, then take the normal gradient and use Eqn. (B.5). This yields

$$\text{grad}_n \left[\text{div}(\mathbf{v}) \right]_o = \left(\frac{\partial D}{\partial n} \right)_o - (-1)^\delta 2\sqrt{3} H(\mathbf{v})_o + \mathcal{O}(l^2) . \quad (\text{B.52})$$

The δ in this expression indicates the orientation of the neighbouring triangle $i(l,1)$ of edge l . In Eqn. (B.52) the truncation error does not change with resolution. An example of numerical results is shown in Fig. B.6a, in which the computation is carried out using the same test function as in the test of divergence (cf. Fig. 2.7 in Section 2.3.3).

Now we take a further step and apply the discrete operator (B.48) again to get the fourth-order hyper-Laplacian, namely computing

$$\nabla_d^4 \mathbf{v} := \nabla_d^2 (\nabla_d^2 \mathbf{v}) . \quad (\text{B.53})$$

It can be verified that

$$(\nabla_d^4 \bar{\mathbf{v}}^e)_l \cdot \mathbf{N}_l = (\nabla^4 \mathbf{v})_l \cdot \mathbf{N}_l + (-1)^\delta 2\sqrt{3} H(\nabla D)_l + \mathcal{O}(l^2) , \quad (\text{B.54})$$

$$(\nabla_d^4 \mathbf{v})_l \cdot \mathbf{N}_l = (\nabla^4 \mathbf{v})_l \cdot \mathbf{N}_l + (-1)^\delta 48\sqrt{3} l^{-2} H(\mathbf{v})_l + \mathcal{O}(l^0) . \quad (\text{B.55})$$

Note that for the stencil in Fig. B.5 we have $\mathbf{N}_l = \mathbf{n}$. Neither Eqn. (B.54) nor (B.55) converges to the continuous counterpart $\nabla^4 \mathbf{v}$. Even if the operator is applied to the accurately computed average velocity along triangle edges, the discrete fourth-order vector Laplacian gives a zeroth order approximation. In case the velocity is regarded as pointwise value, the order of accuracy is -2 (Eqn. (B.55)). The latter has been confirmed by numerical calculations shown in Fig. B.6b.

Appendix C

Notes on linear horizontal diffusion in numerical models

Scale-selective artificial dissipation is commonly used in numerical models as a mechanism to remove small scale noise and retain computational stability. Among various choices, the linear hyper-diffusion

$$\frac{\partial\psi}{\partial t} = -(-1)^q K \nabla^{2q} \psi \quad (\text{C.1})$$

is a widely used form. Here ψ is the physical quantity to be dealt with, q a positive integer, and K the coefficient controlling the strength of the dissipation. In most applications this damping is applied only in the horizontal direction. The vertical diffusion is considered as part of the physics parameterizations, therefore not discussed here.

There are some practical issues related to the horizontal diffusion. First, the coefficient K needs to be sufficiently large to ensure the overall stability of the model, and meanwhile as small as possible to avoid overly strong dissipation on the physically interesting signals. Second, in numerical models the time derivative in Eqn. (C.1) has to be discretized; in models that do not use series-expansion methods, the Laplacian operator needs discretization as well. This leads to the question of accuracy, as well as the stability of the diffusion scheme itself. In this appendix, we first briefly review the motivation of using the diffusion equation for numerical dissipation; Subsequently the damping effect and the stability of the discrete diffusion problem are investigated in a few typical cases. Properties of the numerical diffusion in the ICON models are discussed in Chapter 2 in the main part of the thesis.

C.1 Damping effect in the continuous case

Using the technique called separation of variables, analytical solution can be easily obtained for the diffusion equation (C.1). Suppose the solution can be expressed as the superposition of a series of oscillation functions of time-dependent amplitude, e.g.,

$$\psi(x, t) = \sum_{k=-\infty}^{+\infty} \Psi_k(t) e^{ikx} \quad (\text{C.2})$$

in the 1D case, and

$$\psi(x, t) = \sum_{n=-\infty}^{+\infty} \sum_{m=-n}^n \Psi_n^m(t) Y_n^m(\lambda, \varphi) \quad (\text{C.3})$$

for the 2D problem on a sphere with radius a . Here $i = \sqrt{-1}$; $Y_n^m(\lambda, \varphi)$ is the spherical harmonic with total wavenumber n and zonal wavenumber m . λ and φ are longitude and latitude, respectively. In the following we call each product in the summations in Eqns. (C.2) and (C.3) a "wave component" or "mode".

A key property of the oscillation functions is

$$\nabla^{2q} e^{ikx} = (-1)^q k^{2q} e^{ikx}, \quad \text{and} \quad (\text{C.4})$$

$$\nabla^{2q} Y_n^m = (-1)^q \left[\frac{n(n+1)}{a^2} \right]^q Y_n^m. \quad (\text{C.5})$$

Substitution of the 1D formal solution (C.2) into the diffusion equation (C.1) yields an ordinary differential equation of the amplitude function:

$$\frac{d\Psi_k}{dt} = e^{-k^{2q}K} \Psi_k. \quad (\text{C.6})$$

The solution is

$$\Psi_k(t) = e^{-k^{2q}Kt} \Psi_k(0), \quad (\text{C.7})$$

indicating that the 1D wave component k experiences an exponential decay in amplitude, with the e-folding time being

$$\tau_k = \frac{1}{k^{2q}K} = \frac{1}{K} \left(\frac{L}{2\pi} \right)^{2q}. \quad (\text{C.8})$$

(Here L is the wavelength of mode k .) Since Eqn. (C.8) is valid for all modes, one can introduce a reference wavenumber k_0 with e-folding time τ_0 , and define the amplification factor $\dagger \mathcal{A}_k$ of an arbitrary mode k as

$$\mathcal{A}_k := \frac{\Psi_k(t+\Delta t)}{\Psi_k(t)} = e^{-k^{2q}K\Delta t} = e^{-\frac{\Delta t}{\tau_0} \left(\frac{k}{k_0} \right)^{2q}}. \quad (\text{C.9})$$

Similarly, for the 2D problem on the sphere, we have

$$\tau_n = \frac{1}{K} \left[\frac{a^2}{n(n+1)} \right]^q \quad (\text{C.10})$$

$$\mathcal{A}_n^m := \frac{\Psi_n^m(t+\Delta t)}{\Psi_n^m(t)} = e^{-K \left[\frac{n(n+1)}{a^2} \right]^q \Delta t} = e^{-\frac{\Delta t}{\tau_0} \left[\frac{n(n+1)}{n_0(n_0+1)} \right]^q}, \quad (\text{C.11})$$

in which τ_0 is the e-folding time corresponding to the total wavenumber n_0 .

The scale selectivity of the hyper-diffusion is revealed by Eqns. (C.9) and (C.11): Small scale waves are damped faster than larger scale ones, and the contrast depends on the parameter q . In numerical models the coefficient K and the order $2q$ are often chosen in such a way that the horizontal diffusion scheme can efficiently remove the small scale noise, and at the same time does not affect severely the large scale signal.

[†]Here the name "amplification factor" is given to the parameter \mathcal{A} in order to be consistent with its counterpart that will show up in the next section in the discretized problem. $|\mathcal{A}| > 1$ indicates amplification of the amplitude and $|\mathcal{A}| < 1$ corresponds to damping.

C.2 Damping time and stability in the discrete case

In order to apply the horizontal diffusion in numerical models, equation (C.1) needs to be discretized to different extents, depending on the algorithm used for solving the governing equations of the atmospheric motions. This not only causes changes in the damping effect, but also leads to the possibility of numerical instability.

C.2.1 The temporally discretized cases

Suppose the 1D diffusion equation is numerically solved by the expansion method using the Fourier series as the basis functions. Eqn. (C.4) can still be used for the right hand side of Eqn. (C.1), although the time derivative has to be approximated. The most common choice is to apply a two time level explicit scheme, meaning replacing the differential equation (C.6) by

$$\frac{\Psi_{k,t+\Delta t} - \Psi_{k,t}}{\Delta t} = e^{-k^{2q}K} \Psi_{k,t}. \quad (\text{C.12})$$

This leads to an amplification factor

$$\mathcal{A}'_k := \frac{\Psi_{k,t+\Delta t}}{\Psi_{k,t}} = 1 - k^{2q}K\Delta t. \quad (\text{C.13})$$

The characteristic time scale

$$\tau'_k = \frac{1}{k^{2q}K} = \frac{1}{K} \left(\frac{L}{2\pi} \right)^{2q} \quad (\text{C.14})$$

is the time step to be used if we want to have the amplitude of the Fourier component k reduced to zero after one integration step. Like in the continuous case, one can introduce a reference damping time τ'_0 and rewrite (C.13) as

$$\mathcal{A}'_k = 1 - \frac{\Delta t}{\tau'_0} \left(\frac{k}{k_0} \right)^{2q}. \quad (\text{C.15})$$

For the 2D problem the counterparts are

$$\tau'_n = \frac{1}{K} \left[\frac{a^2}{n(n+1)} \right]^q \quad \text{and} \quad (\text{C.16})$$

$$\mathcal{A}'_k = 1 - \frac{\Delta t}{\tau'_0} \left[\frac{n(n+1)}{n_0(n_0+1)} \right]^{2q}, \quad (\text{C.17})$$

respectively.

The comparison with the continuous case reveals that, after the temporal discretization, the expression of the characteristic damping time remains the same, though the amplification factor changes slightly. In the limit of small $\Delta t/\tau'_0$, Eqns. (C.15) and (C.17) can be considered as first-order approximations to Eqns. (C.9) and (C.11), respectively.

C.2.2 The fully discretized 1D problem

Now consider the general case of a finite difference model, in which the hyper-Laplacian in the diffusion equation (C.1) has to be approximated by finite difference. For simplicity, we consider only the 1D problem.

Suppose the same time stepping scheme is employed as before, while the spatial discretization is done on a 1D grid with constant interval Δx and without boundary. The grid points are labeled by an integer index j . The discrete Laplacian is calculated by

$$\nabla_d^2 \psi = \frac{\psi_{j+1} - 2\psi_j + \psi_{j-1}}{(\Delta x)^2}, \quad (\text{C.18})$$

and the hyper-Laplacian is approximated by applying this formula repeatedly.

Taking into account the spatial differencing, we now assume the wave component k of the discrete solution features the form

$$\psi_{k,j,t} = \Psi_{k,t} e^{ikj\Delta x}, \quad (\text{C.19})$$

which is essentially the same as in the von Neumann's method of stability analysis (cf., e.g., pages 43 - 45 in Durran, 1998). Applying the discrete Laplacian (C.18) to the formal solution (C.19) gives

$$\nabla_h^{2q} \psi_{k,j,t} = (-1)^q \left[\frac{2(1 - \cos k\Delta x)}{\Delta x^2} \right]^q \Psi_{k,t} e^{ikj\Delta x}. \quad (\text{C.20})$$

Subsequent application of the explicit time stepping scheme eventually yields

$$\mathcal{A}_k^* := \frac{\Psi_{k,t+\Delta t}}{\Psi_{k,t}} = 1 - \left[\frac{2(1 - \cos k\Delta x)}{\Delta x^2} \right]^q K \Delta t. \quad (\text{C.21})$$

Now the characteristic damping time that leads to the complete removal of mode k becomes

$$\tau_k^* = \frac{1}{K} \left[\frac{(\Delta x)^2}{2(1 - \cos k\Delta x)} \right]^q. \quad (\text{C.22})$$

The shortest resolvable wave on the grid, the $L (= 2\pi/k) = 2\Delta x$ mode, corresponds to

$$\tau_0^* = \frac{1}{K} \left(\frac{\Delta x}{2} \right)^{2q}. \quad (\text{C.23})$$

Using this definition of τ_0^* we can rewrite the amplification factor as

$$\mathcal{A}_k^* = 1 - \frac{\Delta t}{\tau_0^*} \left[\frac{(1 - \cos k\Delta x)}{2} \right]^q. \quad (\text{C.24})$$

The comparison of (C.22) and (C.24) with Eqns. (C.14) and (C.15) reveals the impact of spatial discretization. If the characteristic damping time was calculated from (C.14), the damping effect on the $2\Delta x$ wave would be overestimated.

C.2.3 Numerical stability

From expressions (C.15), (C.17) and (C.24) the numerical stability of the discrete diffusion problem can be analyzed. Although \mathcal{A} is never larger than unity, the stability condition

$$|\mathcal{A}| \leq 1 \quad (\text{C.25})$$

can still be violated if $\mathcal{A} < -1$, which means the corresponding wave component not only amplifies with time, but also changes its sign after each time step. Under the condition that the scale selectivity provided by the discrete scheme is qualitatively the same as in the original diffusion problem, this situation can be avoided for all wave components as long as it is avoided for the shortest mode. In real applications it is better to be more conservative and ensure $\mathcal{A} \geq 0$ so as to be consistent with the continuous case. $-1 < \mathcal{A} < 0$ would act as an over-relaxation.

Appendix D

Horizontal wind reconstruction using the radial basis functions

Radial basis functions (RBFs) are powerful tools for interpolating scattered data. In the ICON models, they are used for providing accurate approximations to a two-dimensional vector field on the sphere obtained from its components normal to the edges of the icosahedral triangular grid (Baudisch *et al.*, 2006). The interpolation is performed in a 3D Cartesian coordinate rotating with the Earth, whose origin is located at the Earth's center, and the z -axis aligns with the Earth's rotation axis and points to the north. In the following, any point on the sphere of radius a is indicated by the location vector $\mathbf{x} := (x, y, z)$.

The interpolation problem can be described as follows: given an arbitrary destination point \mathbf{x}_0 , define a region surrounding it. In this region at location \mathbf{x}_j ($j = 1, \dots, m$), the projection of the vector field of interest (denoted by \mathbf{v}) in the direction of the unit vector \mathbf{N}_j is known as $\mathbf{v}_j \cdot \mathbf{N}_j =: v_{n_j}$. Assume that within this region the vector field can be approximated by the function

$$\mathcal{V}(\mathbf{x}) := \sum_{j=1}^m c_j \psi(\mathbf{x} - \mathbf{x}_j) \mathbf{N}_j \quad (\text{D.1})$$

which satisfies

$$\mathcal{V}(\mathbf{x}_k) \cdot \mathbf{N}_k = v_{n_k}, \quad k = 1, \dots, m. \quad (\text{D.2})$$

Here ψ is a radial basis function whose value depends only on the great circle distance between \mathbf{x} and \mathbf{x}_j , i.e.,

$$\psi(\mathbf{x} - \mathbf{x}_j) = \psi(r) \quad \text{where } r := \|\mathbf{x} - \mathbf{x}_j\|. \quad (\text{D.3})$$

Commonly used RBFs include

$$\text{Gaussian: } \psi(r) := e^{-(r/\beta)^2}; \quad (\text{D.4})$$

$$\text{Multiquadric: } \psi(r) := \sqrt{1 + (r/\beta)^2}; \quad (\text{D.5})$$

$$\text{Inverse multiquadric: } \psi(r) := \left[\sqrt{1 + (r/\beta)^2} \right]^{-1}; \quad (\text{D.6})$$

$$\text{Thin plate spline: } \psi(r) := \begin{cases} r^2 \ln(r) & \text{for } r > 0; \\ 0 & \text{for } r = 0. \end{cases} \quad (\text{D.7})$$

The parameter β in the first three examples is often called the scale factor. In the ICON models, we use RBFs that are monotonically decreasing with respect to the distance r .

From Eqns. (D.1) and (D.2) one can derived a linear algebraic equation

$$\underline{\Psi} \mathbf{c} = \mathbf{v}_n \quad (\text{D.8})$$

in which

$$(\underline{\Psi})_{kj} = \psi(\mathbf{x}_k - \mathbf{x}_j) (\mathbf{N}_k \cdot \mathbf{N}_j), \quad k = 1, \dots, m; j = 1, \dots, m \quad (\text{D.9})$$

$$(\mathbf{c})_j = c_j, \quad j = 1, \dots, m \quad (\text{D.10})$$

$$(\mathbf{v}_n)_k = v_{n_k}, \quad k = 1, \dots, m \quad (\text{D.11})$$

Formally solving Eqn. (D.8) for \mathbf{c} and substituting the solution into Eqn. (D.1), we get

$$\mathbf{v}_0 \approx \mathcal{V}(\mathbf{x}_0) = (\underline{\Psi}^{-1} \mathbf{v}_n)^T \boldsymbol{\psi}_0 \quad (\text{D.12})$$

in which

$$(\boldsymbol{\psi}_0)_j = \psi(\mathbf{x}_0 - \mathbf{x}_j) \mathbf{N}_j, \quad j = 1, \dots, m. \quad (\text{D.13})$$

For a particular application, once the stencil and the form of the RBF have been determined, the matrix $\underline{\Psi}^{-1}$ and vector $\boldsymbol{\psi}_0$ can be calculated and stored. Each time when the vector reconstruction is needed, the approximation can be obtained by applying Eqn. (D.12).

In the ICON models, the RBFs are used for reconstructing the horizontal wind vector at triangle centers from the normal wind given at some triangle edges in the vicinity. Three stencils of different sizes have been implemented (Fig. D.1). Numerical tests have shown that the three-point stencil produces in general first-order approximations while the nine-point stencil yields second-order accuracy. According to results in these tests, the Gaussian function (D.4) with the scale factor $\beta=0.5$ has been recommended for the wind reconstruction in the ICON models.

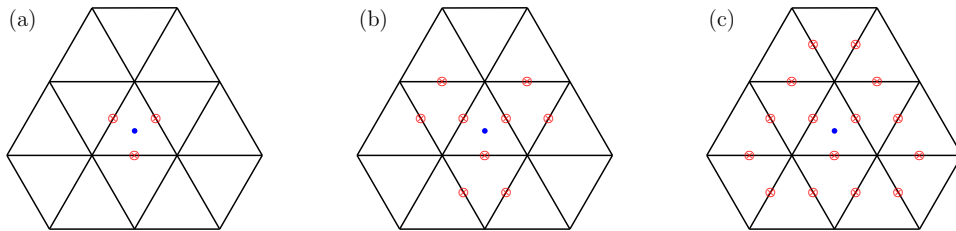


Fig. D.1: The (a) three-point, (b) nine-point and (b) fifteen-point stencils implemented in the ICON models for the RBF wind reconstruction. The red marks indicate the midpoint of triangle edges where the normal wind velocity is known. The blue dots indicate the destination location where the horizontal wind vector is reconstructed.

Appendix E

Supplementary figures

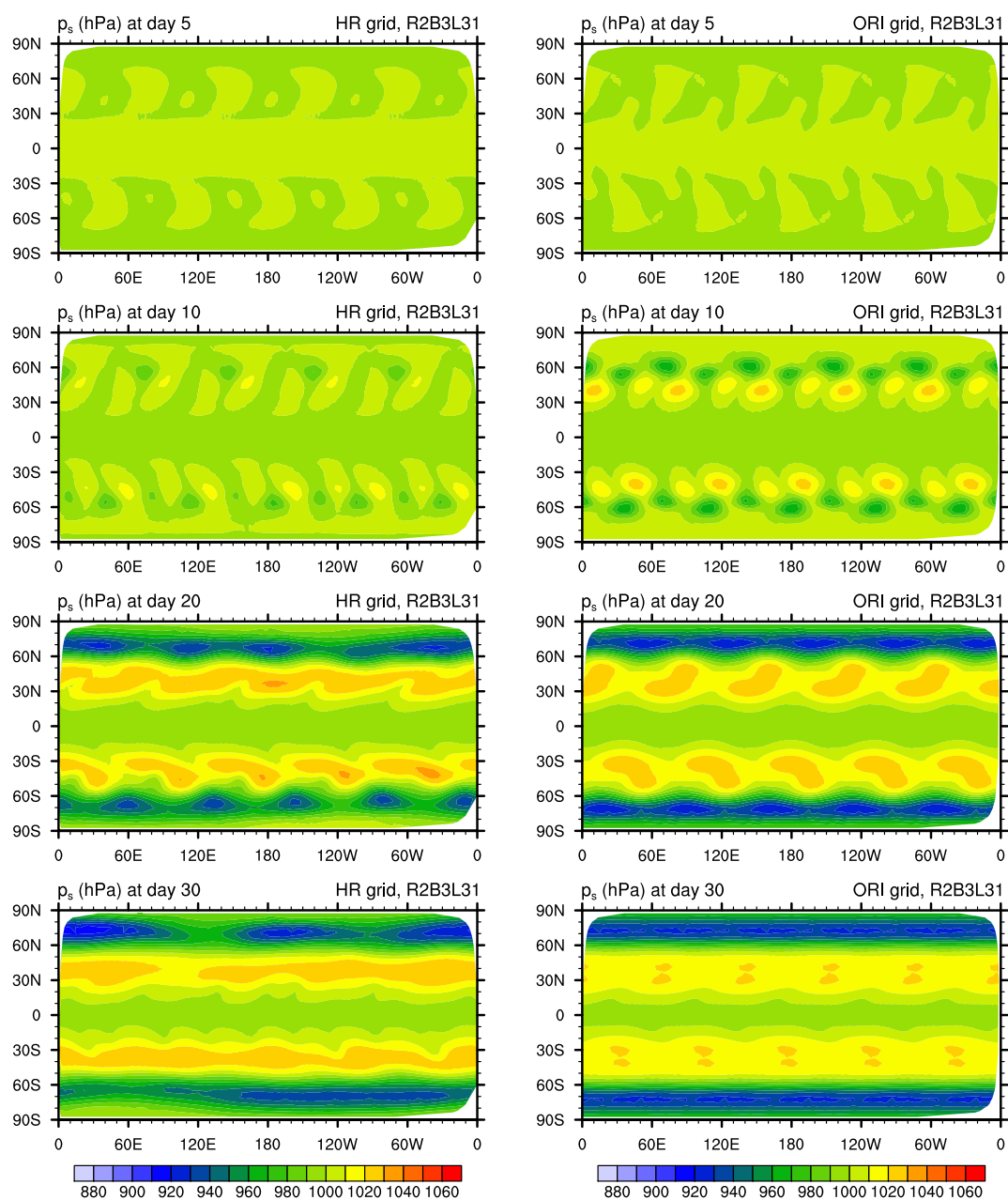


Fig. E.1: Sensitivity of the simulated surface pressure to grid optimization in the Jablonowski-Williamson steady state test. The left column shows results obtained on the Heikes-Randall optimized grid; The right column displays the integration performed on the original icosahedral grid. All the other settings are the same for both simulations: R2B3L31 resolution, semi-implicit time integration scheme with the 2D solver and 1200-second time step, the original divergence operator.

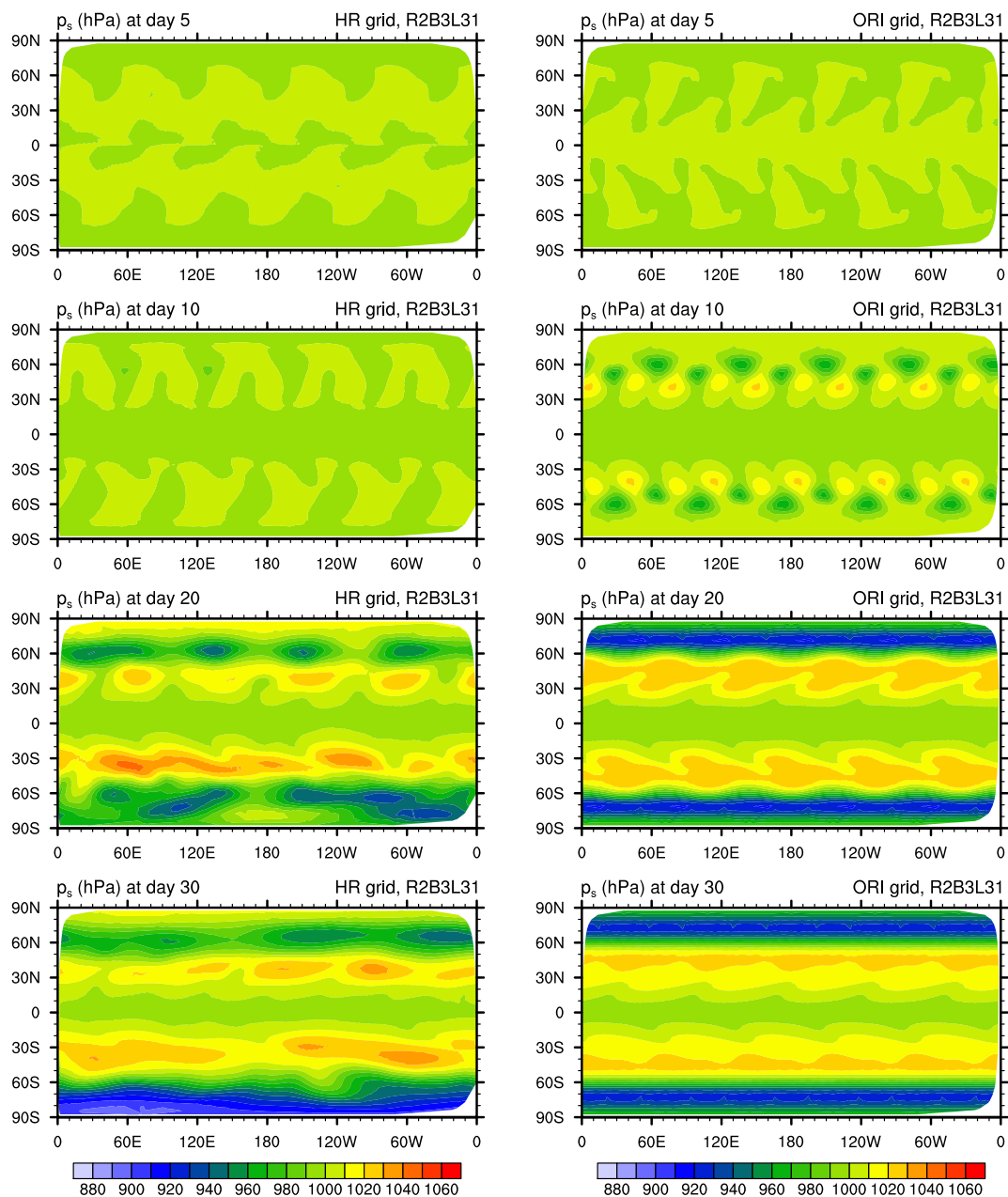


Fig. E.2: As in Fig. E.1 but using the modified divergence operator defined by Eqn. (2.54).

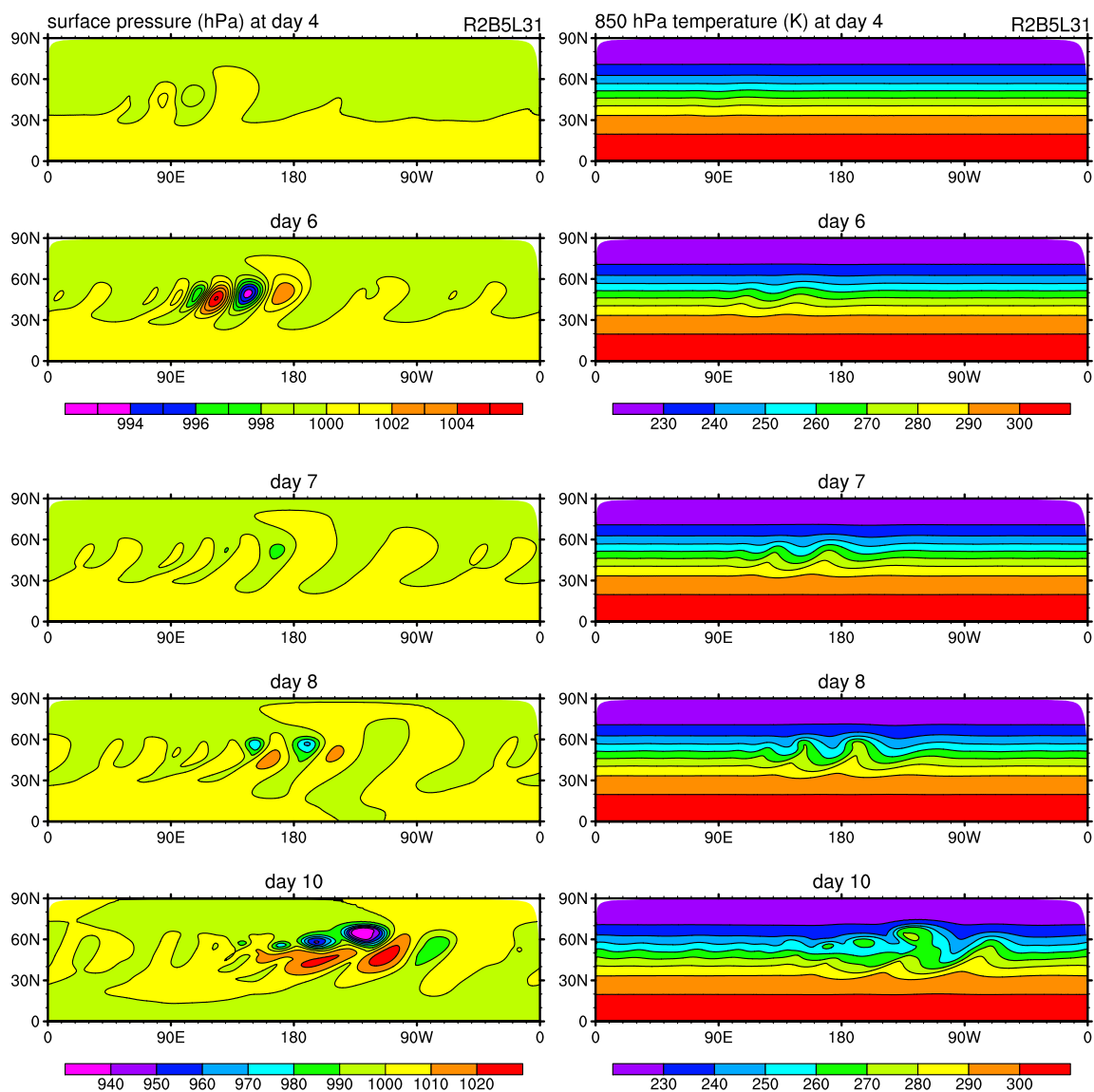


Fig. E.3: Evolution of the surface pressure (left) and 850 hPa temperature (right) in the Jablonowski-Williamson baroclinic wave test performed with the ICOHDC at resolution R2B5L31 using the original divergence operator defined by Eqn. (2.6). The horizontal diffusion parameter used is $\Delta t_D / \tau^* = 4/3$.

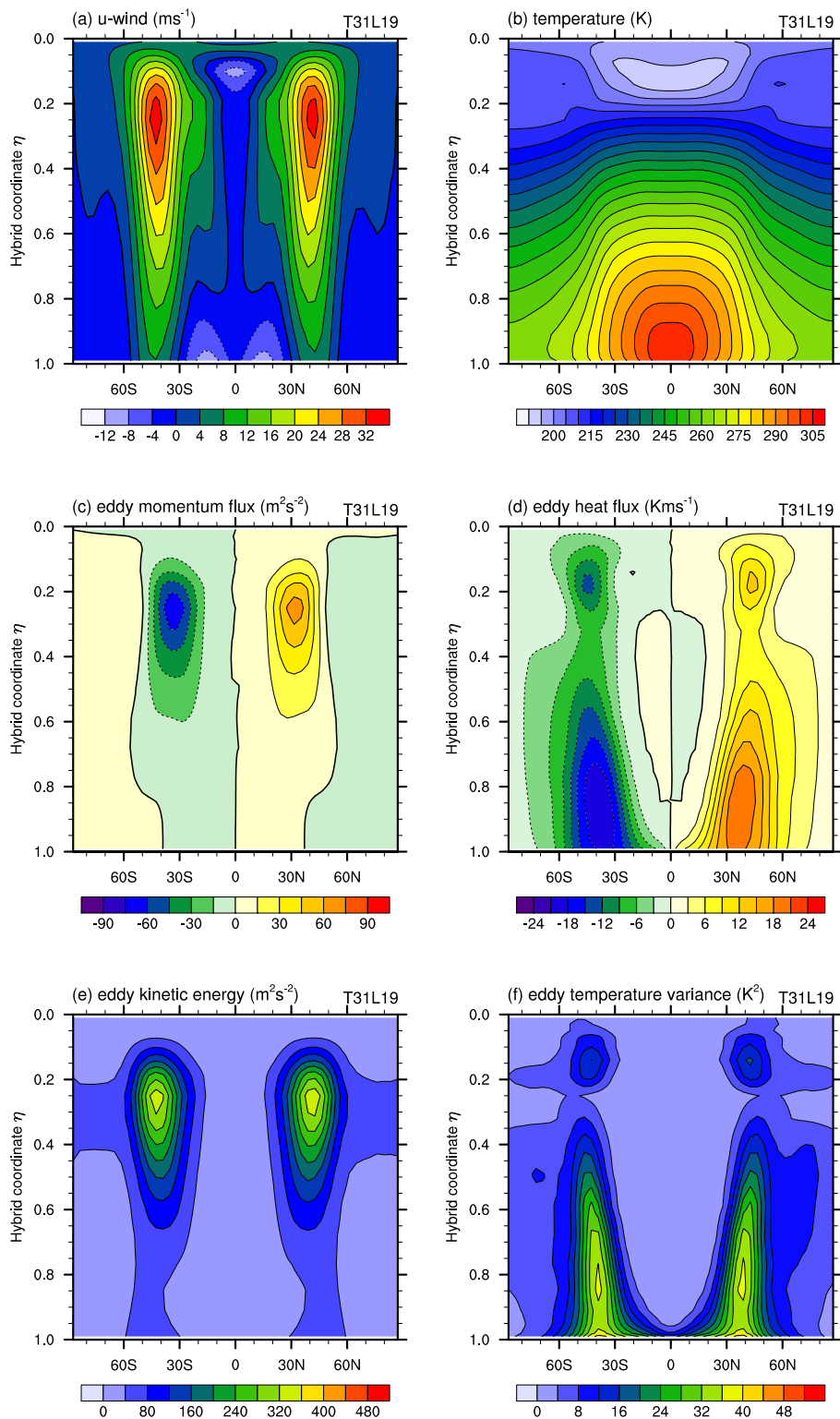


Fig. E.4: The zonal mean climate state of the Held-Suarez test simulated by the dynamical core of ECHAM5 at T31L19 resolution. See Section 4.6.1 for further details of the experiments.

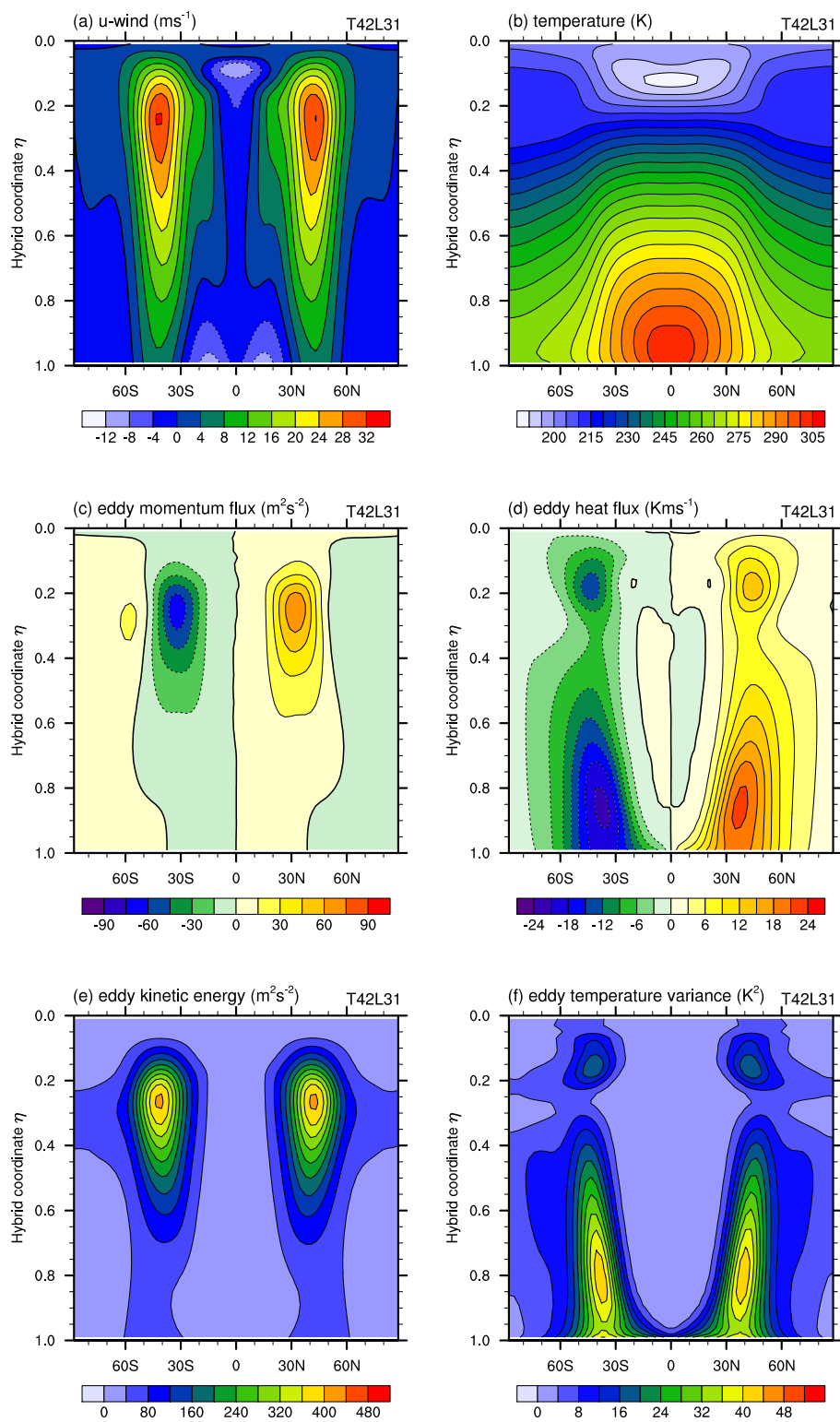


Fig. E.5: As in Fig. E.4 but at T42L31 resolution.

Bibliography

- Arakawa A. and Lamb V. (1977). *Computational design of the basic dynamical process of the UCLA GCM.*, pp. 173–265. J. Chang ed., Academic Press.
- Arakawa A. and Suarez M. (1983). Vertical differencing of the primitive equations in sigma coordinates. *Mon. Wea. Rev.* 111, pp. 34–45.
- Asselin F. (1972). Frequency filter for time integrations. *Mon. Wea. Rev.* 100, pp. 487–490.
- Baines P. G. (1976). The stability of planetary waves on a sphere. *Journal of Fluid Mechanics* 73(2), pp. 193–213.
- Bates J. R., Li Y., Brandt A., McCormick S. F., and Ruge J. (1995). A global shallow-water numerical model based on the semi-Lagrangian advection of potential vorticity. *Quarterly Journal of the Royal Meteorological Society* 121, pp. 1981–2005.
- Baudisch J., Bonaventura L., Iske A., and Miglio E (2006). Matrix-valued radial basis functions for local vector field reconstruction in computational fluid dynamics models. MOX Report 75, MOX Laboratorio di Modellistica e Calcolo Scientifico, Dipartimento di Matematica "F. Brioschi", Politecnico di Milano.
- Baumgardner J.R. and Frederickson P.O. (1985). Icosahedral discretization of the two-sphere. *SIAM Journal of Scientific Computing* 22(6), pp. 1107–1115.
- Boer G. J. (1995). A hybrid moisture variable suitable for spectral GCMs. *Research Activities in Atmospheric and Oceanic Modelling*, WMO/TD-No. 665, World Meteorological Organization, Geneva.
- Boer G. J. and Denis B. (1997). Numerical convergence of the dynamics of a GCM. *Climate Dynamics* 13, pp. 359–374.
- Bonaventura L. and Ringler T. (2005). Analysis of discrete shallow water models on geodesic Delaunay grids with C-type staggering. *Mon. Wea. Rev.* 133, pp. 2351–2373.
- Burridge D. M. and Haseler J. (1977). A model for medium range weather forecasting - adiabatic formulation. Technical Report 4, ECMWF, Reading, UK.
- Charney J. G., Fjórtoft R., and von Neumann J. (1950). Numerical integration of the barotropic vorticity equation. *Tellus* 2, pp. 237–254.

- Courtier P. and Naughton M. (1994). A pole problem in the reduced gaussian grid. *Quarterly Journal of the Royal Meteorological Society* 120, pp. 1389–1407.
- Cullen M.J.P. (1974). Integration of the primitive barotropic equations on a sphere using the finite element method. *Q. J. Roy. Meteor. Soc.* 100, pp. 555.
- Dunst M. and Roeckner E. (1975). A numerical investigation of the connexion between two-dimensional momentum transfer and jetstream formation. *Pure and Applied Geophysics* 113, pp. 549–559.
- Durran D. and Klemp J. (1983). A compressible model for the simulation of moist mountain waves. *Mon. Wea. Rev.* 111, pp. 2341–2361.
- Durran D. R. (1998). *Numerical methods for wave equations in geophysical fluid dynamics*. Springer.
- Eliassen E., Machenhauer B., and Rasmussen E. (1970). On a numerical method for integration of the hydrodynamical equations with a spectral representation of the horizontal fields. Technical Report 2, Institute of Theoretical Meteorology, University of Copenhagen.
- Gates W. L. and Riegel C. L. (1962). A study of numerical errors in the integration of barotropic flows on a spherical grid. *J. Geophys. Res.* 67, pp. 773–784.
- Giraldo Francis X. (2000). Lagrange-Galerkin methods on spherical geodesic grids: The shallow water equations. *J. Comput. Phys.* 160, pp. 336–368.
- Giraldo F. X. and Rosmond T. E. (2004). A scalable spectral element Eulerian atmospheric model (SEE-AM) for NWP: dynamical core tests. *Monthly Weather Review* 132, pp. 133–153.
- Grose W. L. and Hoskins B. J. (1979). On the influence of orography on large-scale atmospheric flow. *J. Atmos. Sci.* 36, pp. 223–234.
- Gross E.S., Bonaventura L., and Rosatti G. (2002). Consistency with continuity in conservative advection schemes for free-surface models. *International Journal of Numerical Methods in Fluids* 38, pp. 307–327.
- Haltiner G. L. and Martin F. L. (1957). *Dynamical and Physical Meteorology*. McGraw-Hill.
- Haurwitz B. (1940). The motion of atmospheric disturbances on the spherical earth. *Journal of Marine Research* 3, pp. 254–267.
- Heikes R. and Randall D. A. (1995a). Numerical integration of the shallow-water equations on a twisted icosahedral grid. Part I: Basic design and results of tests. *Mon. Wea. Rev.* 123, pp. 1862–1880.
- Heikes R. and Randall D. A. (1995b). Numerical integration of the shallow-water equations on a twisted icosahedral grid. Part II: A detailed description of the grid and an analysis of numerical accuracy. *Mon. Wea. Rev.* 123, pp. 1881–1887.

- Held I. M. and Suarez M. J. (1994). A proposal for the intercomparison of the dynamical cores of atmospheric general circulation models. *Bull. Amer. Meteorol. Soc.* 73, pp. 1825–1830.
- Hortal M. and Simmons A. J. (1991). Use of reduced gaussian grids in spectral models. *Mon. Wea. Rev.* 119, pp. 1057–1074.
- Hoskins B. J. (1973). Stability of the Rossby-Haurwitz wave. *Quarterly Journal of the Royal Meteorological Society* 99(422), pp. 723–745.
- Hoskins B. J. and Karoly D. J. (1981). The steady linear response of a spherical atmosphere to the thermal and orographic forcing. *J. Atmos. Sci.* 38, pp. 1179–1196.
- Hoskins B. J. and Simmons A. J. (1975). A multi-layer spectral model and the semi-implicit method. *Quarterly Journal of the Royal Meteorological Society* 101, pp. 637–665.
- Hoskins B. J., Simmons A. J., and Andrews D. G. (1977). Energy dispersion in a barotropic atmosphere. *Quarterly Journal of the Royal Meteorological Society* 103, pp. 553–567.
- Jablonowski C. (1998). Test of the dynamics of two global weather prediction models of the german weather service: The Held-Suarez test. Diploma thesis (in german), Meteorological Institute of the University of Bonn, Germany.
- Jablonowski C., Lauritzen P., Nair R., and Taylor M. (2008). Idealized test cases for the dynamical cores of atmospheric general circulation models: A proposal for the near asp 2008 summer colloquium. Technical report, NCAR, Boulder, Colorado.
- Jablonowski C. and Williamson D. L. (2006a). A baroclinic instability test case for atmospheric model dynamical cores. *Quarterly Journal of the Royal Meteorological Society* 132, pp. 2943–2975.
- Jablonowski C. and Williamson D. L. (2006b). A baroclinic wave test case for dynamical cores of general circulation models: model intercomparisons. NCAR Technical Note NCAR/TN-469+STR, NCAR, Boulder, Colorado.
- Jakob R., Hack J. J., and Williamson D. L. (1993). Solutions to the shallow water test set using the spectral transform model. NCAR Technical Note TN-388+STR, National Center for Atmospheric Research, Boulder, Colorado, USA.
- Jöckel P., von Kuhlmann R., Lawrence M.G., Steil B., Brenninkmeijer C.A.M., Crutzen P.J., Rasch P.J., and Eaton B. (2001). On a fundamental problem in implementing flux-form advection schemes for tracer transport in 3-dimensional general circulation and chemistry transport models. *Q. J. Roy. Meteor. Soc.* 127, pp. 1035–1052.
- Kasahara A. (1974). Various vertical coordinate systems used for numerical weather prediction. *Mon. Wea. Rev.* 102, pp. 509–522.
- Kreiss H.-O. and Olinger J. (1972). Comparison of accurate methods for the integration of hyperbolic equations. *Tellus* 24, pp. 199–215.

- Kuo H.-L. (1949). Dynamic stability of two-dimensional nondivergent flow in a barotropic atmosphere. *Journal of Meteorology* 6, pp. 105–122.
- Kurihara Y. (1965). Numerical integration of the primitive equations on a spherical grid. *Mon. Wea. Rev.* 93, pp. 399–415.
- Li X., Chen D., Peng X., Takahashi K., and Xiao F. (2008). Multimoment finite-volume shallow-water model on the Yin-Yang overset spherical grid. *Mon. Wea. Rev.* 136, pp. 3066–3086.
- Lin S.-J. (2004, october). A "vertically Lagrangian" finite-volume dynamical core for global models. *Mon. Wea. Rev.* 132, pp. 2293–2307.
- Lin S.-J. and Rood R. B. (1996, September). Multidimensional flux-form semi-Lagrangian transport schemes. *Mon. Wea. Rev.* 124, pp. 2046–2070.
- Lorenz E. N. (1960). Energy and numerical weather prediction. *Tellus* 12, pp. 364–373.
- Lorenz E. N. (1972). Barotropic instability of rossby wave motion. *Journal of the Atmospheric Sciences* 29(2), pp. 258–265.
- Lynch Peter (2006). *The Emergence of Numerical Weather Prediction: Richardson's Dream*. Cambridge University Press.
- Majewski D., Liermann D., Prohl P., Ritter B., Buchhold M., Hanisch T., Paul G., Wergen W., and Baumgardner J. (2002). The operational global icosahedral-hexagonal gridpoint model GME: description and high resolution tests. *Mon. Wea. Rev.* 130, pp. 319–338.
- Masuda Y. and Ohnishi H. (1986). An integration scheme of the primitive equation model with a icosahedral-hexagonal grid system and its application to the shallow water equations. *Proceedings of the WMO/IUGG NWP Symposium, Tokyo*, pp. 317. Japan Meteorological Agency.
- Merryfield W. J., McFarlane N., and Lazare M. (2003). A generalized hybrid transformation for tracer advection. *Research Activities in Atmospheric and Oceanic Modelling*, WMO/TD-No. 1161a, World Meteorological Organization, Geneva.
- Monaco A. V. and Williams R. T. (1975). An atmospheric global prediction model using a modified Arakawa differencing scheme. Technical Report NPS-51WU75041, Dept. of Meteorology, Naval Postgraduate School, Monterey, CA.
- Nair R. D., Thomas S. J., and Loft R. D. (2004). A discontinuous galerkin global shallow water model. *Mon. Wea. Rev.* 132, pp. 876–888.
- Orszag S. A. (1970). Transform method for calculation of vector coupled sums. *J. Atmos. Sci.* 27, pp. 890–895.
- Phillips N. A. (1959). Numerical integration of the primitive equations on the hemisphere. *Monthly Weather Review* 87, pp. 333–345.

- Polvani L. M., Scott R. K., and Thomas S. J. (2004, November). Numerically converged solutions of the global primitive equations for testing the dynamical core of atmospheric models. *Mon. Wea. Rev.* 132, pp. 2539–2552.
- Pope V. D. and Stratton R. A. (2002). The processes governing horizontal resolution sensitivity in a climate model. *Climate Dynamics* 19, pp. 211–236.
- Press William H., Teukolsky Saul A., Vetterling William T., and Flannery Brian P. (1992). *Numerical Recipes in Fortran 77: The Art of Scientific Computing* (Second ed.). Cambridge University Press.
- Press William H., Teukolsky Saul A., Vetterling William T., and Flannery Brian P. (1996). *Numerical Recipes in Fortran 90: The Art of Parallel Scientific Computing* (Second ed.). Cambridge University Press.
- Randall D.A. (1994). Geostrophic adjustment and the finite-difference shallow water equations. *Mon. Wea. Rev.* 122, pp. 1371–1377.
- Richardson Lewis F. (1922). *Weather Prediction by numerical process*. Cambridge University Press. Reprinted by Dover Publications, New York, 1965.
- Ringler T.D., Heikes R.P., and Randall D.A. (2000). Modeling the atmospheric general circulation using a spherical geodesic grid: A new class of dynamical cores. *Mon. Wea. Rev.* 128, pp. 2471–2490.
- Ringler T.D. and Randall D.A. (2002a). A potential enstrophy and energy conserving numerical scheme for solution of the shallow-water equations a geodesic grid. *Mon. Wea. Rev.* 130, pp. 1397–1410.
- Ringler T.D. and Randall D.A. (2002b, May). The ZM grid: an alternative to the Z grid. *Mon. Wea. Rev.* 130, pp. 1411–1422.
- Robert A. (1981). A stable numerical integration scheme for the primitive meteorological equations. *Atmos.-Ocean* 19, pp. 35–41.
- Robert A. (1982). A semi-Lagrangian and semi-implicit numerical integration scheme for the primitive meteorological equations. *J. Met. Soc. Japan* 60, pp. 319–325.
- Robert A. (1992). Bubble convection experiments with a semi-implicit formulation of the euler equations. *J. Atmos. Sci.* 50, pp. 1865–1873.
- Robert A., Henderson J., and Turnbull C. (1972). An implicit time integration scheme for baroclinic models of the atmosphere. *Mon. Wea. Rev.* 100, pp. 329–335.
- Roeckner E., Bäuml G., Bonaventura L., Brokopf R., Esch M., Giorgetta M., Hagemann S., Kirchner I., Kornbluh L., Manzini E., Rhodin A., Schlese U., Schulzweida U., and Tompkins A. (2003). The atmospheric general circulation model ECHAM5. PART I: model description. Technical Report 349, Max Planck Institute for Meteorology, Hamburg, Germany.

- Roeckner E., Brokopf R., Esch M., Giorgetta M., Hagemann S., Kornbluh L., Manzini E., Schlese U., and Schulzweida U. (2006). Sensitivity of simulated climate to horizontal and vertical resolution in the ECHAM5 atmosphere model. *J. Clim.* 19, pp. 3371–3791.
- Rossby C.-G. (1939). Relation between variations in the intensity of the zonal circulation of the atmosphere and the displacements of the semi-permanent centres of action. *Journal of Marine Research* 2, pp. 38–55.
- Rossby C.-G. (1945). On the propagation of frequencies and energy in certain types of oceanic and atmospheric waves. *J. Met.* 2, pp. 187–203.
- Saad Y. and Schultz M. H. (1986). GMRES: A generalized minimal residual algorithm for solving nonsymmetric linear systems. *SIAM J. Sci. Stat. Comput.* 7, pp. 856–859.
- Sadourny R., Arakawa A., and Mintz Y. (1968). Integration of the nondivergent barotropic vorticity equation with a icosahedral-hexagonal grid for the sphere. *Mon. Wea. Rev.* 96, pp. 351–356.
- Sadourny R. and Morel P. (1969). A finite difference approximation of the primitive equations for a hexagonal grid on a plane. *Mon. Wea. Rev.* 97, pp. 439–445.
- Satoh M., Matsuno T., Tomita H., Miura H., Nasuno T., and Iga S. (2008). Nonhydrostatic icosahedral atmospheric model (NICAM) for global cloud resolving simulations. *J. Comput. Phys.* 227, pp. 3486–3514.
- Schär C., Leuenberger D., Fuhrer O., and Lüthi D. (2002). A new terrain-following vertical coordinate formulation for atmospheric prediction models. *Mon. Wea. Rev.* 130, pp. 2459–2480.
- Scinocca J. F., McFarlane N. A., Lazare M., Li J., and Plummer D. (2008). The CCCma third generation AGCM and its extension into the middle atmosphere. *Atmospheric Chemistry and Physics Discussions* 8, pp. 7883–7930.
- Simmons A. J. and Burridge D. M. (1981). An energy and angular-momentum conserving vertical finite difference scheme and hybrid vertical coordinates. *Mon. Wea. Rev.* 109, pp. 758–766.
- Simmons A. J. and Chen J. (1991). The calculation of geopotential and pressure-gradient in the ecmwf atmospheric model: Influence on the simulation of the polar atmosphere and on temperature analyses. *Quarterly Journal of the Royal Meteorological Society* 117, pp. 29–58.
- Simmons A. J. and Strüfing R. (1981). An energy and angular-momentum conserving finite difference scheme, hybrid coordinates and medium-range weather prediction. Technical Report 28, ECMWF, Reading, UK.
- Stuhne G. R. and Peltier W.R. (1996). Vortex erosion and amalgamation in a new model of large scale flow on the sphere. *J. Comput. Phys.* 128, pp. 58–81.

- Stuhne G. R. and Peltier W.R. (1999). New icosahedral grid-point discretizations of the shallow water equations on the sphere. *J. Comput. Phys.* 148, pp. 23–58.
- Swinbank R. and Purser R. J. (2006). Fibonacci grids: A novel approach to global modelling. *Q. J. Roy. Meteor. Soc.* 132, pp. 1769–1793.
- Thuburn J. (1997, September). A PV-based shallow-water model on a hexagonal-icosahedral grid. *Mon. Wea. Rev.* 125, pp. 2328–2347.
- Thuburn J. and Li Y. (2000). Numerical simulations of Rossby-Haurwitz waves. *Tellus* 52A, pp. 181–189.
- Tomita H. and Satoh M. (2004). A new dynamical framework of nonhydrostatic global model using the icosahedral grid. *Fluid Dyn. Res.* 34, pp. 357–400.
- Tomita H., Tsugawa M., M.Satoh, and K.Goto (2001). Shallow water model on a modified icosahedral grid by using spring dynamics. *J. Comput. Phys.* 174, pp. 579–613.
- von Storch H. and Zwiers F. W. (2001). *Statistical analysis in climate research*. Cambridge University Press.
- Wan H., Giorgetta M. A., and Bonaventura L. (2008). Ensemble held-suarez test with a spectral transform model: variability, sensitivity, and convergence. *Mon. Wea. Rev.* 136, pp. 1075–1092.
- Williamson D. L. (1968). Integration of the barotropic vorticity equation on a spherical geodesic grid. *Tellus* 20, pp. 642–653.
- Williamson D. L. (1969). Numerical integration of fluid flow over triangular grids. *Mon. Wea. Rev.* 97, pp. 885–895.
- Williamson D. L. (1970). Integration of the primitive barotropic model over a spherical geodesic grid. *Mon. Wea. Rev.* 98, pp. 885–895.
- Williamson D. L. and Browning G. L. (1973). Comparison of grids and difference approximations for numerical weather predicition over a sphere. *J. Appl. Meteorol.* 12, pp. 264–274.
- Williamson D. L., Drake J. B., Hack J. J., Jakob R., and Swarztrauber R. N. (1992). A standard test set for numerical approximations to the shallow water equations in spherical geometry. *J. Comput. Phys.* 102, pp. 221–224.
- Williamson D. L., Olson J. G., and Boville. B. A (1998). A comparison of semi-lagrangian and eulerian tropical climate simulations. *Mon. Wea. Rev.* 126, pp. 1001–1012.
- Williamson D. L. and Rosinski J. M (2000). Accuracy of reduced-grid calculations. *Quarterly Journal of the Royal Meteorological Society* 126, pp. 1619,1640.
- Winninghoff F.J. (1968). On the adjustment toward a geostrophic balance in a simple primitive equation model. Ph.D. Thesis, UCLA.

Yeh T. (1949). On energy dispersion in the atmosphere. *J. Met.* 6, pp. 1–16.

Zhang X.-H., Bao N., Yuan C.-G., and Zeng Q.-C. (1987). Study on the sensitivity of dynamical frame of a general circulation model on initial conditions. *Sci Sinica*.

Zhang X.-H., Zeng Q.-C., and Bao N. (1986). Nonlinear baroclinic Haurwitz waves. *Advances in Atmospheric Sciences* 3, pp. 330–340.

Acknowledgements

A lot of people have contributed in different ways to this thesis, to whom I would like to express my gratitude.

First and foremost, I thank my supervisors Dr. Marco A. Giorgetta and Prof. Dr. Guy P. Brasseur for giving me the opportunity to work on this exciting and challenging topic. Marco provided invaluable guidance throughout my work. Without his steady support, the accomplishment of this thesis could not have been possible. I am grateful to Prof. Brasseur for his keen interest in my work which always made me feel greatly encouraged.

Many thanks to all my ICON colleagues for their cooperation and encouragement. The comments and suggestions from Dr. Marco Restelli on the truncation error analysis, and those from Dr. Almut Gassman and Mr. Detlev Majewski on the time integration schemes were particularly helpful. I also thank Dr. Christiane Jablonowski, Dr. David L. Williamson and Dr. Francis X. Giraldo for helpful discussions on the idealized test cases. The service and help provided by the German Climate Computing Centre (DKRZ) were indispensable for this thesis.

It could not have been possible for me to come to Hamburg without being a member of the International Max Planck Research School on Earth System Modelling. The stipend provided by the ZEIT Foundation "Ebelin and Gerd Bucerius" is acknowledged. I am also greatly indebted to Dr. Antje Weitz and Ms. Cornelia Kampmann for their support.

I would like to thank Mrs. Hanna Stadelhofer, head of the International Office of the MPI-M, and my friends Yingpin Wang, Rita Seiffert, Heinz-Jürgen Punge, Xiuhua Zhu, Dorteia Banse, Qian Li, and Daniela Matei. Their kind help made my life in Germany much more enjoyable.

Deep gratitude goes to my parents and my parents-in-law for their loving considerations and constant support. Last but not least, special thanks to my husband Kai, for his love, patience, and encouragement.

Die gesamten Veröffentlichungen in der Publikationsreihe des MPI-M
„Berichte zur Erdsystemforschung“,
„Reports on Earth System Science“,
ISSN 1614-1199

sind über die Internetseiten des Max-Planck-Instituts für Meteorologie erhältlich:

<http://www.mpimet.mpg.de/wissenschaft/publikationen.html>

